BATES
LARGE ACCEPTANCE
SPECTROMETER TOROID

Technical Design Report

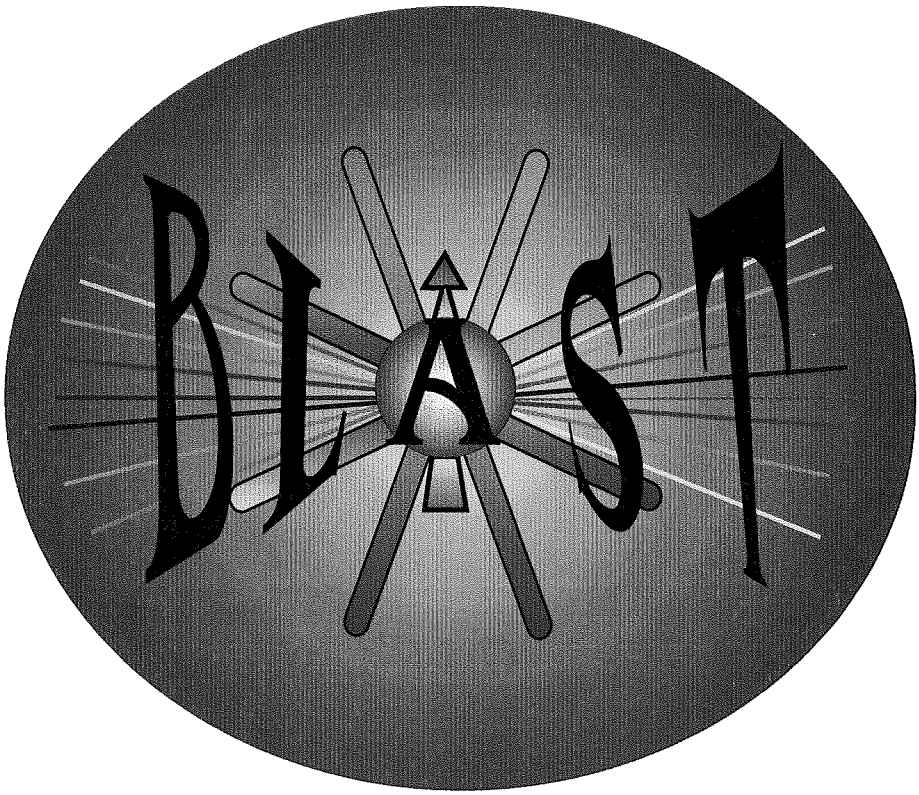

The BLAST Collaboration

http://mitbates.mit.edu/~blast/

August 8, 1997

Contents

1 INTRODUCTION

The Bates Large Acceptance Spectrometer Toroid (BLAST) is a detector designed to study in a comprehensive and precise way the spin-dependent electromagnetic response of few-body nuclei at momentum transfers up to 1 $(\mathrm{GeV/c})^2$ at the MIT-Bates South Hall Ring. It will be used to measure spin-dependent scattering from the elastic to the nucleon resonance region from the proton, deuteron and ^{3}He nuclei by using the longitudinally polarized electron beam of the South Hall Ring at beam energies up to 1 GeV. For these measurements we will use polarized internal gas targets of hydrogen, deuterium and ^{3}He which have been developed by our groups and which are at present operating in other storage rings. Polarized electrons are available at the MIT-Bates Accelerator and have been injected into the ring. The longitudinal polarization at the internal target location will be maintained with a Siberian snake. The ability with BLAST to carry out multiparticle detection over a large solid angle from polarized internal targets will provide an unprecedented and unique opportunity to study simultaneously the spin structure of the few-body nuclear ground states, the reaction mechanism, and nucleon form factors.

The BLAST detector consists of an eight-sector copper coil array producing a toroidal magnetic field, instrumented with two opposing wedge-shaped sectors of wire chambers, scintillation detectors, Čerenkov counters, neutron detectors, a lead glass forward calorimeter and recoil detectors. The open geometry maximizes acceptance while allowing good momentum and angular resolution, and with a luminosity capability that is matched to the densities of the polarized internal targets. The design emphasizes proven technology, commercial electronics, and existing data acquisition system software to achieve low cost and a short implementation time. Clear upgrade possibilities exist so that the detector can evolve to match developing physics priorities.

The BLAST program is made possible by advances in polarized internal target technology. In the past five years members of our collaboration have been leaders in efforts to realize this new technology in experiments at IUCF, NIKHEF, and DESY. The significant advantages over conventional approaches with extracted beams have been demonstrated and are reliable. Routine performance levels have been established which are the basis for the conservative estimates of anticipated results in this document.

The experimental program with BLAST will utilize a thin-walled storage cell that is fed by a high intensity source of polarized atoms providing a target of thickness $2 - 20 \times 10^{14}$ atoms cm^{-2}. This novel technique is superior to conventional polarized target technology because the target atoms are present as pure atomic species, and hence no dilution of the asymmetry occurs in the scattering from unpolarized target material. In addition, polarized internal gas targets allow rapid reversal of the target spin. The expected luminosity for an 80-mA circulating electron beam is $1 - 10 \times 10^{32}$ atoms $\mathrm{cm}^{-2}\mathrm{s}^{-1}$. Such values allow for measurement of the spin-dependent electromagnetic response over a broad kinematic region, for many reaction channels simultaneously, in relatively short data taking

runs with high statistical precision. High statistical precision and the ability to reverse the target spin rapidly are crucial to understanding and minimizing systematic uncertainties.

BLAST takes maximum advantage of the capabilities afforded by the Bates South Hall Ring. This new facility provides the opportunity to utilize polarized internal gas targets which are basic to the proposed experimental scheme. In addition, the high duty factor of the stored electron beam is necessary for multi-particle coincidence detection.

The BLAST collaboration consists of groups from Armenia, Switzerland, the Netherlands and the United States. This Technical Design Report had its origins in a workshop organized by the Bates user community in June, 1989 to consider how best to exploit the new capabilities provided by the Bates South Hall Ring (SHR). The BLAST collaboration was formed in February, 1990 and a Conceptual Design report was prepared in January, 1991. This design was favorably reviewed by a Technical Advisory Panel in April, 1991, and 3,200 hours of beamtime with BLAST were approved by the Bates Program Advisory Committee in May, 1991. In September, 1991 the BLAST proposal was submitted to the Department of Energy and the National Science Foundation for review. In March, 1992 an international workshop on the BLAST physics program attracted 56 physicists to Tempe, Arizona. In 1996 an updated proposal that focussed on the scientific case and which incorporated cost-saving revisions was favorably reviewed by the Department of Energy. In December 1996 funding approval to construct the BLAST detector was granted.

In this report we focus on the technical design of the apparatus required to carry out the approved BLAST physics program. There are about 50 physicists from 12 institutions in the BLAST collaboration. The total cost of the BLAST spectrometer in FY97 dollars including a 20% contingency is $ 4.42 M. This total cost amounts to $ 4.65 M in actual year dollars. We propose a schedule to build BLAST by the end of FY00.

The document is divided into 9 sections. Section 2 provides an overview of the BLAST physics program and Section 3 contains a summary of the technical aspects of the measurements. The properties and implementation plans of the required polarized stored beam in the ring are presented Section 4. The ^{3}He, ^{2}H, and ^{1}H polarized internal gas targets to be used in the initial program of measurements are described in Section 5. A technical description of BLAST, including designs, construction plans and costs, is presented in Section 6. Monte Carlo simulations of BLAST with the code GEANT are presented in Section 7. Section 8 contains a summary of the costs and the schedule to construct the device. Finally, the organization of the manpower and institutional responsibilities are discussed in Section 9.

In summary, this document presents the technical plan for a large solid angle toroidal spectrometer at the internal target location in the Bates South Hall Ring.

2 SCIENTIFIC PROGRAM

2.1 INTRODUCTION

Medium-energy electromagnetic nuclear physics experiments at Bates and other laboratories worldwide in the 1970s and 80s have provided the empirical basis for a partly successful description of few-body nuclei based on hadronic degrees of freedom. For momentum transfers up to about 1 $(\mathrm{GeV/c})^2$, measurements of elastic form factors for the deuteron, the isovector/isoscalar decomposition of ^{3}He and ^{3}H elastic form factors, and quasielastic (e,e'p) measurements have been reasonably described by a non-relativistic theory based on meson and nucleon degrees of freedom. This work has resulted in a moderately successful description of the strong interaction in few-body systems in the non-perturbative region. Thus far, it has not been possible to perform accurate calculations at low Q^2 by using the fundamental theory, Quantum Chromodynamics. The hadronic framework for few-body systems in this kinematic region has been established as one of the most successful in strong interaction physics although significant and possibly serious discrepancies between theory and experiment exist.

However, the insights obtained in the past two decades have raised many new questions with respect to the nuclear structure of few-body systems. Most importantly, how well do we understand the spin of few-body nuclei in terms of the hadronic framework? Note that recent measurements of spin-dependent deep-inelastic scattering show that our understanding of the spin of the nucleon at the quark level is incomplete. A significant issue since the 1980s is the consistency of the transverse and longitudinal responses in medium-energy electron scattering obtained from Rosenbluth separations at quasielastic kinematics. The measurement of spin observables provides new response functions. How consistent are the new response functions? Essentially all measurements of electron scattering on few-body nuclei at low Q^2 have been carried out with relatively small-acceptance spectrometers. This situation has resulted in an incomplete understanding of the reaction mechanism at medium energies. How can a comprehensive understanding of the reaction mechanism over a large kinematic region be obtained? The charge distribution of the neutron is physically understood in terms of an extended pion cloud. Is this charge distribution modified when the neutron is bound in a nucleus? In many cases, while significant progress has been made in establishing the dominant aspects of the problem, serious questions remain concerning the relatively smaller but no less important issues. Examples are: how large are the pre-existing Δ components in few-body systems? What is the magnitude of the small ($\sim 1\%$) S' component in ^{3}He? What is the role of the $C2$ and $E2$ contributions to the $N \rightarrow \Delta$ transition? To answer the above questions, it is important to probe the spin structure of few-body nuclei using the electromagnetic probe.

The experiments which provided the basis for our present understanding of the structure of few-body systems were carried out mostly with unpolarized electron beams and unpolarized nuclear targets. The ability to carry out measurements of spin observables simultaneously over a large kinematic range has been demonstrated at IUCF. The sepa-

ration of different contributions to the reaction mechanism beyond that which is possible with a small-acceptance detector has greatly enriched our understanding of the physics.

A central thrust of the BLAST physics program is to carry out a comprehensive and precise measurement of the electromagnetic spin-dependent response from few-body systems for momentum transfers up to 1 $(\mathrm{GeV/c})^2$. The addition of the spin degree of freedom is important for several reasons. Firstly, the determination of the spin structure of few-body nuclei is an important aspect for understanding the strong interaction in these systems. Moreover, in few-body nuclei, spin involves all of the nucleons, unlike heavier systems where spin effects tend to cancel. Secondly, the addition of spin as an extra degree of freedom allows access to small components of the wave function or reaction mechanism. In this way a "super-Rosenbluth" separation can be carried out to isolate new quantities that are not accessible with unpolarized experiments.

Few-body systems continue to be the focus of considerable theoretical effort. Precise relativistic and non-relativistic calculations are available for the deuteron. Recently, considerable progress has been achieved in the theoretical description of the three-body system, by realizing a Faddeev solution of the continuum wave function. Variational techniques which can be applied to heavier nuclei have also been developed.

The BLAST detector will enable the following studies:

- BLAST will carry out a precise measurement of the spin-dependent momentum distribution in few-body nuclei. It is important to understand the spin structure of few-body systems in terms of the successful theoretical framework which has been developed primarily for unpolarized scattering. In addition, the spin-dependent momentum distributions are used as input for calculations of spin-dependent scattering in the deep-inelastic region where polarized deuterium and ^{3}He are used to determine the neutron spin structure at the quark level.

- BLAST will provide precise information on nucleon form factors for momentum transfers up to about 1 $(\mathrm{GeV/c})^2$. In particular, BLAST will provide data on the neutron magnetic and electric form factors with both deuteron and ^{3}He targets. These are fundamental quantities which are essential to any description of electromagnetic scattering from nuclei. BLAST offers the unique possibility to determine $G_E^n(Q^2)$ with high precision from both deuteron and ^{3}He targets with the same experimental configuration. Because of the significantly larger binding energy of the neutron in ^{3}He compared to that in deuterium, it is possible that the neutron charge distribution in ^{3}He may be modified from its free value. BLAST has the necessary precision to probe for such an effect.

- BLAST will provide a test of our understanding of the spin-dependent scattering reaction mechanism over a large kinematic range. Determination of both the ground-state spin structure and the nucleon form factors rely on applicability of the Plane Wave Impulse Approximation (PWIA). It is known from unpolarized experiments that other effects such as final-state interactions, meson exchange currents, and the

off-shell nature of the bound nucleon can cause significant deviations from PWIA in certain kinematic regions. It is essential to understand the spin-dependent reaction mechanism over the broad kinematic range provided by the BLAST detector.

- BLAST will carry out measurements of spin-dependent charged pion electroproduction on few-body systems from threshold to beyond the $\Delta(1232)$ resonance. Such studies are important for understanding the role of the nucleon resonance in few-body systems. BLAST allows reconstruction of the resonance from its π-nucleon decay channel. In this way, for example, the presence of pre-existing Δ components in the ^{3}He ground state can be studied.

- With a polarized proton target, the $N \rightarrow \Delta$ transition can be studied with polarized beams. The physics motivation is to isolate components beyond the dominant M1 transition. This reaction has been the focus of considerable study at laboratories worldwide. However, to date most of the techniques have used unpolarized observables with coincidence detection. BLAST will allow sensitivity to longitudinal components with inclusive scattering using polarized beam and target.

BLAST will thus provide an unprecedented capability to study the spin-dependent electromagnetic response in few-body systems over a large kinematic range. The program focuses on the structure of both the nucleon and few-body systems and is the natural development of the highly successful program in the 1980s. It establishes a new frontier in the study of the strong interaction in the non-perturbative kinematic region.

The experimental assumptions used in the following simulations of BLAST experiments are summarized in Table 1 . We note that electron currents larger than 120 mA have

Table 1: *Experimental assumptions used in simulating the BLAST experiments.*

I_e (mA)	$\vec{p_e}$ (beam) (%)	Target	Thickness (atoms/cm^2)	$\vec{p_T}$ (target) (%)	Luminosity (atoms cm^{-2} s^{-1})	Time (hrs)
80	70	$^1\vec{H}$	2.0×10^{14}	80	10^{32}	1000
100		$^2\vec{H}$ (tensor)	1.6×10^{14}	50	10^{32}	1000
80	40	$^2\vec{H}$ (vector)	2.0×10^{14}	85	10^{32}	500
80	40	$^3\vec{H}e$	2.0×10^{15}	50	10^{33}	1000

routinely circulated in the NIKHEF storage ring. Electron beams with 40% polarization have been injected into the South Hall Ring (see Section 3). The projected luminosities for $^1\vec{H}$ and $^2\vec{H}$ can be achieved with anticipated improvements to the atomic beam source presently in use at NIKHEF. These improvements include increase flow and optimization of the storage cell dimensions. The assumed target thickness and polarization for ^{3}He are realized straightforwardly from established routine performance values.

2.2 POLARIZED ^{1}H

A central issue in nuclear and high-energy physics concerns the internal structure of the nucleon and its resonances. A topic of interest is the possible D-wave admixtures in the quark wave functions of the nucleon and Δ. Whereas the spherically symmetric quark model is successful in predicting the mass spectrum and magnetic moments of baryons, it fails to describe the values of G_A/G_V, the SU(3) decay ratio (D+F)/(D-F) and the $\pi N\Delta$ coupling constant. Glashow [1] and Vento et al. [2] showed that the description of these observables can be improved if one allows for a large D-state admixture. A small admixture due to the strong hyperfine interaction between quarks in the QCD-lagrangian has been predicted by Isgur et al. [3] Furthermore, several bag models predict a spheroidal deformation of some baryons. Viollier et al. [4] found that the Δ is strongly deformed due to the one-gluon exchange interaction, whereas the nucleon remains undeformed. In the model of Murphy and Bhaduri [5] a deformed bag improves the description of some of the higher lying resonances, while the wave functions for the nucleon and Δ resonance are very similar to those of the spherical model of Isgur and Karl [6, 7]. These issues can experimentally be addressed by measuring observables that are sensitive to a possible D-state admixture in the quark wave function.

Information on the quark wave functions of the nucleon, its resonances and the transition currents between them may be obtained by measuring electromagnetic response functions. Specifically, a D-state admixture can induce a non-zero electromagnetic E2 or C2 amplitude. A quadrupole deformation of the nucleon cannot be determined by elastic scattering, because the spin 1/2 of the nucleon forbids the E2 and C2 electromagnetic multipoles. The logical place to search for these contributions is in the $N \rightarrow \Delta$ transition for a number of reasons: the Δ resonance is the lowest lying resonance and decays purely into two-body final states, which considerably simplifies theoretical calculations of the cross section. It is well separated from other resonances and it dominates in excitation strength at low momentum transfer.

Separations of the longitudinal and transverse structure functions have been published both for inclusive and exclusive [8]– [12] pion electroproduction in the Δ-regime. Unpolarized inclusive experiments have several disadvantages for determining the quadrupole form factors: the Rosenbluth separation enables one to determine the longitudinal and transverse structure functions only. The longitudinal structure function contains the charge form factor squared, but is small compared to the transverse one. The transverse structure function contains contributions from the dominant M1 form factor as well as from the smaller E2 form factor, but these contributions cannot be separated in an unpolarized, inclusive measurement.

Data obtained in polarized experiments will allow for the selection of structure functions that are more sensitive to the C2 or E2 amplitude and can distinguish the relative sign of these amplitudes with respect to the M1 amplitude.

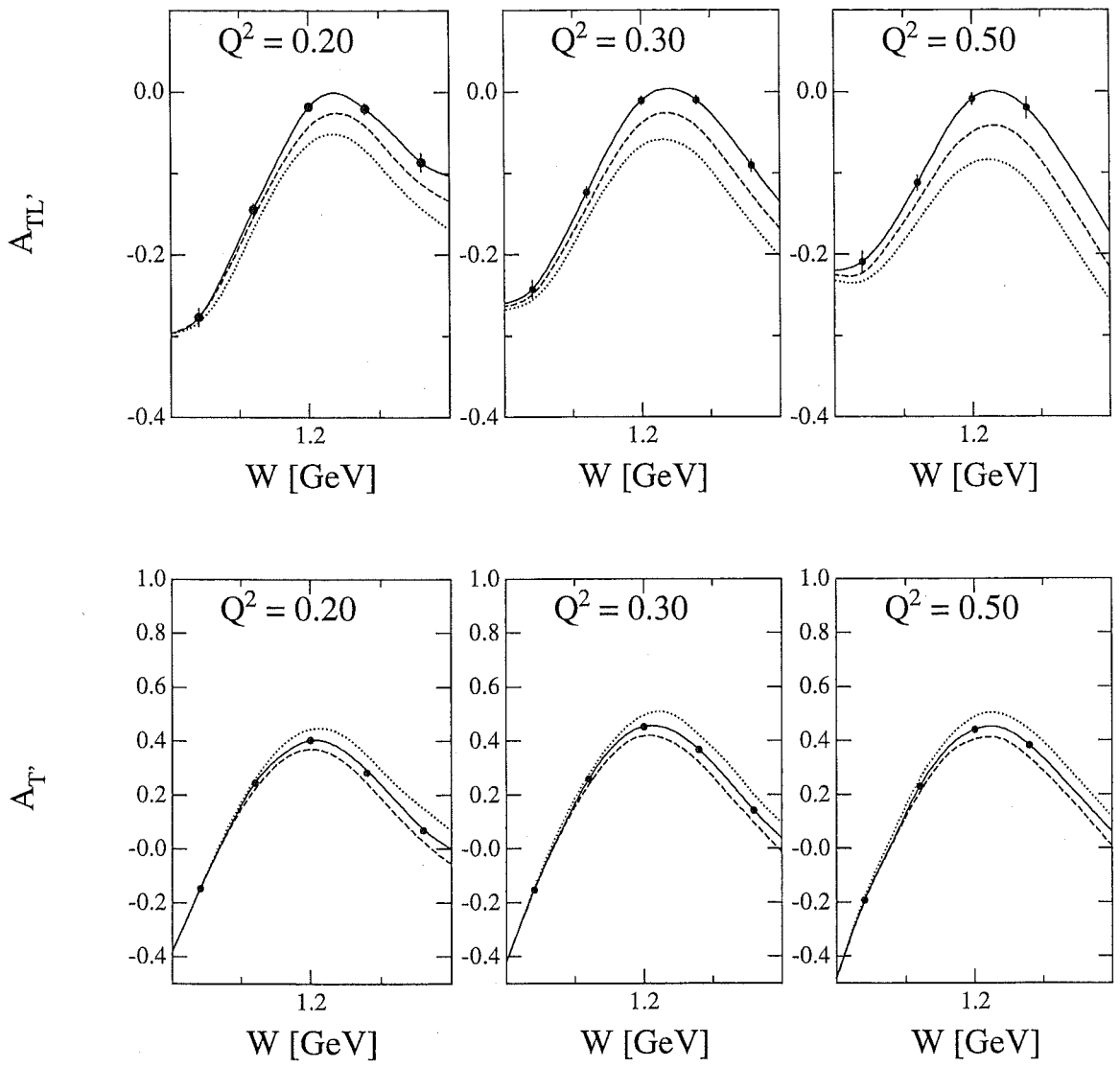

Figure 1: *The spin correlations $A_{TL'}$ (top) and $A_{T'}$ (bottom) as calculated by Nozawa and Lee [14]. The solid, dashed and dotted lines are obtained by setting G_C/G_M equal to 0.15, 0 and −0.15 for $A_{TL'}$ and setting G_E to 0.07, 0.16 and 0 for $A_{T'}$, respectively. The error bars reflect the statistical uncertainty expected for the luminosity conditions described in the text. The horizontal axis divisions are 0.05 GeV.*

Both Nozawa et al. [13]–[15] and Laget [16, 17] have calculated cross sections and asymmetries for pion electroproduction in the Δ-regime. Both groups find sensitivity to the C2 multipole in the inclusive spin correlation parameter $A_{TL'}$ and, to a somewhat lesser extent, to the E2 multipole in $A_{T'}$. Fig. 1 shows the asymmetries $A_{TL'}$ and $A_{T'}$ calculated in the model of Nozawa and Lee [14] for Q^2 of 0.2, 0.3 and 0.5 $(\mathrm{GeV/c})^2$. As can be seen,

sensitivity to the resonant C2 multipole is obtained in $A_{TL'}$ at the top of the Δ, and the qualitative behavior of $A_{TL'}$ as a function of invariant mass W does not depend strongly on Q^2. At low invariant mass W (around 1100 MeV), the resonant part of the cross section only weakly contributes. There the spin correlations $A_{TL'}$ and $A_{T'}$ are dominated by non-resonant contributions.

The large acceptance of the BLAST detector enables one to perform an accurate measurement of the asymmetry $A_{TL'}$ and $A_{T'}$ simultaneously in a range of Q^2 between 0.2 and 0.5 GeV^2, and the invariant mass W^2 in the full range of the Δ resonance. A pure internal hydrogen target can be used. Hence, contributions from heavier nuclei, which have a different cross section dependence on Q^2 and W^2, are small, and high systematic accuracy can be obtained. The statistical accuracy for 1000 hours of running time at a luminosity of 10^{32} atoms cm^{-2}s^{-1} and beam (target) polarization of 70 (80) % is shown in Fig. 1. With the large acceptance of BLAST the Q^2=0.2 GeV^2 data for these observables will extend well into the region of the Roper (1440) resonance. The Roper resonance is considered to be the first breathing mode (radial excitation) of the nucleon. Its study with polarization observables is especially interesting as it is well known that no electro-excitation of the Roper has been seen in spin-independent observables. The extraction of the nucleon resonance transition amplitudes from these observables would constitute important data for testing various microscopic models of the nucleon, e.g. single-quark transition models [18].

2.3 POLARIZED ^{2}H

2.3.1 Introduction

A systematic study of medium energy spin observables from deuterium can be done thoroughly with BLAST and a polarized internal deuterium target. Over most of the kinematical range available with a 1-GeV electron beam, the BLAST detector measures the elastic, quasi-elastic, and resonance scattering from polarized deuterium simultaneously in a single experiment. Internal targets of polarized deuterium gas can be either vector or tensor polarized, with the additional ability of reversing one type of polarization while keeping the other constant and vice-versa. Thus, small systematic uncertainties can be expected.

The electromagnetic structure of the spin–1 deuteron is described by the charge monopole G_C, charge quadrupole G_Q, and magnetic dipole G_M form factors. Over the past two decades, cross section measurements for elastic $e-d$ scattering have yielded precision data for the structure functions A(G_C,G_Q,G_M) and B(G_M) up to large values of momentum transfer. A spin measurement is required for separating the G_C and G_Q charge distributions. From measurements at Bates of the $t_{20}(G_C, G_Q, G_M)$ observable, the first observation of a node in G_C has been reported at Q =4.39$\pm$0.16 fm^{-1}. Recently, it has been pointed out [19] that *no* theoretical model is capable of describing simultaneously the present data set for elastic $e-d$ scattering and the isoscalar charge form factor of the 3–nucleon system.

This is an interesting puzzle for few-body theory. To address it, an improved determination of the G_C node and the first determination of the position and height of the second G_C maximum are needed. We thus need additional t_{20} data with improved precision in the range of momentum transfers already measured and additional data at larger momentum transfers.

Members of the BLAST collaboration have conducted new analyzing power T_{20} measurements [20] by using a tensor polarized ^2H target internal to the NIKHEF electron storage ring, with *in situ* measurement of the polarization of the target gas. These precise measurements are at momentum transfers of 1.6 fm^{-1} and 2.4 fm^{-1}. The feasibility of pursuing higher-Q measurements at NIKHEF is under study. A new program of t_{20} measurements, by using the recoil polarization technique pioneered at Bates, has begun at the Thomas Jefferson National Accelerator Facility (TJNAF). BLAST will provide precise data by using the internal target technique. The complementarity of the Bates and TJNAF programs is obvious. BLAST will take more precise data in the kinematic region sensitive to few-body physics. The next few years can yield polarization data for elastic $e-d$ scattering of comparable quality to that of the unpolarized response functions.

Quasi-elastic nucleon knockout with polarized electrons from polarized deuterium is the prototype reaction for the study of more complicated nuclear targets. By itself it can optimally address two central issues in the intermediate energy region, (a) the determination of the form factors of the nucleon, in particular G_E^n, and (b) the determination of the spin-dependent momentum distribution function for nucleons in the target. Vector polarization in deuterium emphasizes the one-body response and thus is ideal for studies of nucleon observables such as G_E^n. On the other hand, with tensor polarization one can separate the spin-dependent components of observables such as the nucleon momentum distribution in the deuteron.

Recoil $(\vec{e}, e'\vec{n})$ polarimetry experiments to measure G_E^n with polarized electrons and unpolarized ^{2}H targets are presently in progress at Mainz. This technique was pioneered at Bates with a 1% duty factor electron beam [21]. At TJNAF plans are in place to carry out measurements with a solid-state polarized target and the $(\vec{e}, e'n)$ reaction, and also with recoil $(\vec{e}, e'\vec{n})$ polarimetry. BLAST complements these programs well by using the polarized internal gas target and a large acceptance detector.

The momentum distribution function has been measured with the $(e, e'p)$ reaction up to recoil momenta of about 1.0 GeV/c. No data are currently available for the spin dependent components of the distribution. With BLAST these observables can be mapped out up to about 400 MeV/c missing momentum. In addition, for quasifree scattering a wealth of information on the spin dependence of the effects from rescattering, meson-exchange currents and isobar configurations will be obtained by measuring the reaction channels $(e, e'p)$ and $(e, e'n)$ with both vector and tensor polarized deuterium.

Spin observables from deuteron electrodisintegration in the region of the Δ resonance are quite sensitive to subnuclear degrees of freedom, such as isobar configurations and meson

exchange currents from the π- and ρ-exchange. In addition, polarized deuterium is an ideal system for studying the dynamics of the $N \rightarrow \Delta$ transition and the Roper resonance in the nuclear medium.

In the following subsections we discuss specific measurements for elastic, quasi-elastic, and Δ resonance scattering. As a guideline we have used electron scattering proposal 91–09 "*Measurement of Inclusive and Exclusive Deuteron Electrodisintegration by using Polarized Electrons and Internal Polarized Target*" by Alarcon (ASU) and van den Brand (UW-Madison/Vrije Universiteit Amsterdam) [22]. This proposal has been approved by the 1991 PAC at MIT-Bates for 1000 hours of beam time.

2.3.2 Tensor Polarized Elastic Scattering

The cross section for elastic scattering of unpolarized electrons from tensor polarized deuterium can be expressed as [23]

$$\sigma = \sigma_0 \left[1 + \frac{1}{\sqrt{2}} P_{zz} \left(\frac{3\cos^2\theta_d - 1}{2} T_{20} - \sqrt{\frac{3}{2}} \sin 2\theta_d \cos\phi_d T_{21} + \sqrt{\frac{3}{2}} \sin^2\theta_d \cos 2\phi_d T_{22} \right) \right] . \quad (1)$$

Here, σ_0 is the cross section from unpolarized deuterium, and P_{zz} is the degree of tensor polarization defined as $P_{zz} = n_+ + n_- - 2n_0$, where n_+, n_0, and n_- are the relative populations of the various nuclear spin projections on the direction of the magnetic holding field. The polarization of the deuteron is defined by the angles θ_d and ϕ_d in the frame where the z-axis is along the direction of the virtual photon and the y-axis is defined by the vector product of the incoming and outgoing electron momenta. In the one-photon exchange approximation of elastic $e - d$ scattering, and as a result of time-reversal invariance, the deuteron vector polarization is identically zero when using an unpolarized electron beam [24].

The three tensor analyzing powers T_{20}, T_{21}, and T_{22} provide a complete set of observables to determine the form factors G_C, G_Q, and G_M. In practice, only T_{20} is needed because unpolarized elastic $e-d$ scattering provides a direct measurement of both G_M and a linear combination of G_C, G_Q, and G_M [25]. Nonetheless, the determination of both T_{21} and T_{22} is important for consistency checks.

The present data for T_{20} are shown in Fig. 2 together with several state-of-the-art models [30]– [34]. In order to estimate T_{20} data with BLAST we performed a simulation of the experiment. We used a luminosity of 10^{32} atoms cm^{-2}s^{-1}, which is presently achievable with atomic beam sources. Due to the large acceptance most of the kinematic range shown in Fig. 2 is covered in a single experiment. The statistical errors shown in Fig. 2 are obtained for 1000 hours of beam time. Because of the large acceptance symmetric detector, similar quality data will be obtained simultaneously for the other tensor analyzing powers, T_{22} and T_{21}, over the entire Q-range.

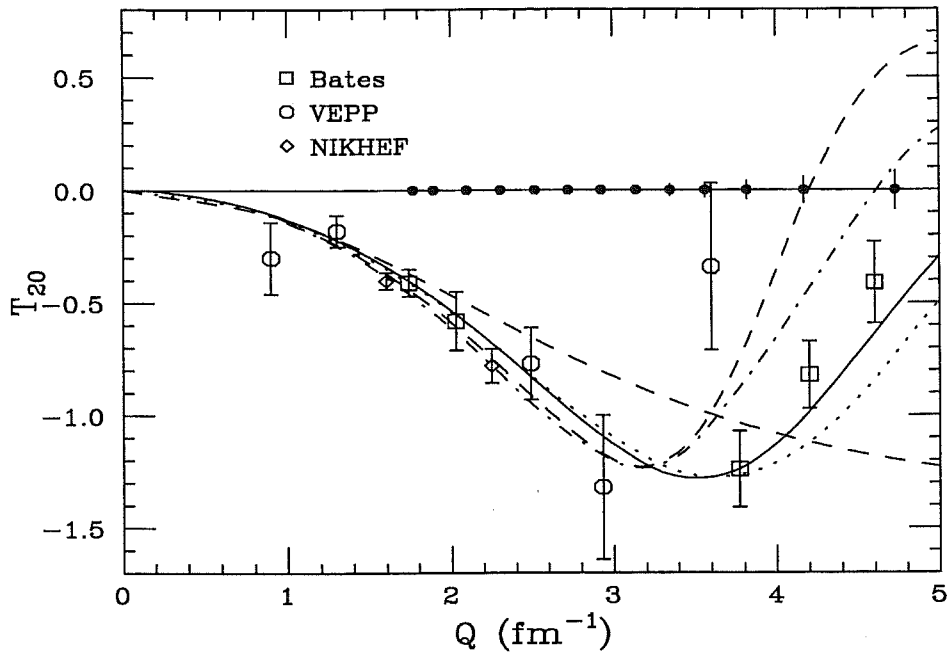

Figure 2: *Data and theoretical predictions for T_{20} as a function of momentum transfer. The data are from Refs. [25]– [29]. The curves represent various theoretical models [30]–[34]. Also indicated are the expected data (solid circles) with BLAST for 1000 h at a luminosity L of 10^{32} atoms $cm^{-2}s^{-1}$.*

2.3.3 Polarized Quasielastic Scattering

In general, the cross section for deuteron electrodisintegration with polarized electrons and a polarized target can be written [35] in terms of various target $(A_d^{V,T})$ and beam-target $(A_{ed}^{V,T})$ asymmetries,

$$\sigma(h, P_1^d, P_2^d) = \sigma_0 \left[1 + P_1^d A_d^V + P_2^d A_d^T + h\left(P_1^d A_{ed}^V + P_2^d A_{ed}^T\right)\right] \quad , \tag{2}$$

where h is the electron helicity, P_I^d are the deuteron orientation parameters, and σ_0 is the inclusive cross section with unpolarized electrons and target. The various asymmetries A depend on the deuteron orientation angles (θ_d, ϕ_d), and they are measured as function of the missing momentum p_m for different momentum transfers Q. To extract a particular asymmetry one has to reverse the spin of the deuteron $(A_d^{V,T})$ and the spin of the electron beam $(A_{ed}^{V,T})$. For example, A_{ed}^V is given by

$$A_{ed}^{V}(\theta_d,\phi_d) = \frac{1}{4hP_1^d\sigma_0}\Big[\ \sigma\left(h,P_1^d,P_2^d\right) - \sigma\left(-h,P_1^d,P_2^d\right) - \sigma\left(h,-P_1^d,P_2^d\right) + \sigma\left(-h,-P_1^d,P_2^d\right)\Big] \quad . \tag{3}$$

From the calculations of Leidemann, Tomusiak, and Arenhövel [35] we have studied the various asymmetries for a range of momentum transfer experimentally accessible with a 1 GeV electron beam. In these calculations the intrinsic two-body wave functions of the initial and final states were obtained for several realistic NN potentials. Relativistic contributions to the potential and to the electromagnetic operators were included in a consistent manner up to order $(p/M)^3$. For the meson exchange currents (MEC), the contributions from both π- and ρ-exchange were taken along with consistent inclusion of hadronic form factors. The most important $N\Delta$, $NN'(1440)$ and $\Delta\Delta$ configurations were considered for isobar configurations (IC).

By measuring the $(\vec{e},e'n)$ parallel and perpendicular asymmetries, $A_{ed}^{V}(0,0)$ and $A_{ed}^{V}(\pi/2,0)$, one can extract the electric and magnetic form factors of the neutron [36]. The sensitivity to G_E^n is contained in $A_{ed}^{V}(\pi/2,0)$, while the information from $A_{ed}^{V}(0,0)$ is used to obtain an independent measurement of G_M^n. The neutrons are detected along $\vec{q}$ where the effects of the reaction mechanism are negligible and the cross sections are the largest. In Fig. 3 the asymmetry $A_{ed}^{V}(\frac{\pi}{2},0)$ is plotted as a function of the cm-angle that the proton makes with respect to $\vec{q}$ for a range of momentum transfers, in quasielastic kinematics. The case for θ_{pq}^{cm}=180^0 corresponds to neutrons emitted along $\vec{q}$. There are two set of curves; one set is for no inclusion of G_E^n and the other is for G_E^n as parameterized by Galster [37]. The dashed curve is a PWBA calculation while the solid line includes the effects of the reaction mechanism in the final state plus the effects of MEC and IC, the last two being negligible in quasielastic kinematics. One can clearly see the effect of G_E^n for θ_{pq}^{cm}=180^0. Also indicated in Fig. 3 are the regions over which $A_{ed}^{V}(\frac{\pi}{2},0)$ will be measured by $(\vec{e},e'p)$ and $(\vec{e},e'n)$, respectively. The measurements at forward θ_{pq}^{cm} provide precise data that can check the reliability of the PWBA calculation over a wide range of momentum transfers.

For an incident electron energy of 880 MeV, BLAST will measure the beam-vector-target A_{ed}^{V} asymmetry for the $^2\vec{\mathrm{H}}(\vec{e},e')$, $^2\vec{\mathrm{H}}(\vec{e},e'p)$, and $^2\vec{\mathrm{H}}(\vec{e},e'n)$ reactions in quasielastic kinematics over a momentum-transfer range between 0.1 and 0.7 (GeV/c)^2. To separate the different form factors that contribute to the asymmetry A_{ed}^{V}, the target polarization will be oriented parallel ($\theta_d = 0$) and perpendicular ($\theta_d = \frac{\pi}{2}$) to $\vec{q}$. The target spin direction will be positioned around 45° with respect to the incident beam direction. The BLAST detector allows detection of electrons at positive and negative scattering angles so the parallel and perpendicular to $\vec{q}$ configurations can be measured simultaneously.

Counting rates have been estimated for the reaction $(\vec{e},e'N)$ at a luminosity L of 10^{32} atoms cm^{-2}s^{-1}. For the beam and target polarization we have assumed $p_e = 0.4$ and $p_T = 0.85$. The resulting statistical uncertainties for a 500 hour run are also indicated in Fig. 3. The resulting uncertainties for G_E^n are shown in Fig. 4

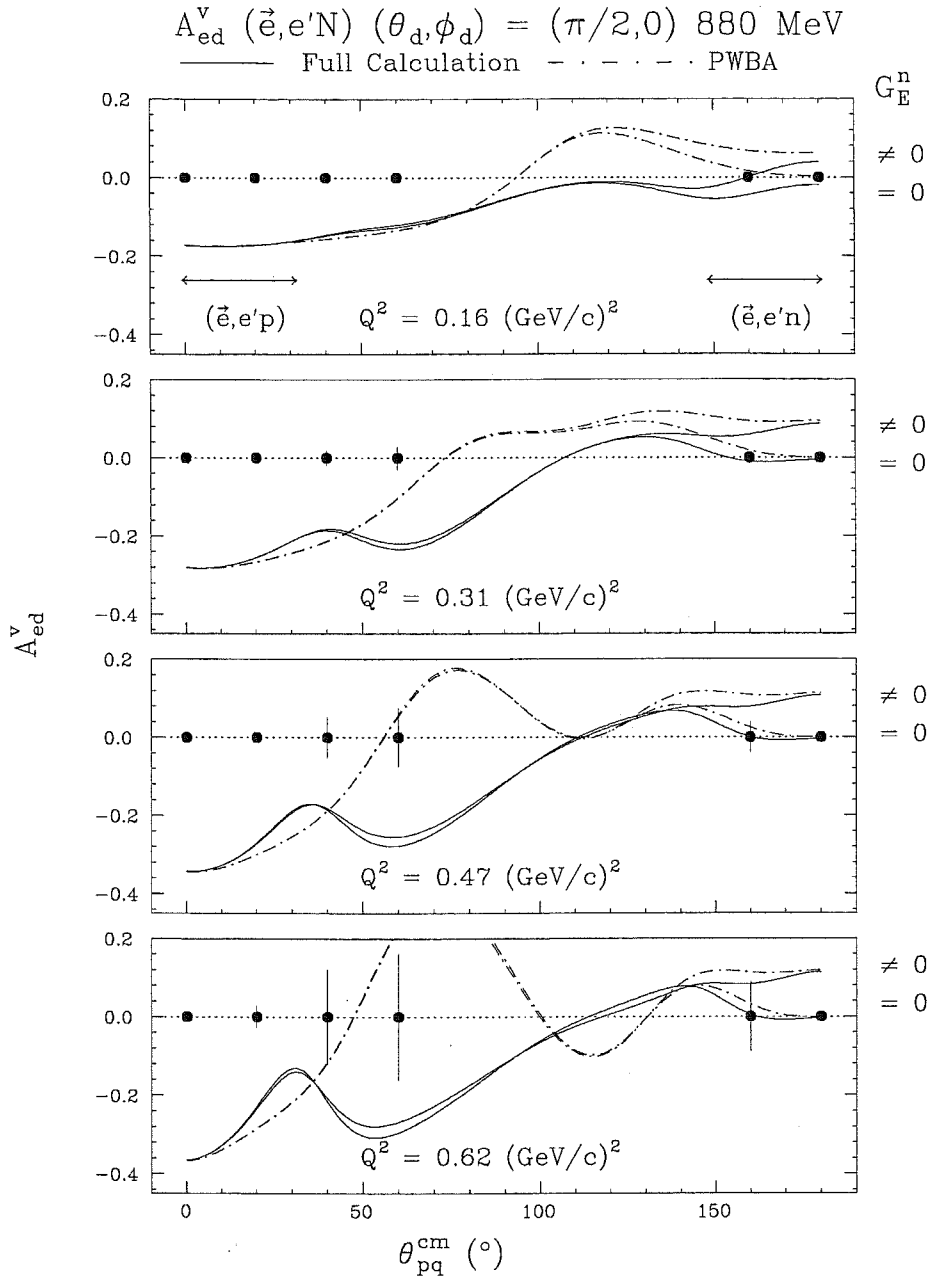

Figure 3: *The asymmetry $A^V_{ed}(\frac{\pi}{2},0)$ in quasielastic kinematics for the reaction $(\vec{e},e'N)$. The dot-dashed lines are PWBA and the solid lines are the complete calculations [35]. The NN interaction is the Bonn potential. The effect of the inclusion of G^n_E=Galster is shown. The expected data quality points with BLAST are also indicated (solid circles). The statistical errors are for a luminosity of 10^{32} atoms cm^{-2}s^{-1} and 500 h of data taking.*

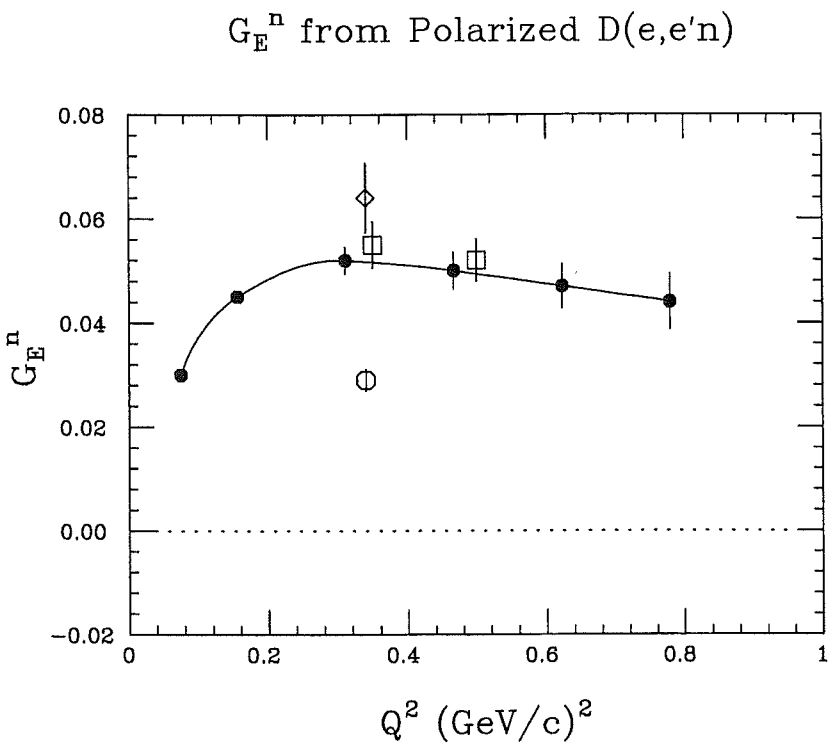

Figure 4: *The projected G_E^n (full circles) as function of Q^2 from the exclusive $(\vec{e}, e'n)$ measurements using a polarized deuterium target in conjunction with BLAST. Also shown are the Mainz data on the polarized ^3He target (open circle) and ^2H target (open diamond) with neutron recoil polarimeter measurement, respectively [38]. The open squares are the projected data from Bates experiment E89-05.*

The $(e, e'N)$ target asymmetry A_d^V vanishes in PWBA. In quasielastic kinematics it is different from zero mainly due to the effects of the reaction mechanism. Sizable A_d^V asymmetries are generated when the spin is oriented perpendicular to the scattering plane. The effect is due to the spin dependent part of the NN interaction. High quality data will be obtained up to 400 MeV/c missing momenta for the asymmetry $A_d^V(\frac{\pi}{2}, \frac{\pi}{2})$ for the range of momentum transfers accessible with BLAST.

The nucleon momentum distribution $\rho(p_m)$ represents the probability of finding a nucleon in deuterium with momentum p_m. In PWIA, it is directly proportional to the $d(e, e'p)$ coincidence cross section. In terms of spin degrees of freedom $\rho = \frac{1}{3}[\rho^+ + \rho^- + \rho^0]$, where ρ^i is the momentum distribution for a particular polarization state of the deuteron, with the property $\rho^+ = \rho^-$. By measuring the tensor analyzing powers A_d^T as a function of p_m the spin components $\rho^\pm$ and ρ^0 can be separated. In fact, in PWIA A_d^T is given by

$$A_d^T = \frac{(\rho^+ + \rho^-) - 2\rho^0}{(\rho^+ + \rho^-) + \rho^0} \tag{4}$$

where the denominator is measured in the unpolarized $d(e, e'p)n$ experiments. To a large extent rescattering effects mask the sensitivity of A_d^T to models of deuteron structure.

Therefore, an accurate evaluation of these effects, which depend strongly on the spin state of the deuteron and the scattering kinematics, is required for the interpretation of the data, especially at high missing momenta.

As in the case of elastic scattering there are three analyzing powers that define A_d^T, and they can be separated by using different spin orientations (θ_d, ϕ_d). Specifically,

$$A_d^T = d^2_{00}(\theta_d)T_{20} + d^2_{10}(\theta_d)T_{21} + d^2_{20}(\theta_d)T_{22}, \tag{5}$$

where the T_{2j} are the different tensor analyzing powers and the d_{j0} functions describe the deuteron density matrix. The ϕ_d dependence has been absorbed in the T_{2j}. BLAST measures the θ_d=0,$\frac{\pi}{2}$ orientations in the same experiment. The two orientations yield T_{20} and a combination of T_{20} and T_{22}, just as in elastic scattering.

We have estimated the statistical accuracy in the asymmetries $A_d^T(0,0)$ and $A_d^T(\frac{\pi}{2},0)$ as a function of p_m and Q^2 for 500 hours of running time. The results are shown in Fig. 5. The dot–dash lines indicate PWBA calculations whereas the full calculation is indicated by a solid (dashed) line when the effects of the reaction mechanism are computed by using the parameterization of the Bonn (Paris) potential.

2.3.4 Δ-resonance Polarized Scattering

Polarization observables in the kinematical region of the Δ-resonance are particularly sensitive to the inclusion of isobars and the effects of meson exchange currents. With BLAST we will measure the inclusive and exclusive beam-vector-target asymmetry A_{ed}^V in Δ-kinematics. Fig. 6 shows the results of calculations [35] for the exclusive asymmetries, $A_{ed}^V(0,0)$ and $A_{ed}^V(\frac{\pi}{2},0)$ for $Q^2 = 5$ fm^{-2} based on the Paris potential, as a function of θ_{pq}^{cm}. There are large differences between the dashed (N + REL) and solid line (N + MEC + IC + REL) for nucleon detection away from the momentum transfer direction. These results indicate a great sensitivity of A_{ed}^V to IC in this kinematical regime. Count rates have been estimated by using the same parameters as in the quasielastic case.

The present discussion on experiments with the reaction $^2\vec{\mathrm{H}}(\vec{e}, e'X)$ (X=0,p,n,d) is far from complete. It is well known that good sensitivity to various multipoles can be obtained by a measurement near threshold. Such experiments are performed at low-energy transfer and high transferred momentum, and with the proposed set-up may be limited by the resolution in momentum of the scattered electrons. In the so-called "dip"-region between the quasi-elastic and Δ-resonance peaks, the study of high-momentum transfer reactions from polarized deuterium is interesting. The cross sections for these reactions may strongly depend on the deuterium polarization in kinematics forbidden for scattering off a free nucleon [39]. Asymmetries will also be obtained in exclusive scattering from the reactions $(e, e'\pi^{\pm})$, $(e, e'N\pi)$, and $(e, e'pn)$. Furthermore, one can carry out searches for the signatures of quark degrees of freedom as predicted in models of short-range hadronic interactions [40].

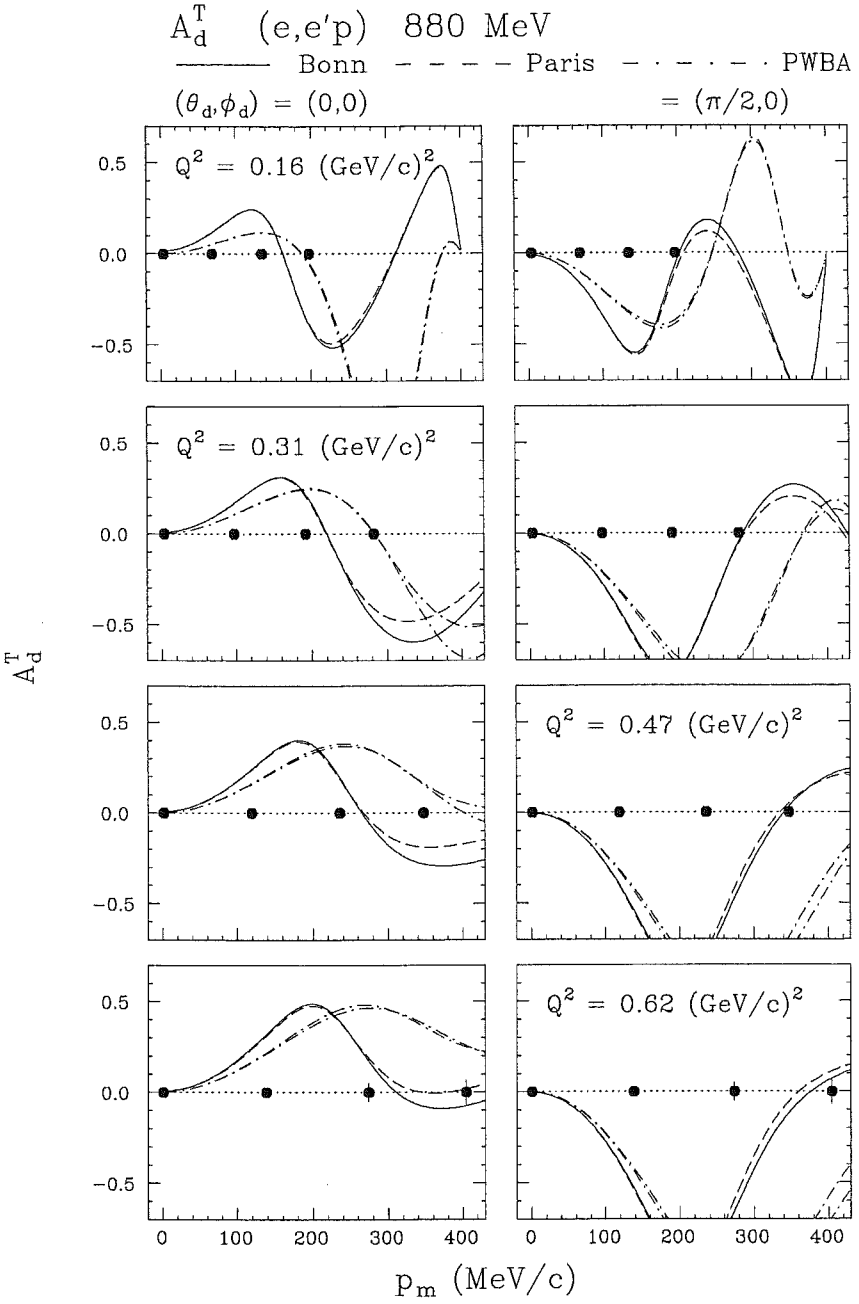

Figure 5: *The tensor asymmetry A_d^T in quasielastic kinematics for the reaction $(\vec{e}, e'p)$ as a function of p_m for a range of Q^2. The dot-dash curves are PWBA and the complete calculations with the Bonn (solid) and Paris (dashed) potentials are also shown. The expected data quality points with BLAST are also indicated (solid circles). The statistical errors are for a luminosity of 10^{32} atoms cm$^{-2}s^{-1}$ and 500 h of data taking.*

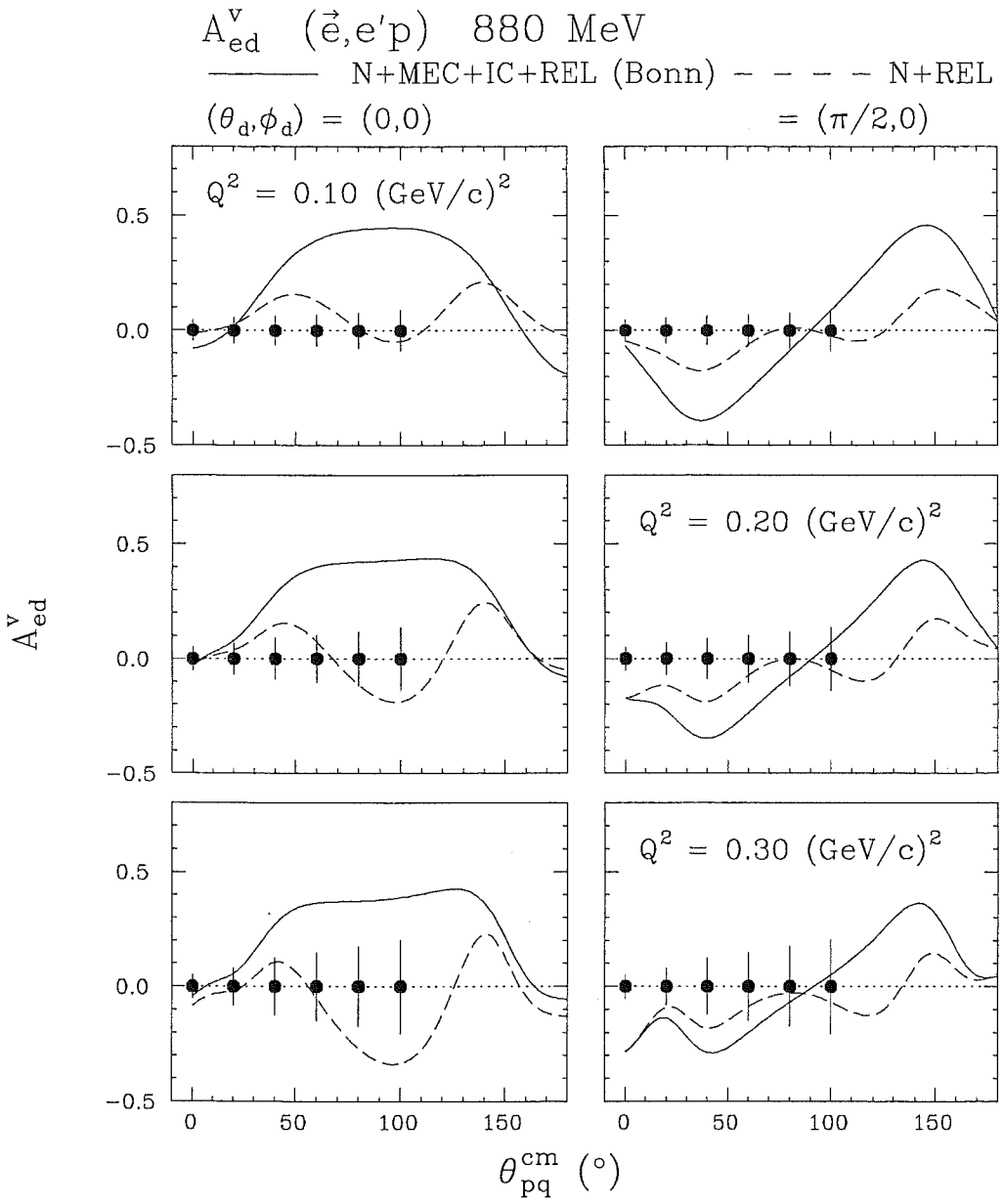

Figure 6: *The A^V_{ed} parallel and perpendicular asymmetries in Δ-kinematics. The beam energy is 880 MeV. The NN interaction is given by the Bonn potential. The solid curve includes MEC and IC. The expected data quality points with BLAST are also indicated (solid circles). The statistical errors are for a luminosity of 10^{32} atoms cm^{-2}s^{-1} and 500 h of data taking.*

2.4 POLARIZED ^{3}He

2.4.1 Introduction

The ^{3}He nucleus has several properties that make the study of its spin particularly interesting. The three body system is unique in that, although it is relatively tightly bound, essentially exact Faddeev solutions in non-relativistic approximation of the ground state have been obtained from a variety of two-nucleon potentials. In addition, unlike a heavy nucleus where the total spin is usually determined by only a few valence nucleons, the spin of ^{3}He involves all the nucleons in the nucleus. Further, Faddeev calculations predict that the ground-state spin of the ^{3}He nucleus is dominated by the neutron. This property has motivated worldwide interest in the use of polarized ^{3}He as an effective neutron target. Measurements of spin-dependent scattering from polarized ^{3}He have been carried out at Bates [41, 42, 43], TRIUMF [44], Mainz [45], IUCF [46, 47], SLAC [48], LAMPF [49], and HERA [50], and experiments are planned at NIKHEF [51] and TJNAF [52, 53]. Members of the BLAST collaboration have been leaders both in developing the target technology and in mounting the accelerator-based experiments. In particular, they have made the first measurements of inclusive spin-dependent quasielastic electron scattering at Bates, the first experimental determination of the spin-dependent momentum distribution of the neutron and proton in ^{3}He at IUCF and the first measurement of semi-inclusive deep inelastic spin-dependent scattering from polarized ^{3}He at HERA. As described in detail in this section, the proposed BLAST program is a natural evolution of this work.

Spin-dependent electron scattering from a polarized ^{3}He internal target with BLAST will focus on the simultaneous measurements of the asymmetries for inclusive scattering, $\overrightarrow{^3\mathrm{He}}(\vec{e}, e'N)$, and $\overrightarrow{^3\mathrm{He}}(\vec{e}, e'\pi^{\pm})$. These measurements will span a kinematic range that covers the quasielastic, 'dip', and Δ-regions. In a single experiment BLAST can simultaneously determine in ^{3}He the ground state spin-dependent spectral function, the nucleon form factors, study the reaction mechanism, the neutron resonance structure, the Δ components in the ^{3}He wave function at the level of about 0.2 %, and the elastic and threshold region.

2.4.2 The Spin Dependent Momentum Distributions of the Neutron and Proton in ^{3}He

Non-relativistic Faddeev calculations of the three-body bound state predict the following components to dominate the ^{3}He ground state wave function: a) a spatially symmetric S-state, accounting for $\sim$90% of the spin-averaged wave function, has the ^{3}He spin as entirely due to the neutron with the two protons in a spin singlet state; b) a D-state due to the tensor force accounts for $\sim$ 8% of the spin-averaged wave function and has the three nucleon spins dominantly oriented opposite to the ^{3}He nuclear spin; c) a mixed-symmetry configuration of the nucleons, the S'-state, arises from spin-momentum correlations and accounts for $\sim$1.5% of the spin-averaged wave function. All other components are predicted

to be negligibly small. In the non-relativistic approximation with Faddeev techniques, the S and S' state contributions to the spectral function are found to be maximum for zero nucleon momentum while the D-state contribution is greatest for larger momenta.

The nuclear structure information is contained in the spin-dependent spectral function $S_{\vec{\sigma}_A}(E,\ \mathbf{p},\mathbf{t})$ defined as the probability density of finding a nucleon N of isospin t with energy E, momentum $\mathbf{p}$ and spin σ_N parallel (antiparallel) to the $^3\vec{He}$ spin indicated by σ_A=+(−), where the kinematics are defined in Ref. [54]. The spectral function has the general form

$$S_{\sigma_A}(E,\mathbf{p},t) = \frac{1}{2}\Big\{ f_0(E,p,t) + f_1(E,p,t)\,\sigma_N\cdot\sigma_A + f_2(E,p,t)\left[(\sigma_N\cdot\hat{\mathbf{p}})(\sigma_A\cdot\hat{\mathbf{p}}) - \frac{1}{3}\sigma_N\cdot\sigma_A\right]\Big\} \quad . \tag{6}$$

The spin-averaged contribution f_0 and the two spin-dependent contributions f_1 and f_2 are scalar functions which depend only on the magnitude of $\mathbf{p}$. The effects of the Coulomb interaction have been neglected. The spectral function describes the spin structure of the ^{3}He nuclear ground state. Thus, it is an essential ingredient in the theoretical description of scattering from polarized ^{3}He. In quasielastic scattering experiments (both inclusive and exclusive), it characterizes the spins of the nucleons. In addition, it is an essential ingredient in the description of polarized ^{3}He as an effective polarized neutron in spin-dependent deep inelastic scattering at high energies. Convolution-model calculations require the light cone momentum distribution, which is constructed from the ground state spin-dependent spectral function.

The momentum distribution for a nucleon of isospin t with spin parallel (anti-parallel) to the nuclear spin is defined as [55]

$$\rho_{\uparrow(\downarrow)}(p,t) \equiv \int dE\ S_{\sigma_A=+(-)}(E,p,t) \quad . \tag{7}$$

To make a direct connection with experiment, it is useful to define the spin asymmetry in the momentum distribution as

$$N^t(p) \equiv \frac{\rho_\uparrow(p,t) - \rho_\downarrow(p,t)}{\rho_\uparrow(p,t) + \rho_\downarrow(p,t)} \quad . \tag{8}$$

$N^t(p)$ is plotted for each nucleon isospin state in Fig. 7. In this calculation the Paris nucleon-nucleon interaction has been assumed. Note that the spin-averaged spin-dependent momentum distribution is the unpolarized momentum distribution which has been determined from unpolarized experiments in quasielastic kinematics.

In simplest approximation, an unbound neutron in ^{3}He can exist only in a state where the two protons are also unbound (the three-body configuration.) However, the proton in ^{3}He can be found in a state where the other nucleons form a deuteron (the two-body

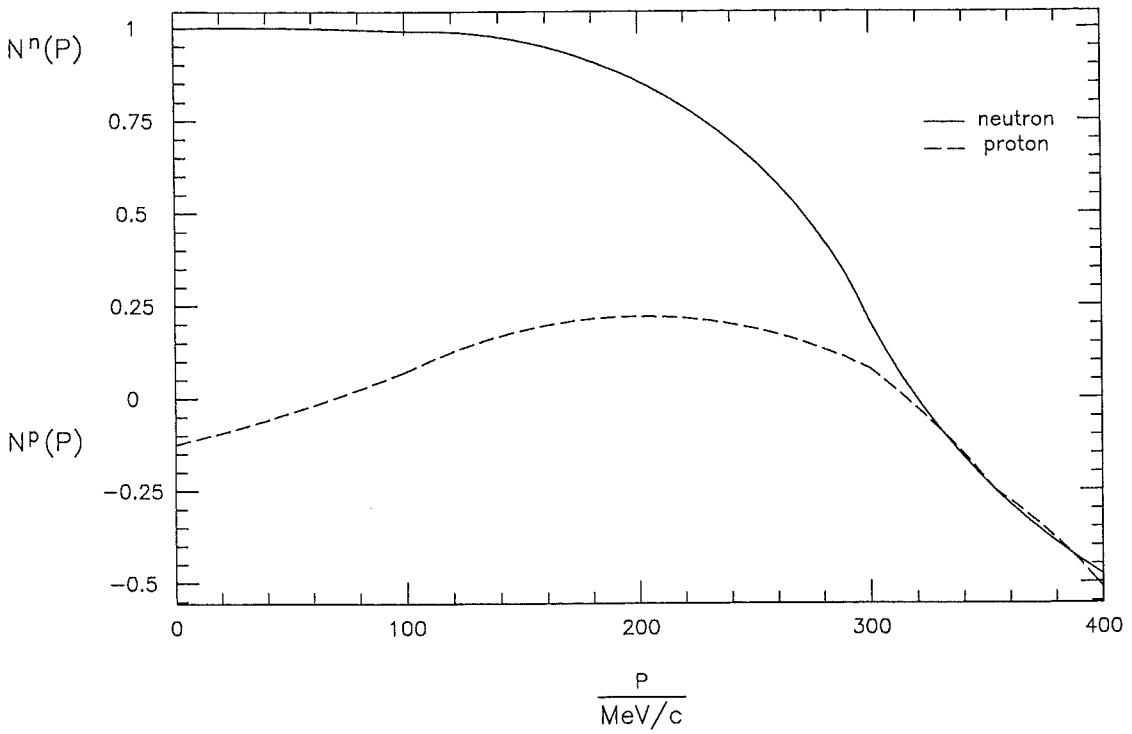

Figure 7: *The spin asymmetry in the momentum distribution of the neutron (solid line) and the proton (dashed line) plotted vs. nucleon momentum p [55].*

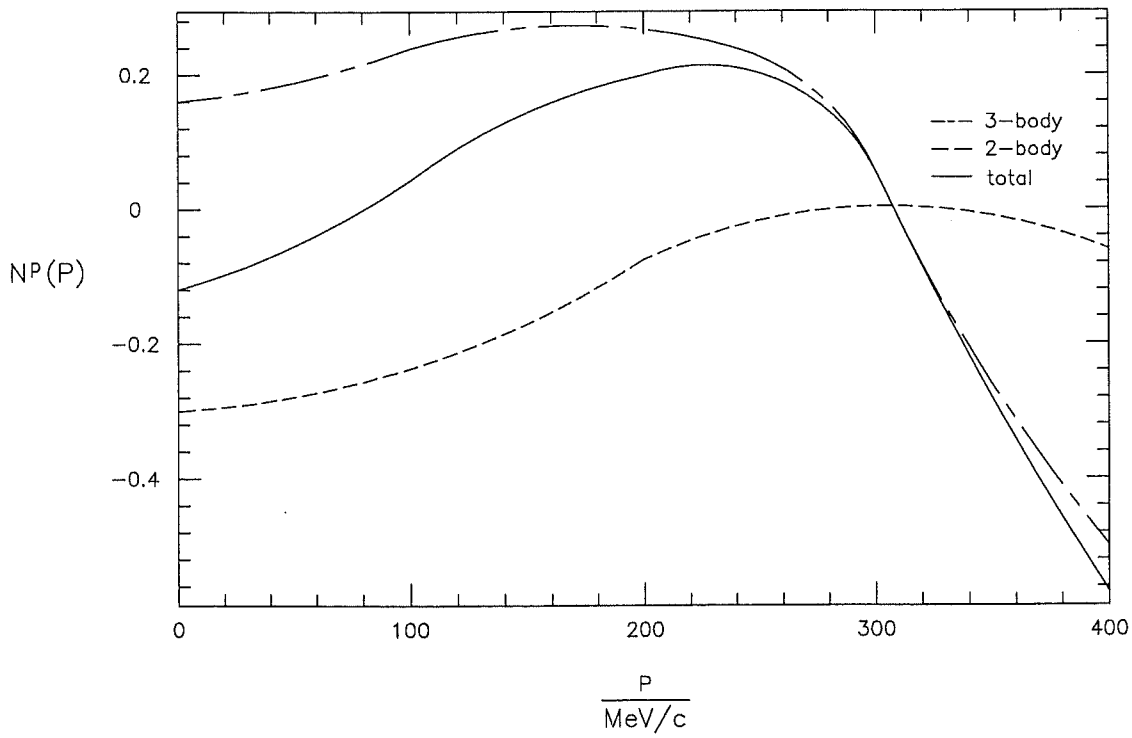

Figure 8: *The two-body contribution (dashed), the three-body contribution (dot-dashed) and the total (solid) proton spin asymmetry in the momentum distribution plotted vs. p [55].*

configuration) or as individual nucleons (the three-body configuration) as observed directly in quasielastic ^{3}He(e,e'p) scattering [11]. In Fig. 8 both two- and three-body contributions and the sum are shown for the proton. Physically, the distributions in Figs. 7 and 8 can be interpreted as the probability that a neutron or proton in ^{3}He has its spin directed parallel to the nuclear spin as a function of the nucleon momentum. Thus, the neutron in Fig. 7 at low p has its spin completely parallel to the nuclear spin but at high p, where the D-state is sizable, the neutron spin can be found with large probability directed opposite to the nuclear spin. In the case of the proton, from Fig. 8 it can be seen that the individual two- ($N_2^p(p)$) and three-body ($N_3^p(p)$) contributions to the total proton spin dependent momentum distribution are sizable and of opposite sign. (Note that even in the pure S-state $N_3^p(p=0) = -N_2^p(p=0) \approx 0.25$.) The addition of the S'-state yields for the complete wave-function $N_2^p(p=0) + N_3^p(p=0) = -0.12$. As with the neutron, at high p the presence of the D-state causes the proton spin to be predominantly directed opposite to the nuclear spin. The spin asymmetries in the momentum distribution were also calculated for the Bonn and Reid soft core nucleon-nucleon potentials with essentially identical results.

Quasielastic spin-dependent knockout of the constituent nucleons of ^{3}He with good resolution in the energy and momentum of the initial state nucleon offers the most direct experimental approach to constrain the spectral function [56]. Consider an incident polarized electron which exchanges a virtual photon of 4–momentum (ν;$\mathbf{q}$) in quasielastic kinematics with a nucleon in ^{3}He resulting in a recoiling nucleon of 4–momentum ($T'+M$; $\mathbf{p}'$). In the plane-wave impulse approximation (PWIA), the scattered nucleon is ejected without secondary scattering from the residual nucleus implying that the missing momentum $\mathbf{p}_m \equiv \mathbf{q} - \mathbf{p}'$ can be identified with the negative of the initial momentum of the struck nucleon, $-\mathbf{p}$. The recoil system is either a deuteron (two-body breakup) or two unbound nucleons (three-body breakup), and in PWIA the missing energy $E_m \equiv \nu - T' - T_{recoil}$ is identified with E. If PWIA is a good approximation to the scattering process, then information on the spectral function can be directly extracted.

Experiment CE–25 at IUCF carried out a measurement of spin-dependent quasielastic scattering from polarized ^{3}He by using the proton probe. Kinematic cuts were used to restrict the events to the region where PWIA was a reasonable approximation in order to extract the spin asymmetries in the momentum distribution $N^N(p)$ for the neutron and proton, respectively. The results are shown in Fig. 9 and compared with the PWIA model. The limits of the PWIA model for different nucleon-nucleon phase shifts and experimental resolutions are given by the solid curves. Good agreement is observed between the data and the model prediction out to 300 MeV/c. The dominance of the S-state is demonstrated by the 100% probability to find a neutron with spin parallel to the nuclear spin at low p_m. The presence of the small S'-state is demonstrated by the negative probability of $N^p(p_m)$ at low p_m. It is noted that $N^p(p_m)$ crosses zero at $p_m \approx 150$ MeV/c. The zero crossing is sensitive to the weighting of the 2–body and 3–body contributions to the proton asymmetry. The lack of agreement at high p_m is consistent with previous unpolarized measurements [57] and is likely due to breakdown of PWIA.

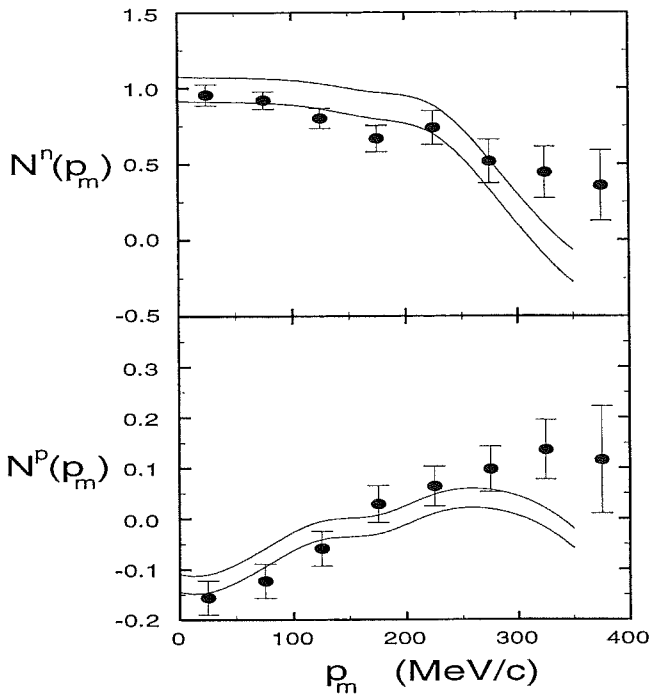

Figure 9: *The asymmetry in the momentum distribution of the neutron (upper panel) and the proton (lower panel) in the ^{3}He nucleus as determined by the CE–25 experiment at IUCF [55]. The solid curves indicate the limits of the PWIA model.*

BLAST can measure the proton and neutron momentum distributions to high values of the initial momentum of the struck nucleon. A careful study of the reaction mechanism can be made with the large acceptance and the different target spin orientations. Thus, one can identify regions where PWIA is valid in order to provide a direct experimental approach to constrain the ground state spectral function. Fig. 10 shows the expected BLAST results for the nucleon momentum distributions. Data will be obtained simultaneously for a wide range of the momentum transfer Q^2. In the simulation we have used 1,000 hours of beam time with a typical luminosity for a polarized ^{3}He target of 10^{33} atoms cm^{-2}s^{-1}.

In Fig. 10 (bottom) both two- and three-body contributions and the sum are shown for the proton. In the same experiment, in addition to measuring the spin dependent momentum distributions of the neutron and the proton in ^{3}He, BLAST can provide clean separation of the two-body and three-body contributions to the proton momentum distribution and determination of the presence of the *D*-state at high missing momenta. The expected results are the points shown in Fig. 10 (bottom).

2.4.3 The Spin-dependent Quasielastic Reaction Mechanism

PWIA describes quasielastic scattering from ^{3}He in the simplest approximation. Mechanisms beyond PWIA such as final state interactions (FSI) and meson exchange currents (MEC) are known to be important in certain kinematic regions. For example, calculations

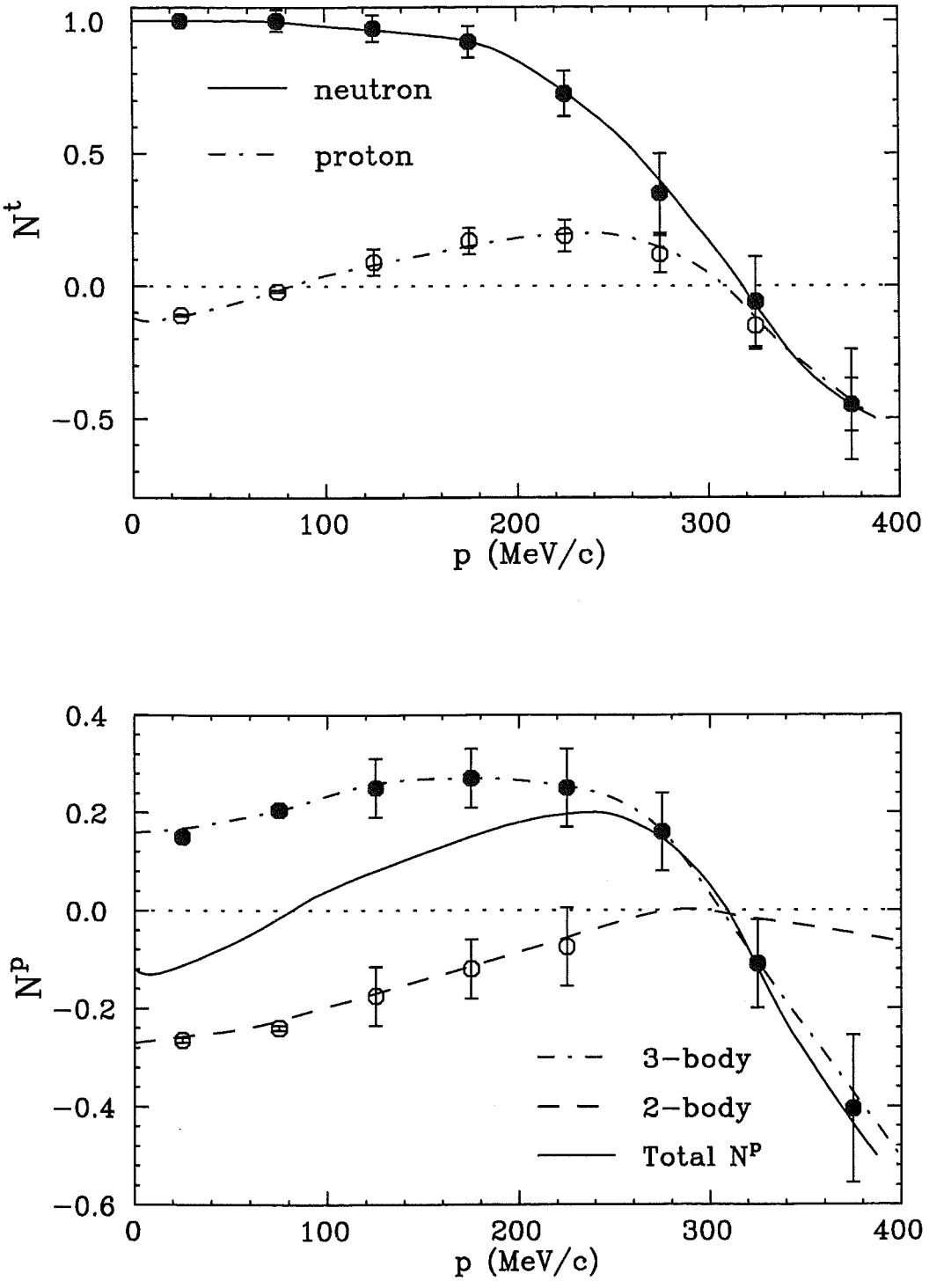

Figure 10: *Top: The spin-dependent momentum distribution of the neutron (solid line) and the proton (dot-dashed line) plotted vs. nucleon momentum p. Bottom: The two-body contribution (dashed), the three-body contribution (dot-dashed) and the total (solid) proton spin-dependent momentum distribution plotted vs. p.*

of these effects have been carried out [58] for the unpolarized responses R_L and R_T which have been measured [59]. As seen from Fig. 11, the continuum Faddeev calculation, with

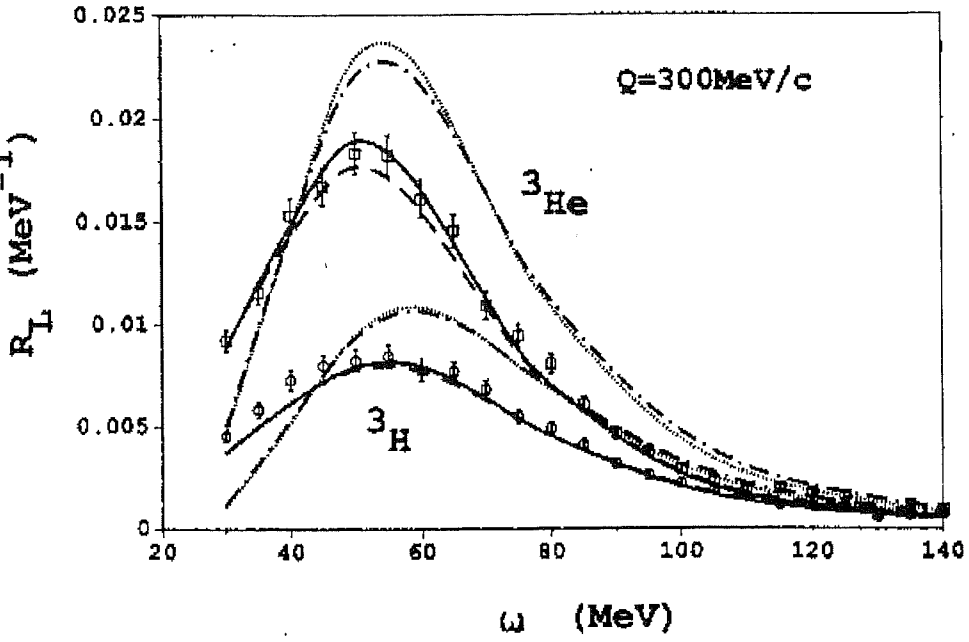

Figure 11: *The longitudinal response functions of ^{3}He and ^{3}H at $q = 300$ MeV/c. PWIA results for Paris (dotted) and Bonn-B potentials (dot-dashed); full results for Paris (solid) and Bonn-B potentials (dashed). Experimental data are from Bates [59].*

FSI exactly taken into account, gives a good description of R_L. It was also observed that the calculated transverse response underestimates the experimental data throughout the entire quasielastic peak. A possible reason for the discrepancy may be the effect of meson-exchange currents, which predominantly affect the transverse component of the nuclear current.

Calculations have been made [60, 61] of the effect of FSI and MEC in spin-dependent quasielastic (e,e'n) scattering from polarized ^{3}He. It is found that for $Q^2 < 0.25$ these effects are sizable. This result is consistent with the observation in CE–25 that PWIA is not a good approximation for neutron momenta less than about 500 MeV/c. BLAST will take data from $Q^2 = 0.1$ to 0.7 (GeV/c)^2 in inclusive and exclusive channels both with spin predominantly along and normal to **q**. It will take data simultaneously over a large range which will allow the reaction mechanism to be studied in a manner that has previously not been possible. This characteristic of the BLAST program was demonstrated by experiment CE–25 [47].

2.4.4 Inclusive Spin-dependent Quasielastic Scattering from ^{3}He

Inclusive electron scattering from nuclei has proven to be an essential tool in understanding the charge and magnetic aspects of nuclear structure. Thus, it is not a surprise that measurements of spin-dependent inclusive quasielastic electron scattering from ^{3}He is essential to the study of the spin-dependent electromagnetic response of ^{3}He.

The differential cross-section for inclusive spin-dependent electron scattering from ^{3}He may be written as [23]

$$\frac{d\sigma}{d\Omega dE'} = \Sigma(\theta^\star, \phi^\star) \pm \Delta(\theta^\star, \phi^\star) \quad , \tag{9}$$

where the + (-) sign corresponds to right (left) helicity state for the incident electron. The asymmetry, $A = \frac{\Delta}{\Sigma}$, is the ratio of spin-dependent to unpolarized cross-sections; and the direction of the target polarization is specified by the angles $\theta^\star$ and $\phi^\star$, as defined in Fig. 12. Further, for ^{3}He, a spin-$\frac{1}{2}$ target, the asymmetry is given by [23]

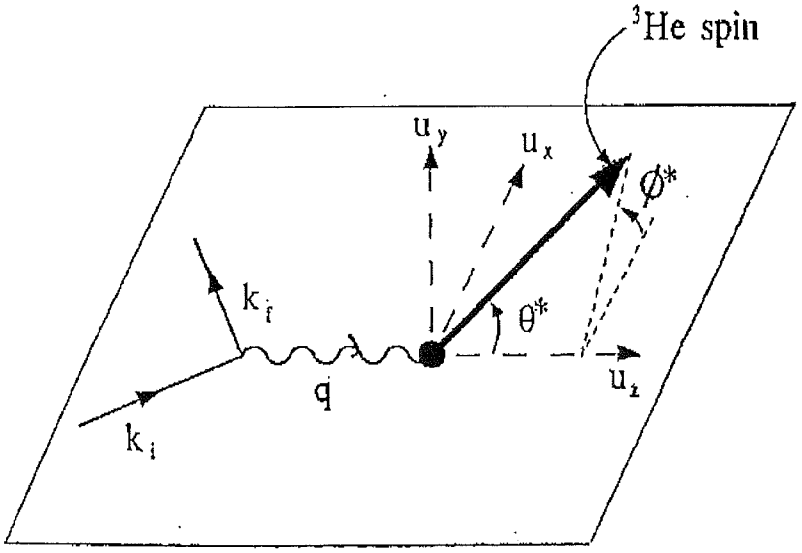

Figure 12: *Kinematics for electron scattering from polarized targets. Here* $\mathbf{u}_z$ *is along the direction of momentum transfer* $\mathbf{q}$. $\mathbf{u}_y$ *is normal to the electron scattering plane and* $\mathbf{u}_x = \mathbf{u}_y \times \mathbf{u}_z$ *lies in the scattering plane. The target polarization direction is then specified by the angles* ($\theta^\star$, $\phi^\star$) *in this coordinate system.*

$$A = -\frac{\{\cos\theta^\star v_{T'} R_{T'} + 2\sin\theta^\star \cos\phi^\star v_{TL'} R_{TL'}\}}{\{v_L R_L + v_T R_T\}} \tag{10}$$

where the v_K are kinematic factors (see reference [23]). $R_L(Q^2, \nu)$ and $R_T(Q^2, \nu)$ are the longitudinal and transverse response functions contributing to the unpolarized cross-section, and $R_{T'}$ and $R_{TL'}$ are two new response functions. R'_T is a transverse response function whereas $R_{TL'}$ arises from interference of transverse and longitudinal multipoles. In PWIA, calculations indicate that $R_{T'}$ is predominantly proportional to the square of the magnetic neutron form factor ${G_M^n}^2$ and $R_{TL'}$ is very sensitive to $G_M^n G_E^n$. The full Faddeev

calculation includes the non-negligible effect of both protons in the S' and D-states. By orientation of the target spin at $\theta^\star = 0°$ (along $\mathbf{q}$) and at $\theta^\star = 90°$ (normal to $\mathbf{q}$), one arranges the asymmetry (A'_T and $A_{TL'}$, respectively) to be proportional to R'_T and $R_{TL'}$, respectively. Thus, the determination of the neutron form factors through experiments on the ^{3}He nucleus entails a super-Rosenbluth separation involving polarization observables.

The Bates Laboratory has pioneered the measurement of spin-dependent inclusive scattering from polarized ^{3}He. To date there have been three experiments which have taken data at low $Q^2 \approx 0.2$ (GeV/c)^2. The first two measurements [41, 42] used independent target schemes and took data in contiguous runs at the same kinematics at the MIT-Bates Linear Accelerator in 1990. In 1993 an experiment with substantially improved statistical precision was carried out. The quasielastic asymmetry $A_{T'}$ was measured [62] as a function of electron energy transfer ω, as shown in Fig. 13. The data are in good agreement

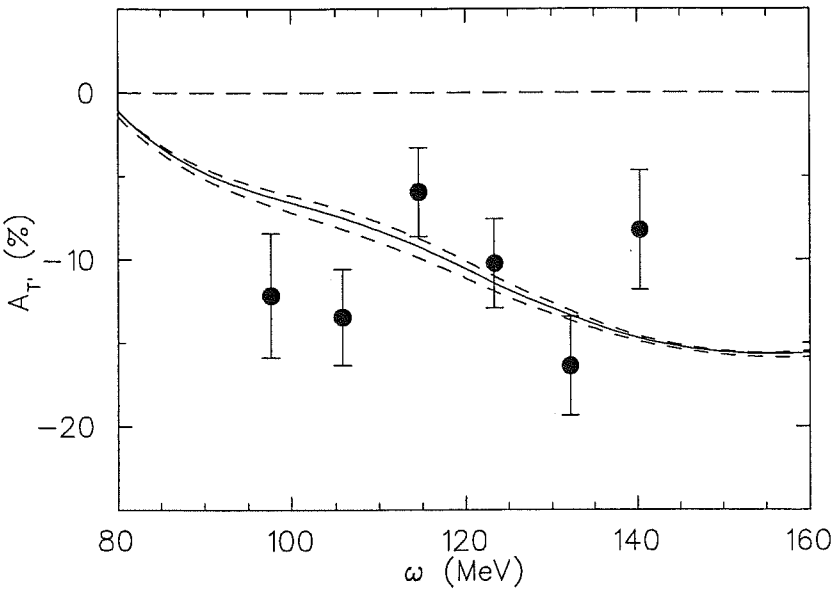

Figure 13: *The transverse asymmetry $A_{T'}$ as a function of electron energy loss measured at Bates [62]. The curves represent the predictions of various PWIA calculations.*

with PWIA calculations, allowing the extraction of a value for ${G_M^n}^2$. Fig. 14 shows the extracted value of ${G_M^n}^2$ in good agreement with the world's data. While $A_{T'}$ is dominated by the effects of the S-state neutron, the asymmetry $A_{TL'}$ in PWIA at the kinematics of the Bates experiment arises from the sum of a contribution due to the S'- and D-state protons (~75%) and a neutron contribution proportional to G_E^n (~25%). Thus, $A_{TL'}$ is significantly smaller than $A_{T'}$ and provides substantially new information which can be used to constrain our understanding of electron scattering at intermediate energies from the three body system. Fig. 15 shows the measured $A_{TL'}$ at Bates as a function of electron energy loss. A detailed study of the PWIA, as it applies to the Bates experiment, has been carried out [43]. Unlike $A_{T'}$, the experimental $A_{TL'}$ data do not compare well with the predictions; the experimental numbers are low at the 1.5–2 σ level. This may indicate the effects of FSI.

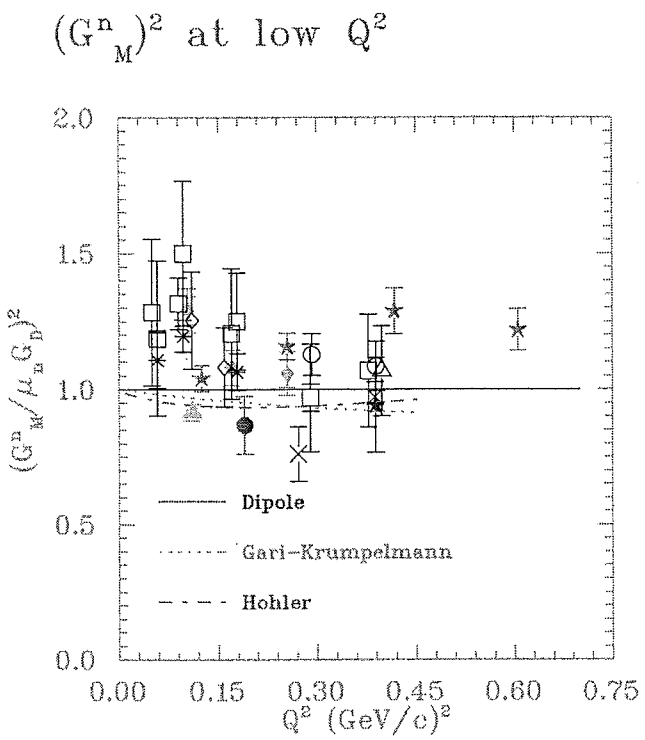

Figure 14: $G_M^n(Q^2)$ *(solid dot) showing the value determined from inclusive spin dependent scattering from* ^{3}*He [62].*

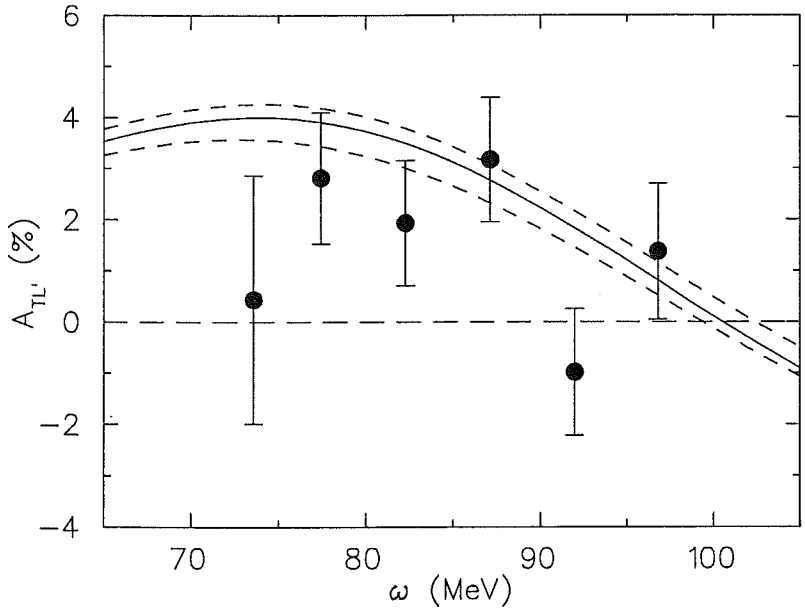

Figure 15: *The asymmetry* $A_{TL'}$ *as a function of electron energy loss measured at Bates [43]. The curves represent the predictions of various PWIA calculations.*

BLAST will simultaneously measure $A_{T'}$ and $A_{TL'}$ as a function of Q^2. We consider the case of 880 MeV incident energy where the target spin is oriented at 50° with respect to the incident beam direction in the horizontal plane. We assume 1000 hours of data taking at 10^{33} atoms cm^{-2} s^{-1} luminosity with 50% (40%) target (beam) polarization. In the sector which contains the target spin, the measured asymmetry will be centered around $\theta^\star = 90°$. In the opposite sector the measured asymmetry will be centered around $\theta^\star = 0°$. By combining data from both sectors $A_{T'}$ and $A_{TL'}$ can be separated. Data will be taken at quasielastic kinematics from $Q^2 = 0.1$ to 0.7 $(GeV/c)^2$. Fig. 16 shows the expected statistical precision in the determination of $A_{T'}$ (top) and $A_{TL'}$ (bottom). It is seen that the asymmetries will be determined to high precision over the kinematic range accessible with BLAST. It is interesting to investigate the precision with which $G_E^n(Q^2)$ can be measured from inclusive scattering. Fig. 17 shows the projected statistical precision and an estimate of the present theoretical uncertainty. As expected, at low Q^2 it is currently impossible to extract any significant information on G_E^n from inclusive scattering because of the large theoretical uncertainty. However, at high Q^2 the statistical uncertainty becomes comparable to the theoretical uncertainty, and it should be possible to determine G_E^n to about $\pm$ 20% [63]. Thus, one can compare the inclusive value with that using the neutron coincidence measurement. Note that both measurements are carried out simultaneously in the same apparatus. Further, it is not precluded that theoretical advances may reduce the size of the systematic uncertainty.

2.4.5 The Charge Form Factor of the Neutron from Polarized ^{3}He

From the discussion of inclusive spin-dependent scattering above, it is clear that given the present systematic errors associated with the PWIA model, accurate determination of $G_E^n(Q^2)$ at $Q^2 < 0.6$ $(GeV/c)^2$ from inclusive scattering is not possible. Further, the calculation of Laget indicates that the FSI of the recoiling neutron in (e,e'n) at $Q^2 <$ 0.25 $(GeV/c)^2$ are sizable. Thus, to determine G_E^n of the neutron in ^{3}He with high precision, one is restricted to high Q^2 and requires the neutron coincidence measurement. High quality measurements of G_E^n through quasielastic spin-dependent (e,e'n) scattering at Q^2 = 0.3 $(GeV/c)^2$ have been made at Mainz [45] and the initial results are shown in Fig. 18
.

The asymmetries for the $^3\vec{H}e(\vec{e}, e'n)$ quasielastic reaction plus the constraints from inclusive scattering can be used to extract G_E^n. The latter can be obtained from the relation [45]

$$G_E^n \equiv \sqrt{1+\tau\,(1+\tau)\left(tan\frac{\theta_e}{2}\right)^2}\;\frac{A_{TL'}}{A_{T'}}\;G_M^n \qquad (11)$$

with $\tau = Q^2/4M^2$, θ_e being the scattering angle of the electron, and $A_{TL'}$, $A_{T'}$ are the beam-target asymmetries for spin orientations perpendicular and parallel to $\vec{q}$, respectively. Both of these asymmetries are measured simultaneously in BLAST as well as the observable G_M^n which comes directly from the inclusive measurements. Fig. 19 shows the projected statistical errors for the extraction of G_E^n from BLAST data as a function of Q^2. We see

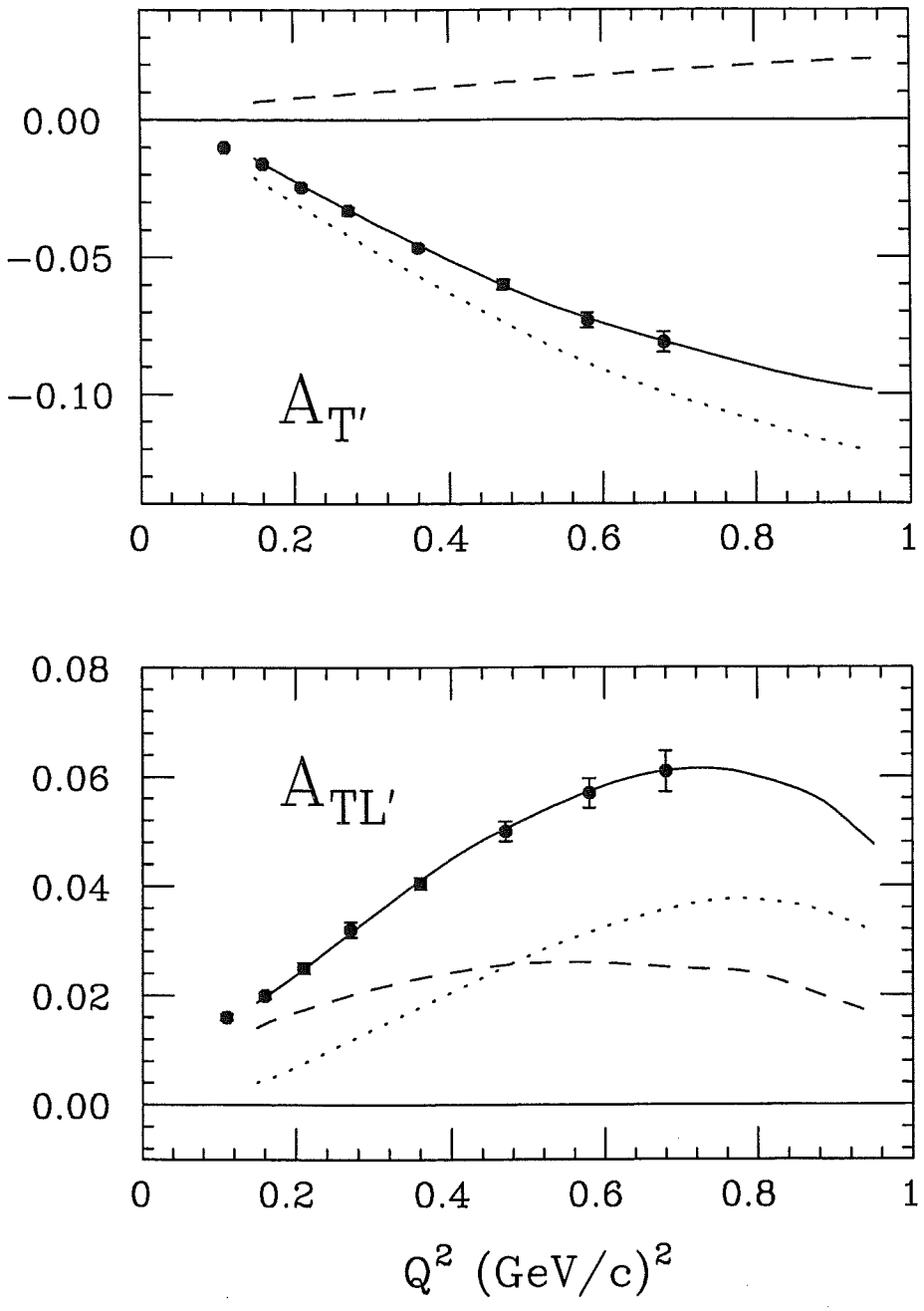

Figure 16: *The asymmetry $A_{T'}$ (top) and $A_{TL'}$ (bottom) as a function of Q^2 at the quasi-elastic peak for 880 MeV incident energy. The total result (solid curve) is compared with the respective neutron (dotted curve) and proton (dashed curve) contributions. The nucleon form factor parameterization of Gari and Krumpelmann was used. The solid points are the projected statistical uncertainties for 1000 hours of BLAST running.*

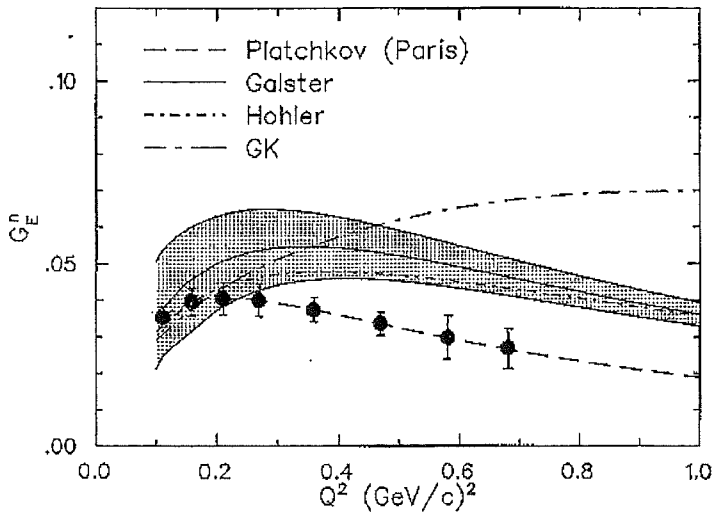

Figure 17: *The estimated present theoretical uncertainty (shown as an error band) for the extraction of G_E^n from quasielastic ^{3}He(e,e') [63]. The uncertainty, calculated in PWIA, is due to variations in the NN potential and off-shell prescription. The curves represent various parameterizations of G_E^n. The solid points are the projected statistical uncertainties for 1000 hours of BLAST running.*

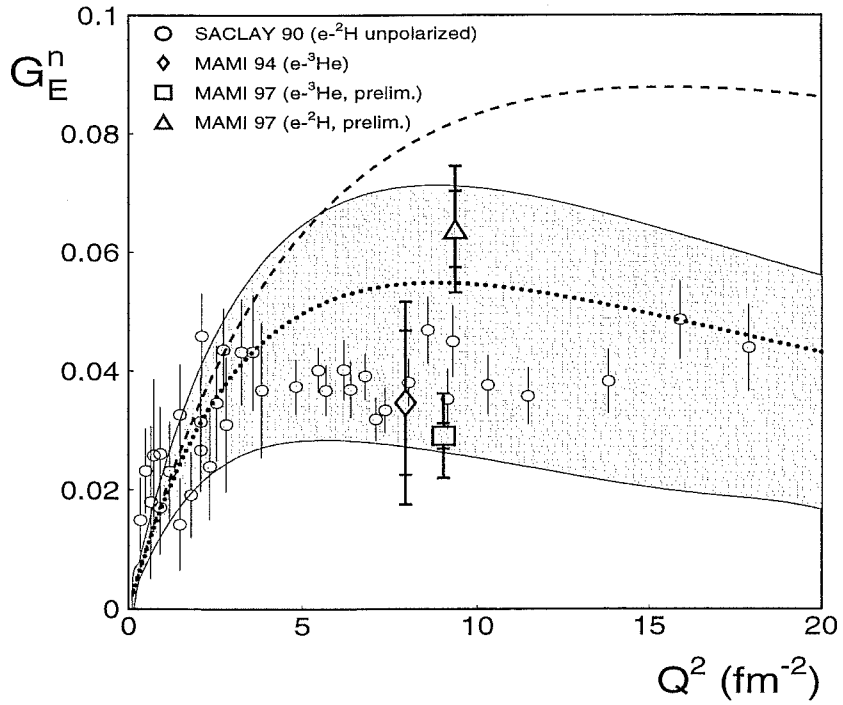

Figure 18: *The open symbols correspond to the data from Platchkov at al. [64] determined from elastic ed–scattering. The curves indicate the model dependence of those data. The Mainz datum from Meyerhoff et al. [45] (open diamond) follows from a measurement on polarized ^{3}He.*

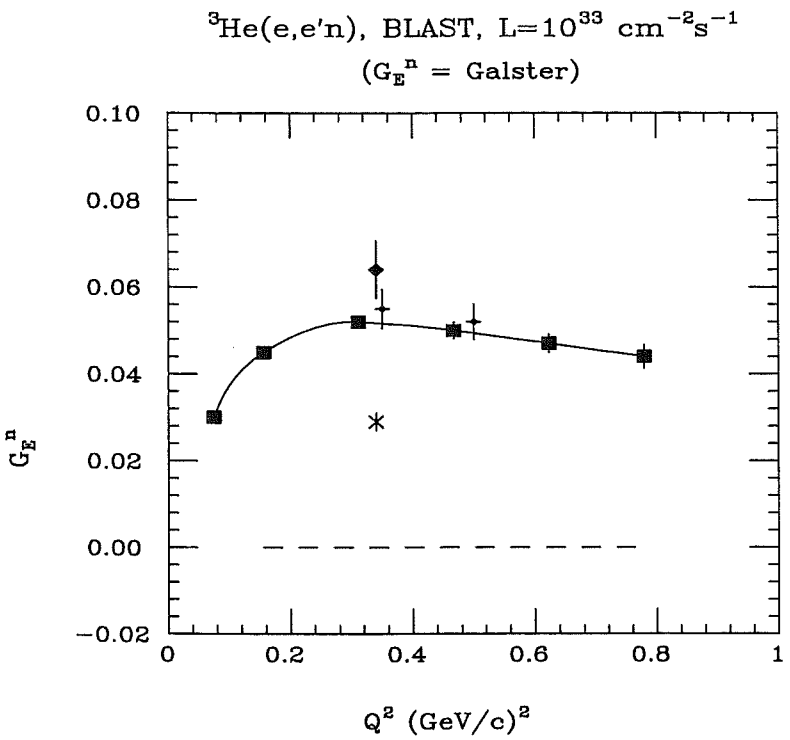

Figure 19: *The solid boxes are the projected G_E^n as function of Q^2 by combining the inclusive and exclusive $(\vec{e}, e'n)$ measurements. The statistical error for 1000 hours of running is shown. The X and solid diamond are the Mainz data on the polarized ^{3}He target and ^{2}H target with neutron recoil polarimeter measurement, respectively [38]. The + are the projected data from Bates experiment E89-05.*

that BLAST will measure G_E^n from 0.25 to 0.7 (GeV/c)^2 with high precision. We see that the projected BLAST uncertainties are such as to explore the discrepancy between G_E^n determinations from ^{2}H and ^{3}He reported from Mainz.

BLAST has the unique capability to measure $G_E^n(Q^2)$ for both the "free" neutron in the deuteron and the bound neutron in ^{3}He with the same experimental apparatus. A high precision comparison of G_E^n in the deuteron and ^{3}He is of great interest. The neutron in ^{3}He is not a free neutron but is bound by the strong interaction. The effects of the nuclear medium on the neutron charge form factor have been estimated. Sizable effects are obtained for the neutron in ^{3}He above $Q^2 \sim 0.6$ (GeV/c)^2.

2.4.6 Spin-dependent Charged Pion Electroproduction from ^{3}He

Measurement of spin-dependent charged pion electroproduction from ^{3}He is of interest for several reasons. Calculations have indicated that polarized ^{3}He is an efficient neutron spin target for pion production. In addition, the neutron and proton structure functions in pion electroproduction are of comparable magnitude. Thus, it is expected that spin-dependent measurements on ^{3}He can determine for the first time the spin-dependent response for charged pion production from the neutron. Further, pion production in the region of the

$\Delta(1232)$ resonance probes the role of the Δ in the nuclear wavefunction. Nucleons in the nucleus can have significant momenta which can result in Δ isobar components in the nuclear wavefunction. Thus, the Δ has a fascinating dual role of being both part of the reaction mechanism and also a nuclear constituent.

Lipkin and Lee [65] considered the question of whether one can see pre-existing Δs in electromagnetic pion production. Assuming that one can quasielastically scatter from a pre-existing Δ and ignoring effects of the D-state and rescattering, they showed that the ratio $\frac{(e,e'\pi^+)}{(e,e'\pi^-)}$ at Δ kinematics was sensitive to the probability of a pre-existing Δ component in the nuclear wavefunction. Milner and Donnelly [66] pointed out that one could enhance this sensitivity by use of spin observables. In particular, measurement of the ratio of sideways asymmetries when the pion was detected along $\mathbf{q}$ suppressed the dominantly transverse Δ production mechanism. It was estimated that a 2% Δ component in the nuclear ground state would change the ratio of charged pion asymmetries by about a factor of two. Further, Laget [17] considered the question of rescattering effects and pointed out the importance of reconstructing the complete Δ from its nucleon and pion decay products.

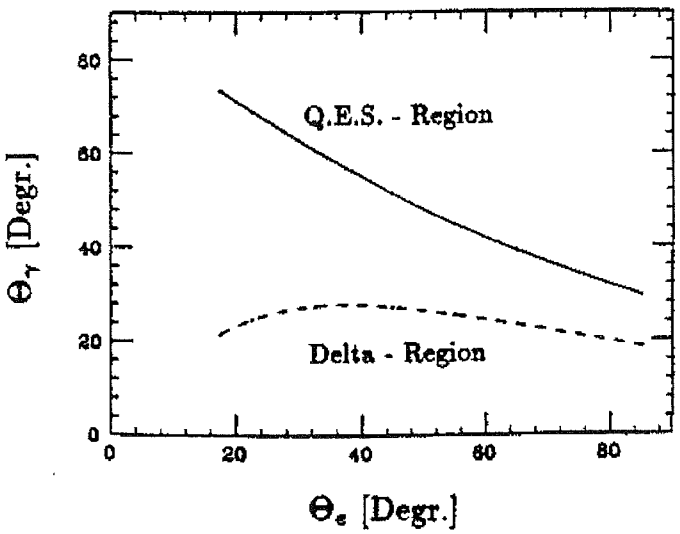

Figure 20: *Angle of recoil momentum as a function of electron scattering angle for 880 MeV incident energy. The dependence is shown for quasielastic scattering and for scattering in the Δ-resonance region.*

BLAST is very well suited to measurement of charged pion electroproduction in the region of the $\Delta(1232)$ resonance. From Fig. 20 it is seen that the angle of recoil momentum with respect to the incident electron is essentially constant over the entire angular range of BLAST. The average recoil momentum direction is at $-24°$. The target spin will be arranged normal to the average recoil-momentum direction, i.e. at $-114°$. In this way $\theta^\star$ will vary from 90° by $\approx \pm 6°$ for Δ-peak kinematics. The scattered electrons will be sorted into θ_e-bins for energies at the $\Delta(1232)$ resonance within ± 50 MeV of the peak and within $\phi = \pm\ 12°$. The variation in W over the Δ-excitation region ($\approx$ 1190 MeV to 1290 MeV) gives rise to a variation in θ_q across the Δ peak. Thus, on the pion side for each θ_e bin

there corresponds a kinematic region in θ_π. For parallel kinematics the spin-dependent part of the cross section has three terms: $W^{TL}(n)$, $W^{T'}(l)$, and $W^{TL'}(s)$. If we neglect non-resonant contributions, then $W^{TL}(n) = 0$ and we consider only the M_{1+}, S_{1+}, and E_{1+} amplitudes. The asymmetry then has the form

$$A = -v_T^{-1} \left(4\sqrt{2} \ \Re e \frac{M_{1+}S_{1+}^\star}{|M_{1+}^2|} \ v'_{TL} \sin\theta^\star \ + \ v'_T \cos\theta^\star \right) \quad . \tag{12}$$

A fit to the data of Siddle [8]– [12] was used to calculate A for each θ_e bin. The asymmetry due to the transverse longitudinal term is large, $\approx$ –0.25 to –0.6, in the kinematics of the proposed experiment. As the invariant mass of the hadronic system varies over the Δ peak, the recoil momentum direction changes as seen from Fig. 20. The effect of this variation on the asymmetry is typically about 15–20%.

For 1000 hours of running under the assumed conditions at low $Q^2 \approx 0.07$ (GeV/c)^2, the longitudinal-transverse asymmetry can be measured with a statistical error of about 3%, while the error increases to about 15% at $Q^2 \approx 0.4$ (GeV/c)^2. Further, BLAST with its large acceptance can allow complete reconstruction of the Δ by coincident detection of the nucleon. This measurement will provide a detailed test of our understanding of charged pion electroproduction in the Δ region and can probe the pre-existing Δ components at the level of 0.2%.

2.5 MULTIPLE COINCIDENCE EXPERIMENTS

There are two general programs of interest with BLAST which fall under the subject of multinucleon processes:

1. The study of NN correlations, for example in $(e, e'NN)$ reactions; and the study of Δ-nucleus interactions, for example in $(e, e'\pi N)$ reactions.

2. The study of the absorption of real or virtual photons involving more than two nucleons.

Reactions involving coincident detection of two nucleons are sensitive to the NN interaction. While the free NN interaction itself is known, the knockout reaction from bound nuclei could reveal new phenomena. At lower relative momentum the NN knockout reaction is described in terms of the two-body graphs: photon coupling to charged meson exchange, Δ production and damping, and the contact term (or Z-graph) arising partially from Lorentz invariance. At higher relative momentum, shorter range phenomena dominate. In this regime, it becomes unclear whether higher mass mesons and baryons are the relevant degrees of freedom, or whether one should talk about overlap of quark bags, quark Pauli exclusion, and fully antisymmetric six quark states.

BLAST provides the capability to measure the triple coincidence $(e, e'NN)$ response with high precision over extensive kinematics. We have performed simulations of ^{3}He$(e, e'NN)$ experiments by using theoretical calculations by Laget [67]. In particular, we have estimated that a ^{3}He$(e, e'2p)$ experiment can be performed with good statistical precision in about one week [68]. We will use ^{3}He and ^{4}He, in comparison with deuterium, to determine medium modifications to the two-nucleon interaction. ^{3}He polarization observables will contribute to the separation of multipole matrix elements. Tagging the reaction ^{4}He$(e, e'pn)$ by exclusive final states, the isoscalar and isovector deuteron, can separate the response for different isospin channels.

Δs produced in nuclei and interacting with remaining nucleons provide an additional baryon-baryon system to compare with the NN interaction. Measurement of the ΔN interaction would provide a distinct channel for testing our understanding of strong forces and baryon structure. A calculation by Oka and Yazaki [69] in a QCD framework of the NN, NΔ, and $\Delta\Delta$ systems in an SU(4) quark symmetry group provides predictions for the various channels. For example, in the channel that dominates pion absorption, the S = 2, T = 1 NΔ channel (2,1), the real part of the interaction is attractive at long range and repulsive at short range, much like the NN interaction. Other NΔ channels, the (1,1) and (2,2) channels, are predicted to be strongly repulsive.

Observed violations of the free isospin ratios for charged and neutral pions have been the strongest guide to date for the properties of the NΔ interaction. For a deuterium target, two nucleons can participate in the pion production. For the reactions ^{2}H(e,e'pπ^-)p and ^{2}H(e,e'nπ^+)n in quasi-free kinematics, one nucleon will most likely contribute dominantly to the strength. The corrections can be determined by comparing the $^1H(e, e'\pi^+)n$ amplitude measured with proton and deuteron targets.

We have estimated single-, double- and triple-event count rates for the reaction ^{2}H(e,e'Nπ) [68]. We have estimated the count rate for an unpolarized deuterium target with a 1 GeV electron beam. In these count rate estimates, a luminosity of 10^{33} atoms cm^{-2}s^{-1} is used.

Table 2: *Kinematics, solid angles and count rates for the proposed ^2H experiments.*

θ_e-bin degrees	Q^2 (GeV/c)^2	θ_q(W=1232) degrees	$\Delta\Omega_e$ msr	$\frac{d\sigma}{d\Omega_e d\Omega_\pi d\Omega_p dE_e}$ pb/sr^3/MeV	N hr^{-1}	$N_{p\pi}$ hr^{-1}	$\Delta N_{p\pi}$(500 hrs) %
20.0–25.0	0.09	28.4	15	236	1826	9.8	1.4
35.0–40.0	0.22	30.5	27	45.5	345	4.0	2.2
47.5–57.5	0.36	28.2	75	8.3	171	2.0	3.2
62.5–72.5	0.49	24.8	90	1.86	46	0.53	6.1

Table 2 gives the cross section as a function of angular bins from 20° to 80°. The momentum transfer direction for Δ peak kinematics is directed between –20° and –30° for electron detection between 20° and 80°. The electron acceptance is indicated in the θ_e-bins of

Table 2 with ϕ covering -15° – +15° at θ=80° and -9° – +9° at θ=20°. Energy acceptance at the $\Delta(1232)$ resonance is within $\pm$100 MeV of the peak.

The coverage of BLAST allows a determination of the cross section over an extended kinematic range. We have performed simulations of the cross section and resulting count rate as a function of out-of-plane angle [70]. We point out that even with two sectors, out-of-plane angles up to and including 90° can be accessed for a range of hadron angles relative to the momentum transfer direction. Response functions R_{TT} and R_{LT} have out-of-plane dependencies behaving like $\cos 2\phi$ and $\cos \phi$, respectively. These response functions are clearly evident in the simulated data.

The motivation to study the absorption of virtual photons involving more than two nucleons comes from the fact that more of the absorption cross section than we are able to explain, for pions and real photons, is going into such channels [71]. We have modeled experiments which would use the upgraded version of BLAST (six instrumented sectors) to study virtual photon absorption in nuclei leading to multinucleon emission, and we have found that useful data could be obtained in a reasonable length of time, i.e. a few weeks. We also continue our efforts to define which observables are likely to provide us a window on new physics. We also are keeping in contact with experimental programs at other accelerators which address similar physics questions. In recent years related data have been taken using SALAD at Saskatoon and DAPHNE at Mainz; CLAS at TJNAF will begin taking data in roughly one year. Before moving toward upgrading BLAST by instrumentation of more sectors, we will of course review the physics case at that time.

Even the two-sector BLAST will provide a very significant improvement in capability for multi-nucleon absorption studies compared to that available previously. We therefore plan experiments with the two-sector BLAST which we expect to provide important advancement in our knowledge of photon absorption. We also expect to learn detailed information concerning the rate capability of BLAST which will be crucial in deciding on the optimal design for instrumenting the extra four sectors.

2.6 RELATION to LIKELY OTHER RESEARCH

In 1989 the consensus of the Bates users was that in order to perform future experiments on spin-dependent electron scattering from polarized targets, a toroidal spectrometer offered the best combination of capabilities. This view has been corroborated by our own experience with alternative approaches in the subsequent years. Two of us (R. Alarcon and J. van den Brand) are among the principal investigators involved in the polarized internal target program of NIKHEF. The initial phase of this program uses non-magnetic detectors to measure the spin dependence of the $(e, e'p)$ reaction from tensor polarized deuterium [72]. The luminosity of 10^{31} atoms $cm^{-2}s^{-1}$ has limited the scope of the measurements up to now. It has been established through unpolarized measurements that the detection setup could operate up to a luminosity 10^{32} atoms $cm^{-2}s^{-1}$. Contingent on

target thickness improvements, this is the expected luminosity for polarized deuterium in upcoming NIKHEF experiments.

The next phase in the NIKHEF program is to carry out inclusive and exclusive measurements from polarized ^{3}He [51]. For this experiment the optimum luminosity is 10^{33} atoms cm^{-2}s^{-1}, and a new detector system will be used. The electron detector is now magnetic (a wedge dipole magnet) with a solid angle of almost 100 msr. At the time of this writing, polarized ^{3}He measurements have just been carried out with a 440 MeV polarized beam. Measurements at the originally proposed beam energy of 900 MeV are conditional on the repair of the spin control solenoids in the ring. The detection of protons and other hadrons continues to be non-magnetic. This instrumentation phase is very likely to be the final one in the NIKHEF program as the facility is scheduled to close next year.

Table 3 compares the experimental parameters of the detectors for the two NIKHEF phases with those of the revised BLAST. The different momentum, angular, and vertex resolutions

Table 3: *Comparison of the BLAST parameters with those of the NIKHEF experiments.*

Parameter	NIKHEF (Phase 1)	NIKHEF (Phase 2)	BLAST
Luminosity (L) (atoms cm^{-2}s^{-1})	$\leq 10^{32}$	$\leq 10^{33}$	$\geq 10^{33}$
Total $\Delta\Omega_e$ (msr)	150	100	760
Total $\Delta\Omega_p$ (msr)	300	300	760
Q^2-range (GeV/c)^2	0.15 to 0.45 *sequential*	0.15 to 0.50 *sequential*	0.10 to 0.70 *simultaneous*
Electron Detection	Non-Magnetic	Magnetic	Magnetic
Proton Detection	Non-magnetic	Non-magnetic	Magnetic
$L\times\Delta\Omega_e\times\Delta\Omega_p$ (10^{32} at cm^{-2}s^{-1}sr^2)	**0.045**	**0.3**	**5.8**

are similar when the detector elements are magnetic, such as BLAST and electron detector of NIKHEF phase 2. For non-magnetic detectors the resolutions are degraded by about a factor of 3, typically.

A quantity relevant to $(e, e'p)$ coincidence experiments is the product of the luminosity times the solid angles of the reaction products, namely $L\times\Delta\Omega_e\times\Delta\Omega_p$, where L is the luminosity and $\Delta\Omega_{e,p}$ the electron and proton total solid angles, respectively. This quantity is also shown in Table 3.

An additional important consideration is that the measurements are sequential with the NIKHEF detectors , i.e., there must be a different data run for each Q^2 under investigation and for each spin orientation. On the other hand, BLAST measurements are simultaneous for a wide range of Q^2, and the symmetry of the detector allows the simultaneous measure-

ment of different spin orientations. These unique BLAST features are necessary to ensure control of systematic uncertainties below the 5% level, a crucial condition to carry out the ambitious scientific program.

The BLAST program is unique and complementary to those envisaged at other electron beam facilities, such as TJNAF and Mainz, with external targets. At Bates and TJNAF measurements of G_E^n are approved with a recoil neutron polarimeter and with a polarized deuterium target. The proposed BLAST measurements are quite competitive with experiments based on these methods, as seen clearly in Fig. 19. The TJNAF polarized target measurement contains only $\sim$ 15% of its target nucleons in the form of polarized neutrons. Also the target requires a relatively high magnetic field resulting in a sizable effect on the trajectories of incident and scattered particles. Because of their associated systematic uncertainties, these techniques are inferior to those planned with BLAST, where the systematic limitation will be the knowledge of the beam and target polarizations, which can be calibrated, monitored and cross-checked *in situ* simultaneously with data acquisition. In addition, measurements at TJNAF with a polarized ^{3}He target have been conditionally approved for the CLAS detector. However, significant technical issues have been repeatedly raised and it is clear that, unlike the BLAST detector, the CLAS detector configuration has not been optimized for measurement of spin observables. This example underscores the fact that TJNAF does not have an experimental configuration optimized to study the spin structure of few body systems.

In Europe the Mainz facility has an ongoing program of measurements to measure G_E^n both by the recoil neutron polarimeter technique and by measurement of ($\vec{e}$,e'n) scattering from polarized ^{3}He. In both cases the electron detection is non-magnetic with consequently limited information on the dependence of the electromagnetic response on the direction of momentum transfer and possible contamination by inelastic processes. Plans to use a magnetic spectrometer for electron detection are in progress.

In summary, the BLAST experimental configuration represents the best method to carry out a comprehensive program of measurements of spin dependent electron scattering from polarized few-body systems. The measurement of nucleon form-factors and the spin structure of few-body systems are of central importance to nuclear physics. To address these important problems, our field must take advantage of the best techniques available and not be content with limited measurements utilizing conventional approaches. Ultimately, the important questions are decided by the best experimental information, and BLAST is in the unique position to provide these answers for the spin structure of few-body systems.

3 BLAST PROJECT TECHNICAL SUMMARY

3.1 The MIT/BATES SOUTH HALL RING

The South Hall Ring (SHR) is designed to operate either as a storage ring for internal target experiments, or as a pulse stretcher ring to convert the low-duty-factor beam from the linac to near CW beam for use by external target experiments. Commissioning the ring is well underway; extracted beam should be delivered to the first experiments within the coming year, and a program of commissioning the ring in storage mode has been developed. This program is driven by the requirements of the experiments which are planning to use BLAST.

The layout of the ring and associated beam lines is shown in Fig. 21, and ring parameters are

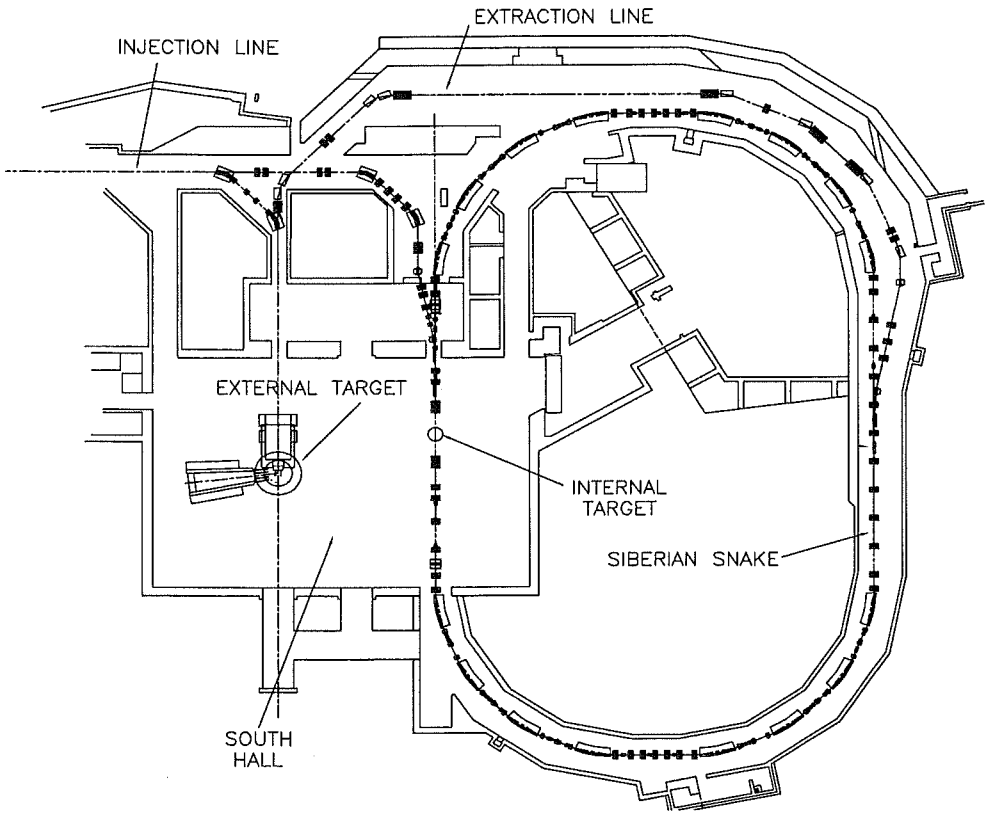

Figure 21: *The layout of the SHR and associated beam lines. The internal target region and the location of the spin–control solenoids are also indicated.*

given in Table 4. The circumference of the ring is half the linac-recirculator circumference. This relation, coupled with operation near a half-integer horizontal tune, allows two-turn injection into the ring, when operating the recirculator in head-to-tail mode. With 40 mA beam current from the linac, one will thus have a stored current of 80 mA. However, by

means of beam stacking currents in excess of 200 mA have been stored at the AmPS ring of NIKHEF. Due to the similarities between the Bates SHR and the AmPS ring we also expect stored currents of the order of 200 mA in the SHR.

Table 4: *SHR design parameters.*

Parameter	Value	Unit
Energy range	300-1000	MeV
Circumference	190.204	m
Revolution frequency	1.576	MHz
Bend radius	9.144	m
Stored current (2-turn inj.)	80	mA
Extracted current (average)	50	μA
Extracted duty factor	85	%
Internal duty factor	99	%
Injection frequency	1	kHz
RF frequency	2.856	GHz
Harmonic number	1812	
Momentum compaction	0.029	
Horizontal tune (stor. mode)	7.420	
Vertical tune (stor. mode)	7.875	
Synch. rad. losses (at 1 GeV)	9.8	keV/turn
Inj. energy spread (with ECS)	0.04	%
Injected emittance	0.01	mm mr

The internal target will be located in the center of the west straight section of the ring. The ring has been designed with small β–functions at this location, to accommodate storage cells with small diameters. The low β's also reduce the angular growth of the beam resulting from small angle and multiple scattering in the target. This design will help to maximize the beam scattering lifetime.

A polarized electron beam will be an important feature of the SHR. The anticipated polarizations are 40% at present, and may be 60% or higher if a high-polarization crystal is installed in the polarized source. In order to maintain longitudinal polarization at the internal target point, for arbitrary energies, two superconducting solenoids (Siberian snake) will be installed in the east straight section of the ring, along with various skew and normal quadrupoles. These components are currently in-house, but have yet to be installed in the ring.

Commissioning the ring for use by internal target experiments has produced encouraging results. Lifetimes (1/e) of several minutes have been achieved at energies of 330 and 750 MeV. Such lifetimes are long enough for internal target experiments. In addition, these lifetimes are much longer than typical damping times (2 seconds at the lowest energies), and

therefore allow stacking of the beam to achieve higher stored currents. The first stacking studies took place in the Spring of 1997. A maximum current of 30 mA was obtained. Further studies are planned to increase the stored current (see Sec. 4).

The ring has also been operated with polarized beam. Polarized electrons were injected into the ring, and stored for a known number of turns. After kicking the beam out of the ring, the electron polarization was measured with the B-Line Møller polarimeter. The spin was thus monitored for thousands of turns, and the frequency of the spin precession measured. By using this technique, the absolute energy of the beam in the ring was measured to better than one part in 10,000. The measurements also showed that the intrinsic spin lifetime was longer than 10,000 turns. The results are shown in Fig. 22 [73].

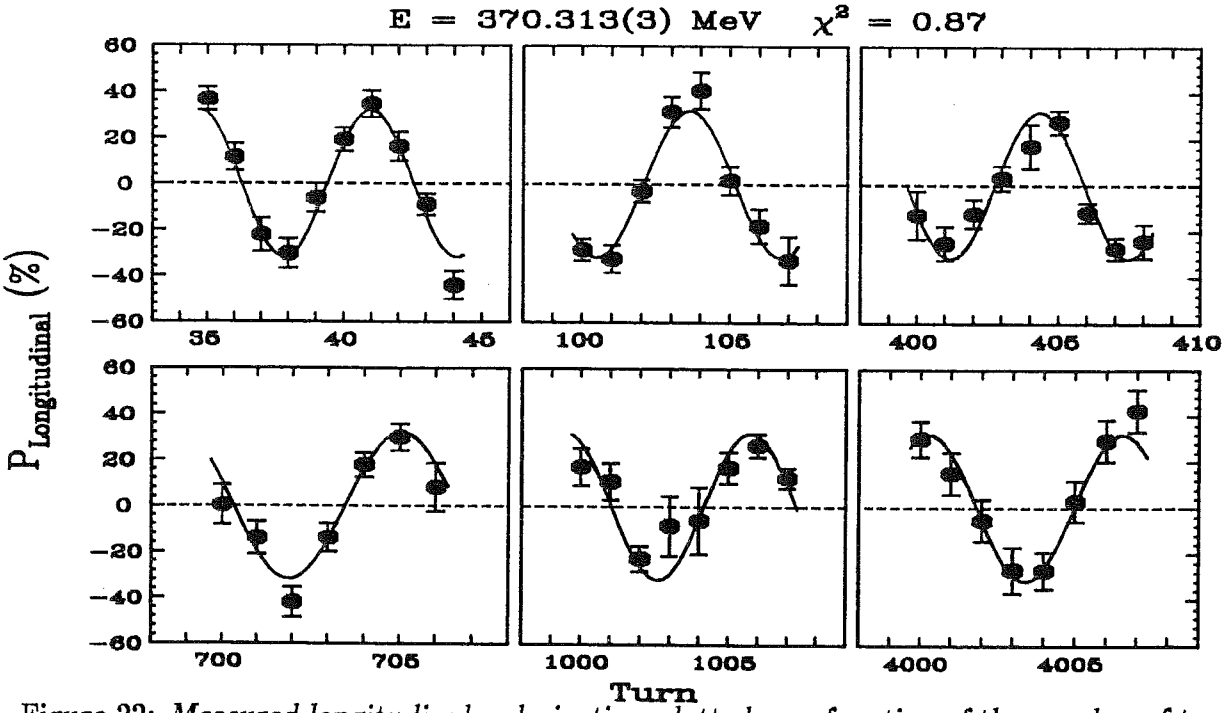

Figure 22: *Measured longitudinal polarization plotted as a function of the number of turns the beam circulated in the SHR (Ref. [73]).*

A systematic program of ring studies focussing on use of internal targets and BLAST was proposed at the April 1997 Bates Program Advisory Committee and given an 'A' rating. These studies will address lifetime, beam current/stacking, backgrounds (both injection flash and halo) with internal targets in place, and polarization control and measurement. A more detailed program for these studies is presented in Sec. 4. This program will be scheduled for the regularly occurring SHR beam developments, in parallel with the BLAST detector development.

3.2 The POLARIZED INTERNAL GAS TARGETS

An internal polarized gas target in a storage ring provides a nearly ideal interaction between polarized beam and polarized target [74]–[76]. The polarized target nuclei are present as pure atomic species so there is no dilution of the spin-dependent term in the scattering cross section; the target cells have no end windows so scattered particles at very forward angles can be cleanly detected; the target polarization can be reversed rapidly; only a relatively low holding magnetic field is required; and the storage cell wall may be thin, which allows for the detection of heavily ionizing recoil particles.

An internal polarized target consists of a source that generates a flux of polarized nuclei directed into a windowless conductance-limiting storage cell, through which the stored circulating beam passes [77]. The storage cell increases the dwell time of the polarized atoms near the interaction region by providing a conductance $C(z,T)$ which is a function of the longitudinal distance z from the center of the target and the temperature T of the cell wall. The conductance also depends on the physical dimensions of the storage cell. In this way the target thickness $\rho(z)$ is significantly enhanced. The flux in (atoms/s) is expressed as

$$F = \int_{-L/2}^{+L/2} \rho(z) C(z,T) dz, \tag{13}$$

where L is the length of the storage cell, and the total areal density encountered by the circulating stored beam is

$$t = \int_{-L/2}^{+L/2} \rho(z) dz \quad . \tag{14}$$

For ^{3}He, the BLAST collaboration will utilize a polarized internal target very similar to the one constructed for experiment CE–25 at the IUCF Cooler Ring [78]. This target was designed to produce vertically polarized ^{3}He atoms in the A-section of the Cooler Ring and to allow detection of scattered nucleons over a large angular range. The target was polarized in a 1-mT magnetic field provided by a 1-m-diameter Helmholtz pair. The polarized ^{3}He source, which uses the technique of metastability exchange optical pumping [79, 80], was connected by a Pyrex precision capillary to the storage cell. The properties of this target are presented in more detail in Sec.5.

The MIT group in HERMES has led the effort in the design and installation of the polarized ^{3}He internal gas target for that experiment for the past several years. The design is based on the target used at IUCF. A cryogenic cooled cell has also been developed [81] which allows the target cell temperature to be varied between 10 K and room temperature. In addition, a target optical monitor has been developed [82] which allows the target cell polarization to be monitored. The target was installed in 1995 and used for HERMES production data taking between August 12 and November 28, 1995. Additional information on this target is presented in Sec. 5 as well as the technical considerations to implement the ^{3}He target for BLAST.

The initial program of BLAST measurements involving polarized ^{1}H and ^{2}H was proposed for an atomic beam source (ABS) available from the University of Wisconsin [70]. Significant improvements have occurred in the development of internal polarized ^{1}H and ^{2}H targets since that time. First, members of the BLAST collaboration led the effort to mount and operate an ABS in the NIKHEF ring [83]. A stable performance was achieved over a five-week running period, with on-line measurement of the polarization of the target gas. Plans to upgrade this source and implement it for BLAST are discussed in Sec. 5. Second, polarized ^{1}H and ^{2}H laser driven sources (LDS), which are based on the principle of spin-exchange optical-pumping [84], have undergone considerable development. Electron polarizations $\geq$70% have been observed at flows ranging from 2×10^{17} to 2×10^{18} atoms/s. The BLAST collaboration is in close contact with the groups developing the LDS for polarized ^{1}H and ^{2}H.

3.3 OVERVIEW of the MAGNETIC SPECTROMETER

Table 5 summarizes the requirements of the spectrometer for the proposed measurements with polarized electron beams and polarized internal gas targets. The proposed measurements of electromagnetic spin observables require a magnetic spectrometer with a solid angle of about 1 sr. The spectrometer must be field-free and gradient-free at the target position, and symmetric in the scattering plane about the incident-beam direction. These requirements lead to the present BLAST design. The various technical aspects of the BLAST detector, including modeling of the proposed experiments, have been discussed in detail in ref. [70].

Table 5: *Requirements of the spectrometer for the proposed measurements with polarized internal gas targets.*

Spectrometer Requirements	Consequences for design
no magnetic field at the target	toroidal field configuration
maximum luminosity = 10^{33} *atoms* cm^{-2}s^{-1}	detector design
magnetic gradients $<$ 50 mGauss/cm at target	8–coil design
large solid angle	$\Omega \sim 1$ sr
target diameter $\sim$ 1 meter	inner diameter $\sim$ 1 meter
q-direction definition	$\frac{\Delta E'}{E'} < 2$ %
	$\Delta\theta_e < 5$ mrad
simultaneous measurement of T′ and TL′ asymmetries	symmetric detector
$e/p/n/\pi^{\pm}$ separation	particle identification

The BLAST detector is a non-focusing magnetic spectrometer with eight copper coils arranged in a toroidal configuration. The initial detector package consists of two opposing sectors instrumented in the forward direction with wire chambers, scintillation detectors,

and Čerenkov counters for tracking, time-of-flight, and particle identification (PID). In addition, two sectors of thick scintillation detectors from 35° – 70° will provide for neutron detection, a lead glass forward calorimeter will provide extra PID capability, and an array of recoil detectors inside the scattering chamber will be used to detect recoiling nuclei. The main parameters of the BLAST detector are listed in Table 6. The design empha-

Table 6: *Properties of the BLAST detector.*

Quantity	Acceptance/Performance
Angular Range	$\theta = 20° - 80°$
	$\phi = \pm 15°$ at $\theta = 90°$
	$\phi = \pm 5°$ at $\theta = 20°$
Solid Angle	0.38 sr/sector
Momentum Range	$\frac{\Delta p}{p} = \pm 20$ % for e^- detect. eff. of 99 %
	$\frac{\Delta p}{p} = \pm 25$ % for e^- detect. eff. of 80 %
Momentum Resolution (for e^-)	1.2 % FWHM at 20° and 1.0 GeV
	2.4 % FWHM at 90° and 0.5 GeV
Particle Identification (TOF)	π/K 3σ up to 0.9 GeV/c
Maximum Luminosity	$\approx 10^{33}$ atoms $cm^{-2}s^{-1}$

sizes conventional detector technology, off-the-shelf electronic components, and existing data-acquisition system software to minimize cost and development time. The proposed configuration including coils, support structure, and detector elements is shown in Fig. 23.

3.4 RUNNING STRATEGY

It is proposed to take data in a running period of several months duration on a specific polarized target. The goal would be to run in a mode where the target, beam, and spectrometer are stable over several months. During this time regular running with unpolarized hydrogen gas will allow monitoring and calibration of the detector acceptance and efficiencies against a well known scattering cross-section.

It is planned to take data in a mode which maximizes the duty factor and also the luminosity. A schematic illustration of the likely running configuration is shown in Fig. 24. The SHR is filled over time t_s by repeated dual-turn beam injections separated by about 2.5 beam-damping times (stacking). Data acquisition proceeds for some time t_d during which the beam current decays exponentially with some time constant t_B. This cycle repeats

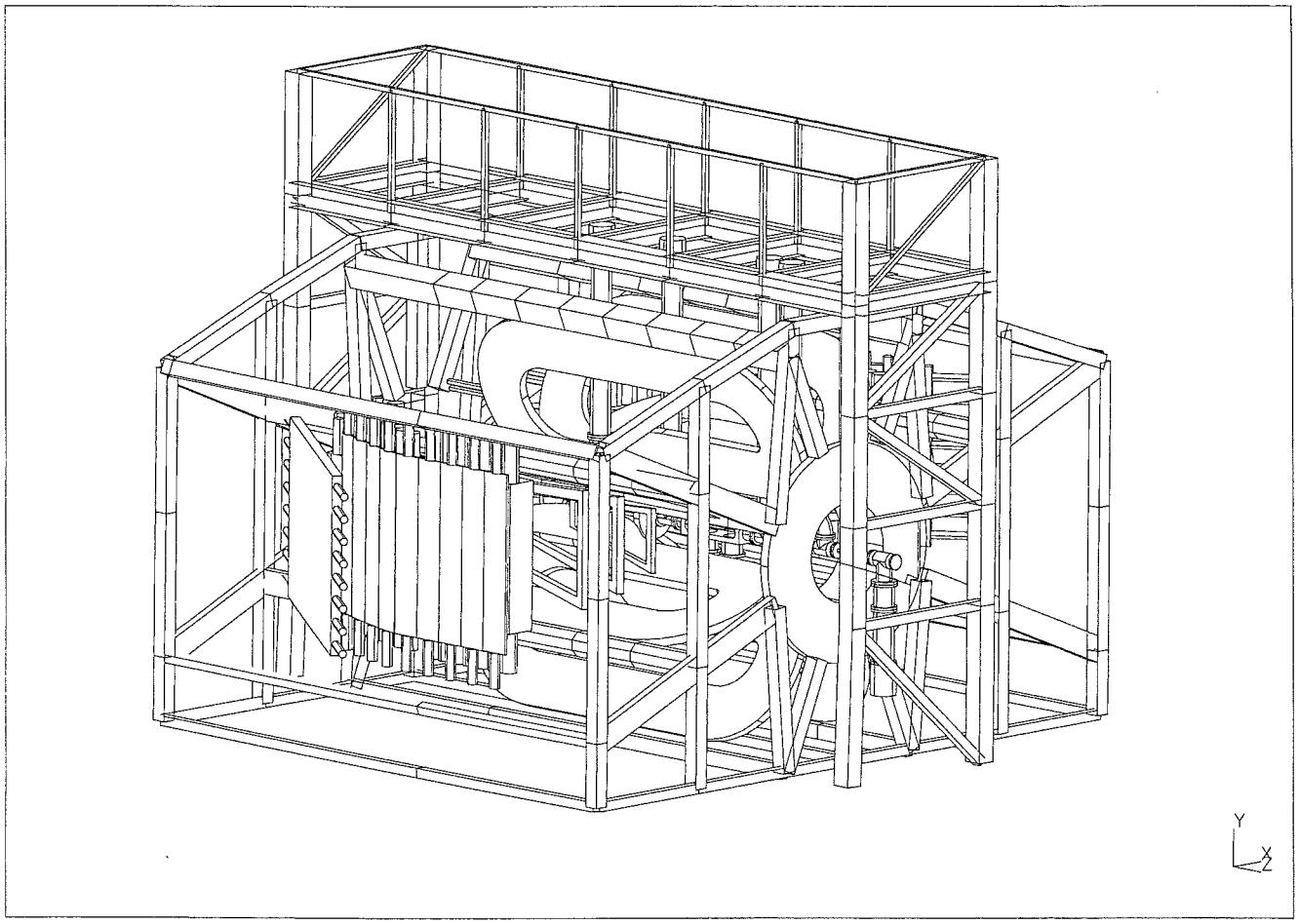

Figure 23: *The BLAST spectrometer showing the instrumented two sectors, the magnetic coils and support structures. The z-axis is directed along the electron beam and the y-axis is the vertical direction, perpendicular to the floor plane. The beam height is 2.15 m above the floor.*

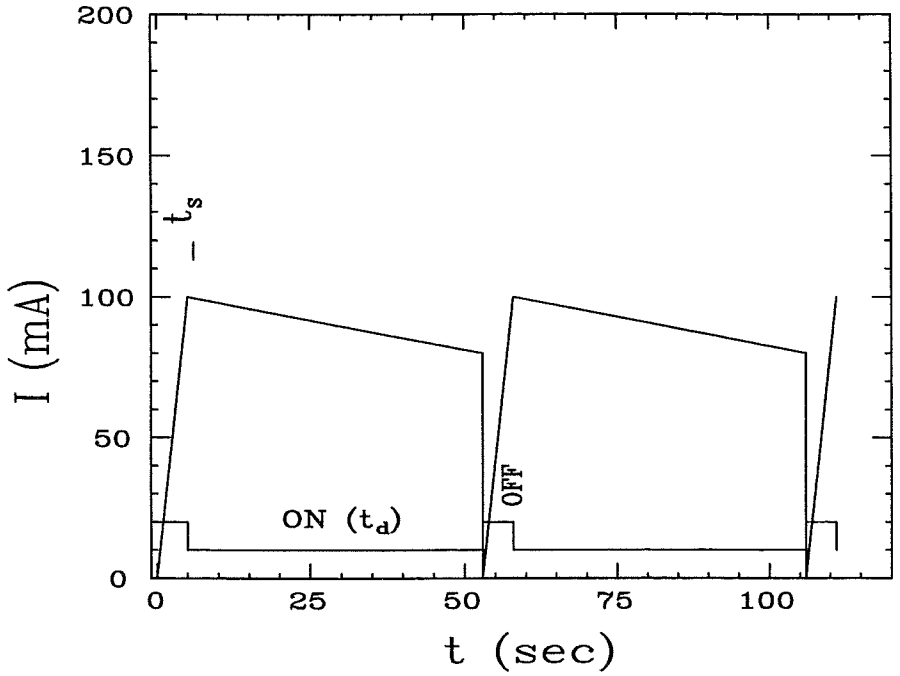

Figure 24: *Schematic diagram of the stored beam current vs. time showing the relevant time constants.*

indefinitely. The duty factor for data taking D is

$$D = \frac{t_d}{t_d + t_s} \,. \tag{15}$$

The current decays as $I(t) = I_0 \exp^{-\frac{t}{t_B}}$ so the average current during data taking $< I >$ is

$$< I >= \frac{t_B I_0}{t_d}[1 - \exp^{-\frac{t_d}{t_B}}] \,. \tag{16}$$

The average current over the full cycle is $D \cdot < I >$. Consider now some realistic expectations. For a 750 MeV beam, the damping time t_{damp} is 0.16 sec. At a beam life time t_B of 4 min. ($t_B/t_{damp} = \tau_B = 1500$) t_s is 5 sec., and t_{daq}=48 sec ($\tau_d = 300$). About 100 mA initial current is needed requiring about 13 stacks of 8 mA injection current (see Fig. 25). Fig. 24 is a schematic diagram of the stored beam current as a function of time showing the ON/OFF data acquisition gate for two consecutive fills. The impact of reversing the target spin direction within one fill has not been addressed in the previous example.

The beam polarization direction is constant over the fill. The orientation will be randomized from fill to fill. To form a spin asymmetry, the target polarization will be reversed at least once per fill. This technique allows the formation of an asymmetry for each fill. The luminosity for each spin state will be monitored by measuring the current and target thickness.

3.5 SYSTEMATIC UNCERTAINTIES

In the determination of the scattering asymmetries there are several sources of systematic uncertainty:

- **beam polarization:** The beam polarization will be measured with a Compton backscattering polarimeter to $\pm 3\%$. Our plans for such a device are discussed in Sec. 4.
- **target polarization:** The target polarization will be measured with a target polarimeter to $\pm 3\%$. In addition, it is planned to simultaneously measure the known asymmetry in elastic scattering. This measurement should allow a determination of the product of beam and target polarization over the running period to $\sim 3\%$ and thus provide an important cross-check on the systematics associated with the individual beam and target polarization measurements.
- **luminosity measurement:** The relative luminosity in each spin state will be determined to $\pm 1\%$ by monitoring the stored current and the target thickness.
- **time-dependent acceptance:** It is imperative that the spectrometer acceptances and efficiencies remain stable on the timescale of the spin-flip i.e. about 2 minutes. These quantities will be monitored on-line.

4 The STORED ELECTRON BEAM

4.1 INTRODUCTION

The reliable availability of the polarized stored electron beam at energies up to 900 MeV over several months per year is essential for the success of the BLAST physics program. The physics measurements projected in Sec. 2 assume 80 mA average current with 40% longitudinal electron polarization at the target position. The stored current must pass through the narrow target cell and its magnitude must be monitored over a fill to better than $\pm$ 1%. The polarization of the beam must be determined to $\pm$ 3 %. Further, the background rate from beam losses in the BLAST detector must be acceptable. As described in this chapter all essential properties of the beam have been demonstrated at the AmPs ring in Amsterdam. However, experience at several laboratories has shown that the development of the stored beam will require a substantial effort over several years. The outline of this beam development program is described here.

4.2 BEAM LIFETIME

Stored electrons colliding with gas atoms at rest in the storage ring can be scattered outside the acceptance of the ring and intercepted at ring apertures. Those electrons which are scattered out of the beam emittance but not out of the ring acceptance will continue to circulate in the ring and will eventually be brought back into the beam phase space by synchrotron radiation damping. The beam lifetime is determined by contributions from several effects: Coulomb scattering from neutral gas atoms (either from residual vacuum or internal target); scattering from ions generated by the stored beam interacting with gas in the ring (ion trapping); bunch-bunch instabilities at high currents, etc. Based on experience at NIKHEF and calculations by C. Tschalär [85] it is likely that the dominant effect up to 250 mA at 10 minute lifetime is due to ion trapping.

Ring electrons will ionize the rest gas and trap those ions in their electrostatic (and to a lesser extent their magnetic) field thus increasing the density of atoms in the beam and multiplying the scattering losses. At typical rest-gas pressures of several nTorr, the ion densities build up to their natural limit (equaling the beam electron density) within less than a few seconds. This ion saturation density is a large multiple of the rest gas density for beam currents in the 100 mA range.

Scattering losses from ions at saturation density reduce beam lifetime to a minute or less at higher beam currents. To reach storage times of order 10 minutes, these ions must be cleared from the beam continuously. Two methods of ion clearing have been considered. The first one introduces a 20 to 30% gap in the circulating electron beam. The resulting periodic interruptions of the electric containment field of the beam causes instabilities in the ion cloud which, under certain conditions, disperses the ion cloud. An alternative way

to clear ions is by introducing a set of electrostatic clearing electrodes at intervals around the ring. This method relies on thermal migration of ions along the beam because the installation of continuous electrodes all around the ring is impractical. Calculations show that ions created outside the bending magnets are reflected at the magnet boundaries, thus requiring clearing electrodes between all magnets. Ions created inside the bending fields are expelled from the benders by the combined action of the magnetic field and the electrostatic field of the beam. The ion density in the drift regions is then determined by the distance between the clearing electrodes and the rest-gas pressure for a given beam energy and current. The scattering losses, and thus the beam lifetimes, are entirely dominated by the heavy rest-gas components such as N_2, CO, and possibly Ar. Beam lifetimes of many minutes require clearing electrodes every few meters within the straight sections of the ring along with N_2 or CO partial pressures in the 10^{-10} Torr range whereas He and H_2 pressures of 10^{-8} Torr are acceptable. Near an internal H_2 or He target, an ion saturated region of up to 10 m between clearing electrodes would not limit beam lifetimes below about 20 minutes.

Beam lifetimes due to synchroton radiation induced by electron losses from the RF bucket were measured in the Spring of 1997. These lifetimes were larger than 6 min. for a beam energy of 750 MeV. These losses are therefore not likely to dominate total beam lifetimes.

Scattering from rest-gas ions and atoms results in a beam halo which will produce background when it is intercepted by the storage cell of the internal target and other apertures. It is assumed that a collimator system will reduce the beam halo to an emittance smaller than the storage cell acceptance. Thus, only halo produced between the collimator and the internal target can produce direct background from the storage cell. Estimates for the background electron flux from the storage cell inside a 6° angle show rates below 1% of the flux from a ^{3}He target of 10^{15} atoms/cm^2 at energies below 50 MeV for a N_2 rest gas pressure of 10^{-9} Torr.

4.3 WAKE-FIELD EFFECTS

In the design of an internal target system for the SHR, wake-field effects have to be considered [86]. Such wake-fields will be excited in the target chamber and storage cell and could damage the special wall coatings on the storage cell which prevent depolarization, and could lead to instabilities in the circulating electron beam.

Wake-field heating of the storage cell structure has been calculated [70] and it is found that by tapering the conductance limiters the RF power stored in a given cavity (i.e. storage cell and target chamber) can be reduced considerably. It is also found that most of the power loss is generated by the reflections at the end of the vacuum chamber. For an optimized design there is total power loss of only 0.25 W. From this we conclude that wake-field effects do not pose a problem for the proposed internal target. Wake-field heating is not a problem in the NIKHEF internal target which does not use tapered limiters. Wake-field effects also can limit beam storage lifetime, but this was not observed at NIKHEF

where 100 mA beams have been routinely stored for more than 30 minutes. Although the NIKHEF experience is very encouraging, the AmPS ring is not identical to the Bates SHR so we will make a target designed to minimize wake-field effects.

4.4 INJECTION FLASH and BACKGROUNDS

Injection flash is the high detector rate expected during the 1.3 μsec injection period. It is caused by electrons scattering forward from the injection septum into the beam pipe walls inside BLAST.

4.4.1 Simulation

Studies of the effects of the injection flash were the subject of a report [87]. The program modeled the electron interaction with the injection septum and followed the shower down the beam line, through the walls of the beam pipe, and into the BLAST detector. The shower through the walls of the beam pipe gives a luminosity during the injection which is in agreement with the rough calculations made previously. Molybdenum was found to be the septum material giving the lowest background. Energies of 350 MeV and 880 MeV were used, with the expected sharp increase of background at the higher energy. The shielding effects of the septum chamber, beam-line quadrupole magnets, and lead around the beam pipe were studied. At 880 MeV the GEANT results predict that the ratio of the number of electrons coming out of the beam pipe to the number hitting the septum is about 50 for no shielding, 25 if the shielding of the collimator box is included and 10 if a 1" lead shield is placed around the beam pipe, indicating that shielding will reduce the injection flash by a factor of 5. The GEANT calculations also gave the angle and energy distribution for the number of photons and electrons per 100 electrons hitting the septum. It turned out that the electron angular distribution is not strongly peaked forward, and most of the electrons have energies below 20 MeV and will be swept away by the magnetic field. The GEANT calculation did not include the effect of the magnetic field. The calculated instantaneous current in the drift chambers during injection is a factor of 10^5 larger than the average current trip point. However, the injection flash from the septum should last for a maximum of 1.3 μs. With the magnetic field on and the low energy electrons removed, this current could drop by a factor of 100.

Calculations [70] of the effect on BLAST drift chambers indicate that their operating voltages need to be reduced by a few hundred volts during injection. This procedure has been routinely used in the internal target experiments at NIKHEF and IUCF. With the anticipated injection period of 10 sec and a beam cooling time of order 1 sec we do not expect problems from injection flash or early-time beam loss.

4.4.2 Measurements

Over the last five years the South Hall Ring has been operated several times to study the properties of the stored beam. At every opportunity, measurements of the background rates into detectors in the region of the internal target have been carried out.

In August 1992 measurements were made which allowed an estimate of the rate in BLAST arising from injection flash. A 1.5" $\times$ 1" scintillator on a PMT at 10" from the beam pipe at the BLAST position produced a rate of 1 MHz/mA of injected beam. The BLAST (0.76 sr) rate would have been 65 MHz/mA or 2,600 MHz at 40 mA injection. The original BLAST proposal to the DOE estimated a rate of 10,000 MHz at 40 mA assuming 10^{-5} of the injected beam hits the injection septum. The BLAST rate during production data acquisition at 40 mA is estimated to be about 0.1 MHz. It is clear that detector systems need to be gated off during injection. On the other hand, the overall radiation stress on the BLAST detector is less from injection flash than from production data acquisition. For example, a 40 mA injection for 0.6 μsec every 30 seconds has a duty factor of 2×10^{-8}, bringing the estimated average rate down from 10,000 MHz to 200 Hz, a factor of 500 less than the data rate. The measurements were made with a injected beam 5 mm from the injection septum. The injection flash measurements will be repeated with the additional restrictions of injecting with good beam storage times and the internal target in place.

In addition, measurements were made to estimate the magnitude of background rates in BLAST arising from beam losses during cooled beam. A 1.5" $\times$ 1" scintillator on a PMT attached to the beam pipe 5 m downstream from BLAST gave a rate of 5 kHz/mA with cooled beam. The BLAST rate (0.76 sr) would have been 17 kHz/mA or 1.7 MHz at 100 mA. The expected BLAST rate from the ^{3}He target alone is about 0.3 MHz at 100 mA. The rate from the counter on the beam pipe is roughly that expected for uniform beam loss around the ring with the measured lifetime (4 minutes) and also agrees roughly with the measured bremsstrahlung rate at the end of the straight section. This result was obtained with no target in the ring. The losses to the beam pipe should increase with increased gas load in the ring, but may be controlled by the use of halo scrapers and electrostatic sweepers to limit ion trapping.

4.5 SPIN CONTROL

Polarized beams, as they are injected into the SHR, will be longitudinal at the internal target location. Owing to the electron's $g - 2$ anomaly, the spin will precess around the momentum. To correct for this precession a Siberian Snake, which will maintain the longitudinal polarization at any energy, both of the stored beam at the location of the internal target and of the extracted beam on the B-Line, will be installed in the east straight section of the ring.

4.6 ELECTRON POLARIMETER

A polarimeter, which provides real-time data independent of the operating mode, is necessary both to tune the beam spin direction and to monitor its status during storage and/or extraction. Polarimeters based on the scattering of laser light from the circulating electron beam meet this requirement and are in use in a number of high energy storage rings: SPEAR, HERA, and LEP, for example. It is feasible to use such a polarimeter in the SHR. The main difficulty to be overcome arises from the fact that the Compton asymmetry decreases as the beam energy decreases (as does the scattered photon energy). For a laser of 514 nm wavelength (Argon ion laser) the scattered photon at 180° varies between 3.5 and 35 MeV as the electron energy is varied between 300 and 1000 MeV; the longitudinal asymmetry varies between .005 and .0175 over the same range. The low photon energy makes one vulnerable to bremsstrahlung from the residual gas in the ring while the small asymmetries require high statistics for good precision. With commercially available lasers (few Watts) measurement times would be of the order of minutes to a few hours depending on the beam energy and the stored current. Recently, a successful test has been done at NIKHEF with an unpolarized beam in the ring. A statistical precision of about 3% is expected for measurements lasting a few minutes, with a 900 MeV beam 70% polarized and with laser power of 10 W [88]. Measurement times could be reduced to a few seconds by increasing the laser intensity. This would also be useful in distinguishing the signal from the bremsstrahlung and other backgrounds.

In addition, measurements of the spin dependent elastic scattering from polarized targets of ^{1}H, ^{2}H, ^{3}He can be used to obtain the product of the beam and target polarization. For example, measurements of the elastic scattering asymmetry from polarized ^{3}He to a statistical accuracy of $\pm 10\%$ can be done within 5 hours assuming an electron beam with a current of 40 mA, 440 MeV energy, and 40% polarization [89]. The target thickness is 2×10^{15} cm^{-2} with a 50% polarization.

4.7 DEVELOPMENT PLAN

To reach the design goal of an average 80 mA of 40% polarized beam through the internal target, several parallel lines of SHR developments are required.

4.7.1 Internal Gas Target

The collaboration together with the Laboratory is proceeding with the realization of a complete internal gas target in the Bates South Hall Ring. The vacuum pumping has been ordered and is expect to be at Bates by September, 1997. A retractable target cell is under design and will be fabricated in the coming months. Further important components include the BLAST mechanical mezzanine, the gas feed system, and the vacuum control system. It is planned that the complete system will be installed in early 1998. In addition,

a complement of detectors to detect scattered particles from the target gas will be available to carry out measurements. The maximization of the luminosity and the investigation of background, injection flash, and stored lifetime in the presence of a realistic target can then proceed.

4.7.2 Beam Storage

We approximate beam stacking by a beam injection $I_0\nu$, where I_o is the injected current for each stack and ν the number of stacks in one beam lifetime, and assume an exponential beam decay. It can then be shown that the average current $\overline{I}$ available for data taking, averaged over the entire cycle of injection and data taking is

$$\overline{I} = I_0\nu \left(1 - e^{-\sigma}\right)\left(1 - e^{-\mu}\right) / \left(\sigma + \mu\right) \tag{17}$$

where σ and μ are the times allowed for stacking and data taking in units of beam lifetime. The maximum value for $\overline{I}$ of about 20% of the maximum attainable injected beam current $I_0\nu$ is obtained for

$$\sigma = \mu \cong 1.256. \tag{18}$$

Assuming the currently available peak polarized beam of 4 mA from the polarized source and an interval of 2.5 times the damping time between dual turn stacks of 8 mA, the minimal beam lifetime to obtain the nominal 80 mA average beam has to be at least 125 times the beam damping time. The corresponding maximum beam current of 280 mA would be reached after 63 stacks. For longer beam lifetimes, the maximum required stored beam current I_{max} decreases. Fig. 25 shows the minimally needed I_{max} as well as the corresponding number of stacks, and the stacking and data taking times τ_s and τ_d as functions of the beam lifetime τ_B. All times are in units of the SHR beam damping time:

$$t_d = 0.0672(s) \times \left(GeV^3\right) / E^3, \tag{19}$$

where E is the beam energy in GeV. At the two energies of 330 MeV and 750 MeV, the required beam life times are 3.9 min and 0.33 min. They have both been surpassed in commissioning tests at beam currents of up to about 40 mA. Stacking to higher currents to reach 80 mA average current (see Fig. 25) has still to be developed which will require about three commissioning runs of 10 days dedicated to stored beam.

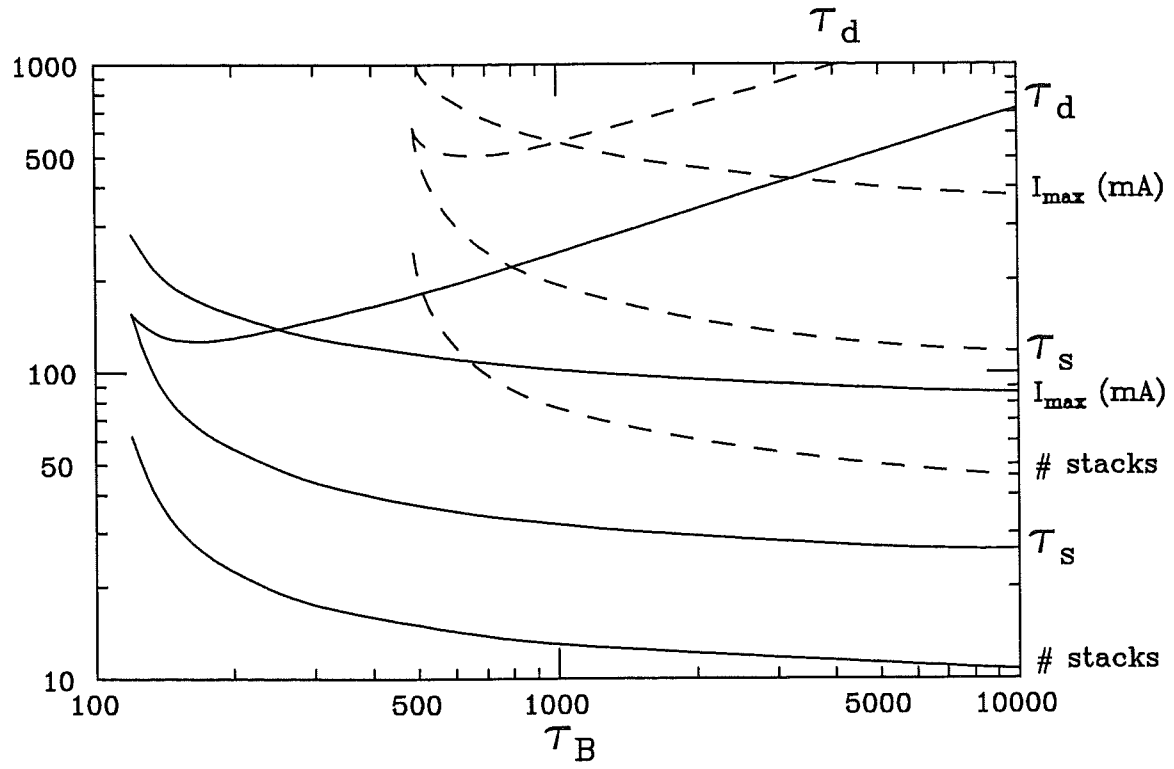

Figure 25: *Stacking time τ_s and data taking time τ_d as a function of the beam lifetime τ_B. They are plotted in units of beam damping time, defined in Eqn. 19, for two average currents, 80 mA (solid lines) and 320 mA (dash lines). Also shown are minimally needed I_{max} as well as the corresponding number of stacks.*

4.7.3 Polarized Beam

A second, parallel program concerns the installation and commissioning of the spin rotators (Siberian Snake) and of a beam polarimeter. The spin rotators are ready for installation.A beam polarimeter measuring laser light backscattered from beam electrons and described above will be installed in the SHR. There is a possibility of obtaining such a polarimeter from NIKHEF after they shut down operations at the end of next year. Commissioning polarized stored beam is estimated to require several dedicated runs of about 10 days each.

4.7.4 Schedule Outline

With BLAST completion projected for Fall 2000, it is clear that the stored polarized beam must be developed in advance of this date. The beam development is estimated to require at least five commissioning runs of about 10 days duration each. A significant effort to instrument SHR diagnostic elements and implement a complete control system is also required. Further, some modification of the ring vacuum system is anticipated.

To develop the beam for BLAST, a dedicated commissioning run of about 10 day duration must be scheduled approximately every six months for the next three years. This frequency should allow for detailed analysis and substantial hardware modification (if necessary) between commissioning runs. A reasonable timeline with some contingency to achieve this would focus on the stored beam development until the end of 1998. By this time an average current of 80 mA at 880 MeV should be routinely available through the internal target cell. In 1999 the focus would turn to development of the polarized beam. Thus, installation of the Siberian Snake cannot be delayed much beyond the end of 1998. In addition, the beam polarimeter must be fully operational by the latter half of 1999. Note that the full BLAST coils and supports together with prototype detectors are projected to be on the floor by early 1999 so it is likely that a polarized target would be installed also at this time. A reasonable goal would be to have stored polarized beam available by the year 2000. This schedule has about 9 months contingency with the possibility of another commissioning run in Spring 2000. A schematic chart of the schedule is shown in Fig. 26.

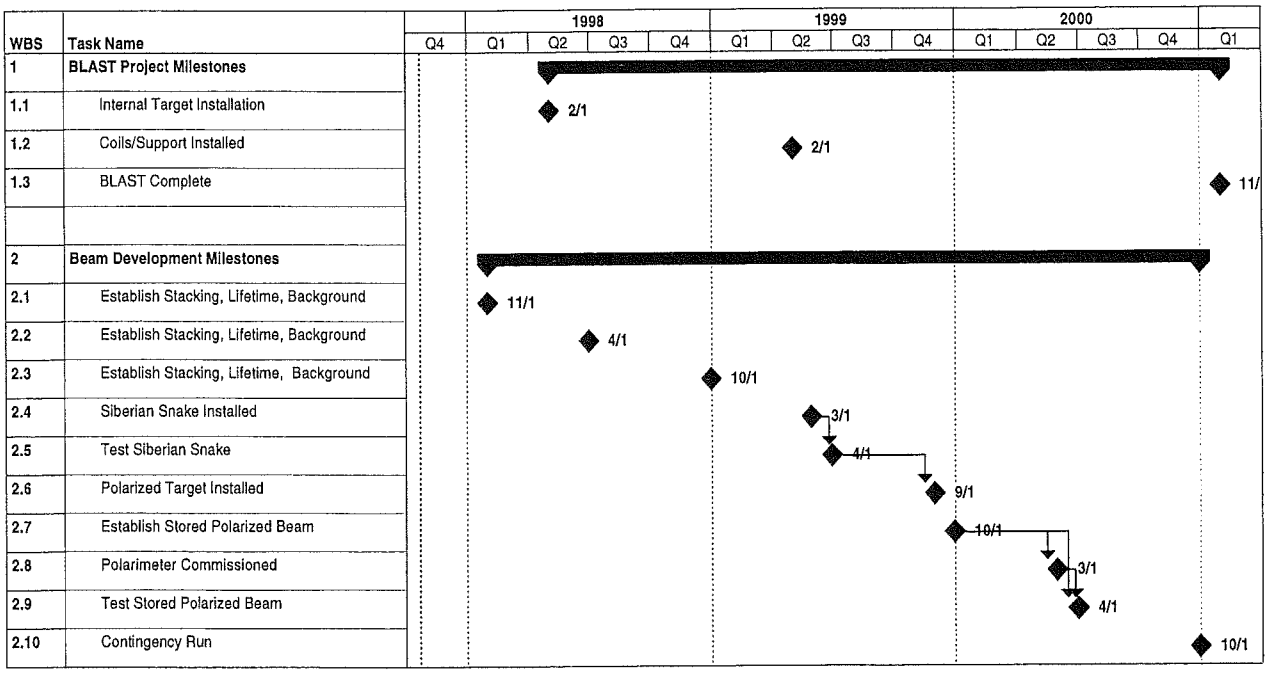

Figure 26: *Outline of schedule for BLAST beam development. The specific dates indicating milestones are in calendar years. The header is in fiscal years.*

5 The POLARIZED INTERNAL GAS TARGETS

5.1 The POLARIZED ^{3}He INTERNAL TARGET

The polarized ^{3}He internal gas target to be used with BLAST was developed at Bates in the early 1990s by R. Milner's group [78, 90, 91] with the primary motivation to measure spin-dependent electron scattering from polarized ^{3}He in the Bates South Hall Ring. Since that time targets based on this principle have been used at IUCF to measure the spin-dependent momentum distribution of the nucleons in ^{3}He [55]; at HERMES to measure spin-dependent deep inelastic scattering from polarized ^{3}He [92], and at NIKHEF [51] to measure quasielastic spin-dependent scattering from polarized ^{3}He. Here we describe the basic principle of the target, review the three previous realizations, and detail the important technical issues relevant for the BLAST target.

5.2 PRINCIPLE of the POLARIZED ^{3}He TARGET

The metastability exchange technique for optically polarizing helium was developed in the early 1960s [93]. High-polarization targets become realizable after the LNA laser became commercially available in the 1980s [94]. The technique has the advantage that it produces samples of pure ^{3}He gas with high polarization.

5.2.1 The Optical Pumping Mechanism

When an RF field is applied to a low pressure ^{3}He gas, electrons can be accelerated to speeds where a collision with an atom can produce another electron. This action causes a sustainable avalanche. A collision can also excite the atom. Its deexcitation will produce electromagnetic radiation with frequencies corresponding to the energy differences between the different states of the atom. The impact excitation can populate levels that cannot easily decay by emitting electromagnetic radiation. These levels have comparatively long lifetimes and are called metastable. Sustaining a weak discharge in a low pressure helium gas will produce a small fraction of the atoms ($\approx 10^{-6}$) in the long-lived 2^3S_1 metastable state, illustrated in Fig. 27 . This state is essential for the optical pumping mechanism used in the target.

Circularly polarized light incident upon the sample along the axis of a weak magnetic field can cause transitions between the $^3S_1$ and $^3P_0$ states. Angular momentum is thus transferred from the pumping light to the metastable atoms, and the metastable atoms become polarized. Transfer of the nuclear polarization to the ground-state atoms is achieved through metastability exchange collisions.

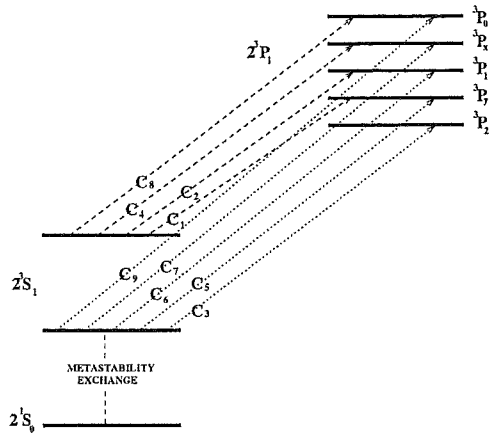

Figure 27: *Dipole transitions relevant for optical pumping. The energy levels are NOT to scale.*

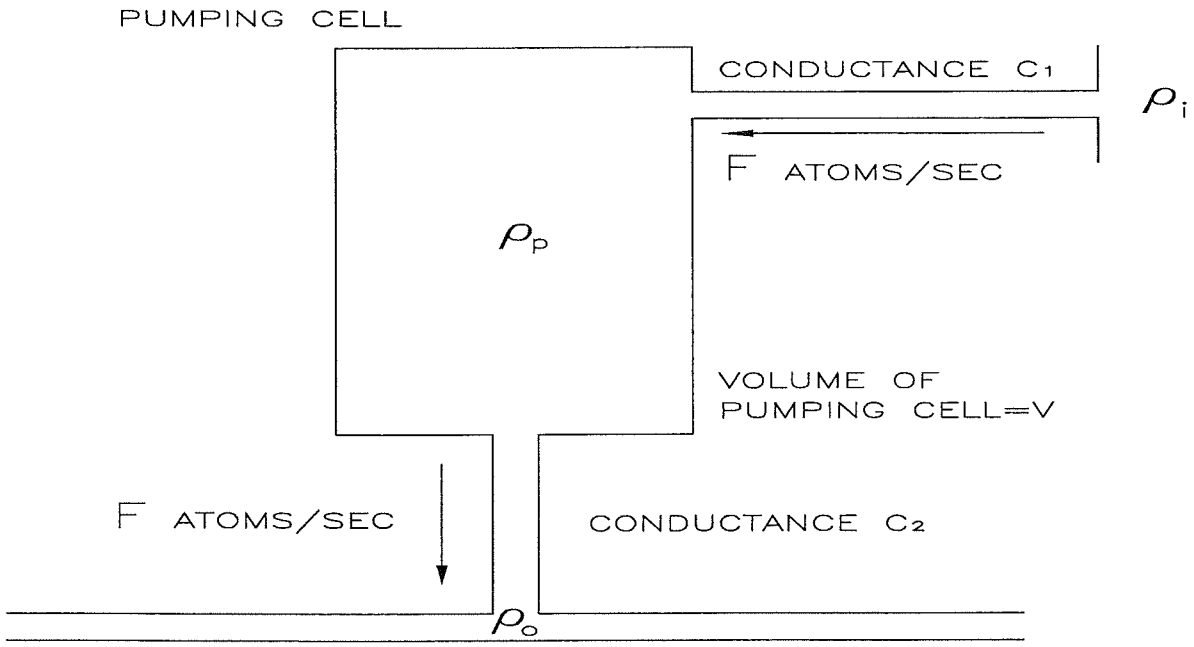

Figure 28: *Schematic of pumping cell flow system.*

5.2.2 The Flow-through Pumping Cell

In order to create an internal target, ^{3}He gas is flowed through the pumping cell and into the storage cell, which is located inside the storage ring [78]. A schematic diagram of the target is shown in Fig. 28 . The ^{3}He atoms flow through a glass pumping cell of volume V at a rate of F atoms/sec. As shown, the ^{3}He gas has an input density of ρ_i and traverses an input conductance C_1. The gas in the pumping cell has an average density of ρ_p and

exits through a conductance C_2 to the storage cell. The average residence time of an atom in the pumping cell, t_r, is given by

$$t_r = \frac{\rho_p V}{F} \quad . \tag{20}$$

For equilibrium flow with $\rho_0 \approx 0$, one has

$$F = C_1(\rho_i - \rho_p) \approx \rho_p C_2 \tag{21}$$

and so

$$t_r \approx \frac{V}{C_2} \quad . \tag{22}$$

Thus, to a very good approximation the average residence time of an atom in the pumping cell depends only on the quantities V and C_2.

We can also deduce the following relation:

$$\frac{\rho_p}{\rho_i} = \frac{C_1}{C_1 + C_2} \tag{23}$$

and so a measurement of ρ_p as a function of ρ_i measures the ratio of conductances C_1 and C_2. Note that in the intermediate flow region C_1 and C_2 become functions of ρ_p and ρ_i. For the usual pressure range this is not a problem for C_2, but it needs to be taken into account for C_1 design calculations.

In the pumping cell the atoms are polarized by absorption of angular momentum from the laser pumping light at the 1.083 μm transition. Consider a sample of ^{3}He atoms in a sealed cell, i.e. a pumping cell where there is no flow and the sample of ^{3}He atoms is static. In the approximation that the polarization rate does not depend upon polarization, the ^{3}He atoms will be polarized to an equilibrium polarization P_0^v with a pump-up time-constant of t_p^v given by

$$P(t) = P_0^v(1 - e^{-\frac{t}{t_p^v}}) \quad . \tag{24}$$

Consider now the atoms in an identical pumping cell but flowing at a constant rate of F atoms/sec. We can treat the flow as a depolarizing effect, taking away polarized atoms at a rate F times P and replacing them with unpolarized ones. Hence we have:

$$\frac{dP}{dt} = -1/t_p^v \times P - 1/t_r \times P \quad . \tag{25}$$

The gas in the cell will be polarized to an equilibrium polarization P_0^f with a pump-up time constant t_p^f where

$$\frac{1}{t_p^f} = \frac{1}{t_r} + \frac{1}{t_p^v} \quad . \tag{26}$$

The equilibrium polarization obtained with a flowing system, P_0^f, and the equilibrium polarization obtained on a sealed copy of the pumping cell, P_0^v, are related by

$$P_0^f = P_0^v \frac{t_r}{t_r + t_p^v} \tag{27}$$

where the difference between sealed and flowing systems is the presence of a polarization relaxation with time constant t_r due to unpolarized atoms entering the pumping cell through C_1. Hence, t_r is equal to the residence time of the atoms in the pumping cell.

From Eq. (24) it is seen that high polarization in the flowing system requires that $t_r \gg t_p^v, t_p^f$, i.e., the pump-up time must be much shorter than the residence time in the pumping cell.

To study the operation of the flowing system it is convenient to define two quantities. First, we define the polarization rate R of a sample of ^{3}He to be

$$R = \frac{NP_0}{t_p} \tag{28}$$

where the sample contains N ^{3}He atoms that are polarized to an equilibrium polarization P_0 with a pump-up time constant t_p. Secondly, the ^{3}He atoms are polarized by means of a discharge whose intensity is characterized by τ_d, which is the time constant associated with the polarization decay in the absence of optical pumping and in the presence of the discharge. As we shall see below, the performance of the polarized ^{3}He internal target is strongly dependent on R and τ_d.

5.3 PREVIOUS EXPERIMENTS with the ^{3}He TARGET

Since the development of the target at Bates, similar targets have been operated at the IUCF ring in the CE-25 experiment [90] at the HERA ring in the HERMES experiment [92] and at the AmPS ring at NIKHEF [51].

5.3.1 The CE-25 Experiment

Fig. 29 shows a schematic of the target used in the CE-25 experiment at IUCF. The target polarization was typically about 50%, as shown in Fig. 30 and operated at a flow rate of 1.2×10^{17} atoms/sec. The target cell operated at room temperature and had a rectangular cross-section of dimensions 16.6 mm (high) $\times$ 13.1 mm (wide) $\times$ 400 mm (long). The target thickness was 1.4×10^{14} atoms/cm^2.

5.3.2 The HERMES Experiment

Fig. 31 shows a schematic of the target used in the HERMES experiment at DESY. The target polarization was typically about 50%, as shown in Fig. 32 for over a period of three months. It was only accessible for 10 hours per month during this time. This configuration is close to the situation envisaged with the BLAST experiment where we expect the data

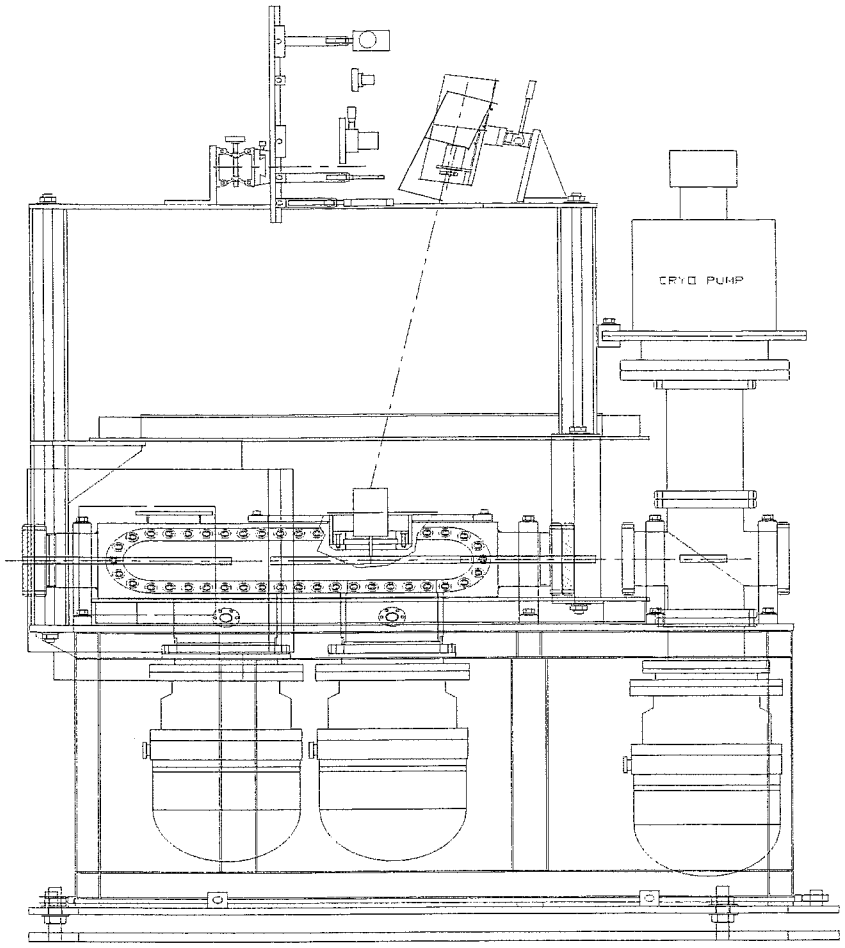

Figure 29: *The ^{3}He target used in the CE–25 experiment at IUCF.*

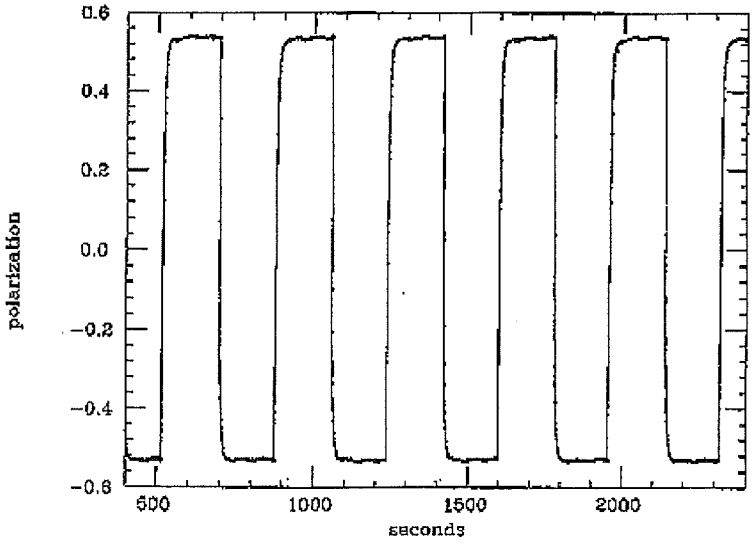

Figure 30: *^{3}He target polarization, inferred from the circular polarization of the 667 nm fluorescence in the pumping cell discharge, as a function of time for the CE–25 run at IUCF The ^{3}He polarization was reversed at regular intervals as indicated.*

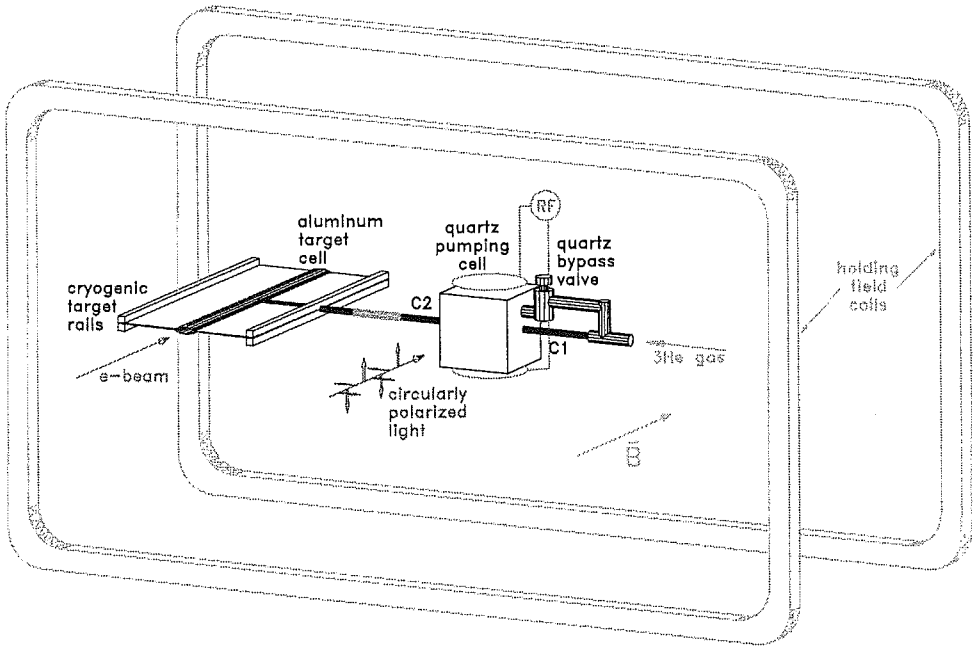

Figure 31: *Schematic illustration of the HERMES target.*

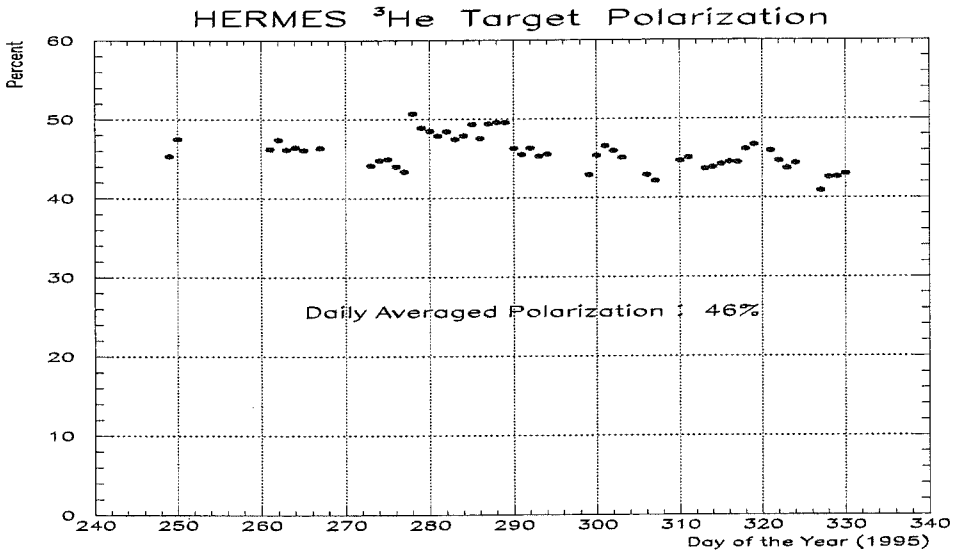

Figure 32: *HERMES target polarization during 1995 data taking.*

taking also to continue for several months. The HERMES target operated at a flow rate of 1×10^{17} atoms/sec and this was limited by the impact on the stored beam lifetime. The target cell typically operated at 25 K and had an elliptical cross-section of dimensions 29.6 mm (horiz.) $\times$ 13.1 mm (vert.) $\times$ 400 mm (long). The target thickness was 3.3×10^{14} atoms/cm^2.

5.3.3 The AmPS Experiment

A polarized ^{3}He target internal to the NIKHEF ring is currently installed and is being used to take data for spin correlation measurements. The performance and properties of this target are quite similar to those previously described.

5.4 The BLAST ^{3}He TARGET

The BLAST polarized ^{3}He target will be very similar to the previous targets. With a flow rate of 2×10^{17} atoms/cm^2, a cylindrical target cell of inner diameter 12.5 mm and length 400 mm at a temperature of 25 K will produce a target of thickness 2×10^{15} atoms/cm^2. As seen from the Table 7, the BLAST target is a comfortable extrapolation from the CE-25 and HERMES targets where the thickness was limited by the effect on the beam lifetime in each case. The assumed target polarization is 50%, a value that has been obtained routinely.

Table 7: *Summary of internal polarized ^{3}He target performance.*

experiment	cell shape	cell dimensions	cell temperature (K)	target thickness atoms/cm^2
IUCF CE-25	rectangular	16.6 mm × 13.1 mm	300	1.4×10^{14}
HERA HERMES	elliptical	29.6 mm × 9.6 mm	25	3.3×10^{14}
BLAST	circular	12.5 mm dia.	25	2×10^{15}

5.4.1 The Target Cell

Optimizing the target cell size includes minimizing the transverse dimensions to maximize the target density while keeping them large enough so that the beam does not interact with it. For the HERMES experiment, a thin-walled cell constructed from ultra-pure aluminum (99.9999 %) was developed at MIT [81]. The HERMES elliptical cell had dimensions of 29.0 mm (horiz.) × 9.8 mm (vert.) × 400 mm (length). The BLAST cell will be circular with a diameter of about 12.5 mm. To increase the target density, the target cell will be cooled by conductive connection to a cold head. Several Watts of cooling power at 15 K should be sufficient.

5.4.2 The Laser System

An infrared laser system will be used as the source for the 1.083 μm photons. A cylindrical crystal with dimensions 4 mm × 79 mm of $La_{.85}Nd_{.15}MgAl_{11}O_{19}$ (Nd:LNA) will be used as the lasing rod in a standard Lasermetrics 9550 Nd:YAG cavity. The output mirror has

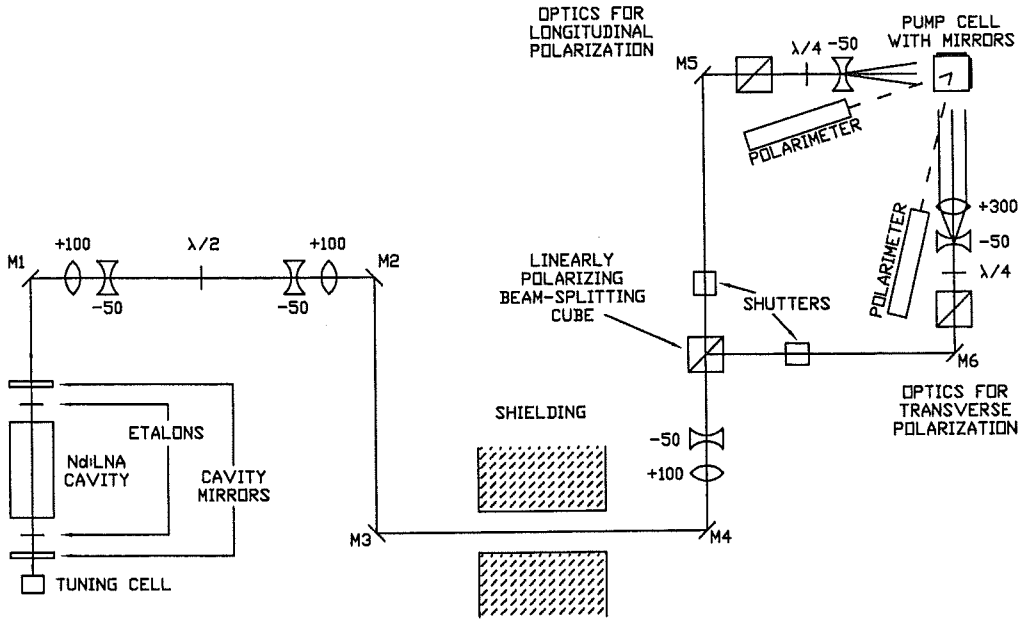

Figure 33: *Schematic diagram of the laser transport optics system used in the HERMES target. The lenses are labelled with their focal length in mm. Retardation plates are labelled as "λ/2" (half-wave) or as "λ/4" (quarter-wave). The figure is not to scale. The total pathlength from laser to pumping cell is about 10 meters.*

a reflectivity of 92.5%, the back mirror has maximal reflectivity. The Nd:LNA gain curve has peaks at 1.054 and 1.084 μm. Two uncoated etalons, one 0.3 mm and the other 1.0 mm thick, are placed inside the cavity to select the desired frequency. Both etalons can be mounted in rotatable, temperature-controlled *ovens* to stabilize the tune. To facilitate the tuning process a *tuning cell* is installed behind the back mirror of the cavity. The laser light leaking through this highly reflecting mirror passes through a small cell filled with 0.5 Torr of pure ^{3}He gas. A small discharge creates a metastable population in the same way as it does in the pumping cell. The scattering cross section for the laser light will increase dramatically when its frequency corresponds to the energy difference between the metastable 2^3S_1 and one of the 2^3P levels. By observing the laser light with a simple photomultiplier tube at 90°, the increase in the scattering cross section is translated into an easily detectable signal. This signal can be monitored while rotating the etalons to scan through the different resonances. With some experience one can distinguish the different resonances fairly easily. To make the signal easier to observe, the leaked laser light is chopped and the resulting periodic signal is displayed on a standard oscilloscope. The average signal is measured and displayed in the control room to provide a continuous measure of the laser tune. Up to 7 Watts can be extracted at 16 Amps. A schematic diagram of the laser transport optics system used in the HERMES target is shown in Fig. 33 .

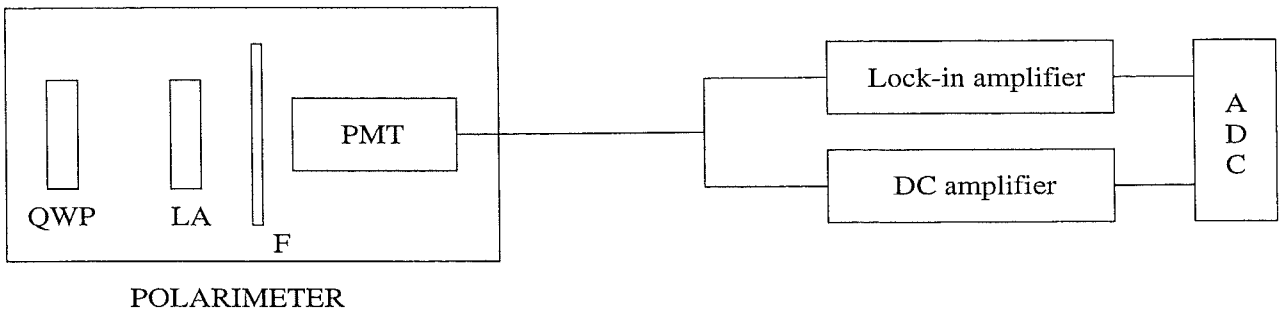

Figure 34: *The optical polarimeter. QWP: rotating quarter wave plate ; LA: fixed linear analyzer ; F: 667 nm filter ; PMT: photo-multiplier tube.*

5.4.3 The Target Holding Field

A holding field is required to determine the quantization axis of polarization, and the strength and uniformity of that field play a key role in obtaining good polarization. Gradients in the transverse components of the holding field (*i.e.* transverse to the quantization axis) contribute a relaxation time τ_{GRAD} to the total relaxation time of the polarization. Taking into account the velocity, mean free path, and diffusion time in the pumping cell, one can show that $\frac{1}{\tau_{GRAD}} \simeq \frac{1}{3}\frac{|\vec{\nabla}B_\perp|^2}{|\vec{B}|^2}$ for ^{3}He at room temperature and at 0.5 Torr pressure. The residence time in the pumping cell is about 125 seconds. Thus, the target holding field must be designed so that $\tau_{GRAD} \geq 300$ sec in order that the gradients will not be the determining factor in the ultimate polarization. This requirement implies that the gradient-to-field ratio above should be less than 0.1 m^{-1}, or about 10 mGauss/cm for a 10 Gauss field. Such conditions are easily achieved by using holding coils in a Helmholtz pair configuration. However, space constraints may not allow the ideal Helmholtz geometry. For example, in the case of the HERMES target a pair of rectangular coils of dimensions 1560 mm by 1200 mm, separated by 640 mm were used. Even so, significant transverse gradients of order 200 mgauss cm^{-1} required the implementation of an active cancellation dipole field.

5.4.4 Target Polarimetry

The polarization of the target needs to be measured accurately in order to minimize the error on the extracted asymmetry. The polarization will be measured in the pumping cell by detection of the circular polarization of the 667 nm light from the 3^1D_2 level to the 2^1P_1 level. The relation of the circular polarization of this photon to the nuclear polarization of the gas has been determined experimentally by using NMR [95]. Fig. 34 shows a schematic of the 667-nm polarimeter. A similar system will allow a determination of the target polarization to $\pm 3\%$.

5.5 POLARIZED HYDROGEN and DEUTERIUM TARGETS

Significant improvements have occurred in the development of internal polarized ^{1}H and ^{2}H targets in the past few years. First, members of the BLAST collaboration led the effort to mount and operate an ABS in the NIKHEF ring [83]. A stable performance was achieved over a five-week running period, with on-line measurement of the polarization of the target gas. Plans to upgrade this source and implement it for BLAST are discussed below. Second, polarized ^{1}H and ^{2}H laser driven sources (LDS), which are based on the principle of spin-exchange optical-pumping [84], have undergone considerable development. An update of this new initiative is presented below.

5.6 The NIKHEF ATOMIC BEAM SOURCE

Fig. 35 shows a schematic outline of the internal target setup. A polarized hydrogen or deuterium beam produced in an atomic beam source is fed into a cooled storage cell located inside the AmPS electron storage ring at NIKHEF. A detailed description of the apparatus can be found in Ref. [83]. The ABS is based on the well-known principle of Stern-Gerlach separation. An intense atomic beam is produced by means of an RF dissociator with a cooled nozzle (typically $\sim$ 70 K) and a powerful differential pumping system with a skimmer and a collimator. The upper hyperfine states with $m_J = +1/2$ (J = electron spin) are focused into the target cell feed tube by two sextupole magnets, while the lower hyperfine states are defocused. In order to populate the required nuclear spin substates, high-frequency transitions are induced. A medium-field transition unit (MFT), located between the two sextupole magnets, can be used to remove one hyperfine state from the atomic beam. Strong-field (SFT) and weak-field (WFT) transition units are used after the second sextupole to produce the actual nuclear polarization (see Table 8 below). A thorough description of the currently available high-frequency transition units is given in Ref. [96].

The luminosity of the experiment $\mathcal{L}$ is governed approximately by

$$\mathcal{L} \simeq I_e \, f_{\rm ABS} \, L/C \tag{29}$$

where I_e is the electron beam current, $f_{\rm ABS}$ the intensity of the injected deuterium beam and

$$C \simeq 3.81 \left(\frac{4\, D_{\rm cell}^3}{L_{\rm cell}} \sqrt{\frac{T_{\rm cell}}{M}} + \frac{D_{\rm ft}^3}{L_{\rm ft}} \sqrt{\frac{T_{\rm ft}}{M}} \right) \tag{30}$$

is the total vacuum conductance (in ℓ/s) of the storage cell, including the feed tube (ft). Here, $T_{\rm ft,cell}$, $L_{\rm ft,cell}$ and $D_{\rm ft,cell}$ are the temperature (K), length and diameter (cm) of the target cell and feed tube, respectively. M is the target mass in atomic mass units. From these expressions it is clear that one will try to minimize the diameter, increase the length, and lower the temperature of the cell. The minimum diameter of the storage cell is determined by the charge distribution of the stored electron beam, while the length of the

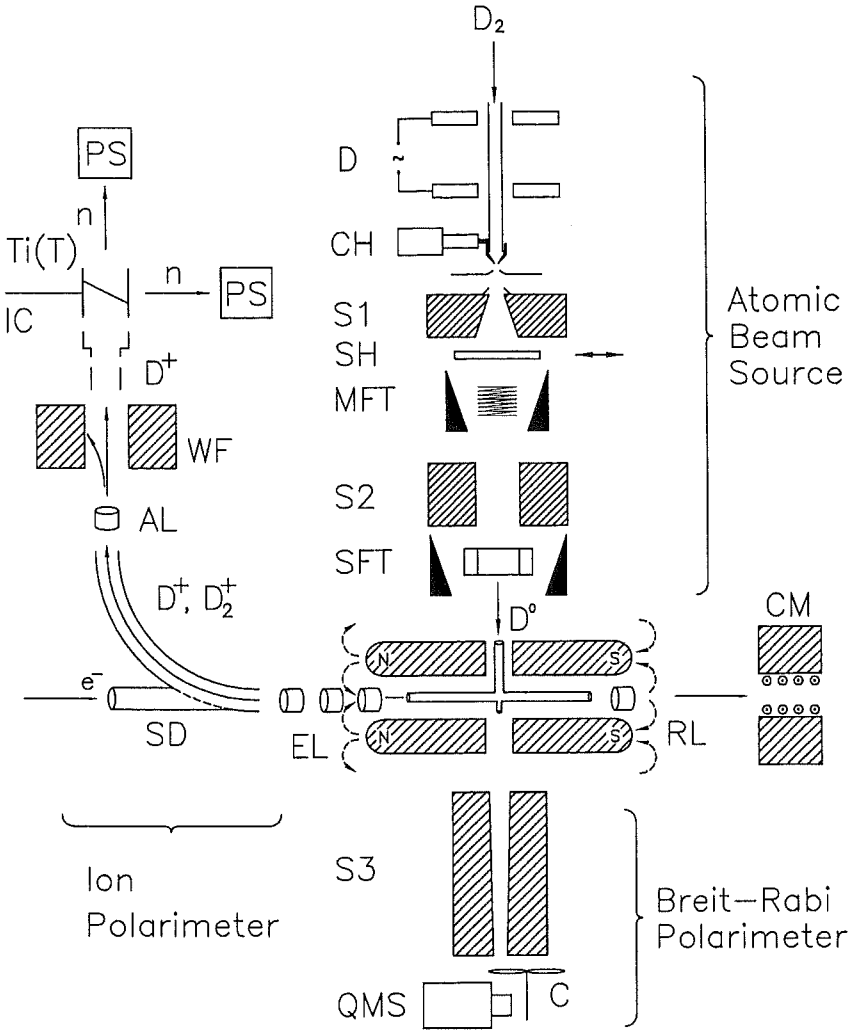

Figure 35: *Schematic outline of the atomic beam source, Breit-Rabi polarimeter, internal target, and ion-extraction system. All components, except the neutron detectors (PS), correction magnet (CM) and target holding field magnet, are inside the vacuum system. D: RF dissociator; CH: cold head; S1, S2, S3: sextupole magnets; MFT, SFT: medium- and strong-field transition units; SH: shutter; C: chopper; QMS: quadrupole mass spectrometer; RL: repeller lens; EL: triplet of ion-extraction lenses; SD: spherical deflector; AL: electrostatic lens; WF: Wien filter; IC: ion collector; Ti(T): tritiated titanium target.*

cell is constrained by the detector acceptance as well as the variation of the beta-functions in the field-free region near the interaction point. The cell diameter is also limited by the divergence of the atomic beam, because the latter constrains the dimensions of the feed tube.

A magnetic holding field is applied over the entire target cell region by using two electromagnets. The direction of the magnetic field, and thus of the polarization axis, can be oriented at will in the scattering plane. Corrector magnets are added outside the target

chamber to counterbalance the transverse target holding field and to preserve a closed orbit in the storage ring. The holding field coils are provided with two holes, one for injection of the deuterium atoms into the storage cell, and one to sample a small fraction of these atoms in a Breit-Rabi Polarimeter (BRP). This polarimeter consists of a sextupole magnet, a chopper and a quadrupole mass spectrometer (QMS).

The BRP is used to optimize the intensity of atoms injected into the storage cell as a function of e.g. nozzle temperature, deuterium flow into the RF dissociator, and sextupole fields. Furthermore, it is used to test the performance of the high-frequency transition units. A drop of 1/2 (1/3) in the amount of hydrogen (deuterium) atoms detected by the QMS when the with high-frequency transition units are turned on indicates a 100% efficiency of the transition. These measurements also indicate that the polarization of the injected atoms is not lost in passing through the target holding field magnets, where the field components have zero crossings. In addition, the BRP is used to set the holding field strength such as to avoid resonant electron beam-induced depolarization of the target atoms. We have performed extensive studies of such beam-target interactions. The results are discussed in detail in Ref. [97].

Several effects can decrease the polarization of the injected atoms inside the storage cell. Polarization losses can originate, e.g., from the dilution of the target by unpolarized molecules, from spin-exchange collisions among the target atoms [98], from the interaction with the cell walls, and/or from the interaction of the atomic spin with the RF magnetic fields radiated by the circulating beam bunches [97]. For NIKHEF experiment 91-12 we have built and used a dedicated polarimeter, based on ion extraction and analysis, that measures the absolute target polarization in the storage cell with the same weighting over target gas and electron beam density as in the actual experiment. This polarimeter is described in detail in Refs. [99, 100]. Ions, produced by the electron beam, are extracted and analyzed by using a combination of electrostatic lenses, a spherical deflector, a Wien filter, and an ion collector. These ions are prevented from reaching the walls of the storage cell by a longitudinal holding field. They are on one side of the cell reflected by an electrostatic repeller lens, on the other side extracted by using a triplet of lenses and a deflector. A Wien filter separates the atoms from molecules, and the atomic fraction is measured in an ion collector. The tensor polarization of the D^+ ions is measured by accelerating them to 60 keV to bombard a tritiated foil. The neutron anisotropy of the $^3H(d,n)^4He$ reaction is used to measure the tensor polarization directly. The ion extraction polarimeter allows invaluable systematic studies on the target polarization. In experiment 91-12 we obtained crucial information on the fraction of molecules present in the storage cell and on their polarization [101]. Furthermore, it allowed us to observe spin-exchange effects (at the level of $\delta P_{zz} \simeq 0.01$) on the target polarization in the storage cell [98]. With this polarimetry technique, we were able to measure the absolute target tensor polarization with an overall accuracy of 5 %.

In order to carry out the experiments proposed here, we intend to upgrade the target setup. Compared to the NIKHEF experiment 91-12, the main improvements are

- construction of high-frequency transition units, needed to obtain vector polarized deuterium and hydrogen beams with the highest possible figure-of-merit;
- a set of new focusing (permanent) magnets in the ABS, that will increase the flux of injected atoms by a factor of three and, because of the reduced molecular beam fraction, the absolute target polarization by a factor of 1.2;
- the use of a longer (600 mm instead of 400 mm) storage cell, which will boost the target thickness visible to the detectors by a factor larger than two;
- an improved cryogenic system to cool the cell to 80 K (instead of $\sim$ 180 K), which will increase the target thickness by a factor 1.5;
- twice the pumping speed on the scattering chamber, which will reduce by half the dilution by unpolarized background H_2 or D_2 gas;
- for deuterium, a larger target guide field $B_{\rm target}$ (with new correction magnets) that will increase the polarization by about a factor of 1.1 .

Most of the above listed modifications have been or are being carried out. In addition, new beam scrapers will be installed in the ring section (south straight) preceding the ITF section (west straight). In combination with the currently available scrapers (east straight), this new slit system is expected to considerably reduce the background generated by beam halo scattering from the ITF storage cell walls, while hardly affecting the beam lifetime. Such an improvement will substantially increase the efficiency of the proposed measurements in the ^{2}H$(e,e'p)$ channel at high missing momenta (see Section 2).

In Table 8 we list the most relevant parameters for the polarized H and D targets. For the

Table 8: *Target parameters for the proposed measurements with polarized hydrogen and deuterium.*

	Hydrogen	Deuterium (vector)	Deuterium (tensor)
MFT	off	3-4	1-4
SFT	2-4/off	2-6/off	2-6/3-5
WFT	off/1-3	off/1-4	off
P_z	$\pm$0.8	$\pm$0.8	0
P_{zz}	-	0	0.6/-1.2
flux (10^{16} at/s)	8	4	4
target thickness (10^{14} at/cm^2)	1.5	1.1	1.1

total target polarization, a dilution factor by unpolarized molecules of 0.84 was included. A strong target holding field is assumed for all cases ($B_{\rm target}$ > hyperfine critical field).

The target thickness for hydrogen (deuterium) will amount to 1.5 (1.1) $\times 10^{14}$ cm^{-2}, which results in a luminosity of 1.0 (0.7) $\times 10^{32}$ cm^{-2} s^{-1} at $I_e = 100$ mA.

For the BLAST experiments, we intend to make use of a mezzanine to support the targets (see the following section). In this case the atomic beam source must be positioned vertically, above the scattering chamber. The new vacuum chamber and frame needed for this modification are being designed at the Vrije Universiteit of Amsterdam.

5.7 The LASER DRIVEN SOURCE

A laser-driven polarized hydrogen or deuterium internal target is currently being tested at the Indiana University Cyclotron Facility [102]. This target is based on the principle of spin-exchange optical pumping technique [103]. Polarized laser light optically pumps the alkali atoms, typically potassium. The photon angular momentum is transferred to the target atoms through spin-exchange collisions of the laser polarized alkali atoms and the hydrogen or deuterium atoms.

The source is typically operated at high flow rate ($\sim 10^{18}$ nuclei/s) in which frequent H-H or D-D spin-exchange collisions increase the probability of hyperfine interactions and drive the system into spin temperature equilibrium even at high magnetic holding field ($\sim$ 1 kGauss), a condition necessary to overcome radiation trapping and achieve efficient optical pumping. In spin temperature equilibrium, relatively high nuclear vector polarization can be obtained from this type of source without RF transitions. In spin temperature equilibrium, the nuclear polarization and the electron polarization are of the same magnitude for hydrogen and the nuclear vector polarization is larger than the electron polarization for deuterium. Electron polarization as high as 50% are obtained for both hydrogen and deuterium from the laser-driven source at flow rates higher than 6×10^{17} nuclei/s [104]. The typical K/D or K/H ratio is $\leq$0.5%. Spin temperature equilibrium in the laser-driven polarized hydrogen source and laser-driven polarized deuterium target have been verified recently by the Erlangen group [105] and the Argonne group [106]. This target has the advantage of potentially higher figure-of-merit than that of the conventional atomic beam source. In addition to that, compactness is a unique feature of this target.

5.8 INTERNAL TARGET INFRASTRUCTURE

The internal target infrastructure consists of large pumping systems and additional equipment necessary to mount and operate the polarized targets. Most of this infrastructure will be mounted on a special support system, a mezzanine, over the BLAST frame. In the following, we discuss our plans for the scattering chambers and the vacuum system. Fig. 36 shows the mezzanine with some of the vacuum equipment.

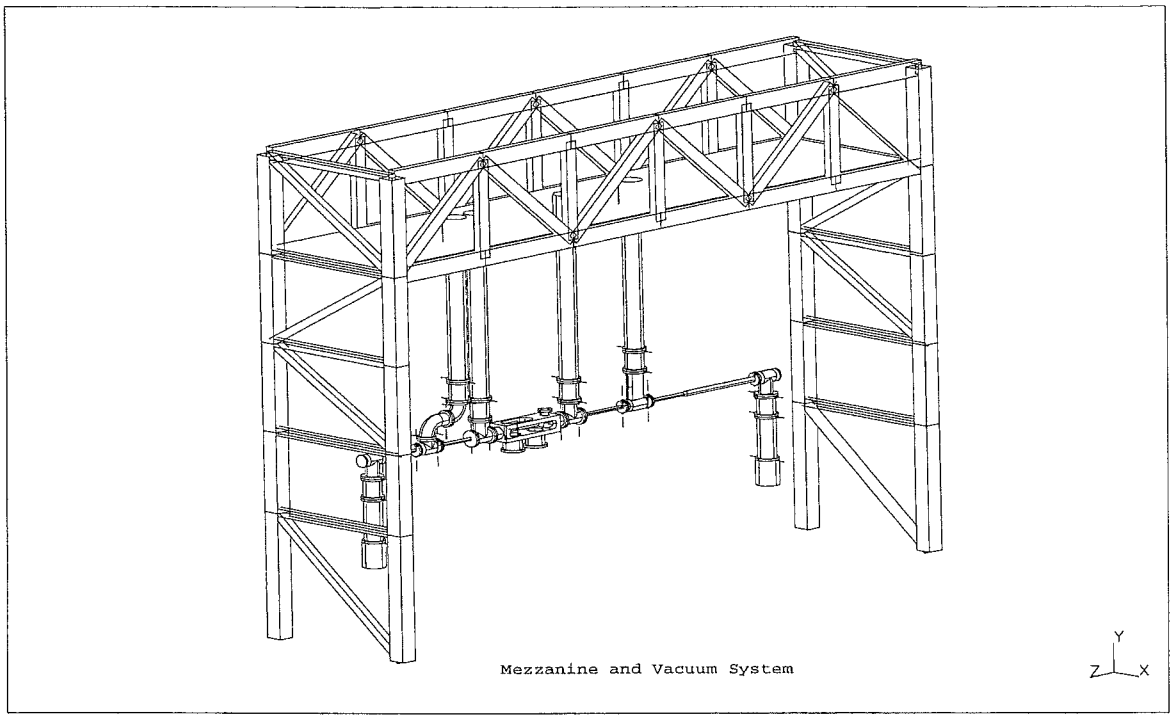

Figure 36: *The mezzanine used to support the vacuum pumps, the atomic beam source, and additional target equipment.*

5.8.1 Scattering Chamber

The scattering chamber has several requirements to meet the specifications of the ring as well as the BLAST experiments. The chamber must be made to fit inside the BLAST toroidal coils including all services, (cryogenics, laser pumping cell, etc.). The chamber must have the appropriate opening to allow for all the angles that the experiments require. To ensure compatibility with the ultra-high vacuum of the SHR, all components will be machined and cleaned according to good vacuum practice. The methods include the use of only hydrocarbon-free cutting fluids and solvents. All seals for the system will be made with metal seals, including the aluminum flanges which will utilize Altine TiN coated aluminum conflats with aluminum gaskets. All components of the system will be capable of repeated bake-outs to 150 ^{0}C. The system must also be "non-magnetic", having materials that cannot be excited to magnetism. The chamber and seals will be entirely of aluminum construction, with the bolts and threaded inserts being the only steel (stainless steel) components inside the toroidal field. The bolts will be specified to be 316 SS and the threaded inserts will be 304 SS. These materials will minimize the perturbations to the magnetic field. Finally, the chamber must be compatible with the target, so that different chambers will be needed for the different target gas sources. The laser-driven sources can be accommodated by one chamber type and the Atomic Beam Source will require another chamber type.

For the laser-driven sources, an existing chamber used in a previous ^{3}He experiment will meet all of the above requirements. New flanges and supports will need to be designed and manufactured for this chamber to be used in the BLAST spectrometer. Included in these designs will be cryogenic cooling capability which was not used with this chamber previously. This chamber is currently at Bates and is being refurbished. A second chamber will have to be designed and manufactured for the Atomic Beam Source. Estimated costs for this chamber are $ 28,800 for engineering and drafting and $ 22,500 for manufacture, plus the cost of any transfer lines from the source to the chamber.

5.8.2 Internal Target Vacuum System

The vacuum system must be capable of pumping the severe gas load created by these internal targets. The gas flow is estimated at 5×10^{17} atoms/sec for ^{3}He and 1×10^{17} atoms/sec for hydrogen and deuterium. These values correspond to rates of 0.0167 Torr-l /sec and 0.0033 Torr-l /sec, respectively. The nominal ring vacuum is in the 1×10^{-9} Torr range and it will be necessary to be in the 1×10^{-7} Torr level in the target section in order for the ring vacuum to remain at its nominal level. The system also needs to be a "dry" pumping system so as not to introduce contamination, especially hydrocarbons. The only components capable of pumping this amount of gas for an extended amount of time while maintaining a "dry" environment are turbo pumps backed by "dry" roughing pumps.

Another consideration is *RF* wake-field heating from the beam. The beam should perceive a continuous wall as it travels through the interaction area. This requirement is accommodated by wake-field suppressers, perforated tubes that allow gas to get to the vacuum pumps but have enough material remaining to have the appearance of a continuous wall to the electron beam. The perforated tube will be made of a 316 SS mesh that is 1/32" thick with 3/32" diameter holes and a 50% open area. This design utilizes the same basic design of current pumpouts used in the SHR.

The proposed system design is based on the previous considerations as well as vacuum calculations [107] and experience from the HERMES experiment at DESY. In choosing the pump size for the target system the gas load contribution due to outgassing, permeation and leakage of the vacuum system is ignored because it is orders of magnitude lower than the source gas (^{3}He and ^{2}H) contribution. The system will include six 1000 liter/sec turbo pumps backed by a hook and claw pump. Diaphragm pumps were eliminated from consideration because of their tendency to retain helium, making leak checking impossible. The same size pumps were chosen to give part redundancy so that a spare of only one type of pump is required. The system will provide a vacuum level of 2×10^{-7} Torr at the end of the pumping section for ^{3}He. The vacuum level for hydrogen gas flow will be 5.6×10^{-8} Torr. These numbers meet the specifications as given by Ernie Ihloff, the Associate Group Leader for Mechanical Engineering at Bates.

Several manufacturers were consulted and asked to give quotations for the above vacuum pumps. Of the manufacturers that bid, we have decided to use OSAKA TG 1120 MC

magnetic levitation 1000 l/s turbo pumps. The OSAKA bid was competitive with even Ceramic bearing pump manufacturers making it the clear choice for the turbos. For the "dry" backing pumps, there are fewer manufacturers that meet our requirements. The main pumps under consideration are the Edwards Drystar, Leybold Vacuum Dryvac, and Ebara. The Edwards Scroll pump has reliability problems and the Kashiyama has no support network in the United States. All three of the hook and claw pumps require cooling water and a nitrogen purge. These pumps have far in excess of the backing requirements for one pump, so it is planned to manifold two turbo pumps per roughing station. This arrangement will justify the high cost of the roughing stations, approximately $ 17,000 per station. The low bidder of this group of three was Leybold Vacuum, and after examining the pump we have chosen to use the Leybold pump.

5.8.3 Costs and Personnel

The costs for the internal target system for the SHR have been calculated in conjunction with those of the BLAST project. These costs are part of the capital equipment section of the Bates budget and, therefore, do not appear in the BLAST budget presented in Sec. 8.

The personnel to implement the polarized internal gas targets in the SHR come from the Medium Energy Group at MIT, the ETH Institute in Switzerland, Vrije Universiteit and NIKHEF in the Netherlands, and the University of Wisconsin-Madison. All these groups have expertise on doing experiments with these targets at other laboratories around the world. The available manpower from these institutions for target development and implementation is discussed in Sec. 9.

6 The LARGE ACCEPTANCE DETECTOR

6.1 INTRODUCTION

The BLAST detector is an open geometry, non–focusing spectrometer toroid with eight copper coils. The initial detector package consists of two horizontal opposite sectors installed in the forward direction back to $\theta = 80°$. It contains multiwire drift chambers for tracking, scintillation detectors for time-of-flight measurements, and Čerenkov counters for e^-/π^- separation and two sectors of thick scintillation detectors from 35° – 70° will provide for neutron detection. The design emphasizes conventional detector technology, off-the-shelf electronic components, and existing data acquisition system software to minimize cost and development time. The proposed configuration including coils, support structure, and detector elements is shown in Fig. 23. The design requirements and their consequences have been summarized in Table 5, and the main properties are listed in Table 6 (see Sec. 3).

In each of the two instrumented sectors there will be three drift chambers covering the scattering angle range from 20° to 80°. Each chamber consists of four planes of wires. Behind the wire chambers there will be three Čerenkov counters and fourteen vertical scintillators, with the scintillators located behind the Čerenkov counters. Each of the two instrumented sectors is backed up by eight neutron scintillator bars with a PMT at each end. Finally, a movable shower counter to eventually consist of 64 lead-glass bars can be moved behind one sector or the other, and detectors for recoiling nuclei will be located inside the scattering chamber at about 10 cm from the target. Upgrade paths to this instrumentation are relatively straightforward and will be investigated if they are important for physics.

In this Section we present the technical design of all the spectrometer components. First, we explain the design requirements that have been summarized in Table 5. Then we present each of the designs: magnet and its support structure, different detector elements, electronics, and data acquisition. Costs and work plans are also discussed for each of these branches.

6.2 REQUIREMENTS of the SPECTROMETER

The spectrometer has been designed to satisfy the requirements of the physics program. This program will take advantage of the capability to select the polarization of the initial state, as well as to determine multi-particle final states. The following are the main constraints on the design of the spectrometer:

1. **Luminosity:** In the Bates South Hall Ring, the high intensity circulating beam (average currents ranging from 40 to 80 mA) allows luminosities of the order of 10^{32}

to 10^{33} atoms/cm^2/s to be achieved with typical polarized target thicknesses of the order of 10^{14} to 10^{15} atoms/cm^2. Compared to a typical external unpolarized electron scattering experiment, with luminosity of the order of 10^{37} atoms/cm^2/s, there is a reduction in luminosity of four orders of magnitude. To compensate for this reduction in luminosity, a large acceptance spectrometer with solid angle of about one steradian is needed.

2. **Magnetic Field:** There are several reasons for having a toroidal magnetic spectrometer. First, a non–magnetic spectrometer will not provide sufficient electron and hadron energy resolution to carry out precise measurement of electromagnetic spin observables. Second, the use of polarized targets requires a well defined magnetic holding field to define the target spin. If a holding field of the order of 30 Gauss is used, the field due to the spectrometer at the target position must be less than about 5 Gauss. In addition, the polarized ^{3}He target currently under development requires a field gradient of less than about 50 mGauss/cm for optimal polarization. Thus, the spectrometer must provide an essentially field-free and zero-gradient magnetic region around the target position. Finally, the magnetic field should be able to shield the first set of drift chambers from the Mϕller scattered electrons. Hence, the field integral between the target and the position of the first drift chamber must be about 0.05 T–m.

3. **Energy Resolution:** To perform a generalized Rosenbluth separation with polarized electron beam and targets, the direction of the three-momentum transfer must be accurately determined. It is also necessary to know θ^*, the angle between the direction of the spin and the three momentum transfer $\mathbf{q}$. The direction of the target spin can be measured directly to high accuracy, and the direction of $\mathbf{q}$ is determined by measurement of the initial and final energies E and E', and the scattering angle θ of the electron. Hence, the accuracy in determining E' and θ has a direct impact on the determination of the response functions. Thus the spectrometer must have good energy and angular resolution. We require $\Delta E'/E' \leq 2\%$ and $\Delta\theta < 5$ mrad.

4. **Particle Identification:** The proposed experiments require the separation of electrons, protons, neutrons, π^+ and π^-.

5. **Other Considerations:**

   In addition to the above considerations, the detector should contain a region of about 1 meter in diameter in the center where the polarized target will be located. A vertex resolution of approximately 1 cm is desirable to allow the binning of the measured asymmetry in longitudinal target position. Finally, in order to measure simultaneously the transverse and longitudinal-transverse interference asymmetries, the detector package has to be symmetric in the scattering plane with respect to the incident beam direction.

6.3 The MAGNETIC SYSTEM

A non–focusing spectrometer with a toroidal field configuration has been chosen to meet the physics goals. The field is non-uniform and varies approximately as $B(r) = B_i r_i / r$, where r_i is the inner radius. Because the magnetic field lines form circles around the beam, no return yoke is needed for this configuration. One thus obtains a large solid angle for particle detection and provides a field-free and low-gradient region at the beam and target position. The toroidal configuration has the additional advantage that no compensating magnets are necessary for operation of the electron ring. An eight-coil design with 1.4 MA-turns yields sufficient $\int B \cdot dl$ to meet the required momentum resolutions and minimizes the magnetic field gradients around the target region. Normal-conducting coils have been selected in order to decrease costs.

6.3.1 Coil Specifications

The shape of the coil and its specifications are shown in Fig. 37 . The geometry of the coil consists of straight sections and arcs in order to simplify the winding procedure. The coil has been designed around a 1.5-in^2 copper hollow conductor with a 0.8 in inner diameter for the passage of cooling water. It is made up of two layers of conductors with a total of 26 turns per coil. The total DC current is 6,750 A. The power supply is planned to be near the coil assembly. A total of 1.85 MVA in AC distribution must be supplied to the power supply location.

Coil sections will be epoxy vacuum cast in a permanent mold. Due to the nature of the coil supports and the tolerance requirements dictated by the field quality, the coil sections must be cast, cured, handled and stored to minimize permanent deformation. While the permanent mold technique will represent a higher tooling cost, it was chosen because it yields reproducible dimensions, identical coil sections and will provide accurate positioning of the coil mounting pads. Such uniformity is essential to provide accurate knowledge of the magnetic field. A total of nine coils will be ordered out the same original mold so one spare will be available in case one of the coils fails. Glass reinforced plastic (G10) sheets of 3 mm thickness will be used on the sides of the coils for additional stiffness and thermal insulation. The G10 mounting pads are to be wrapped with the glass-tape ground layer to the coil section prior to casting for added strength. Tests and inspections at the vendor's facility will include hydrostatic tests of splices and fittings, voltage impulse and ground tests before and after casting.

6.3.2 The Magnetic Field

To achieve the desired momentum resolutions the required values of the $\int Bdl$ over the detected particle trajectory should be between 0.6 and 0.2 Tesla-m, with the highest values for forward particles. The operation of the internal ^{3}He polarized target requires that the

NOTES:

1. ALL DIMENSIONS ARE IN MM [INCHES].
2. COIL WEIGHT IS 5400 LBS.

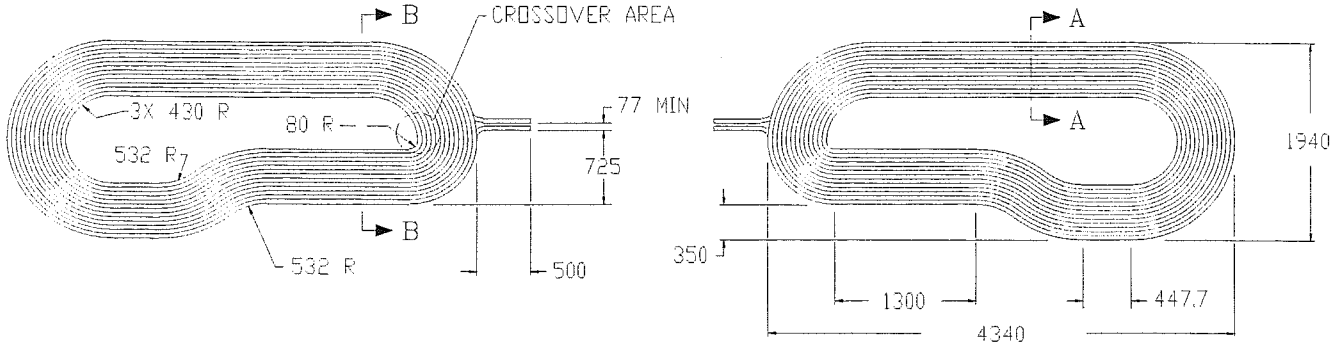

COIL SPECIFICATIONS	
CONDUCTOR (OFHC CU)	
OD (INCHES)	1.500×1.500
ID (INCHES)	0.800
TURNS/WINDINGS//LAYER	13/1
LAYERS/COIL	2
TURNS/COIL	26
CONDUCTOR (MICRO-OHMS/FT)	5.11033
COIL SERIES R (m-OHMS)	4.10564
COIL CURRENT (AMPERES)	6730.77
COIL VOLTAGE (VOLTS)	27.63
COIL POWER (k-WATTS)	186.0
CURRENT DENSITY (A/sq INCH)	3864
LENGTH OF COOLING PASSAGE (FT)	402
COOLANT PASSAGES/COIL	2
FRICTION FACTOR (k)	0.0045
FLOW/PASSAGE (GPM)	11.78
VELOCITY/PASSAGE (FT/SEC)	7.56
PRESSURE DROP/PASSAGE (PSID)	67
ΔT	30°C

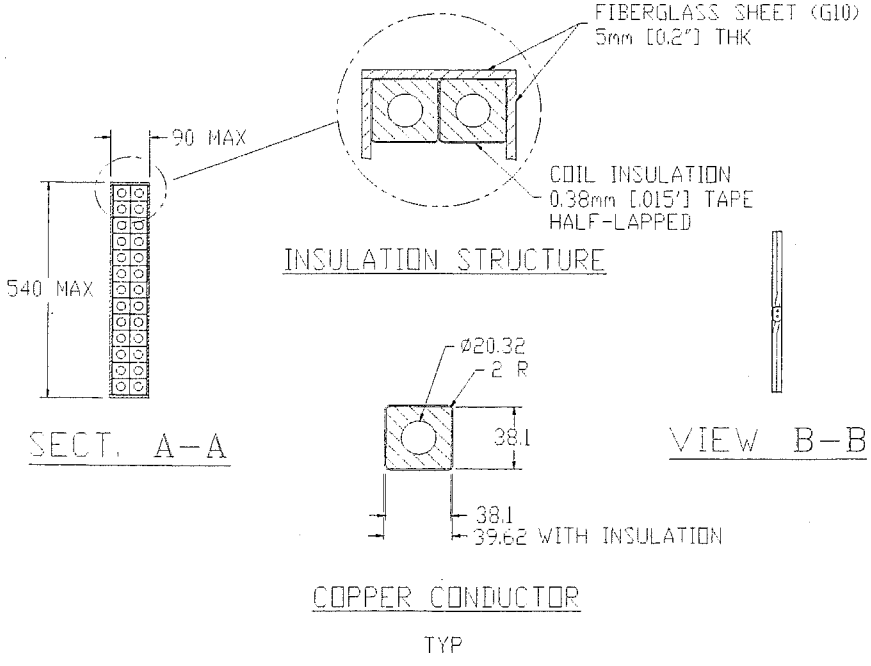

Figure 37: *Specifications for the BLAST magnetic coils.*

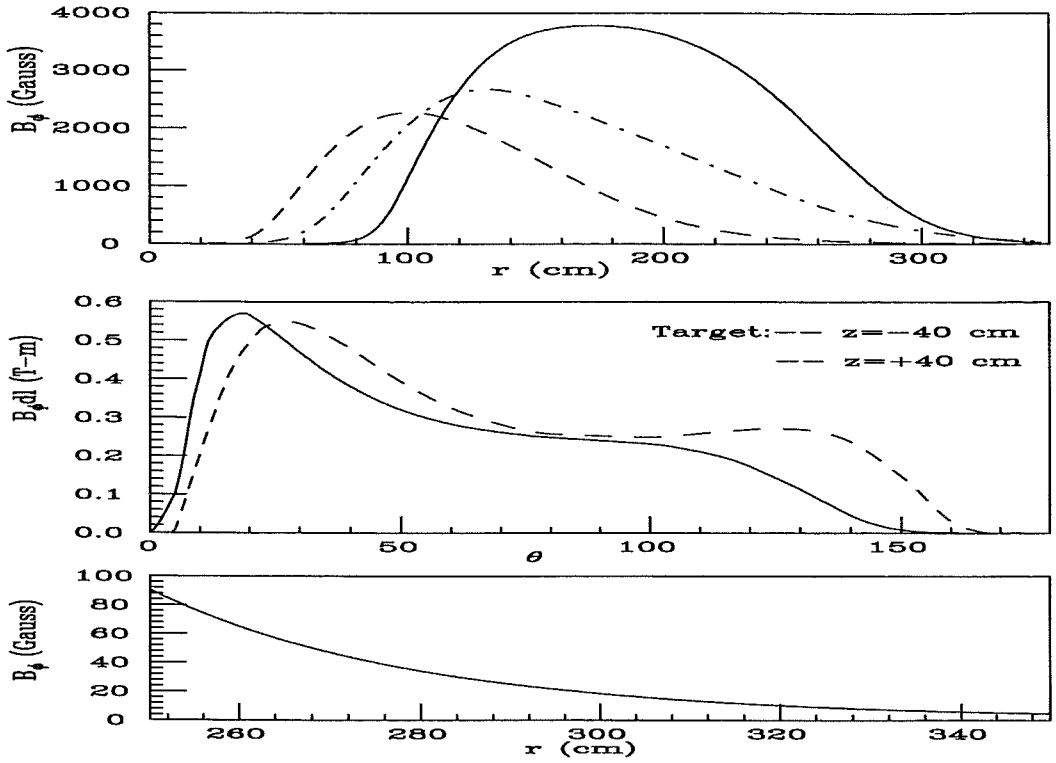

Figure 38: *TOP: B_ϕ on the midplane between two coils along straight trajectories from the target center at angles of 90° (dashed), 45° (dot–dashed), and 20°(solid). MIDDLE: The $\int Bdl$ as a function of the scattering angle. BOTTOM: B_ϕ as a function of the radial distance from the toroid center at θ=90°.*

magnetic gradients due to the main coils be less than 0.05 Gauss/cm in a region of ± 15 cm around the target center. However, about 0.05 Tesla-m should be available in the region between the target and the first set of wire chambers in order to provide shielding from low-energy Møller electrons. The magnetic fields will be realized with normal-conducting coils in order to decrease costs and block less solid angle. Consideration of the above, coupled with the physics program, has led to the choice of an eight-coil device with a toroidal field configuration capable of operating with field excitations as high as 1.4 MA-turns.

In Fig. 38 the azimuthal field B_ϕ is plotted for straight trajectories from the target center at angles of 90°, 45°, and 20°, respectively, and on the midplane between two coils. Going radially out in the midplane the field increases quite fast and then falls off as 1/r. The peak value depends on the scattering angle of the detected particle. The $\int Bdl$ is shown as a function of the scattering angle θ for the extreme target positions, z = -40 cm and z = 40 cm. It can be seen that forward-angle particles will have much more $\int Bdl$ than backward-angle particles. The field is zero along the beam line and a flat region to operate internal targets is available between the coil 1.3 m straight segment and the beam line. The field value at a radius of 3 m is about 20 Gauss in the midplane at θ = 90°. This amount of residual field will require careful magnetic shielding of the photomultiplier tubes. The fields have been calculated at the actual position of the photomultipliers for the timing scintillators and Čerenkov detectors. They are discussed below in the design sections corresponding to each of these detector elements.

The total magnetic field $\vec{B}$ around the $^3\vec{\text{He}}$ target is a superposition of a weak spatially varying field due to the main coils upon a much stronger homogeneous field $\vec{B}_0$ due to the Helmholtz coils. It has been shown [93] that Brownian motion in the presence of magnetic field gradients causes the moving $^3\vec{\text{He}}$ atoms to experience randomly fluctuating magnetic fields. Such fluctuations contribute to spin relaxation. This time relaxation of the spin should be $\geq$300 s to insure that there is no depolarization of the target atoms. To achieve these spin relaxation times, it is required that in the pumping cell the field gradients be kept to $\leq$0.05 Gauss/cm.

Our calculations show that for radial distances of the order of 12 cm or less, the fields are extremely small and flat. For radii greater than 15 cm the values of the fields grow faster approaching 0.2 Gauss at a radius of 17 cm. For radial distances $\leq$15 cm the gradients $\delta B_x/\delta x$ and $\delta B_y/\delta y$ are below the 0.05 Gauss/cm value thus ensuring relaxation times greater than 300 s. The effect of the number of coils on the fields around the target has also been studied. Our results show that the field for a six-coil device would grow much faster thus making the fields incompatible with the operation of the ^{3}He target without field correction coils.

The above results indicate that the magnetic gradients are less than 0.05 Gauss/cm, which is very convenient for the operation of the internal polarized target. The underlying assumption is that the coils have been aligned perfectly. Misalignment in the x and y directions have been examined by shifting an entire coil by an amount Δx or Δy and then calculating the fields and corresponding gradients in the region around the target. We have examined values of $\pm$ 1 and $\pm$ 2 mm for Δx and Δy. The BLAST windings can be constructed to within a tolerance of 1 mm. Our results indicate that the *maximum* allowed misalignment is of the order of $\pm$ 2 mm.

6.3.3 Power Requirements

When all 208 turns are energized at 6,750 A the power required will be 1.50 MW with 208 GPM water flow resulting in a water temperature rise of 30°C at a pressure drop of 58 psi. This design results in a coil assembly weighing about 43,500 pounds.

Free-wheeling diodes will clamp the voltage across the coil in the event of a power supply trip. Connections can be made to minimize the potential between adjacent circuits. The dielectric strength of the glass reinforced epoxy holding a coil section together is about 500 V/mil. Insulation between turns is nominally about 2 mm, and is ample to withstand the induced voltages between adjacent windings and pancakes.

Currently the flow rate of cooling water available in the South Hall at Bates is 500 GPM. The heat capacity of the cooling towers for the South Hall system is 2 MW. There is also approximately 0.5 MW capacity available from the primary water system used for the South Hall Ring. The inlet temperature of the water is 30^0 C and the inlet pressure is 120 psi. The coils will be cooled utilizing the South Hall water system. The requirements

for the toroidal coils are 208 GPM and 1.5 MW. The calculated temperature rise across the coils is 30^0 C and the calculated pressure drop across the coils is 60 psi. Therefore the South Hall cooling system, with the added capacity of the primary system available in the South Hall, can accommodate the total requirements of the BLAST detector.

Both water flow switches and thermal switch interlocks will be incorporated for coil protection. The coil sections are operated at reasonable temperature rise and water pressure drop values. Since the coil section terminations will be buried between the detector segments we will include pairs of thermal switches on each end of the conductor to allow a variety of connection possibilities and provide spare circuit strings in the event of failures. In addition, a water flow-rate meter will be interlocked with the power supply, so that the power can be cut off in case of restricted water flow before the temperature rises.

6.3.4 The Mechanical Structure

A mechanical frame has been designed to support the eight magnet coils. The requirements on this structure are as follows:

1. The deflections caused by gravity and the magnetic forces should not exceed $\pm$ 2 mm in any member of the frame under full load;
2. The frame must allow access to the target and inner detector elements without breaking the ring vacuum;
3. Non–magnetic materials must be used;
4. The frame should maximize use of the area that is shadowed by the coils.

A 3–D finite element model of the frame has been made by utilizing beam elements in the Ideas finite element program. The original conceptual design of the BLAST frame [70] utilized $3" \times 6" \times 5/16"$ 316 SS tubing for most of the structural elements. This frame has been analyzed with the 3-D Ideas model and deflections were found to be larger than the $\pm$ 2 mm range. The associated stresses were in the 11,000 psi range where the yield strength is 25,000 psi. A redesign of the original frame has been carried out. This work involved increasing the cross section of existing beams as well as slight manipulation of the location of key members in the frame. The final design numbers for the revised frame are 1.3 mm deflection and stresses of 2,820 psi maximum.

The revised frame has been analyzed to determine if it can be split into two halves in order to facilitate access to the target, scattering chamber, and interior detectors. A linear drive system for the BLAST halves has been designed with linear roundway bearings and 2" shafts. We are also investigating a system with Hillman rollers in order to reduce costs and improve reliability. However, in our first study we used the Thomson costs to be

conservative. The Thomson system will have a capacity of over 130 tons and be capable of moving the BLAST halves at a rate of 1 m/min. The drive system for each section will have a direct drive motor with 2020 oz-in torque and a recirculating ball nut on an acme thread and will have a capability of moving the section 1.8 m. This distance gives a total space of 3.6 m that will ensure adequate room to access the central components of BLAST. This redesign assumed three support rails on the floor to help distribute the gravity loads and minimize the size of the support beam for the bottom two coils. The design was made so that the floor height beneath BLAST does not have to be lowered.

The large pumpout stacks, the turbo and roughing pumps with their electronics, the atomic beam source for polarized hydrogen and deuterium, and the cryogenic and laser systems will be supported by a mezzanine above the BLAST frame. The mezzanine will allow access to these systems without separating the two halves of the BLAST frame. This arrangement will give access to the vacuum pumps for maintenance, access to the cryogenics, access to the laser system for adjustments and maintenance, and access to the gas system for adjustment and maintenance.

Fig. 39 shows the BLAST frame and the mezzanine when the two halves are 3.6 m apart. The total weight of the structure is approximately 25 tons.

6.3.5 Frame Assembly

Assembly of the structure will start with the base, followed by the lower support structure, the rings and the two lower coil sections. The remaining coil sections and radial members will be added from the lower sections to the upper sections. Periodic alignment checks must be performed as the assembly proceeds. The detector segments will be installed last and appropiate fixtures will be constructed to allow installation without disturbing the rest of the assembly. The detector segments will be supported as independently as possible to minimize the effect of any deformation of the support structure. This could include some dedicated members for the detector support coming up from the main support base.

The assembly procedure will require special handling fixtures for the coil sections during installation and future maintenance. The total weight of each half of the BLAST spectrometer could exceed 25 tons. As stated earlier, each half of the spectrometer will have a linear drive system allowing 1.8 m of travel. In the event that we find it necessary to move a half of the spectrometer with the crane the detectors will be removed from the corresponding half and thus the remaining support structure and coils will be well within the load rating of the crane (40 tons). Lifting fixtures will be designed and constructed to allow the crane to lift a BLAST spectrometer half safely.

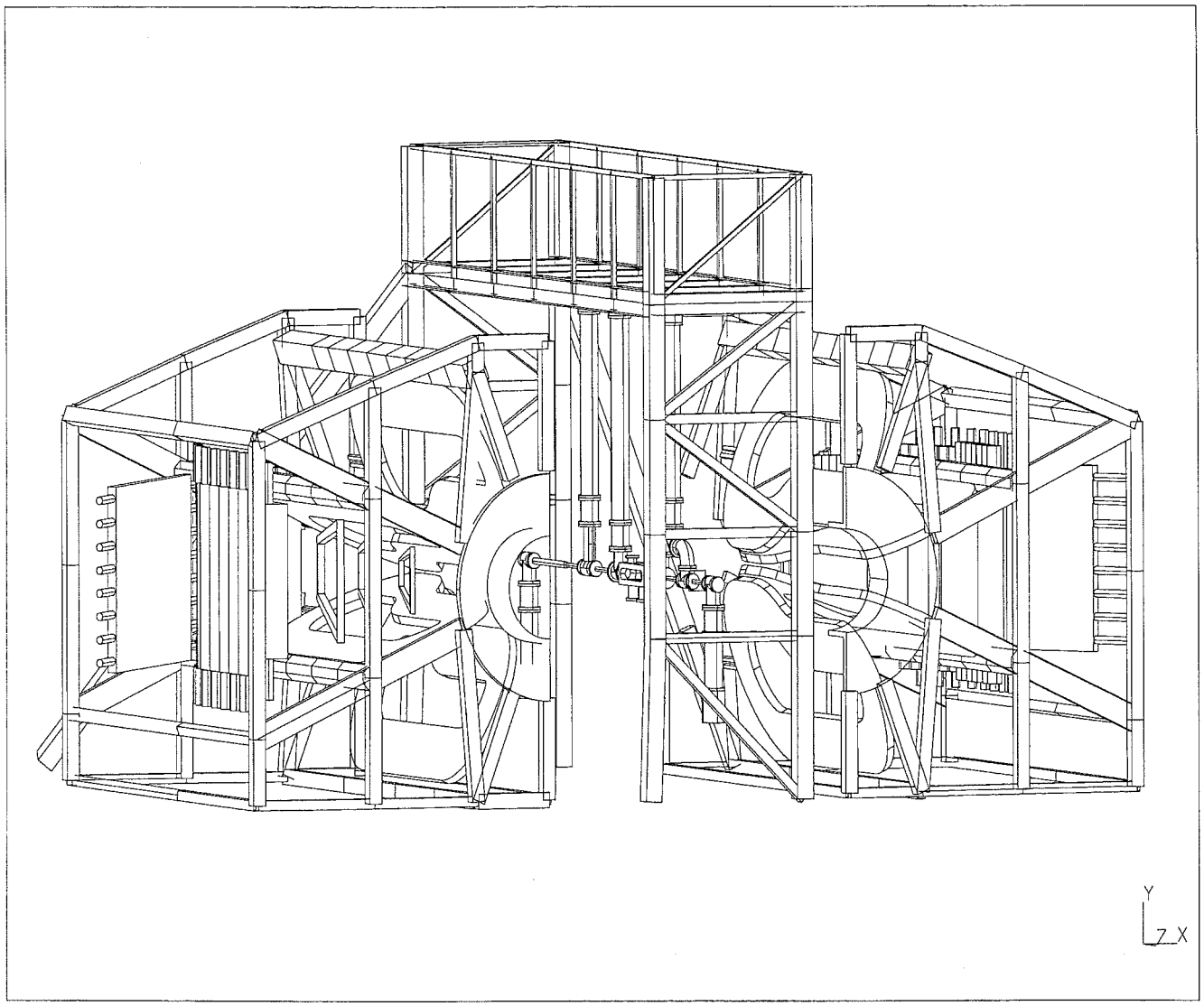

Figure 39: *The BLAST support structure showing the mezzanine and the two halves apart.*

6.3.6 Surveying and Alignment

The design requirements can be discussed with respect to the four major components which need to be surveyed and aligned: magnet coils, drift chambers, internal targets and beam line elements. The position tolerances on the magnet coils are estimated to be $\pm$ 2 mm in both x and y. Larger displacements would result in magnetic field gradients greater than 0.05 Gauss/cm in the target region. The position tolerances for the drift chambers are such that, locally, the individual wire locations need to be determined to better than $\pm$ 80 microns, but globally the absolute chamber positions can be uncertain by several millimeters. Even though the internal targets will have translation stages for fine positioning, initial positioning to at least $\pm$1 mm is desirable for efficient operation. Meeting this position tolerance should be straightforward with appropriate fiducialization.

The transverse position tolerance for quadrupole installation in the ring is $\pm$ 100 microns, magnet-to-magnet. The stability requirement is $\pm$ 10 microns. The quadrupoles inside BLAST will have to be independently alignable and probably supported separately from the BLAST frame. Surveying the internal quadrupoles will require opening BLAST.

For survey and alignment the primary tools at our disposal are mechanical and optical tooling, 'industrial measurement systems' (based on precision, automated triangulation) and electronic devices such as tiltmeters and level sensors. It should be noted at the outset that the required tolerances discussed above have been achieved (and exceeded) at other laboratories. Bates personnel are well experienced in surveying techniques because of their work with the pulse stretcher ring. Our task is primarily one of selecting the most overall cost-effective techniques and assuring that survey and alignment issues are considered in all stages of the design, construction and installation.

The principal steps involved in meeting the design goals begin with fiducializing the components: survey targets on the magnet coils and the three support rings will be located relative to their respective mechanical axes; targets on the drift chamber frames will be located with respect to the sense wires. This placement is done primarily with conventional mechanical tooling. The two outer support rings are large enough that the primary survey targets located at their peripheries will not be shadowed by nearby quadrupoles when BLAST is installed in the ring. The coils and chambers will be aligned with respect to the support rings by using optical tooling. Secondary survey targets will be mounted on the outer portions of the support structure and will be referenced to the primary targets with SIMS, an industrial measurement system developed at SLAC. SIMS will also be used during magnetic mapping of the toroidal field to relate the Hall probe positions to the primary fiducials on the support rings. This mapping will be a multi-step process as our automated measurement table has a range of 1.75$\times$0.90 m, and the vertical axis is manual drive with a range of 7 cm. Electronic tiltmeters and/or level sensors will also be attached to the support structure to aid vertical alignment after the preassembled BLAST is moved into location on the ring. Several of these devices will be necessary because the support structure is not rigid and will be supported by several jacks. A precision optical level will be used to check the tiltmeters and level sensors. Horizontal alignment will be made with

respect to a network of fixed floor monuments, which have already been surveyed with respect to the design orbit of the ring. This final step will most likely be performed by using CLASH and GEONET, triangulation survey systems from SLAC.

6.3.7 Safety

The size, weight, currents, voltages and magnetic fields associated with this device will present many potential safety hazards. A thorough safety review and detailed assembly procedure prior to construction will be performed. All special handling equipment and lift fixtures will be load tested prior to use.

6.3.8 Costs and Personnel

The costs for the magnetic coils and the mechanical structure were developed by Bates personnel. They are listed, in actual year dollars, in Table 9 . The cost for the copper

Table 9: *Cost estimates for the BLAST magnetic system in actual year dollars including a 20% contingency.*

Sub–system	Cost (k$)
Copper conductor	198.0
Coil fabrication	363.0
Magnet power supply	255.0
Mechanical support structure	103.0
Engineering and design	312.0
Installation in the SHR	98.0
Total	1329.0

conductor is a quote from Outokumpu, and the fabrication cost a quote from the Budker Institute of Nuclear Physics in Novosibirsk. The plan is to fabricate the magnet coils in Novosibirsk from the conductor supplied directly by Outokumpu. Shipping costs are included in the quotes. The magnet power supply estimate follows from a quote by Alpha Scientific. The cost of the support structure is split almost equally among the material (SS for the structure, aluminum for the support rings), fabrication costs, and the Thomson bearing assemblies to split BLAST in two sections. The engineering and design cost listed here includes a Project Engineer with responsibility for the assembly and integration of all the BLAST components as well as the design of detector support systems and drift chamber stress calculations. This position is costed through the entire project. The installation cost was estimated by Bates personnel responsible for the water and power systems, and includes

the cost of the custom quadrupole doublet which will lie in the downstream coil support ring inside BLAST. A uniform 20% contingency has been added to estimate the total cost.

The Bates Laboratory would make available a manpower of 10 FTEY (full time equivalent years) in the next three fiscal years (FY98, FY99, and FY00). This personnel will finalize the design, supervise the construction and carried out the implementation in the SHR of the toroidal magnet and its associate support structure.

6.4 The DRIFT CHAMBERS

6.4.1 Introduction

It is of course necessary to track charged particles through the magnetic field in BLAST to determine their points of origin and vector momenta. This task will be accomplished by using drift chambers of fairly conventional design. The sense wires and cathode wires will be in parallel planes, as shown in Fig. 40. There will be three drift chambers per sector, covering the angular range between 20° and 80°. Because the side sectors will be the ones instrumented, the wires will be vertical or nearly vertical. Fig. 40 shows the arrangement

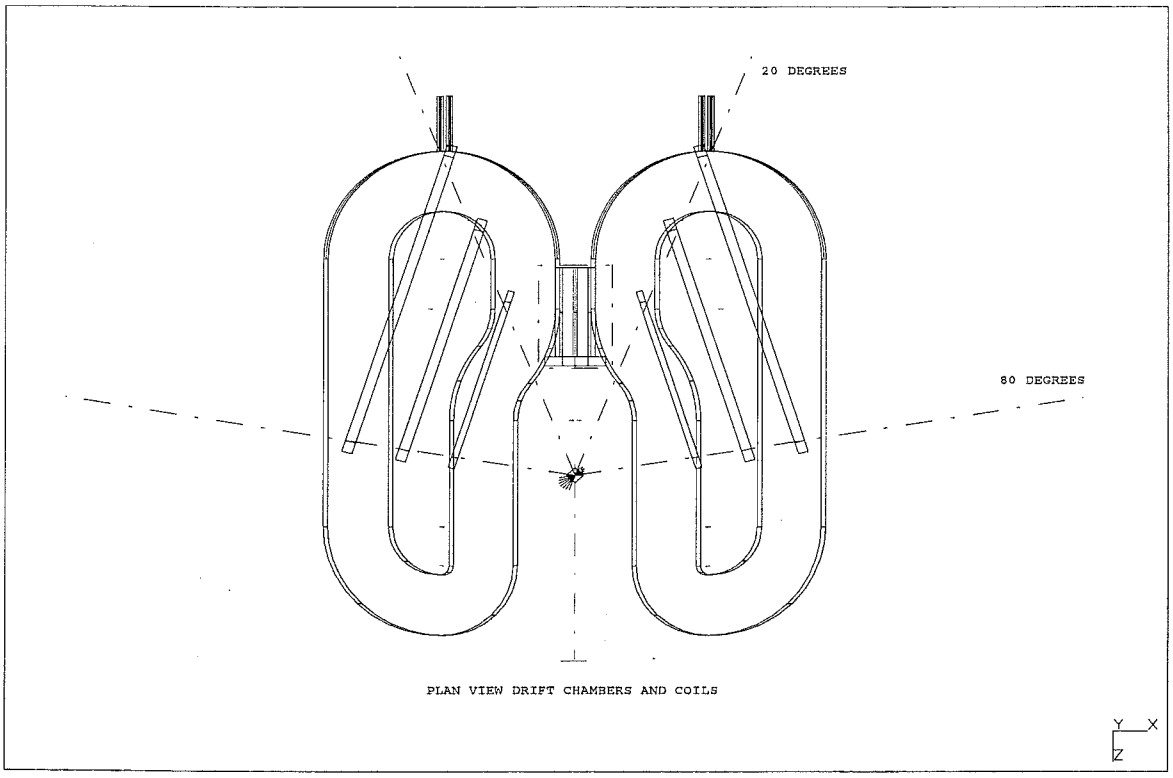

Figure 40: *Plan view of the BLAST drift chambers. The system of coordinates is such that z-axis is along the beam direction and the y-axis is the vertical direction perpendicular to the floor. The figure is in the $x - z$ plane.*

of the chambers between the coils. The system of coordinates is such that z-axis is along the beam direction and the y-axis is the vertical direction perpendicular to the floor. Thus the plane of Fig. 40 is the $x - z$ plane, which is the traditional scattering plane.

6.4.2 Design Specifications

The dimensions of the chambers are indicated in Fig. 41. The drift chambers are of

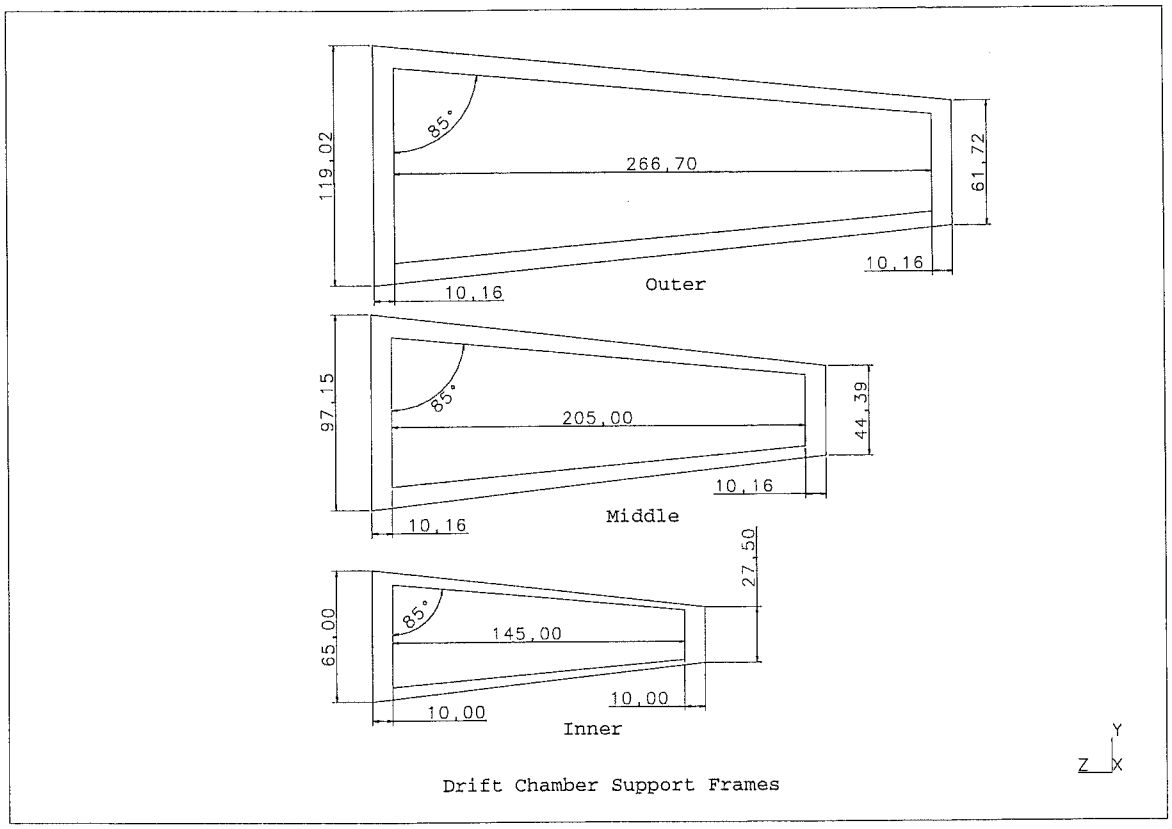

Figure 41: *Frame dimensions of the BLAST drift chambers.*

trapezoidal form as they must fit inside the coils. Each drift chamber consists of 4 layers of sense wires. Two of these layers (called axial) will have the signal wires vertical (parallel to the magnetic field at the center of the sector) whereas the other two (called stereo) will be tilted by $\approx 10°$ with respect to the axial wires. Fig. 42 shows the arrangement of sense and cathode planes for the inner drift chamber together with the cell dimensions and a schematic electric field pattern. The outer two chambers are similar, but the distance between sense wires is increased by a factor of two. Configurations of drift chambers with similar cell structure have been built by members of the collaboration and used in other magnetic spectrometers.

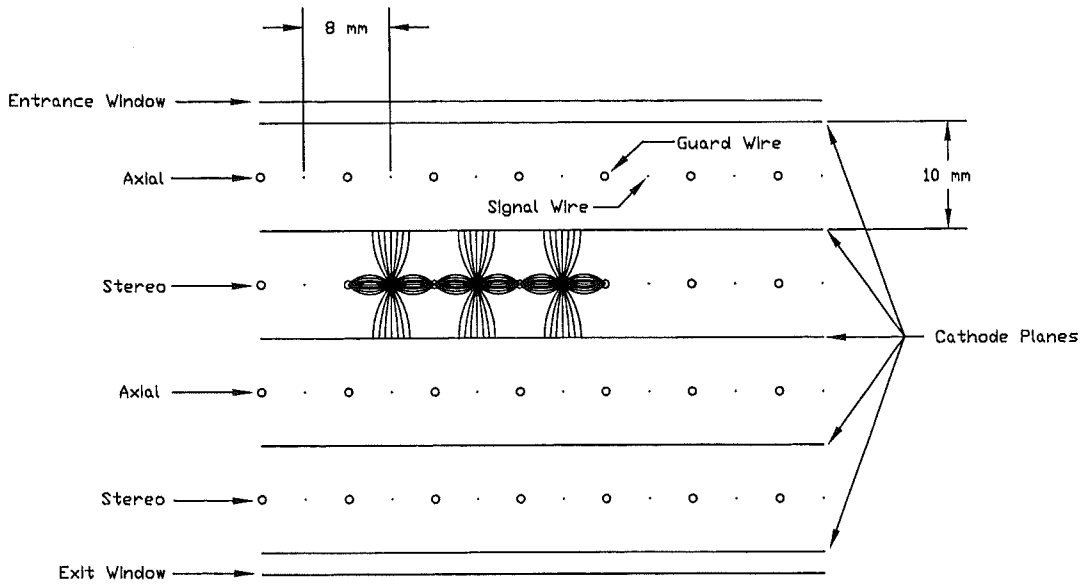

Figure 42: *Cross sectional view of the inner drift chamber.*

The dimensions of the proposed drift chambers do not present mechanical stability problems for the wires under electrostatic forces. We have estimated that, for the proposed arrangement, the maximum wire length for stable operation is 5.0 m. The longest wire we propose to use is about 1.5 m.

The primary technical challenge for the drift chambers will be to maintain the largest possible angular coverage, both in the polar angle θ and in the azimuthal angle ϕ. This is an issue because of the solid angle subtended by the coils and because of the size of the frames of the drift chambers. Ideally one would like the drift chamber frames to stay within the shadows of the coils, and indeed this is likely possible for all but the inner chamber. However, it will be important to keep the frame size as small as possible for the inner chamber. This is especially important at forward angles, as there, the shadow of the coils is fractionally the greatest.

Given the necessity to keep the drift chamber frames as thin as possible, the issue of deformation of the frames caused by the wire tension is especially important. We are considering using aluminum instead of G10 as a frame material because of its considerably higher ($\times 4$) modulus of elasticity. We also expect to pre-stress each plane frame before attaching the tensioned wires so that the wires do not cause any additional deformation and resulting lowering of wire tension.

In the kinematical range relevant to electron beams up to 1 GeV, multiple scattering dominates the momentum, angular, and vertex reconstruction resolutions for electrons and protons. Detailed GEANT tracking simulations show that the angular resolutions are mainly determined by scattering from the various foils in the target region (see Sec. 7).

The intrinsic position resolutions of the proposed chambers should be small compared to the contributions from multiple scattering. Drift chambers built at MIT with cell structure identical to that proposed here have reported intrinsic average position resolutions of about 175 μm FWHM. In addition, the present drift chambers have 4 planes of wires stacked together, 2 axial and 2 stereo, in order to constitute a redundant set in each chamber. This redundancy should remove left-right ambiguities.

The arrangement of the proposed drift chambers is such that a track curvature measurement is done by three clusters of points, each with an accuracy ϵ. In the equidistant case the momentum resolution, in the absence of multiple scattering, is given by

$$\frac{\Delta p}{p} = \frac{8p}{0.3L_0}\frac{1}{\int Bdl}\sqrt{(\epsilon_1/2)^2 + (\epsilon_2)^2 + (\epsilon_3/2)^2} \tag{31}$$

where p is the particle's momentum and $\int Bdl$ is the integral of the field along particle's trajectory. The accuracies $\epsilon_i = \frac{\sigma_i}{\sqrt{N}}$ where σ_i are the intrinsic position resolutions of the drift chambers and N is the number of measurements. Under these circumstances we estimate an intrinsic momentum resolution for 1 GeV electrons of about 1% (slightly worse at forward angles), which is the design goal of BLAST.

Because multiple scattering is expected to be the dominant contribution to the eventual momentum resolution, we may still improve the resolution by eliminating some material along the trajectory. In particular, the current design includes an atmosphere of air in the two volumes between the three drift chambers. This air is a significant contributor to the multiple scattering. If needed, the air could be replaced by an atmosphere of He if the corresponding resolution improvements were important for physics.

In Sec. 7 we have also used GEANT to estimate the occupancy of the drift cells, which is of course related to the number of redundant planes which will be required. Our simulation studies for BLAST have indicated that the toroidal field acts as a magnetic bottle for low-energy scattered particles, which constitute the major source of background. The number of sense wire planes appears comfortable in terms of providing the necessary redundancy. It is interesting to note that our experience at NIKHEF shows that for luminosities of 10^{32} cm^{-2}s^{-1}, one can achieve tracking efficiencies of 99% for individual planes of wire chambers in the forward direction and in a non-magnetic environment.

It may be of interest to comment on the differences between our drift chamber design and that of the CLAS detector at TJNAF. CLAS is physically significantly larger and has drift chambers with non-parallel endplates. That is, the endplates follow the faces of the magnetic coils. This design produces somewhat larger solid angle coverage and somewhat better momentum resolution than does the more conventional design presented here. It is also very much more complicated and expensive than the conventional design. BLAST will operate at momenta much lower than those needed for the CLAS program, and therefore the requirements on relative momentum resolution are considerably relaxed. The size of the drift chamber frames in our design reduces solid angle coverage most significantly at forward angles, where the cross sections of interest are in general highest. For these reasons

we believe that, in adopting a relatively conventional drift chamber design, there is little compromise in the ability to access the most important physics issues for which BLAST is designed. The advantages in a simpler, less expensive option for the drift chambers are obvious.

Table 10 summarizes the specifications for the proposed drift chambers.

Table 10: *Specifications for the horizontal drift chambers.*

Wire Chamber	**Vertex**	**Middle**	**Outer**
Dimensions	143×54 cm	205×81 cm	267×109 cm
Cell size	8 mm	16 mm	16 mm
Position resol.	180 μm typ.	180 μm typ.	180 μm typ.
Gas Mixture	50%Ar/50%Ethane	50%Ar/50%Ethane	50%Ar/50%Ethane
Anode Wire Dia.	20 μm W+Au	20 μm W+Au	20 μm W+Au
Cathode Wire Dia.	140 μm W+Au	140 μm W+Au	140 μm W+Au
Cathode foils	10 μm Al	12 μm Al	15 μm Al
Cathodes/chamber	5	5	5
Window foils	10 μm Al	12 μm Al	15 μm Al
Windows/chamber	2	2	2
Sense wires/plane	180	128	167

6.4.3 Drift Chamber Electronics

The high voltage will be supplied to the drift chambers from a central, computer controllable high voltage distribution system. Currently this is specified as the LeCroy 1489HP High Voltage Mainframe system with 1469 High Voltage Pods. The readout of the drift chambers is done as follows: LeCroy 2735DC amplifier-discriminator cards will be local to the drift chamber, probably mounted on the coil support structure. The cable runs to the amplifier discriminators will be short to reduce noise pickup and to minimize signal attenuation. The discriminated signals will be run from BLAST to a shielded electronics area, probably inside the SHR and immediately downstream of BLAST. The cable runs will be less than 50 m, so signal slewing will not be a problem. Time digitization will take place in LeCroy 1877S FASTBUS TDCs. The TDC information will be read out via the Struck FASTBUS Interface (SFI) as discussed in Section 6.11. Currently, the plan is to provide one TDC channel per active wire. This approach is a conservative one. We are exploring the possibility of multiplexing the readout by a factor of two in the same manner as is done in CLAS at TJNAF. There, an active wire is multiplexed with another one four physical wires away. The multiplexing is done by using short or long pulses from the amplifier-discriminator boards. The TDC then digitizes not only the arrival time of the pulse, but its pulse length as well, allowing for de-multiplexing to be done by the software.

If this scheme works and can be adapted in a cost effective manner, we can realize some cost savings in the FASTBUS electronics.

6.4.4 Costs and Personnel

The costs for the Drift Chamber branch are listed in actual year dollars in Table 11. The

Table 11: *Cost estimates for the BLAST drift chambers in actual year dollars including a 20% contingency.*

Sub–system	Cost (k$)
Prototype	110.0
Electronics	614.0
Manufacture	363.0
Total	1087.0

drift chambers are similar, in principle, to those that have been built at Bates, LAMPF and other laboratories. As with the other branches, there is a strong emphasis on standard commercially available technology with little emphasis on custom development. The estimates for the fabrication, stringing and assembly are based on many years of building this kind of drift chamber system. The electronics costs are principally catalog prices.

The MIT Medium Energy Group will provide the personnel resources for the drift chambers. They amount to a total of 15 FTEY over three years. Of this total 7.0 FTEY come from faculty, a full-time research physicist, and post-docs; and 8.0 FTEY from students.

6.5 The ČERENKOV DETECTORS

6.5.1 Introduction

Gas threshold Čerenkov counters are widely used in medium energy electron scattering to discriminate electrons from pions and thus generate the trigger signal indicating the detection of an electron. Typical gases, such as isobutane, have an index of refraction at atmospheric pressure that can discriminate between electrons and pions with momenta up to about 2.0 GeV/c. This value is more than adequate for experiments with a $\leq$ 1 GeV electron beam.

Originally we decided to instrument BLAST with an array of gas threshold counters similar to the array being considered at that time for the CLAS detector. Large acceptance, non–focusing devices such as BLAST and CLAS present the typical gas threshold counter with

new problems. First, very high quality mirrors of ellipsoidal and flat shapes are needed to maximize the solid angle and the number of detected photoelectrons. Second, due to the different degrees of curvature for the particle trajectories, the optics may have to be adjusted across the acceptance in order to obtain a uniform efficiency over the large solid angle. On the other hand, to facilitate the production of high quality mirrors it is convenient to standardize the parameters of the ellipsoids so the mirrors can be replicated from a negative mold. Thus one may have to give up the standardization of the mirrors for the sake of a uniform efficiency. This compromise can produce the desired Čerenkov array but it would in all likelihood increase the tooling costs.

Recently we have reviewed the possibility of building the BLAST Čerenkov counters by using the well-known material aerogel. Several years ago we rejected this option on the grounds that the aerogel was difficult to handle and prone to damage and, when low enough indexes of refraction were available, not enough light was produced to guarantee the desired performance. However, in the past few years there have been significant improvements in the optical quality of aerogel. Moreover, large silica aerogel Čerenkov counters with dimensions and properties very similar to that required for BLAST have been built and operated very successfully [108]. Consequently, we have reviewed the BLAST Čerenkov original design and adopted as a final design an array of counters having silica aerogel as radiator with indexes of refraction n =1.020 for angles forward of 40° and n =1.030 for angles backward of 40°. This arrangement is good enough to discriminate pions up to at least 700 MeV/c. Each counter is equipped with a large single diffusion box to collect the light into properly arranged photomultiplier tubes.

6.5.2 Conceptual Design of the BLAST Aerogel Detector

To design the BLAST aerogel detector we have used a simulation technique developed in conjunction with the construction of a large diffusely reflective aerogel Čerenkov detector for internal target experiments at NIKHEF [109]. For a wide range of aerogel detectors reported in the literature, the code was found to predict quite well the average number of electrons, the uniformity, timing resolution, and the photomultiplier multiplicity.

First, we examine the momentum and angular distributions of pions in BLAST. Consider the single pion photoproduction cross sections from ^{3}He for a 880 MeV electron beam, shown as a function of the pion momentum in Fig. 43 for scattering angles between 20° and 80°. It can be seen that pions with momenta $\geq$ 600 MeV/c are present only for angles $\leq$ 40°. To choose the n of the silica aerogel and therefore the momentum threshold one must balance between complete pion rejection and sufficient light output from the β=1 electrons. For example, the light output for pions from silica aerogel with n =1.03 is shown relative to that of the electron in Fig. 44 as a function of the particle momentum. From the results we have chosen n =1.03 for angles backward of 40°, and n =1.02 for the forward angles. These forward Čerenkov detectors cover the angular range 20°–40° and, due to the coil shadow, their length is shorter than those covering the range 40°–80°. This difference is an advantage because the forward detectors will yield approximately the same number

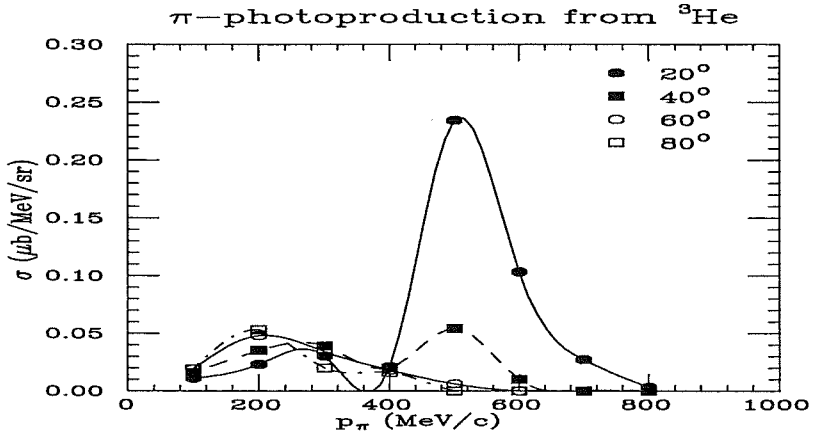

Figure 43: *Single pion photoproduction cross sections for a 880 MeV electron beam.*

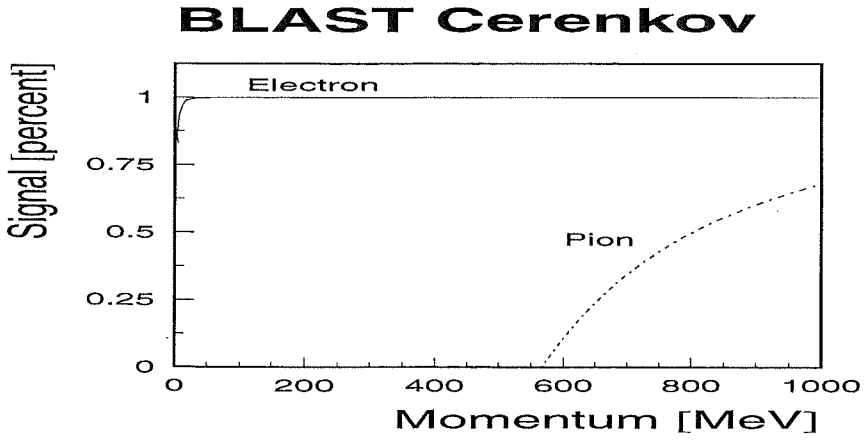

Figure 44: *The percentage of signal in the BLAST Čerenkov for electrons and pions versus particle momentum is shown.*

of photoelectrons as the backward detectors. The threshold for n =1.02 is 700 MeV/c. In addition, the presence of the lead glass calorimeter discussed below will, to the extent necessary, complement pion rejection in the 20°–40° angular range.

A conceptual design of a BLAST Čerenkov detector unit is shown in Fig. 45. The detector

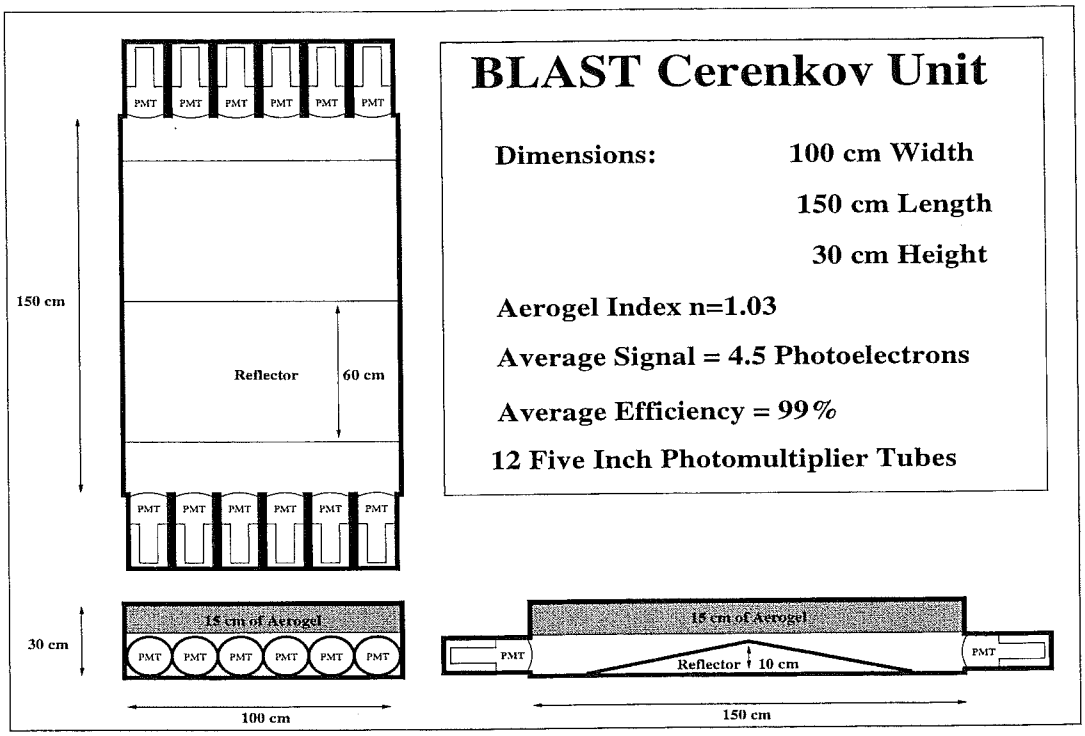

Figure 45: *A schematic design for one of the BLAST Čerenkov units. Each detector will be filled with 15 cm of 1.03 refractive index aerogel. The light box region of the detectors will be covered with aluminized mylar and viewed by twelve 5" photomultiplier tubes. The center reflector is added to produce a uniform detector efficiency over the entire width of the detector.*

is filled with an average thickness of 15 cm of n =1.03 aerogel and has a light collector box, the area that the Čerenkov radiation is emitted into, of 100 cm×150 cm×15 cm. The light box region is viewed by twelve 5" photomultiplier tubes. The diffusely reflective walls of the light box are covered by millipore diffusely reflective paper for the case without a center reflector and with aluminized mylar with the reflector. The choice of n, thickness of aerogel, light box dimensions, and number of phototubes was optimized to yield an average number of about 5.0 photoelectrons for β=1 particles, i.e., a detector efficiency $\geq$ 99%.

6.5.3 Previous Results from Similar Arrays

A large silica aerogel Čerenkov counter with dimensions and properties very similar to that shown in Fig. 45 was built for the superconducting kaon spectrometer (SKS) at the KEK

12-GeV proton synchrotron to veto pions of 0.7 GeV/c [108]. It features a large single diffusion box with a sensitive area of 140 cm×120 cm and a thickness of about 40 cm. The aerogel was 9 cm thick with n =1.06. We have simulated the results of the SKS prototype diffusely reflective Čerenkov detector. This Čerenkov is nearly as wide as the BLAST design so it represents a very good benchmark to test the ability of the simulation code to deal with these wide detectors. The results of the simulation are compared with experimental results in Fig. 46 where the average number of photoelectrons is plotted as

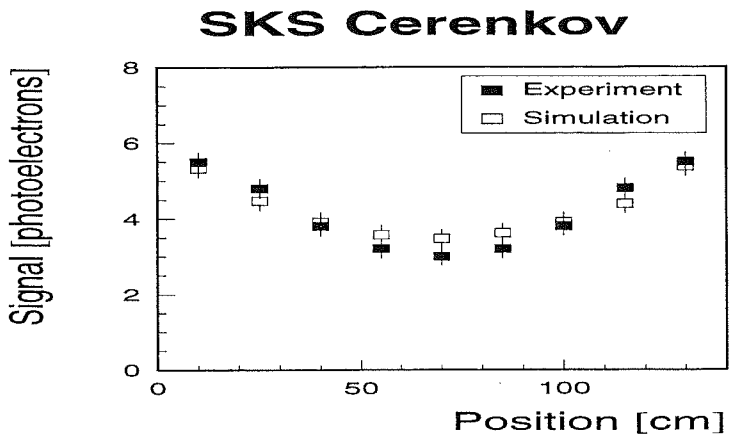

Figure 46: *The SKS Čerenkov's experimental and simulated signal as a function of the width of the detector. Both results are for the case without the center reflector.*

a function of the event position across the width of the detector. The code reproduces the experimental results for the SKS prototype Čerenkov results. The final SKS Čerenkov included a center reflector in order to provide a uniform efficiency across the sensitive area. These results are summarized in Fig. 47. The effect of the center reflector is to increase

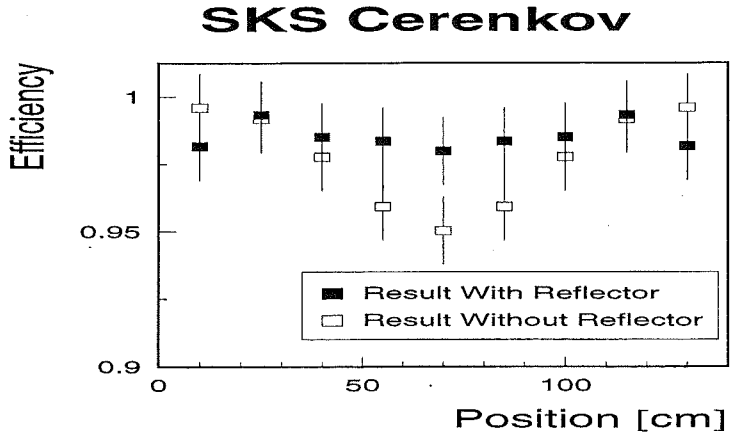

Figure 47: *The SKS Čerenkov's experimental efficiency with and without the center reflector.*

the signal from the central region of the box, thereby producing a uniform efficiency across its entire length.

6.5.4 Simulations for the BLAST Array

By changing only the refractive index of the aerogel and the size of the detector in the input file, the code was used then to simulate the proposed Čerenkov unit shown in Fig. 45. The results are summarized in Figs. 48 and 49 where the results for the number of photoelec-

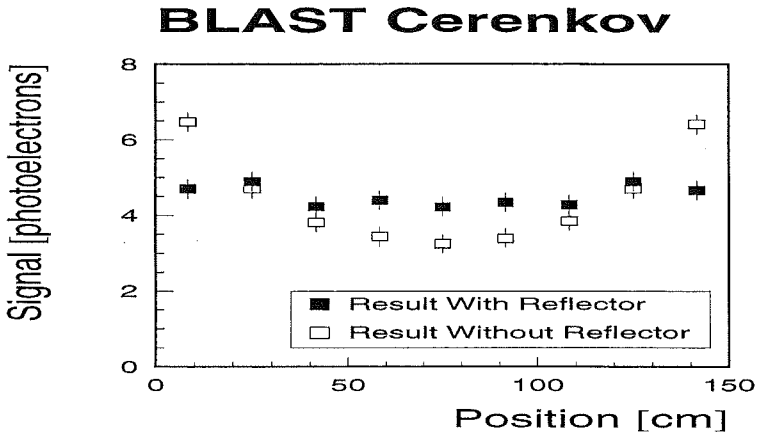

Figure 48: *The BLAST Čerenkov's signal as a function of the width of the detector is shown for both with and without the center reflector.*

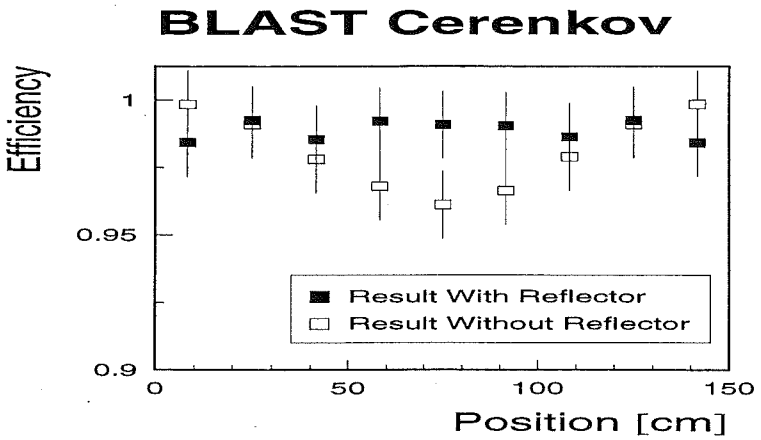

Figure 49: *The BLAST Čerenkov's efficiency as a function of the width of the detector is shown for with and without the center reflector.*

trons and β=1 efficiency as a function of the event position are shown with and without the central reflector. From these figures, it can be seen that, for n =1.03, the Čerenkov will be able to produce 4.5 photoelectrons with an average electron detection efficiency of 99%. Thus this design of the BLAST Čerenkov will misidentify 1% of the electrons

as non–radiating pions. With the addition of a central reflector the detector's detection efficiency becomes uniform over the entire 150 cm of width.

6.5.5 Arrangement in BLAST

A plan view of the aerogel Čerenkov array is shown in Fig. 50 . The array consists of

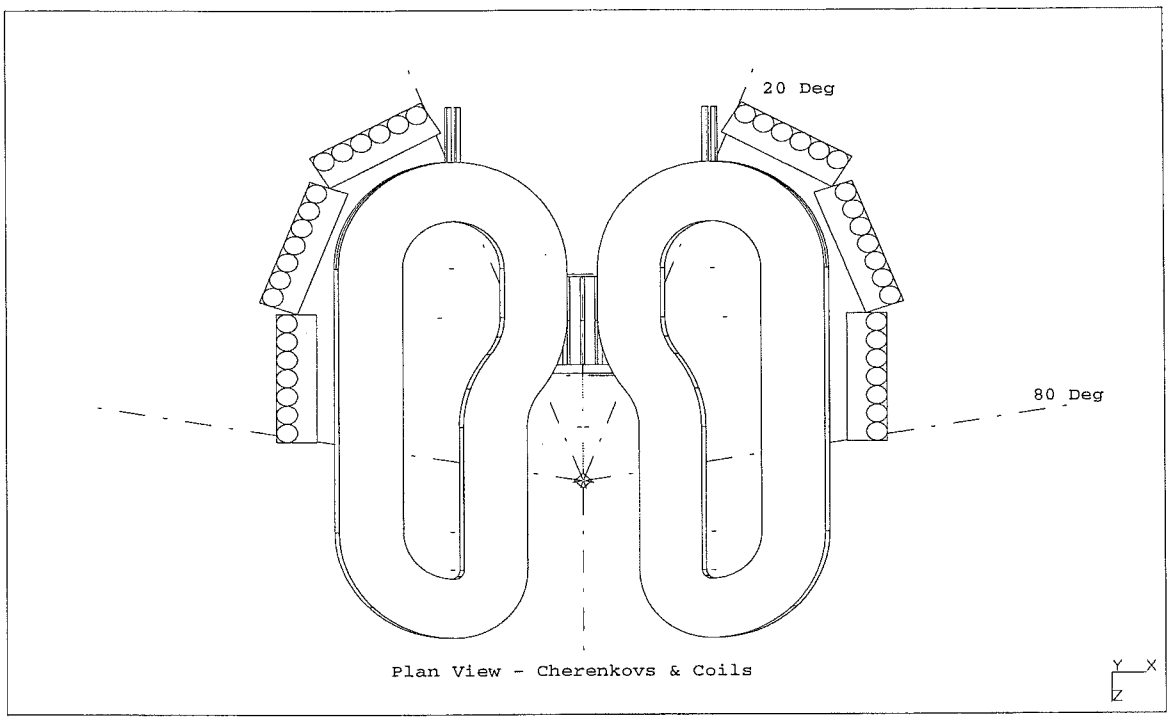

Figure 50: *Plan view of the Čerenkov array. There are 3 units per sector, each viewed by photomultipliers on both ends. The angular coverage from the center of the target is 20° to 80°. The figure is in the $x - z$ plane. The coordinate system is that of Fig. 40.*

three units per sector. The forward unit has the lowest index of refraction and it is viewed by six 5" phototubes from each end. The other two units in each BLAST sector have n =1.03 with seven 5" phototubes at each end. We have calculated the magnetic field over the region where we expect to locate the photomultiplier tubes. Fig. 51 shows the B_x, B_y, and B_z components of the magnetic field across the front face of the photomultiplier tubes. They are plotted as a function of the z–position for the rearmost Čerenkov unit. The target center is located at (0,0,0). Similar field values hold for the other two panels. The field is predominantly vertical, i.e. along the phototube, and of the order of 100 G. The photomultiplier tubes must be fitted with the appropriate magnetic shields that will extend at least one photocathode diameter beyond the photocathode region.

To avoid any deterioration of the optical properties of the silica aerogel the humidity around it must be kept below 30% at all times. The units will be built air tight and nitrogen will

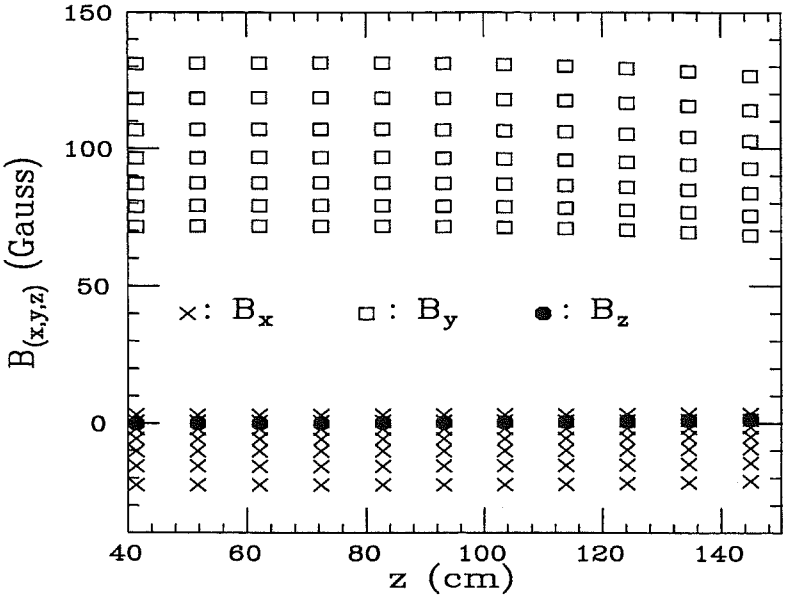

Figure 51: *The B_x, B_y, and B_z components of the magnetic field across the front face of the photomultiplier tubes. They are plotted as a function of the z–position for the rearmost Čerenkov unit.*

be flowed into the unit during operation. Due to the length of the units the central reflector is necessary to guarantee uniform efficiency. Our plan is to build a prototype unit of a size similar to that simulated here. This prototype can be built and tested within one year. Production of the remaining units will proceed right after, and it is estimated that they can be mounted in BLAST approximately a year later.

6.5.6 Costs and Personnel

The costs for the Čerenkov detectors are listed, in actual year dollars, in Table 12 . The

Table 12: *Cost estimates for the BLAST Čerenkov system in actual year dollars including a 20% contingency.*

Sub–system	Cost (k$)
Phototubes, bases, and magnetic shields	254.0
Silica Aerogel Cost	32.0
Light boxes (material and fabrication)	178.0
Electronics	56.0
Miscellaneous	88.0
Total	608.0

cost for the phototubes, bases and shields is a quote from Burle. The cost of the light boxes include the final design specifications, material, fabrication, and shipping. The plan

is to fabricate the Čerenkov light boxes in the relatively dry climate of Arizona. A uniform 20% contingency has been added to estimate the total cost.

Arizona State University will provide the personnel resources for the Čerenkov detectors. They amount to a total of 5.0 FTEY over three years. Of this total 1.0 FTEY come from faculty, 1.0 FTEY from the ASU post-doc, and 3.0 FTEY from students.

6.6 The TIMING SCINTILLATORS

6.6.1 Introduction

The scintillation time-of-flight system provides timing signals for particle identification and triggering. The timing and position information is also used for wire chamber track reconstruction. The time-of-flight resolution required by BLAST to separate hadronic particles below 1 GeV/c is not particularly stringent. Pions are separated from protons at 1 GeV/c by 3 nsec. High segmentation would allow timing measurements for closely spaced tracks. This challenge is also not a significant one for the physics program described above, because particle multiplicities are low. Consequently the scintillator array can easily meet the physics requirements of BLAST.

The array provides geometrical coverage of the active detection region of BLAST, extending beyond the wire chambers to include curved tracks. Fig. 52 shows a plan view of the array of scintillators. The angular coverage from the center of the target is 15° to 85°. The scintillators are hung vertically on the two BLAST sectors, 14 per sector in three panels. The three panels are positioned behind the three Cerenkov units. The five scintillators in each of the two rearmost panels will be identical to each other, while the four scintillators in the most forward panel will have decreasing length as the scattering angle decreases. Scintillator thickness is chosen to be 2.5 cm, as a compromise between cost and performance.

6.6.2 Specifications

The scintillator material will be fast timing plastics with long attenuation length. NE-110 from Nuclear Enterprises, BC-408 from Bicron, and SCSN-38 from Kuraray are known candidate materials. The requirement for long attenuation length may be traded for faster timing for the two shortest scintillators. Most scintillator bars are 180 cm long, 30 cm wide, and 2.5 cm thick; the ones forward of 40° are progressively shorter.

Photomultipliers on each end will convert the light signal to current. Because the face of the scintillator plastic is 75 cm^2, more light can be collected with a 3" tube than with a 2" tube. Tests performed for the CLAS detectors at TJNAF yielded an improvement in

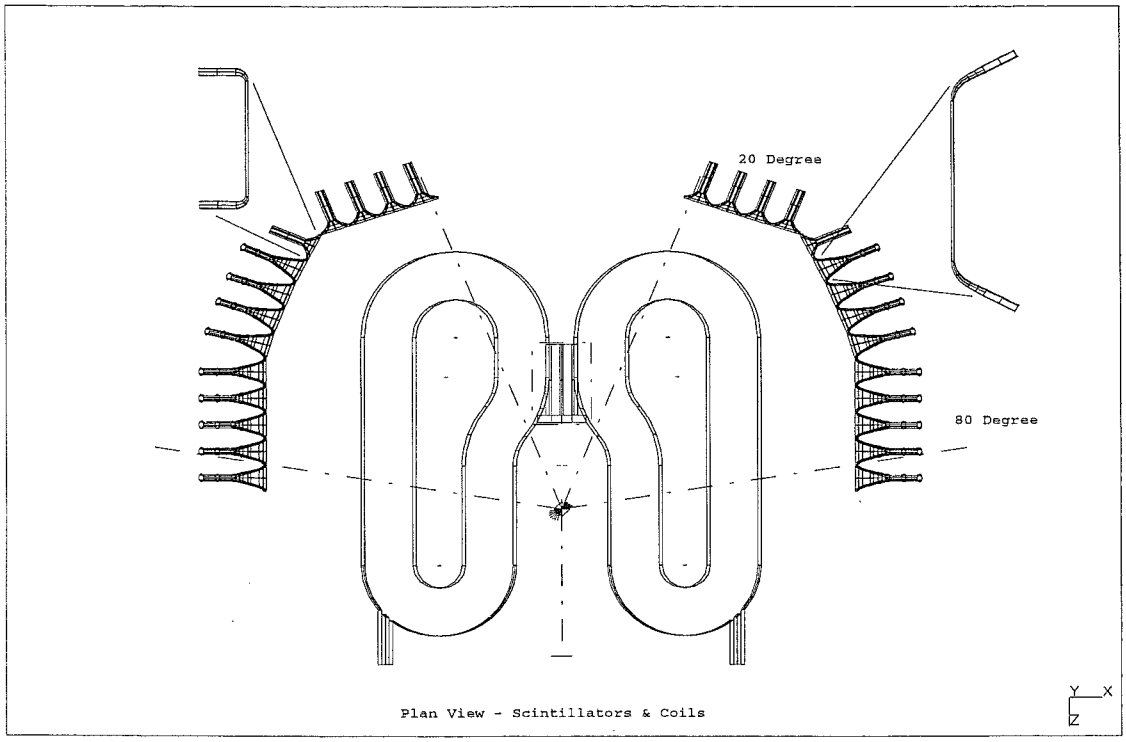

Figure 52: *Plan view of the scintillator array. There are 14 scintillators per sector, each viewed by photomultipliers on both ends. The angular coverage from the center of the target is 15° to 85°. See Fig. 40 for the coordinate system.*

timing of nearly 30% when 2" tubes were replaced with 3" tubes on those 20-cm by 5-cm plastic bars.

An actively stabilized voltage divider network will be used to supply the phototube voltages. This divider network was developed by the UNH group for the CLAS detector, and has been adopted by TJNAF as a standard. It contains four high voltage field effect transistors to stabilize the voltage differences across the last four sections. The stabilization scheme acts only on changes induced by signal currents from the dynodes and does not fix the voltage differences as zener diodes would. The photocathode to first dynode voltage is set by a zener diode to provide excellent timing regardless of phototube gain.

The scintillators are fitted with two adiabatic light guides, which serve several purposes. They adiabatically collect light from the 2.5-cm×30-cm cross section of the scintillator plastic and match it to the 3" photocathode. They serve to optimize the position and orientation of the photomultiplier tubes in the field region. We have calculated the magnetic field over the region where we expect to locate the photomultiplier tubes, and found them to be less than 30 Gauss. The photomultiplier tubes will be fitted with the appropiate magnetic shields. These will extend at least one photocathode diameter beyond the photocathode region.

Each scintillator will be wrapped individually in a light-tight covering. The innermost layer will be a lead foil of 10 mil thickness to shield the scintillator from low-energy x-rays and bremsstrahlung. This layer has a minimal influence for charged particles. Next will be two layers of aluminum foil to provide the primary light barrier over the body of the scintillator. The outer sheath will be black kapton, taped at the joints and the ends with black tape. The light guides and photomultiplier tubes will be wrapped with two layers of flexible aluminized plastic, and heat sealed. The scintillators will be supported by individual composite sandwich structures consisting of fiberglass skins separated by 2" plastic honeycomb. The ends of this sandwich material will be fitted with drilled plates that provide for the assembly of the scintillator panels onto an intermediate substructure. This substructure will also include the patch panels for signal and high voltage. These substructures will then be hung onto the main BLAST support structure.

6.6.3 Electronics

The scintillator package will be attached to an electronics package that includes high voltage power supplies, constant fraction discriminators, time to digital converters (TDCs) and analog to digital converters (ADCs), as well as passive cable delays and signal splitters. Each photomultiplier tube base will supply two negative signals, the anode signal and an inverted dynode signal. The dynode will provide signals through cables of minimum length to the trigger, via threshold discriminators and coincidence units that assure pulses on both the top and bottom PM tubes. This arrangement is discussed below in Section 6.10 on BLAST triggering. The anode signals are delayed by long cables and then passively split. One branch is provided to the ADCs. The other branch is provided to the constant fraction discriminator, which produces a TDC stop.

The photomultiplier tubes typically operate at about 2000 volts and draw currents of about 0.5 mA. The high voltage supply will provide independently controlled voltages for the 56 tubes. The high voltage mainframes will be controlled remotely by the Experimental Physics and Industrial Control System (EPICS) over a local area network.

Discriminators will be selected based on their sensitivity, speed, and channel-to-channel independence. Tests performed for the CLAS detector at the TJNAF revealed that some commercial discriminators are far from ideal in this last requirement. The problem of cross talk between channels was explored by pulsing two adjacent channels at known times, and shifting the relative time between the pulses through positive to negative values. The Philips 7106 exhibited reproducible time shifts of over 300 ps when the pulses were separated by a few nanoseconds. The LeCroy 2313 showed shifts of only 50 ps and are preferred for our implementation. The two ends of a single scintillator will not be plugged into adjacent channels of a discriminator, or even into the same discriminator unit if possible.

The time-of-flight TDC will be selected on the basis of fast conversion and readout time, high resolution, high linearity, and cost. The LeCroy 1872 TDC, modified to provide fast conversion times (1872A), was selected for the CLAS detector. The original unit had a fixed

conversion time of 177 μs. The modified version converts channels at a rate of 2.7 μs per channel, significantly reducing the average conversion time for the sparse data anticipated for the CLAS configuration. The least significant bit was set to 50 ps, allowing for a 205 ns dynamic range for this 12 bit TDC. The rms uncertainty was measured to be 80 ps, with counts spread over six or seven channels for fixed input time.

The analog-to-digital converter will be selected on the basis of conversion time, noise, linearity, and cost. The CLAS collaboration selected the LeCroy 1881M ADC. This unit is a 64-channel, 13-bit FASTBUS ADC with a fixed conversion time of 12 μs. Noise was measured at 50 fC (one count) when good ground connections were provided. Dynamic range was 400 pC. Linearity was good with maximum deviation of 400 fC (eight counts), and typical deviations of 100 fC (two counts).

6.6.4 Costs and Personnel

The costs for the scintillator array are listed, in actual year dollars, in Table 13 . The cost

Table 13: *Cost estimates for the BLAST scintillator system in actual year dollars including a 20% contingency.*

Sub–system	Cost (k$)
Phototubes, bases, and magnetic shields	67.0
Scintillator and lightguide material	100.0
Labor and misc.	173.0
Electronics	126.0
Total	466.0

for the phototubes, bases and shields is a quote from Philips. The cost of the scintillator and lightguide material comes from Bicron, and the fabrication cost is based on our experience in the assembly of the CLAS scintillators. The plan is to fabricate the scintillator array at the University of New Hampshire. Shipping costs are included in the quotes. The electronics estimate follows from catalog prices. A uniform 20% contingency has been added to estimate the total cost.

The University of New Hampshire group will provide a total 1.0 FTEY of physicists and supervisory support over three years to the personnel resources for the scintillator detectors. This personnel is in addition to the full-time technician costed in Table 13.

6.7 The NEUTRON DETECTORS

6.7.1 Dimensions

An array of neutron detectors will be located behind the Čerenkov detectors. The angular coverage will be about 30°, between θ= 38° and θ= 70°, in each sector of BLAST. The detectors will be made of 300-cm-long, 22.5-cm-tall and 10.0-cm-thick BICRON type BC-408 plastic scintillators, with 3" photo multiplier tubes (PM) coupled at each end. Fig. 53 shows the arrangement of the neutron detectors relative to BLAST. These detectors will

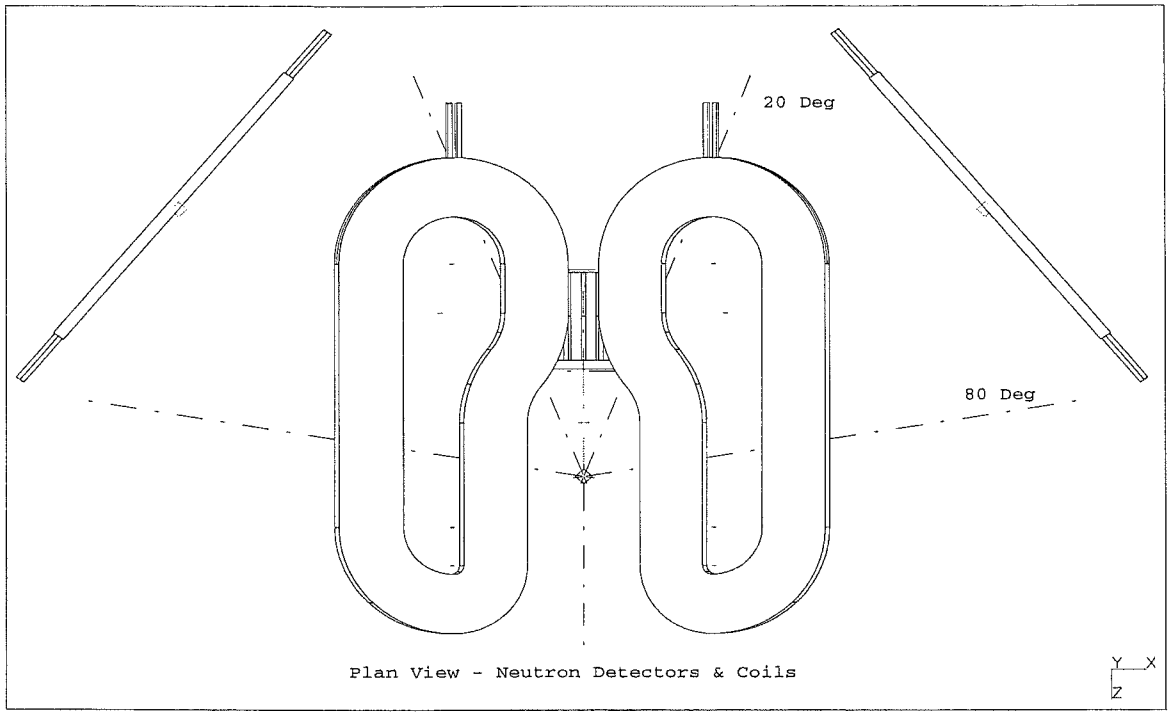

Figure 53: *Plan view of the neutron array. There are 8 neutron bars per sector, each viewed by photomultipliers on both ends. The angular coverage from the center of the target is 35o to 70o. See Fig. 40 for the coordinate system.*

be mounted horizontally and eight of them will cover an area of 3.0×1.8 m^2. The detector thickness was chosen as a good compromise between efficiency and energy resolution. The flight time of a 200 MeV neutron across the 10.0 cm thickness is about 590 ps. A similar intrinsic time resolution is expected from the combined performance of the detectors deriving the stop/start signals. A thicker neutron scintillator would provide a better detection efficiency, at the expense of lower energy resolution.

The horizontal mounting was chosen for several reasons. First, we will have better angular resolution (θ as opposed to ϕ). An estimated 1"-2" position resolution of the event in the scintillator is expected, which at 4-m corresponds to $\delta\theta \approx 1°$. The width of the bar gives rise to a resolution in ϕ of about 4.5°. Second, the bars can be easily calibrated with cosmic

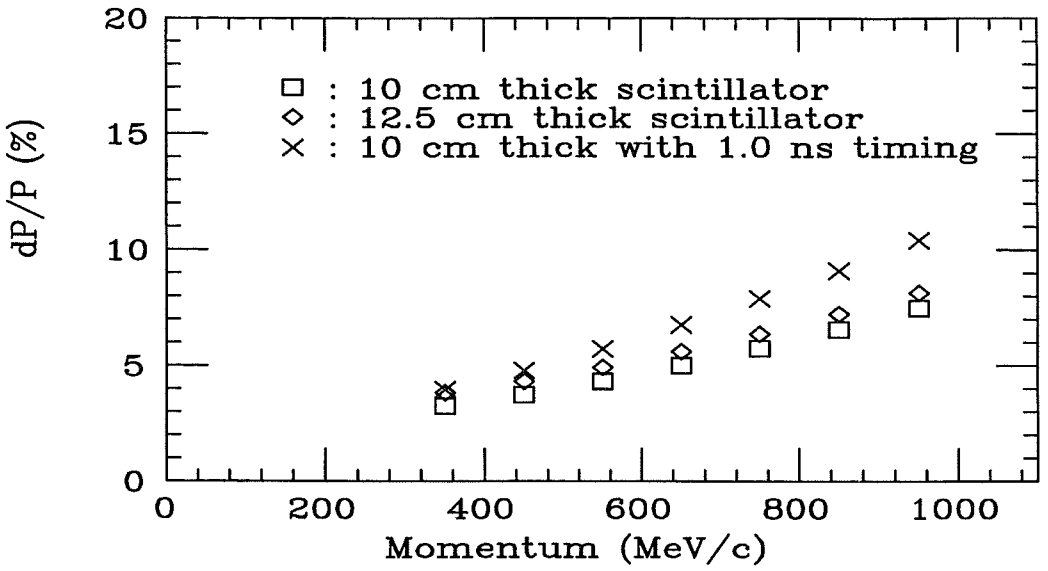

Figure 54: *Calculated momentum resolution for the neutron detectors. For the diamonds and squares a timing resolution of 600 ps has been assumed to which, in quadrature, the detector thicknesses contributions have been included. The crosses represent the case for a 1.0 ns timing resolution.*

rays. A trigger event requiring an eight–fold vertical coincidence will select cosmic rays depositing about 50 MeV of energy in each scintillator bar. Time and energy calibration are achieved simultaneously while data are being acquired. Finally, the mounting is more straightforward and stable. Separate stands will hold the neutron walls and they can be easily moved to other locations.

The chosen material combines a good light output and a good bulk light attenuation length. The surfaces will be diamond milled.

6.7.2 Momentum Resolution

The momentum resolution for neutrons has been estimated and is shown in Fig. 54. A 600-ps timing resolution from all sources other than detector thickness was assumed and added in quadrature with the latter contribution. The 600-ps time resolution corresponds to intrinsic time resolutions of the start and stop time detectors, added in quadrature. These values are realistically achievable. A flight path of 4-m has been assumed for the neutrons. Calculations were made for a 10-cm and a 12.5-cm-thick scintillator assuming the 600-ps timing resolution. A worst-case scenario in which a 1.0-ns timing resolution is achieved is also presented in Fig. 54, for the 10-cm-thick scintillator. Under the stated conditions, a 200 MeV neutron will have a 5.0% (5.6%) momentum resolution for a 10-cm (12.5-cm) thick scintillator. Values for other neutron energies are shown in Fig. 54.

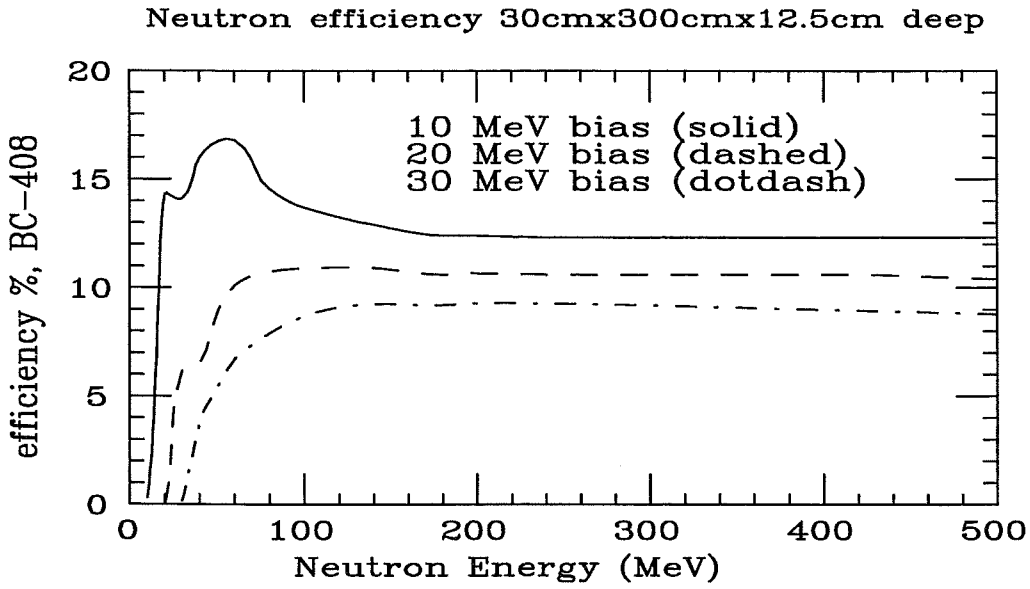

Figure 55: *Monte Carlo calculated neutron efficiencies obtained at the indicated thresholds for a detector 300-cm long, 30.0-cm high and 12.5-cm deep. Normally incident neutrons penetrate the detector along its depth.*

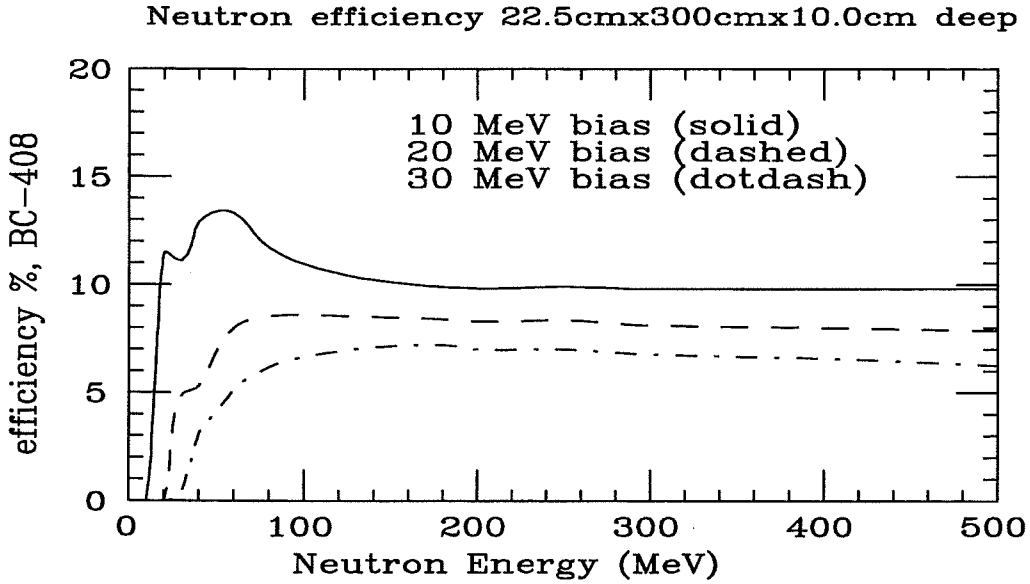

Figure 56: *Same as in Fig. 55, but for a 300-cm long, 22.5-cm high and 10.0-cm deep scintillator.*

6.7.3 Neutron Detector Efficiencies

We have used the Monte Carlo code Stanton to calculate the neutron detector efficiencies for neutrons in the energy range between 0 to 500 MeV. Several energy thresholds for 10, 20 and 30 MeV neutrons, have been assumed. The calculations for the two cases, scintillators of 5"x12" and 4"x9", both 300-cm-long, are shown in Figs. 55 and 56 . For a suggested

bias of 20-MeV neutrons, the 5" thick scintillator is about 11% efficient compared to a 8.7% efficiency for the 4" scintillator and neutrons in the 100-200 MeV range.

6.7.4 Monte Carlo Calculations

We have used a Monte Carlo program (Guide7) to evaluate the performance of detectors coupled with different length light guides and different sizes of PMs. Scintillators of 4"x9" and 5"x12" cross sectional area and 300 cm long were assumed in the study. A linear light source in the direction of the detector thickness was located at several distances from the phototube. Assuming a 3" PM, the study showed similar light collection efficiency for the two types of scintillators. The 5" PM coupled to the 5"x12" scintillator resulted in almost a factor of 3 better light collection. This factor is similar to the ratio of areas of the two types of PM. What was found to be important in order to get the best time resolution for photons arriving at the photocathode was the length of the light guide. Double pulsing was observed with some light guide lengths and the best result, less than 500 psec FWHM single peak in the arrival time, was obtained with a 25-cm-long light guide in the 4"x9" scintillator and a 35-cm-long light guide for the 5"x12" scintillator.

Although efficiency considerations are important, the effective cost of the 5"x12" scintillator coupled to a 5" PM compared with the cost and better momentum resolution of a 4"x9" scintillator coupled to a 3" PM, have led us to select the latter solution.

6.7.5 Costs and Personnel

The costs for the neutron detectors are listed, in actual year dollars, in Table 14 . The cost

Table 14: *Cost estimates for the BLAST neutron detectors in actual year dollars including a 20% contingency.*

Sub–system	Cost (k$)
Phototubes, bases, and magnetic shields	52.0
Scintillator and lightguide material	184.0
Electronics	52.0
Labor and misc.	83.0
Total	371.0

for the phototubes, bases and shields is a quote from Philips. The cost of the scintillator and lightguide material comes from Bicron, and includes the fabrication cost of the neutron bar. The electronics estimate follows from catalog prices. A uniform 20% contingency has been added to estimate the total cost.

Most of the assembly of the neutron bars as well as the testing of the detectors will be done by Ohio University (OU) personnel. For these tasks OU will make available 2.0 FTEY over three years.

6.8 LEAD GLASS CALORIMETER

6.8.1 Introduction

Particle identification (PID) in BLAST is provided by scintillators and silica aerogel Čerenkov detectors. Time of flight (TOF) information can resolve protons from pions and electrons up to about 1700 MeV/c, and dE/dx information can resolve protons from pions and electrons up to about 500 MeV/c. However, pions cannot be resolved from electrons above about 250 MeV/c with TOF, and perhaps 100 MeV/c with dE/dx. The aerogel Čerenkov detectors should give about 1 photoelectron for a pion and 4 photoelectrons for an electron, providing good but not perfect particle identification. One purpose of the lead glass calorimeter is to give a redundant separation of electrons from pions as a check on the efficiency and discrimination of the Čerenkov detector. For this purpose the calorimeter should cover a reasonable fraction of the solid angle to provide adequate sampling, and should be placed at strategic positions where the PID efficiency of the Čerenkov detectors may vary. The signal from the lead glass blocks placed close outside the neutron detectors can be included in the trajectory information obtained from the drift chambers and the scintillators. Multiple scattering in the TOF scintillators and the bottom of the Čerenkov detectors detectors will not change the hit point on the lead glass by more than 2 cm. A total of 32 lead glass detectors (each 15 cm x 15 cm x 30 cm) at 3.9 m from the target covers about 0.10 sr or 10 % of the BLAST solid angle. This coverage is an adequate sampling of the PID efficiency.

The lead glass array may also be used in the early stages of the BLAST detector development, before the Čerenkov detectors are in place. The lead glass can be used as the primary PID device for the testing of other prototype detectors or in any preliminary experiment that may be proposed. With 64 blocks, about 20% of the eventual BLAST solid angle would be covered. A plan view of the lead glass arrangement is shown in Fig. 57.

6.8.2 Resolution and Calibration

The lead glass energy resolution is of order 25% (FWHM) for electrons. The ability to separate pions from electrons is seen in Fig. 58 , which shows the pulse height distributions for 750 MeV/c electrons and pions in two layers of 10 cm x 10 cm x 25 cm lead glass placed in the focal plane of the OHIPS spectrometer at Bates. The particle separation is substantially better for 20 cm of lead glass than for 10 cm. The lead glass blocks available for BLAST at Bates are 15 cm x 15 cm x 30 cm and should be good for pion-electron separation. The pion signal is produced by charge exchange and other photon-producing

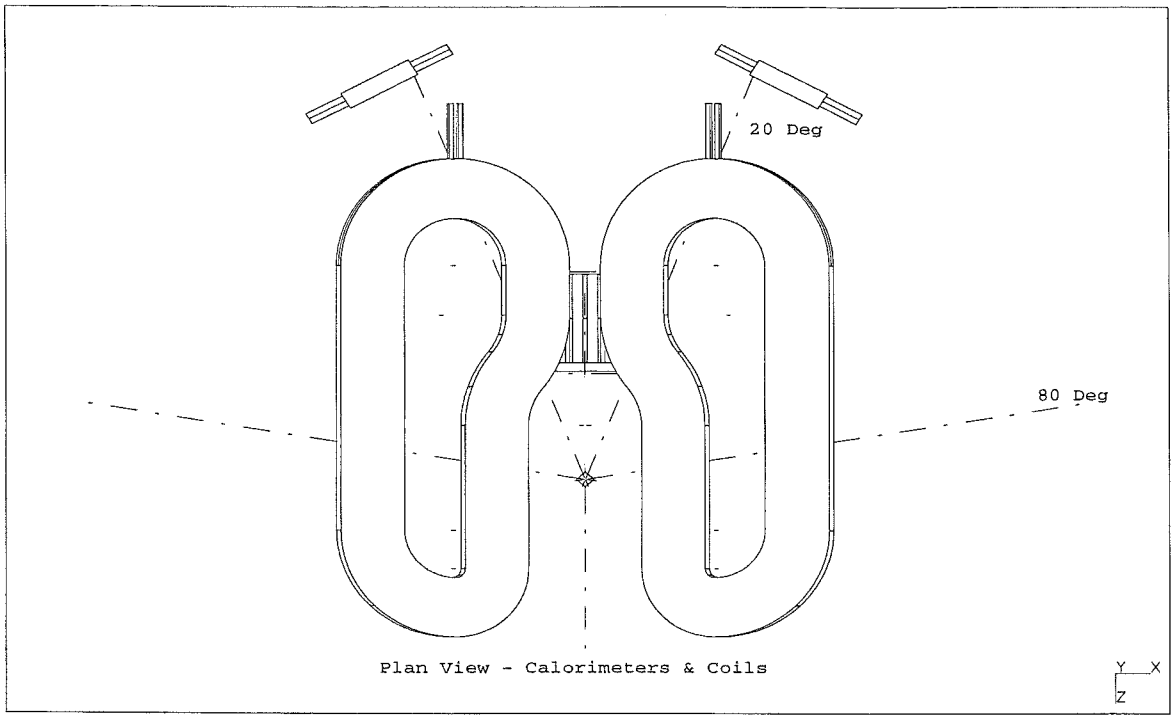

Figure 57: *Plan view of the lead glass calorimeters. The θ angular coverage from the center of the target is 18° to 27°. See Fig. 40 for the coordinate system.*

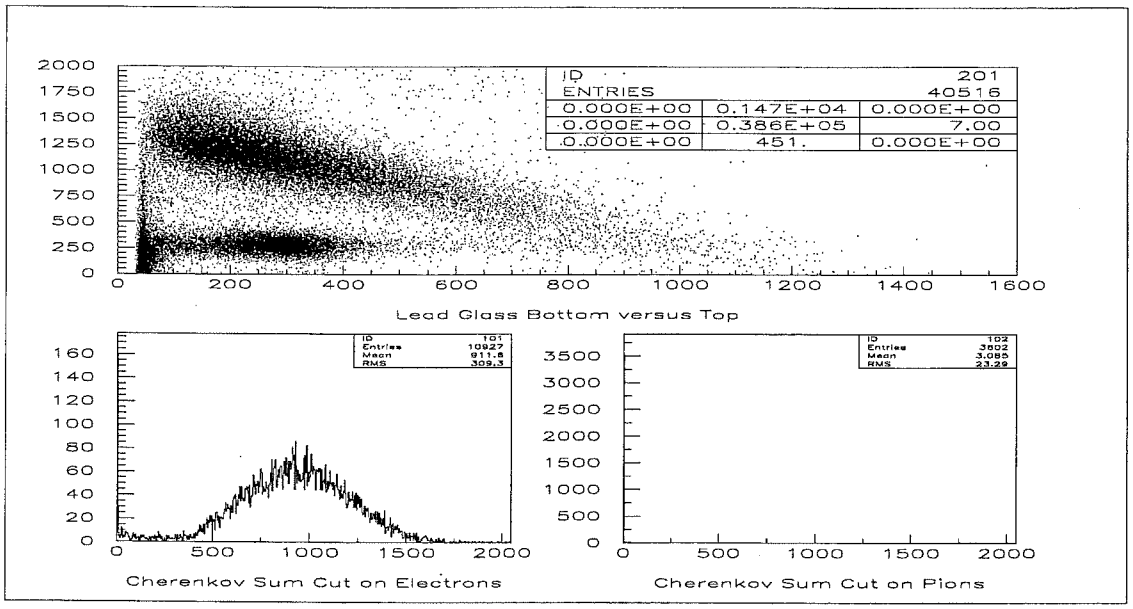

Figure 58: *Pion/electron discrimination results for the OHIPS lead glass detector. The two bands on the upper panel are electrons (top) and pions (bottom), respectively. The lower two panels show the signals from a gas Čerenkov detector with cuts on the electron band (left panel) and on the pion band (right panel).*

reactions. Some of the production will also occur in the thick (10-20 cm) neutron detectors, but the contribution will not exceed that from the lead glass itself. The electron resolution will be better for the blocks pointed toward the target than with their long dimension presented to the target. The resolution in the latter case is adequate to do the pion-electron separation, but one might want to use the better angular, energy, and timing resolution of the former geometry at the expense of losing half of the solid angle.

The lead glass blocks will be calibrated in the reduced electron beam in the 14° Extension at Bates and the response measured at 400 MeV. The response is immediately cross calibrated with the cosmic ray response which can be referred to at any time when the lead glass is used on BLAST. Fortunately, the proposed uses of the lead glass calls for the blocks to be in the horizontal plane where the cosmic ray peak will be unchanged. Radioactive flashers and LEDs or fiber optic flashers are also useful for calibration and linearity checks.

6.8.3 Magnetic Field Effects

The fringing magnetic field effect on the PMTs should be manageable. Outside the Čerenkov and neutron detectors the fields are only a few Gauss. For the lead glass detectors at 90° close to the coils the field is of order 100 Gauss. The field is perpendicular to the axis of the PMTs so magnetic shielding with μ-metal cylinders and wrapping is possible. The Bates blocks are already provided with this type of shielding. In addition, it is possible to box in an array with 1/8" iron sheet, with an insignificant loss in energy resolution.

6.8.4 Packaging and Support

Fig. 59 shows the planned stacking of a standard 16 block array used to separate pions from electrons. The package is designed so that it can be placed as close as possible to the neutron detectors. It is tall enough to both overlap the shadow of the magnet coils and get well into the region where the PID system should be close to 100% efficient. Because the array will need to be moved around as a unit from place to place, provision is made to restrain the blocks against a tip angle of 10°, which might occur in handling. Provision will be made to support a 1/2" scintillator over the front of the lead glass array in case it is needed for improved spatial resolution or to reject photons and neutrons.

In their position outside all other BLAST detectors, the support framework for the lead glass should be fairly simple to design. The weight of 64 blocks is about 2.5 tons. Most of this weight can be taken by posts to the floor rather than by the BLAST framework. In this case, the lead glass will have to be removed when the two halves of BLAST are rolled away from the target. However, such moves will not occur very often and it is likely that the neutron detectors will also need to be supported in the same way and removed

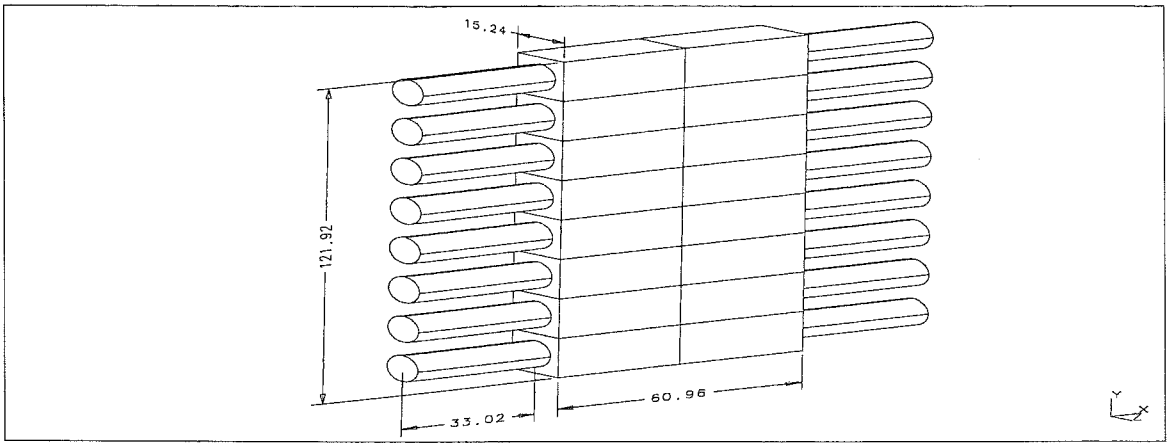

Figure 59: *An array of 16 lead glass blocks.*

on such occasions. The base and the package will be bolted to the BLAST framework to give stability in the horizontal plane.

6.8.5 Work to Date

There are 28 unused lead glass blocks at Bates and 14 available from Boston University. Work is underway at both places to optimize the resolution of the lead glass. Many of these blocks are provided with radioactive scintillators for calibration purposes. Additional lead glass can be obtained, but we have enough on hand now for two 16 block arrays.

Work on the calorimeter has been underway part-time since September 1996. Fourteen lead glass blocks at Bates have been tested. Resolution with the NaI flasher for one of the blocks with a EMI 9870 PMT was improved from 14% to 3.5%. The average time to refurbish and test a block is about 4 hours, so about six weeks of technician or student time is required to get 64 blocks ready for use. One 16 block package will be ready for use in the South Hall when the internal target is ready for testing in the ring, presumably in the winter of 1997-98. Before that time, a few blocks can be used on a detector testing frame looking at the B-line target while running with the extracted high-duty-factor beam. A test in April 1977 indicated that room background will not be high.

6.8.6 Costs and Personnel

The budget for the calorimeter is $ 125,000 in actual year dollars. This value assumes very little cost for the lead glass, light guides, PMTs, phototube bases and magnetic shields. Most of these items are on hand or are inexpensive. The cost per channel for electronics is

about $ 2000. We plan to fan in blocks in pairs as needed, losing resolution in either the θ or ϕ direction. We hope eventually to supply 64 channels of electronics for the blocks, plus any channels needed for scintillators belonging to the lead glass system.

The 32 lead glass blocks will be prepared and assembled into packages during the period 9/1/97–9/1/98 using E. Booth (6 months FTE), 6 weeks of technician time, an undergraduate assistant (4 months FTE), and a week of engineering/drafting.

6.9 RECOIL DETECTORS

Detection of heavy nuclear reaction products offers a simple method to improve the performance of the BLAST detector. In particular, the two-body electrodisintegration of ^{3}He can be cleanly identified by detection of the low-energy deuteron recoiling at a known momentum. Detection of recoiling nuclei cleanly isolates pion production from the background at threshold, while detection of the recoiling ^{3}He nucleus in elastic scattering results in a simple, effective polarimeter. These techniques were demonstrated in the CE25 experiment at IUCF, in which 300 and 500 micron thick, totally depleted silicon strip detectors were mounted only 3-cm from the beam axis [90]. Even in the higher backgrounds of an electron storage ring, pioneering measurements at NIKHEF show that measurements of low-energy reaction products from an internal target are feasible in an electron storage ring [110].

Detection of heavily-ionizing ^{3}He nuclei should be straightforward, given the excellent energy resolution of silicon detectors and the kinematic correlation between the electron momentum and ^{3}He kinetic energy. A 500 micron thick silicon detector would stop ^{3}He nuclei with kinetic energies up to 28 MeV, furnishing a simple method of monitoring the target polarization.

The recoil detector system must also separate the two-body and three-body electrodisintegration of ^{3}He by isolating the deuteron from the two-body disintegration. Measurement of the deuteron position and energy loss should be sufficient, however, since the momentum of the outgoing deuteron and the event vertex are known from measurements of the momentum of both the outgoing electron and struck proton. Modern detectors, either silicon microstrips or microfabricated gas counters, can easily furnish position measurements of several hundred microns.

For the initial physics program we plan to build a simple system very similar to that presently being used in the AmPS ring at NIKHEF. The costs of duplicating this system are summarized, in actual year dollars, in Table 15 . A uniform 20% contingency has been added to estimate the total cost.

The design, construction, and testing of the recoil detectors will be done by University of Louisville personnel. For these tasks Louisville will make available 1.0 FTEY over three years.

Table 15: *Cost estimates for the BLAST recoil detectors in actual year dollars including a 20% contingency.*

Sub–system	Cost (k$)
Read-out Electronics	60.0
Detectors	39.0
Total	99.0

6.10 BLAST TRIGGER DESIGN

6.10.1 Overview

The trigger-level logic configuration for BLAST has been designed around a two-level system. The first level will consist of coincidences between various scintillators and Čerenkov detectors to determine that (a) there has been an event and (b) whether the particle is an electron or a hadron. The second level trigger will consist of a fast coincidence between ORed subsets of various wire chamber planes and individual scintillators to test if that event coarsely tracks from the target.

The logic configuration for both levels of the BLAST trigger has been designed assuming that, while the data acquisition will be done via FASTBUS for the sake of speed, the trigger logic can be done via an ECL system based in CAMAC and/or VXI. The advantages provided by such a logic system are (1) compactness, (2) full programmability of the logic configuration providing maximum flexibility, and (3) immediate availability of the appropriate modules. Because the logic-system configuration output need not be read for each event, there is no loss of data acquisition speed by going to such a hybrid system.

The BLAST trigger design is further driven by three existing conditions and/or goals: (1) BLAST is based on the design and operation of the CLAS instrument at TJNAF; (2) CLAS, and its trigger system, exists and is operational; (3) Bates has decided to use the TJNAF data acquisition software package CODA as the standard for the laboratory. At the very least, the third goal dictates that all gates and common starts/stops be generated by the TJNAF Trigger Supervisor (TS), a VXIbus unit that enables the ADCs and TDCs and interacts with CODA. In fact CODA was designed to work through the Trigger Supervisor or a unit which identically mimics it, and the TJNAF DAQ group supports both CODA and upgrades in the TS system.

Hence, the simplest solution for the BLAST trigger is to purchase a TS module from TJNAF and build a trigger system around it. Because that module requires a VXIbus, and the CLAS logic is also VXI-based, the simplest solution for the trigger logic is to

purchase as much of it as possible from TJNAF as well. Options based on commercial modules are also considered.

6.10.2 The First-Level Trigger

The first-level trigger is fully programmable by the user on an experiment by experiment basis. It can vary from the loosest possible, where an event is defined by any electron (or hadron) in singles mode, to more restrictive programmable combinations of electrons in coincidence with any combination of hadrons, where a hadron is defined as any non-electron-generated event in a scintillator. An electron is defined by a scintillator signal in coincidence with a physically adjacent Čerenkov. For the purpose of this document, we assume a trigger model where an event consists of an electron in coincidence with any hadron. Because essentially all inelastically scattered electrons result in the emission of at least one hadron, the only events lost, within the geometrical acceptance, by this trigger definition are those in which all emitted hadrons are neutral (and there will be some lower but non-zero efficiency for these).

BLAST is an eight-sector toroid with two opposing sectors instrumented from 20° to 80°. Each sector will consist of 3 Čerenkovs and 14 scintillators, with the scintillators located behind the Čerenkov counters. The forward Čerenkov detector can be in coincidence with one of the first 4 scintillators. The next two Čerenkov detectors can be in coincidence with one each of the next two groups of five scintillators each. In addition, each of the two instrumented sectors is backed up by eight neutron scintillator bars with a PMT at each end. Finally, a movable shower counter to eventually consist of 64 lead-glass bars can be moved behind one sector or the other. Instrumentation of the remainder of the two sectors, or any of the other six sectors, can be achieved through a simple extension of the trigger logic to be outlined below.

The first-level trigger is required to take the raw PMT signals from the scintillators, Čerenkov detectors, neutron detectors, and shower counters and determine, through acceptable logical combinations, whether they arise from a possible candidate event. Fig. 60 shows such a scheme based upon a combination of commercial ECL modules (CAMAC-based) and VXIbus TJNAF modules. The scintillators each have two PMTs, one on each end, noted as L(eft) and R(ight). The PMT signals are sent directly to ECL discriminators (LeCroy 3412) which have software-controllable thresholds set close to the noise level in order to provide good leading-edge timing. LeCroy 4418 delay fanouts (not shown) provide multiple ECL outputs (3 per input) and separately software-controllable delay for each input. Because of the low thresholds, a two-fold L/R coincidence is formed in ECL AND's (LeCroy 4516) to eliminate a possible high rate of noise events associated with either PMT. The output of the AND units signifies a real event in a particular scintillator (although not necessarily yet a good event). Likewise, the Čerenkov PMTs (14 each from the rear two detectors and 12 from the forward detector) are OR'ed in groups of signals to the trigger logic. This is done by an analog sum of the signals at each end of the respective Čerenkov into each of the ECL discriminators. The two ends of each Čerenkov will be a logical OR.

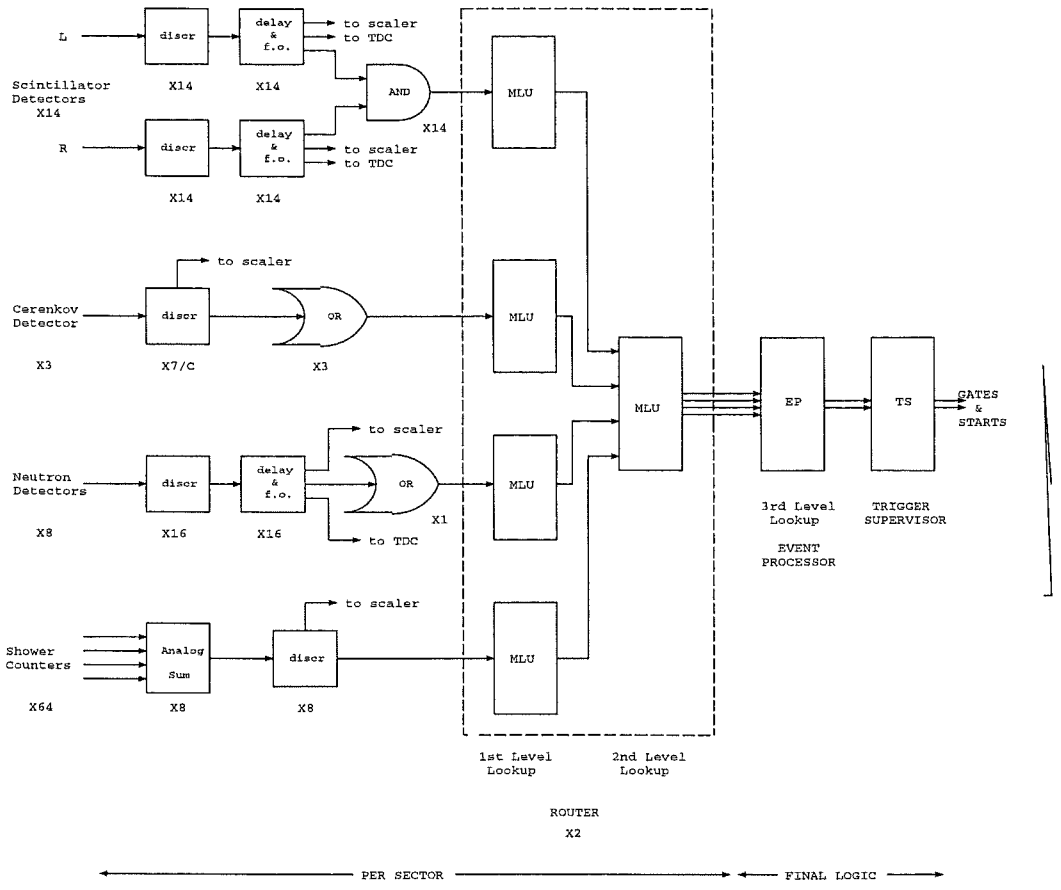

Figure 60: *Coincidence trigger logic.*

The 16 neutron detector outputs are shown going to an OR that provides one signal to the event logic. This will be decomposed into groups of signals based on azimuthal angle, or even individual signals.

The shower counters are shown grouped into an 8×8 array by providing an analog sum of 8 counters into each of 8 discriminators.

The ROUTER accepts the array of inputs and maps programmable logical combinations of those inputs [111]. It consists of two levels of programmable MLUs. The first level allows the experimenter to group adjacent detectors together, reducing the number of bits to be passed on to the second level. It consists of four parallel 16-input × 4-output MLUs. The second level lookup allows the experimenter to define sector events as combinations of the 4 bits from each of the first level MLUs in order to provide a fully programmable coincidence configuration between physically adjacent Čerenkov detectors and scintillators. A programmed OR of these coincidences, within the same MLU, provides an e-event signal for that sector. The MLU's will also select events in which scintillators fire but there is no coincident Čerenkov signal, and output these as h-events on a separate output. Outputs from the second level MLU's in each sector (as shown in Fig. 60) are passed on to a third-level MLU, the Event Processor (EP), housed in a separate VXI module, which forms logical combinations of the events from each of the two sectors so as to generate a final

trigger. The output is then passed to the TJNAF Trigger Supervisor which generates the ADC gates and TDC common starts (or stops) and interfaces to CODA.

Clearly, the advantage of using the MLU's is that they not only provide fully programmable logic, allowing them to be modified in software for particular experiments, but also that they provide multiple independent programmable outputs, allowing the experimenter to keep track of different particular logic combinations. For example, in this $e-h$ trigger configuration, we will wish to select events in the most forward Čerenkovs for later prescaling. With 16 totally independent logical combinations available, this task is easy to accomplish. The MLU's provide multiple independent outputs for different programmable logical combinations of e's and h's. In addition, the MLU's can be programmed to pass all e-events on a separate output. This option is particularly important for purposes of calibration and normalization. Other requirements, such as 'beam gate' (to avoid the ring injection flash) and 'run in progress' can also be applied as inputs to this unit. Any one or more of these combinations can then be prescaled. Such prescaling will certainly be done for the selected forward angle $e-h$ coincidences and/or all single e-events. Independent programmable prescaling for multiple triggers is available in the TJNAF TS module.

6.10.3 Costs and Personnel

The costs for the first level trigger system are summarized in Table 16.

Table 16: *Cost estimates for the BLAST Trigger system in actual year dollars including a 20% contingency.*

Sub–system	Cost (k$)
Router(s)	32.0
Trigger Supervisor	21.0
CAMAC	90.0
Cables	48.0
VME	21.0
Misc.	22.0
Total	234.0

The costs for the trigger supervisor and router were obtained in consultation with E. Jastrzembski and D. Doughty, respectively. The CAMAC, VME, and Cables costs come from the LeCroy Research Systems 1996 Catalog. The University of New Hampshire group will provide a total 2.0 FTEY over three years for the implementation and testing of the trigger electronics.

6.10.4 A Second-Level Trigger

A *second level* trigger has been designed which incorporates fast wire chamber logic outputs in order to coarsely determine that the event was initiated in the region of the target in order to eliminate background from external sources. As mentioned at the beginning, this trigger involves OR'ing the ECL outputs from a selected number of adjacent wires from each of the planes of wire chambers and determining if the pattern of such cells, in coincidence with the appropriate scintillator, is consistent with the event originating from the target.

Three methods of generating the OR of individual ECL signals have been considered. In one approach the wire chamber preamplifier-discriminator cards, to be purchased from either LeCroy or TJNAF (which is currently developing an in-house design), will provide, in addition to ECL signals for each wire, an ECL OR for some predetermined number, say 16, of adjacent wires. This design would then provide a logical division of, for example, a 96-wire layer into a 6-segment hodoscope. In the second method, the 96 LeCroy FASTBUS TDC's are factory modified to provide a rear panel logical OR of a predetermined number of adjacent inputs, 16, 32, 48, or 96, again allowing division of a layer into segments. If neither of these methods is available (we do not plan to make such modifications in-house), then the OR will be made by using the 64-input LeCroy 4564 modules, providing simultaneous rear panel availability of 4×16, 2×32, and 1×64 logical OR combinations. This last option is by far the most expensive, and we will proceed here under the assumption that either one of the first two options will be available.

The wire chambers consist of three groups of planes with 4 planes per group. The innermost plane is likely to be noisy due to Møller scattered electrons. Therefore, we propose to use the outermost plane of group 1 plus the vertical wire planes in groups 2 and 3 to do coarse track recognition. This plan minimizes accidentals. We propose to segment each of these planes into cells of 8-16 wires, by using 32-fold OR logic from either the wire preamp-discriminator cards or the FASTBUS TDC's. This feature provides up to 64 signals, in coincidence with the array of 14 scintillators, per sector, to determine whether or not the track is acceptable.

The ECL signals from the individual cells are input, together with the coincidence-gated scintillator ECL outputs and the "electron" output from the first coincidence array from the first level, into an additional TJNAF ROUTER module per sector which provides a logical "no" if the input pattern does not correspond to a track within acceptable limits. The output of these ROUTERs can then be OR'ed and put into the the FAST CLEAR of the ADC's and TDC's. This arrangement allows programming freedom to demand that either (1) the acceptable track correspond to detection of a "good" electron with no similar requirement for hadrons, so as to eliminate any detection efficiency for neutrons or π^0's which might interact with the scintillators, or (2) tracks be demanded for both, thereby limiting events to include charged hadrons only.

The cost of implementing this second level trigger is driven mainly by the method of obtaining the ECL OR signals from the wires. If the wire chamber cards provide the appropriate ORs, then the only requirement is an additional ROUTER and EP per sector for a total of about $32K.

6.11 DATA ACQUISITION SYSTEM

6.11.1 Introduction

BLAST is a departure from the traditional instrumentation at Bates in terms of its complexity and the data rates that are anticipated. It was clear from the outset that the traditional combination of a MicroVAX, MBD, and CAMAC would be inadequate. It was also unreasonable to expect that any simple modification of these traditional building blocks would suffice. We are therefore required to provide a totally new system.

There are several requirements that the data acquisition system must satisfy:

- FASTBUS for digitization and scalers
- VME and CAMAC for the programmable trigger
- A data rate of at least 200 kBytes/sec (kB/s) to tape
- Maximize the ratio of computer power to cost
- Minimize in-house support required.

Taking these items into consideration, we have chosen to use the TJNAF CODA system. The laboratory data acquisition systems for the conventional spectrometers will be converted to CODA from the LAMPF Q system over the next several years, as LAMPF is no longer upgrading Q to keep pace with new computing technology.

6.11.2 Data Acquisition System Hardware

Information from a given sector of BLAST will be digitized in two FASTBUS crates. Each crate will be read out by a Struck SFI over Ethernet into the host Sun UltraSparc workstation memory. The Sun will analyze events as well as archive them. The FASTBUS crates will be located near the detector while the host workstation will be located in the South Hall Counting Bay. Graphics workstations can access the event information in the host machine, for further analysis and event display.

Data rates of 250 kB/sec have been achieved already in Hall A at TJNAF, passing data over Ethernet. The system can be upgraded to handle higher event rates and software

rejection by passing the sector information to Motorola 68k preprocessors in VME. Hall C at TJNAF passes crate data over Ethernet to Motorola 68040's in VME, and from there to the host via FDDI; peak rates of 2 MB/sec have been observed. Data will be written to disk, and initially archived on 8mm tape from the Sun workstation. Another possibility for archiving is optical disks.

6.11.3 Data Throughput

In high energy physics experiments, the zeroth-level trigger rate (e.g. the beam crossing rate) can be 50,000 events/sec, at an event size of up to 10 kiloBytes (kB). These rates are accomplished with the use of large-scale parallelism in the FASTBUS front-end readout system and with fast front-end data rejection of roughly 10^{-3}. Additional levels of triggering, including software rejection, bring the event rate down to more like 1 to 10 Hz, for a data archiving rate of around 100kB/sec.

These rejection factors do not apply in the Nuclear Physics environment. A large fraction of the BLAST events which pass the first-level hardware trigger are useful data and should not be discarded. In BLAST, a track is expected to involve times from twelve wires, two pulse-heights and times from scintillator PMTs, two pulse-heights from a Čerenkov, a pulse-height and time from a lead-glass block, and two pulse-heights and times from a neutron detector. A typical event with three tracks, background signals, status information plus some contingency might have a size of about 0.5 kB.

The LeCroy TDC's and ADC's are all rated at 40 MB/sec. The SFI is capable of running at rates up to 3 MB/sec. The nominal fast Ethernet bandwidth is about 10 MB/sec; practical data rates are somewhat less, perhaps 5 MB/sec. A conservative limit for archiving from the host is currently about 200 to 300 kB/sec.

The CODA system is currently capable of running at 1 to 3 MB/sec to disk. For the typical BLAST 3-track event size of 0.5 kB, we thus have 2,000 to 6,000 events per second. Currently proposed experiments anticipate trigger rates of at most 500 events per second, with *no* forward angle electron prescaling; this trigger rate is well within the capabilities of the CODA system. In fact, experiments will likely prescale the forward angle electrons, and so data rates will be less than 250 kB/sec.

It is conceivable that one might run with a very loose hardware trigger for a given target and write all data to tape, and then sort the data off-line onto multiple tapes for various users, according to a more refined software trigger. This scheme would make better use of available beam time, and would mean that a user interested in an exclusive trigger would not have to analyze all events (at a significant cost in CPU time), but only the ones of interest. This capability has not been costed here; to provide trigger-sorted data tapes, the laboratory would need at least a dedicated workstation connected to multiple "tape" drives (4, at a minimum). This estimate assumes that only a very coarse analysis pass will be necessary to make a trigger determination, and so the trigger sorting will not fall

behind the data acquisition. If detailed track information is needed, for example to cut on particle momenta, missing mass, or other calculated quantities, then trigger-sorting CPU power will have to increase accordingly.

6.11.4 Costs and Personnel

The anticipated hardware and commercial software costs for data acquisition, for the core device, are summarized in Table 17.

Table 17: *Cost estimates for the BLAST DAQ system in actual year dollars including a 20% contingency.*

Sub–system	Cost (k$)
Host computer	18.0
Graphics WS (Single Event Display)	56.0
FASTBUS Crates	42.0
SFI	29.0
FASTBUS Crate Spy	16.0
FASTBUS Calibration Module	4.0
Racks	14.0
Dedicated LAN	6.0
Cables, misc	18.0
VME Crates	20.0
CAMAC Interface	5.0
VME CPUs	90.0
VME Network Card	13.0
Total	331.0

The host computer was purchased as part of a generic internal target development, so only the peripherals (tape drives, for example) are costed here. A FASTBUS crate, SFI and CAMAC interface were also purchased for internal target development. Those devices are spares for BLAST; other spares are included above.

The Bates laboratory will provide 3.0 FTEY over three years for the implementation of the system software. This manpower will be complemented by collaboration personnel working on the data analysis software. The manpower for data analysis is closely associated with that working on the Monte Carlo Simulation of BLAST and will be discussed in Sec. 7.

7 MONTE CARLO SIMULATION of BLAST

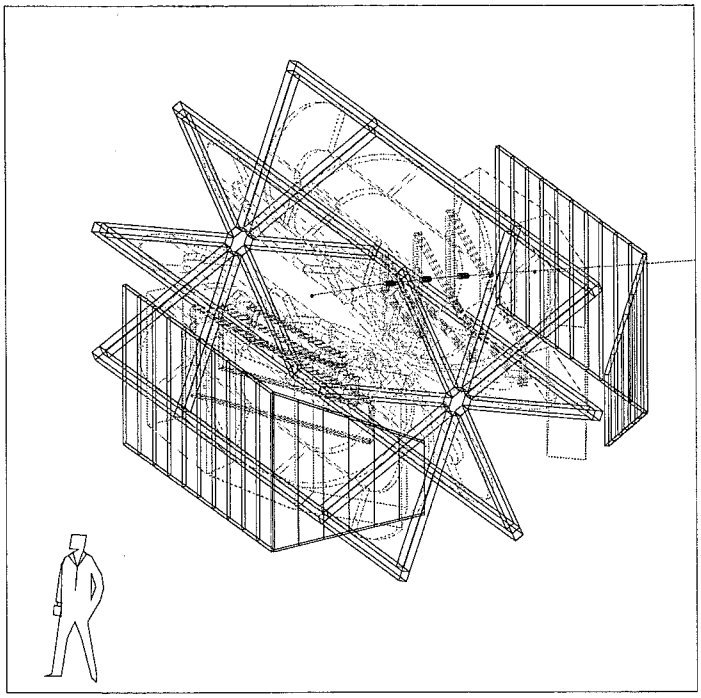

The design of any detector that will study physics as complex as that which BLAST will investigate, must first be modeled with a sophisticated Monte Carlo simulation. The simulation of BLAST is built out of the GEANT libraries from CERN.

The primary goal of the Monte Carlo studies at this stage is to assist in the design of the detector packages. We have been able to address questions primarily related to acceptance and resolution as a function of the geometry and choice of materials. We will also be simulating data such that reconstruction and analysis algorithm can be built and tested while BLAST is being built.

Towards this end we have divided our Monte Carlo effort into several different points.

- **Code Management:** Because the GEANT code will be developed by various members of the BLAST collaboration at many different universities, on multiple computing platform we have instituted a code repository and are using the code management system **CVS** (Concurrent Version System).
- **Magnet Field Tables:** The original code could simulate a single track event in roughly 20 seconds on a DEC-alpha. Most of this time was spent calculating the field the particle traversed. We have replaced these calculations with a lookup table and a second-order interpolation between table points, providing a factor of 700 improvement in speed.

- **Flexible Geometry:** We have built the GEANT geometry around a few parameters that the code reads in from an external file. This approach allows a detector designer to alter such things as dimensions, angles, position and number of components quickly and easily without recoding and recompiling.

- **Acceptance Studies:** We can currently calculate the acceptance of BLAST as a function of particle type, 3-momentum vector, and target position.

- **Resolution Studies:** A critical issue about the design of BLAST is the overall resolution of the detector. Resolution in itself is not a simple quantity. It is somewhat a function of angle, and is a very sensitive function of momentum. It is also a function of a number of factors in the design, such as the air between the wire chambers or the gaps between the wire chambers.

- **Simulation of Spin Physics Experiments:** We have written event generators that calculate the BLAST resolutions for the missing-energy E_m and the missing-momentum p_m. Work is under way to implement a fully spin-dependent electron-proton cross section and a spin-dependent spectral function in order to estimate physical asymmetries.

- **Magnetic Field Information for Targets and PMTs:** We have produced field maps for BLAST. This information is important for the design of the targets and the PMTs in time-of-flight, Čerenkovs, neutron counters and shower counters. Although the details of the field around these components might be best calculated by TOSCA, the GEANT code works well as a cross check, and to provide some large scale field maps.

- **Target-Generated Background due to Møller Electrons:** We have written event generators to simulate the production of low–energy electrons from the ^{3}He target.

The BLAST GEANT development is a dynamic process. After the initial stage of detector design studies it will be continued to be used in the design of experiments. It will also be utilized for building the analysis code. We will be using GEANT to simulate data that will then be used to test the reconstruction/analysis code.

7.1 The ACCEPTANCE of BLAST

We have calculated the acceptance of BLAST for a range of momenta and charges, i.e., electrons (or any negatively-charged in-bending particle) and protons (positive out benders). A hit in all three wire chambers defines an accepted event. Scatter plots of accepted events are shown in Fig. 61. The solid angle related to each plot of Fig. 61 is reported in Table 18. These results are smaller than the designed value of 0.76 sr quoted in Sec. 6. Most of this difference is due to the use in the GEANT code of a 3" frame around the

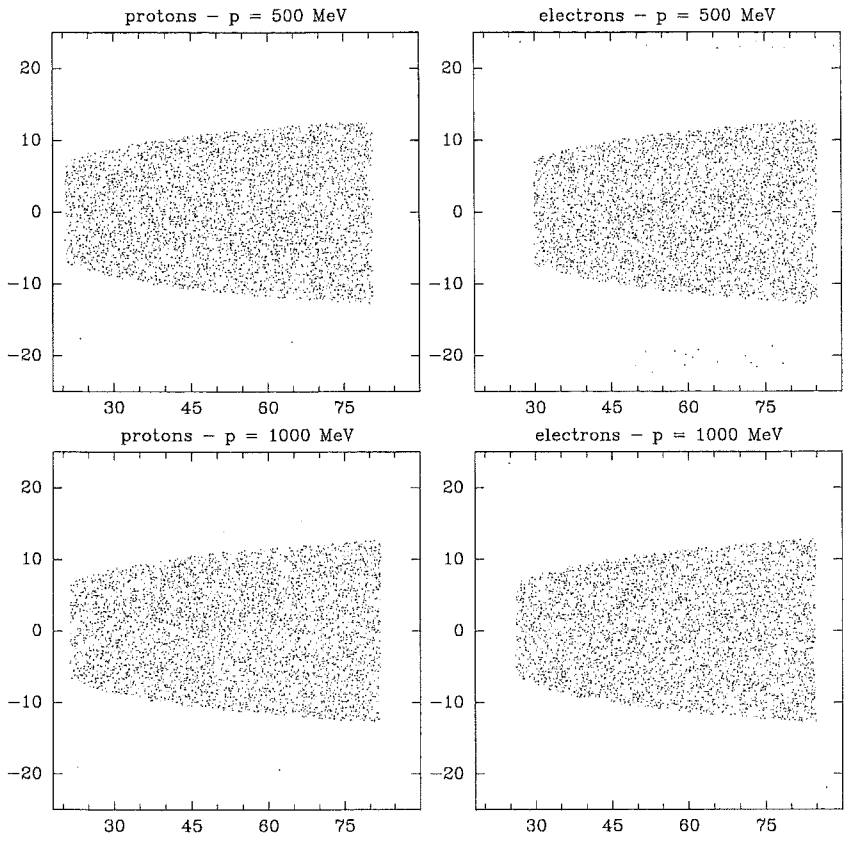

Figure 61: *Acceptance for high and low momentum electrons and protons. An accepted event generates at less one hit in all three wire chambers. The horizontal and vertical axes correspond to the scattering angle θ in (°) and the azimuthal angle ϕ in (°), respectively.*

Table 18: *Solid angle per sector calculated from the acceptances of Fig. 61.*

particle	mom. (MeV)	Solid Angle (sr.)
electron	500	0.303
electron	1000	0.313
proton	500	0.306
proton	1000	0.307

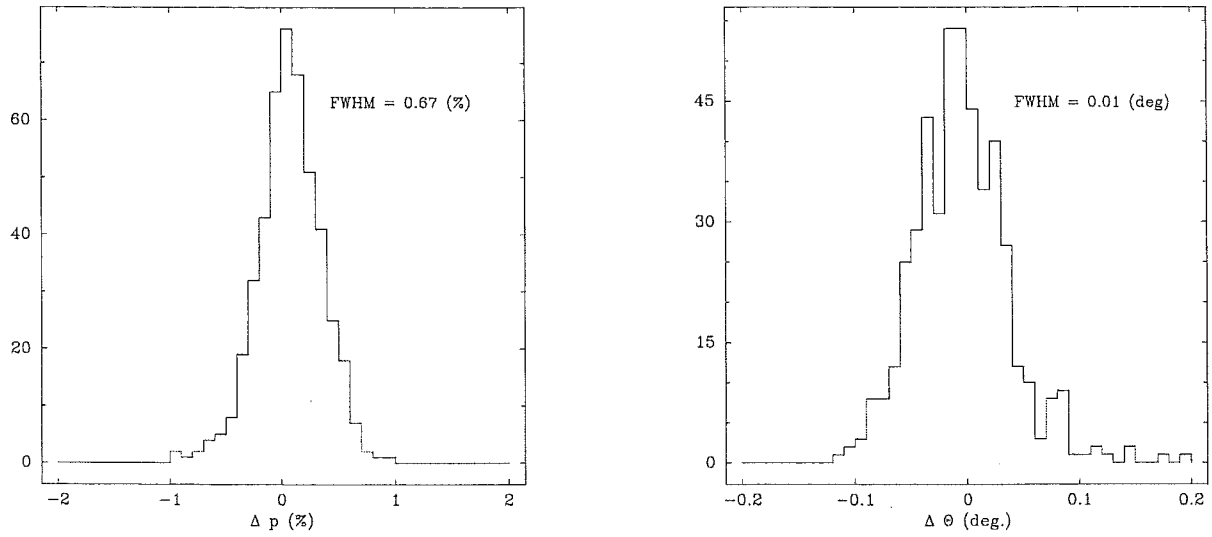

Figure 62: *The distribution of the deviation between original event parameters and reconstructed event parameters. The trial shown contains only 500 events. This trial was with electrons with p=1000 MeV, $\theta = 20^o$.*

innermost wire chamber. Recent mechanical engineering studies of this wire chamber indicate that a 2" frame is acceptable. The design presented in Sec. 6 assumes a 2" frame for this chamber, which will increase the solid angle to 0.38 sr per sector.

7.2 BLAST PERFORMANCE

After an event is generated with GEANT, we know where its track crosses each wire plane. This position information can then be converted into wire number, ADC and TDC information. We then randomly 'smear' the timing information by the intrinsic resolution of the wire chambers, 175 μm for the inner chamber and 250 μm for the outer chamber. We then generate new tracks and calculate the χ^2 deviation between the original 'smeared' wire chamber hits, and the new track. By varying the event parameters (p, θ, ϕ) and repeatedly calculating new tracks until we have minimized the χ^2 deviation, we can obtain the best fit track parameters. This fitting technique is a standard method of analyzing events in a detector built around a non-homogeneous magnetic field.

To study the resolution at a certain set of kinematics or with a particular geometry or material, we generate thousands of events, and then reconstruct or fit them. The statistical distribution (see Fig. 62) of the difference between the original track and the reconstructed track is the resolution of that configuration.

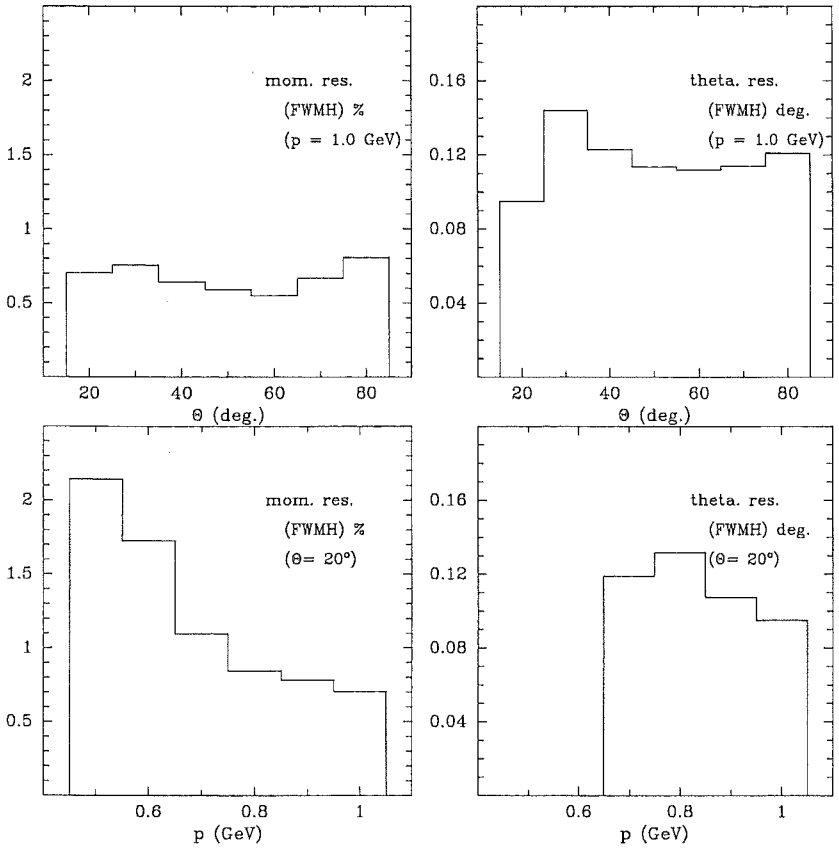

Figure 63: *The results of resolution studies with respect to p and θ reconstruction for a range of event parameters.*

7.2.1 Resolution as a Function of p and θ

We have studied the resolution of BLAST as a function of the initial p and θ of the track. A summation of the most significant results are presented in Fig. 63.

These results can be understood in terms of a few factors.

- Multiple scattering dominates the resolution at low momentum.
- Tracks at forward angles pass through a strong magnetic field, and so are deflected more, which increases sensitivity.

- Tracks at backward angles have better position resolution because the track is more perpendicular to the chamber.

These last two effects tend to cancel each other, but can also be seen as the 'horns' in the angular dependence curves at 30^o and 80^o.

7.2.2 Contributions to Resolution

We can study the contribution to the uncertainty from various effects by "turning-off" those effects. Table 19 lists a resolution study for 1000-MeV electrons at 30^o. We have turned off the multiple scattering, and have also alternatively set the intrinsic position resolution of the wire chamber to zero.

Table 19: *Contributions to the momentum and angular resolution.*

	Δp (%) (FWHM)	$\Delta\theta$ (deg.)(FWHM)
normal	0.70	0.12
no mult.	0.28	0.06
wire res.$\rightarrow$ 0	0.69	0.11

Clearly the greatest contribution to the resolution of BLAST is from multiple scattering. The effect may be reduced by the use of helium between the target and wire chambers. However, the improvement will likely be less than shown here by the time target windows, chamber foils, etc. are fully incorporated into the simulation.

7.2.3 Effects of Geometry

We have studied the effect of the physical arrangement of the wire chambers in BLAST by calculating the resolution, and then varying the geometry. As a simple demonstration, the wire chambers are expected to be 50 cm apart. We have let the first chamber be fixed and then moved the other two chambers such that the gap is 25, 50, 75 and 100 cm, and then calculated resolutions for each geometry. The results are summarized in Table 20. So a smaller gap gives more accurate information on the angle, but is less sensitive to the bending in the field and so is less sensitive to the momentum.

7.2.4 Effects of Occupancy

It is also important to know how well we can reconstruct the tracks if we are missing the information from one or more layers in the chamber. The numbers cited below (see Ta-

Table 20: *Resolutions in p and θ as a function of the distance between wire chambers.*

	Δp (%) (FWHM)	$\Delta\theta$ (deg.)(FWHM)
25 cm	0.72	0.10
50 cm	0.70	0.12
75 cm	0.78	0.14
100 cm	0.82	0.16

ble 21) reflect the effects of having only one measurement of position in each wire chamber, and so the results are comparable to the effect of the intrinsic wire chamber resolution.

Table 21: *Occupancy effects on the p and θ resolutions.*

chamber	no. missing	Δp (%) (FWHM)	$\Delta\theta$ (deg.)(FWHM)
-	0	0.70	0.12
1	1	0.77	0.16
2	1	0.71	0.13
3	1	0.75	0.12
1+2	2	0.78	0.17

One important point to realize is that these numbers do not reflect lost tracks or the track finding efficiency. If a layer of a wire chamber is missing and there are a great many background events or false signals, the reconstruction may completely mis-identify a track. This problem is very complex and is beyond the scope of the present GEANT effort.

7.3 RESOLUTIONS for E_m and p_m

The above momentum and angular resolutions of BLAST are sufficient for the measurement of $(e, e'p)$ asymmetries in the quasi-elastic scattering region [70]. The missing-energy resolution, averaged over the whole acceptance, amounts to ΔE_m =12 MeV (FWHM), while the average FWHM missing-momentum resolution amounts to Δp_m =20 MeV/c. The latter does not change when the momenta are restricted to parallel kinematics. For the $(e, e'n)$ asymmetries we expect similar resolutions in E_m and p_m due to the good θ-resolution of the horizontal neutron bars.

7.4 BACKGROUND due to Møller ELECTRONS

The design luminosity of the BLAST is 3×10^{33} electron-nucleons/cm^2/s. We have investigated whether the design luminosity is limited by target-related background for the ^{3}He internal target. With no contributions from windows, we found that [112] the major source of target-generated background is Møller scattering from the atomic electrons of the target.

In BLAST, the toroidal field itself is used to sweep away the Møller electrons. To shield the sensitive wire chambers from low-energy Møller electrons, it is estimated that a value of approximately 0.05 Tesla-m for $\int B_\phi \cdot dl$ over the particle trajectory is required in the region between the target and the first set of wire chambers. To optimize the design and to justify the design luminosity, the background due to Møller electrons in the wire chambers has been studied in detail. We have found that [112] most of the target–generated background was caused by Møller electrons concentrated in the very forward region, i.e., $\theta \leq 20°$. As the drift chambers cover angles backward of 20°, the BLAST detector should not be limited by target–generated background at the designed luminosity of 3×10^{33} electron-nucleons/cm^2/s.

7.5 DATA ANALYSIS PERSONNEL

The development of the data analysis software is done in conjunction with the Monte Carlo simulations of BLAST. The personnel resources for these tasks will come from most of the institutions in the collaboration. The group presently working on GEANT simulations consists of physicists from ASU, MIT, and UNH. A total of 13.0 FTEY over three years have been identified from these groups. The ASU group will provide 3.0 FTEY, the MIT Medium Energy Group 7.0 FTEY, and UNH 2.0 FTEY. We expect additional contributions from other collaboration institutions.

8 COSTS AND SCHEDULE

8.1 COSTS SUMMARY

In Section 6 the costs for the BLAST subsystems were estimated based on quotations from industry and estimates provided by the institutions responsible for building the different detector components. A uniform contingency of 20% was applied to all the cost estimates. Table 22 summarizes the costs of the different detector elements as previously discussed.

Table 22: *Costs of BLAST detector elements in actual year dollars including a 20% contingency.*

BLAST Subsystem	Cost (k $)
Magnetic Coils	1329.0
Drift Chambers	1087.0
Čerenkov	608.0
Scintillators	466.0
Neutron Detectors	371.0
Forward Calorimeter	125.0
Recoil Detectors	99.0
Trigger Electronics	234.0
Data Acquisition	331.0
TOTAL COST	**4,650.0**

In Section 6 various cost tables contain a breakdown of the above total costs for each subsystem.

The schedule depends on the construction and implementation time and on the funding allocations. Responsibility for the construction of each of the BLAST systems lies with the different institutions and the work can proceed largely in parallel. We have produced a schedule to build BLAST from the time and manpower estimates done by each institution.

8.2 PROPOSED SCHEDULE

We have arrived at a schedule assuming that: (*i*) the construction of the magnetic coils and its support structure starts in FY97; (*ii*) we can start and finish construction in FY98 of one single component of each major detector subsystem , i.e., the first drift chamber, the first Čerenkov unit, the first scintillator panel, and four neutron bars; (*iii*) in FY98 the construction of the forward calorimeter is carried out as well as the first recoil detectors

to monitor elastic scattering; and (*iv*) we acquire, starting in FY97 and through FY98, enough detector and trigger electronics and DAQ components to test and conduct first measurements in the SHR.

This approach allows us to have an early diagnostic of the BLAST performance. The construction of the rest of the detector systems is carried out during FY99 and FY00. Table 23 shows, for the proposed schedule, the funding profile required for each of the

Table 23: *BLAST funding profiles in actual year dollars for the proposed schedule. It includes a uniform 20% contingency.*

PROJECT SUBSYSTEM	FY97	FY98	FY99	FY00
Magnetic Coils	263	656	345	65
Drift Chambers		428	226	433
Čerenkov		80	211	317
Scintillators		60	367	39
Neutron Detectors		73	130	168
Forward Calorimeter		50	75	
Recoil Detectors			48	51
Data Acquisition/Trigger	129	187	69	180
TOTAL	392	1,534	1,471	1,253

detector subsystems in actual year dollars, including the 20% contingency. Under this schedule BLAST is finished at the end of FY00. Fig. 64 shows a Gantt chart summarizing the timelines for the different sub-systems. Allocation of the $ 400k for FY97 funds has already occurred. DOE has projected that the more likely funding allocation for BLAST beyond FY97 is at the rate of $ 900k per year until the device is fully constructed. The realization of the proposed schedule will depend on securing funding additional to that indicated by the DOE thus far.

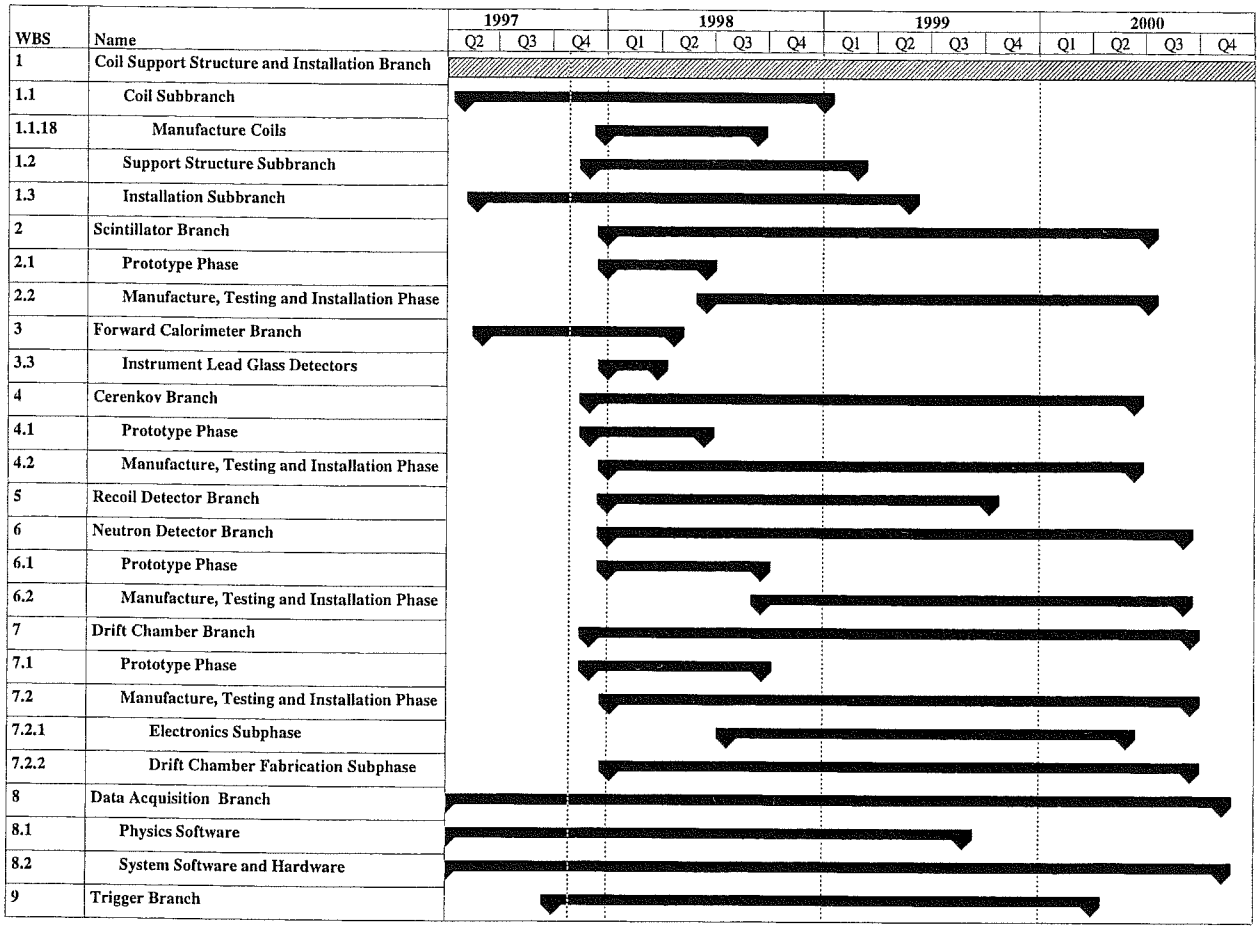

Figure 64: *BLAST proposed schedule. The times are in fiscal years.*

9 MANPOWER and ORGANIZATION

9.1 PERSONNEL and RESPONSIBILITIES

Personnel available to build the beam polarimeter, the polarized targets, the different BLAST subsystems, and the data analysis systems were estimated in FTEY over three years in Sections 4, 5, 6, and 7, respectively. Table 24 summarizes this manpower for each responsible institution along with the corresponding responsibilities.

Table 24: *Physicist manpower per institution for the various BLAST subsystems in full time equivalent years (FTEY) over three years. The FTEY numbers include contributions from faculty members, research scientists, post-doctoral associates, and students.*

INSTITUTION	RESPONSIBILITIES	FTEY
Arizona State	Čerenkov	5.0
	Data Analysis	3.0
Bates	Coils/Structure/Installation	10.0
	Data Acquisition	3.0
	Project Management	3.0
Boston U.	Lead Glass Calorimeter	1.0
Louisville	Recoil Detectors	1.0
MIT	Drift Chambers	15.0
	Polarized Targets	7.0
	Data Analysis	7.0
	Beam Polarimeter	7.0
New Hampshire	Scintillators	1.0
	Trigger Electronics	2.0
	Data Analysis	2.0
Ohio U.	Neutron Detectors	2.0
Virginia	Beam Polarimeter	2.0
Vrije U./NIKHEF	Polarized Targets	3.0
Wisconsin	Polarized Targets	1.5

A total number of 75.5 FTEY results from Table 24. This manpower is the total uncosted manpower that is now available to carry out the project. We obtain 52.0 FTEY from Table 24 when the numbers for beam, targets, and project management are subtracted. This manpower compares well with the uncosted 45.1 FTEY needed according to the project model used in Sec. 8 for estimating the costs and the schedule.

The impact of BLAST on the institutions listed in Table 24 is explained below.

- *Arizona State University*: The ASU group consists of two faculty (Ricardo Alarcon and Joseph Comfort), one Bates-based postdoc, and five graduate students. Funding comes from the NSF. From this manpower we are committed to generate a total of 5.0 FTEY (over the three fiscal years) to design, build, and deliver the Čerenkov detectors. In addition, 3.0 FTEY will be used to develop the data analysis software.

- *Bates Linear Accelerator Center*: Bates has assumed responsibility for the project management, final engineering and procurement of the magnet coils and support frame, the installation of the CODA system for data acquisition, and the installation of BLAST. From existing personnel a total of 16 FTEY have been identified to carry out these tasks.

- *Boston University*: The BU group (Ed Booth) has the necessary manpower to build and deliver the lead glass calorimeter.

- *University of Louisville*: The Louisville group (Karl Pitts) will supply 1.0 FTEY over the three fiscal years to design and construct the initial recoil detection system.

- *Massachusetts Institute of Technology*: BLAST is the major research focus for the MIT Medium Energy Physics Group for the next several years. In particular, Richard Milner, June Matthews, and Robert Redwine expect BLAST to be the center of their efforts and those of the younger people working with them for the construction period and for the first few years of data-taking. Haiyan Gao will join the MIT faculty this fall and she will be active in the BLAST project. William Turchinetz, a Senior Research Scientist, has been heavily involved in BLAST and will be in the future. We also expect important contributions from Aron Bernstein and Claude Williamson. The MIT Medium Energy Group has assumed responsibility for the design and construction of the BLAST drift chambers. Further, the group will be involved in the design and construction of the polarized targets, the implementation of beam polarimetry and software development. The BLAST manpower contribution by the Medium Energy Group will be 36 FTEY and will be provided with existing and anticipated resources, assuming constant level of effort.

- *University of New Hampshire*: The UNH participation in BLAST includes two faculty (John Calarco and Bill Hersman), three postdoctoral scientists, and graduate students. Continued staffing at the present level allows a commitment of 5.0 FTEY over two years to assume responsibility for the BLAST scintillation detectors, trigger electronics and participation in the data analysis software. This commitment includes design, procurement, and oversight. A separately costed technician will perform the assembly and testing.

- *Ohio University*: The Ohio U (OU) group (Jack Rapaport) will assume responsibility for the neutron detectors. In particular OU will be involved in the specifications for scintillators and light guides, tube bases and its mechanical supports, and the

liaison with the structural engineer that will provide the mechanical support for the detectors. OU personnel will assemble and test the detectors.

- *University of Virginia*: Virginia (Blaine Norum) is committed to the construction of the electron beam polarimeter. A senior graduate student (Doug Higinbotham) is very familiar with the construction and operation of the NIKHEF polarimeter. A commitment of 2.0 FTEY of scientific manpower over three years is in place.

- *Vrije Universiteit/NIKHEF*: This group (Jo van den Brand) has taken responsibility for polarized targets and brings into BLAST valuable expertise and resources.

- *University of Wisconsin*: Wisconsin (Willy Haeberli) is one the world leaders in polarized gas targets. An involvement of 1.5 FETY of unique expertise is available for BLAST.

- *Yerevan Physics Institute*: This group is led by Kim Egian and will work on detector and software development. A contribution of up to 2.0 FTE per year is under discussion.

9.2 The BLAST COLLABORATION

The present collaboration membership is listed below. This list includes senior scientists, faculty members and postdoctoral associates.

R. Alarcon and J. Comfort
Department of Physics and Astronomy, Arizona State University, Tempe, AZ 85287

E. Booth
Department of Physics, Boston University, Boston, MA 02215

J. Lang
Eidgenössische Technische Hochschule-Zürich, Zürich, Switzerland

K. Pitts
Physics Department, University of Louisville, Louisville, KY 40292

A. Ahmidouch, A. Bernstein, F. Casagrande, M. Distler, G. Dodson, K. Dow, M. Farkhondeh, H. Gao, K. Jacobs, J. Kelsey, A. Mateos, J. Matthews, K. McIlhany, R. Milner, M. Pavan, R. Redwine, W. Schmitt, D. Tieger, C. Tschalär, W. Turchinetz, C. Williamson, E. Tsentalovich, B. Yang and T. Zwart
Department of Physics, Laboratory for Nuclear Science and Bates Linear Accelerator Center
Massachusetts Institute of Technology, Cambridge, MA 02139

J. Calarco, W. Hersman, M. Holtrop, M. Leuschner and T. Smith
Department of Physics, University of New Hampshire, Durham, NH 03824

R. W. Finlay, K. Hicks, A. K. Opper and J. Rapaport
Department of Physics and Astronomy, Ohio University, Athens, OH 45701

D. Higinbotham and B. Norum
Department of Physics, University of Virginia, Charlottesville, VA 22901

J.F.J. van den Brand, H.J. Bulten, M. Ferro-Luzzi and H.R. Poolman
Department of Physics and Astronomy, Vrije Universiteit and NIKHEF, Amsterdam, The Netherlands

J.F.J. van den Brand (on leave), W. Haeberli, P. A. Quin and T. Wise
Department of Physics, University of Wisconsin, Madison WI

R. Asaturian, G. Asrian, N. Dashian, K. Egian, G. Gavalian, S. Mailian, T. Mkrtchian, M. Ohanganian, Y. Sharabian and G. Yechian
Yerevan Physics Institute, Armenia

9.3 PROJECT ORGANIZATION

The BLAST Collaboration currently contains about 50 physicists from 12 different institutions. A Steering Committee was formed for the BLAST Project to represent the collaboration. This Steering Committee includes, as an *ex-officio* member, the BLAST Project Manager as appointed by the Laboratory Director. The committee is currently co-chaired by R. Alarcon (ASU) and R. Milner (MIT).

The BLAST Project is managed from MIT-Bates. A management information system has been set up for maintaining the baseline of the project. This baseline includes the target schedule, obligation and funding profiles, and personnel utilization profiles. Control and management of the system is the responsibility of the Project Manager.

In order to carry out these responsibilities effectively, a project management system has been installed and is operational. The system has the following capabilities:

- Identify critical paths and determine effects of early or late starts on project milestones.
- Provide cost and schedule data.
- Provide planned and actual work progress data.
- Properly relate cost, schedule and work progress.
- Summarize costs (planned and actual) by cost category, branch or Work Breakdown Structure (WBS) at various task levels.
- Interface with MIT/LNS Fiscal and Purchasing systems.

The BLAST project is separated into a number of independent branches, each with its own area of responsibility. Each branch is directed by a Branch Manager. The BLAST Project Manager will report to the BLAST Steering Committee and the Bates Directorate on various aspects concerning the project.

A GANTT CHART for the BLAST PROJECT

This Appendix contains one view of the Gantt chart for the project. This view includes the Work Breakdown Structure (WBS) number, the task name as well as the chart. The years shown are fiscal years. Predecessor and successor relationships among tasks are shown as descending arrow lines. Summary tasks are shown as solid bars. Critical path lines are shown as bars with diagonal lines. Baseline, tracking and current status views are available. Associated tables with start and completion dates, resources, costs etc. are also available. This project management model is the primary tool for tracking the project. It was prepared with Microsoft Project.

WBS	Name
1	**Coil Support Structure and Installation Branch**
1.1	**Coil Subbranch**
1.1.1	Freeze Concept
1.1.2	Coil Layout
1.1.3	Specify Survey Fiducials
1.1.4	Coil Design
1.1.5	Conductor Specs
1.1.6	Coil Drawings
1.1.7	Coil Specs
1.1.8	Coil RFQ
1.1.9	Review Coil Quotes
1.1.10	Coil RFP
1.1.11	Design Handler
1.1.12	Detail Fixtures
1.1.13	Fixture RFP
1.1.14	Fixture Fabrication
1.1.15	Inspect Fixtures
1.1.16	Deliver Fixtures
1.1.17	Purchase Copper for coils
1.1.18	**Manufacture Coils**
1.1.18.1	Start of Coil Manufacture
1.1.18.2	Middle of Coil Manufacture
1.1.18.3	End of Coil Manufacture
1.1.19	Obtain Coil Power Supply
1.1.20	Ship Coils
1.1.21	Inspect, Test Coils
1.1.22	Coils Complete
1.2	**Support Structure Subbranch**
1.2.1	Freeze Coil Design
1.2.2	Layout Structure
1.2.3	Design Coil Support
1.2.4	Design Detector Support
1.2.5	Assembly Procedures
1.2.6	Specify Survey Fixtures
1.2.7	Finite Element Analysis
1.2.8	Design Structure
1.2.9	Detail Structure
1.2.10	Detail Rings
1.2.11	Ring Vendor List
1.2.12	Ring Material RFP
1.2.13	Obtain Ring Material
1.2.14	Ring Fabrication RFQ
1.2.15	Review Ring Fab Bids
1.2.16	Structure Vendor List
1.2.17	Structure Specs
1.2.18	Structure RFQ
1.2.19	Review Structure Bids
1.2.20	Ring Fabrication RFP
1.2.21	Fabricate Rings

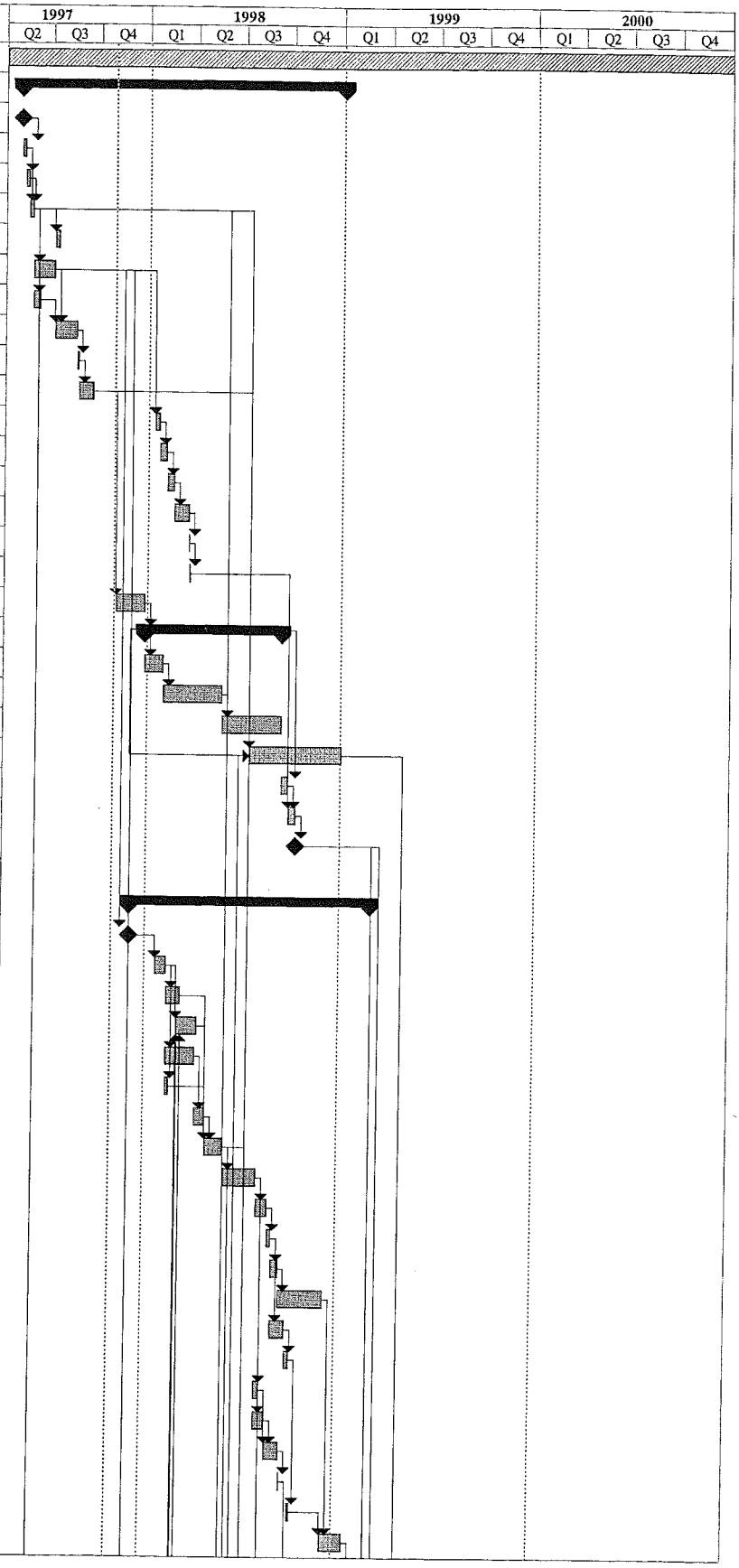

WBS	Name
1.2.22	Inspect Rings
1.2.23	Ship Rings
1.2.24	Structure RFP
1.2.25	Order Structure Matl
1.2.26	Fabricate Structure
1.2.27	Order Jacks, Casters
1.2.28	Order Thompson Bearings
1.2.29	Order Hardware
1.2.30	Assemble at Shop
1.2.31	Inspect Structure
1.2.32	Disassemble at Shop
1.2.33	Ship Structure
1.2.34	Store Structure
1.2.35	Inspect Fiducilization
1.2.36	Structure Complete
1.3	**Installation Subbranch**
1.3.1	Design Quadrupole magnets
1.3.2	Design Quadrupole Supports
1.3.3	Design BLAST Water Connection
1.3.4	Design BLAST Magnet Electrical Connecti
1.3.5	Design Magnet Power Supply Control
1.3.6	Specify AC Services to BLAST Area
1.3.7	Manufacture Quadrupoles
1.3.8	Manufacture Quadrupole Supports
1.3.9	Install Quadrupole Supports
1.3.10	Install quadrupoles
1.3.11	Obtain Materials for Water Connection
1.3.12	Install Water Connections for BLAST
1.3.13	Obtain Materials for Magnet Electrical Conr
1.3.14	Install Magnet Electrical Connections for BI
1.3.15	Fabricate Magnet Power Supply Controls
1.3.16	Install AC Services to BLAST Area
1.3.17	Assemble BLAST Core Device
1.3.18	Test Core Device with Alpha 4 Power suppl
1.3.19	BLAST Ready for Low Field Testing
1.3.20	Install BLAST Power Supply
1.3.21	Field Map Core Device
1.3.22	Blast Core Device Complete
1.4	**Personnel Costs**
2	**Scintillator Branch**
2.1	**Prototype Phase**
2.1.1	Freeze Scint Design
2.1.2	Scintillator Specs
2.1.3	PMT Specs
2.1.4	Light Guide Specs
2.1.5	Scintillator Configuration

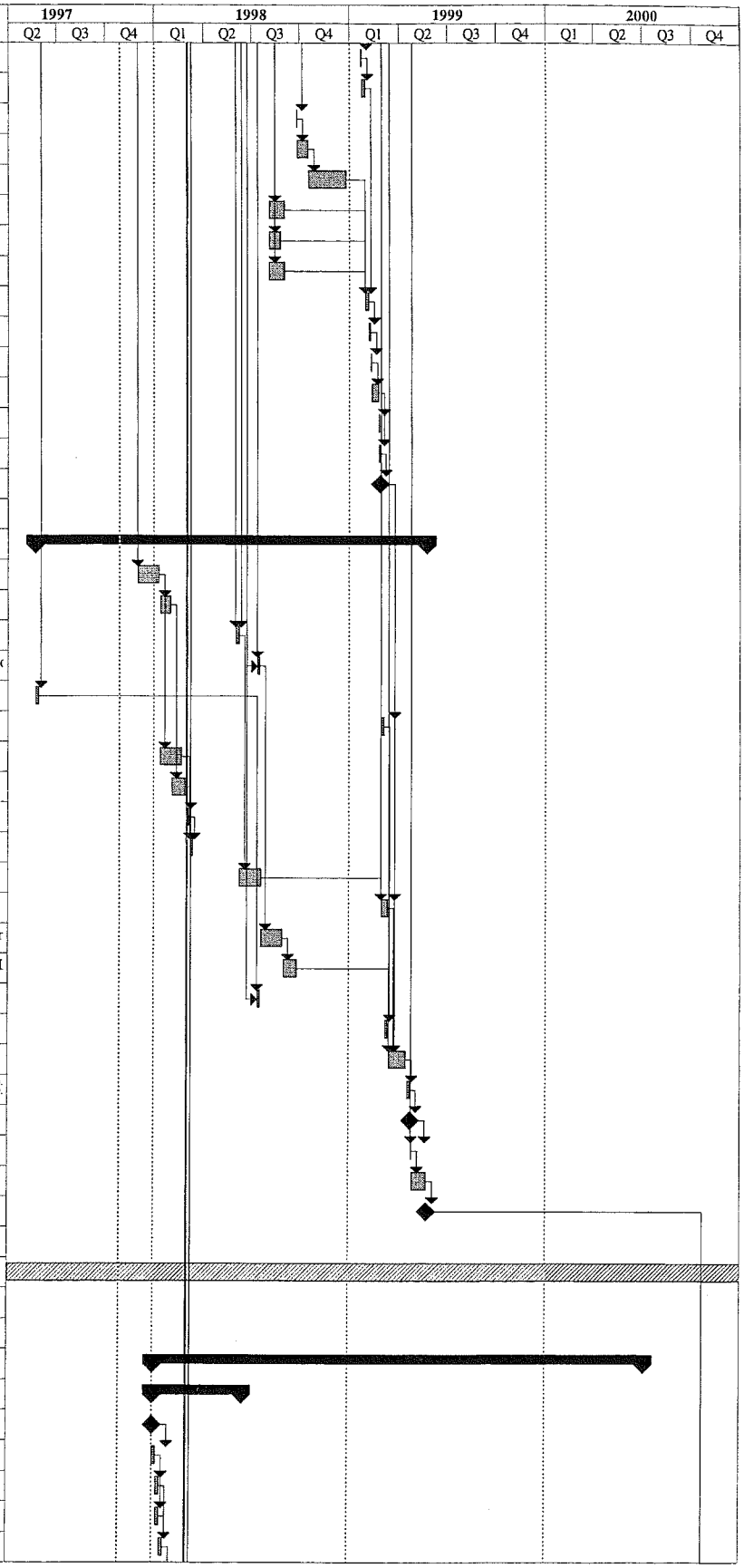

WBS	Name
2.1.6	Design Scintillator and Support
2.1.7	Design Test and Assemble Fixtures
2.1.8	Acquire Scintillator Prototype Materials
2.1.9	Fabricate and Test Prototype
2.2	**Manufacture, Testing and Installation Phase**
2.2.1	Finalize Design
2.2.2	Detail Scintillator Support
2.2.3	Green Light to Proceed
2.2.4	RFQ for Electronics
2.2.5	Review Electronics Bids
2.2.6	RFP for Electronics
2.2.7	Electronics Delivery
2.2.8	Assemble and Test Electronics
2.2.9	Install Electronics
2.2.10	Install Wiring
2.2.11	Test Electronics
2.2.12	RFQ for HV System
2.2.13	Review HV System Bids
2.2.14	RFP for HV System
2.2.15	HV System Delivery
2.2.16	RFP for Support Material
2.2.17	Support Material Delivery
2.2.18	Fabricate Supports
2.2.19	RFQ for PMTs
2.2.20	Review PMT Bids
2.2.21	RFP for PMTs
2.2.22	PMT Delivery
2.2.23	Test PMTs
2.2.24	RFQ for Scintillator/Guide
2.2.25	Review Scintillator/Guide Bids
2.2.26	RFP for Scintillator/Guide
2.2.27	Scintillator/Guider Delivery
2.2.28	Procure Misc. Material
2.2.29	Glue, Wrap and Assemble
2.2.30	Test Scintillators
2.2.31	Crate Scintillators for Shipping
2.2.32	Ship Scintillators
2.2.33	Install Scintillator Assemblies
2.2.34	Scintillator System Checkout
3	**Forward Calorimeter Branch**
3.1	Design Lead Glass Support
3.2	Obtain Lead Glass Detectors
3.3	**Instrument Lead Glass Detectors**
3.3.1	FY 98 Instrumentation
3.3.2	FY 99 Instrumenation
3.4	Lead Glass System Checkout
3.5	Forward Calorimeter Branch Complete
4	**Cerenkov Branch**

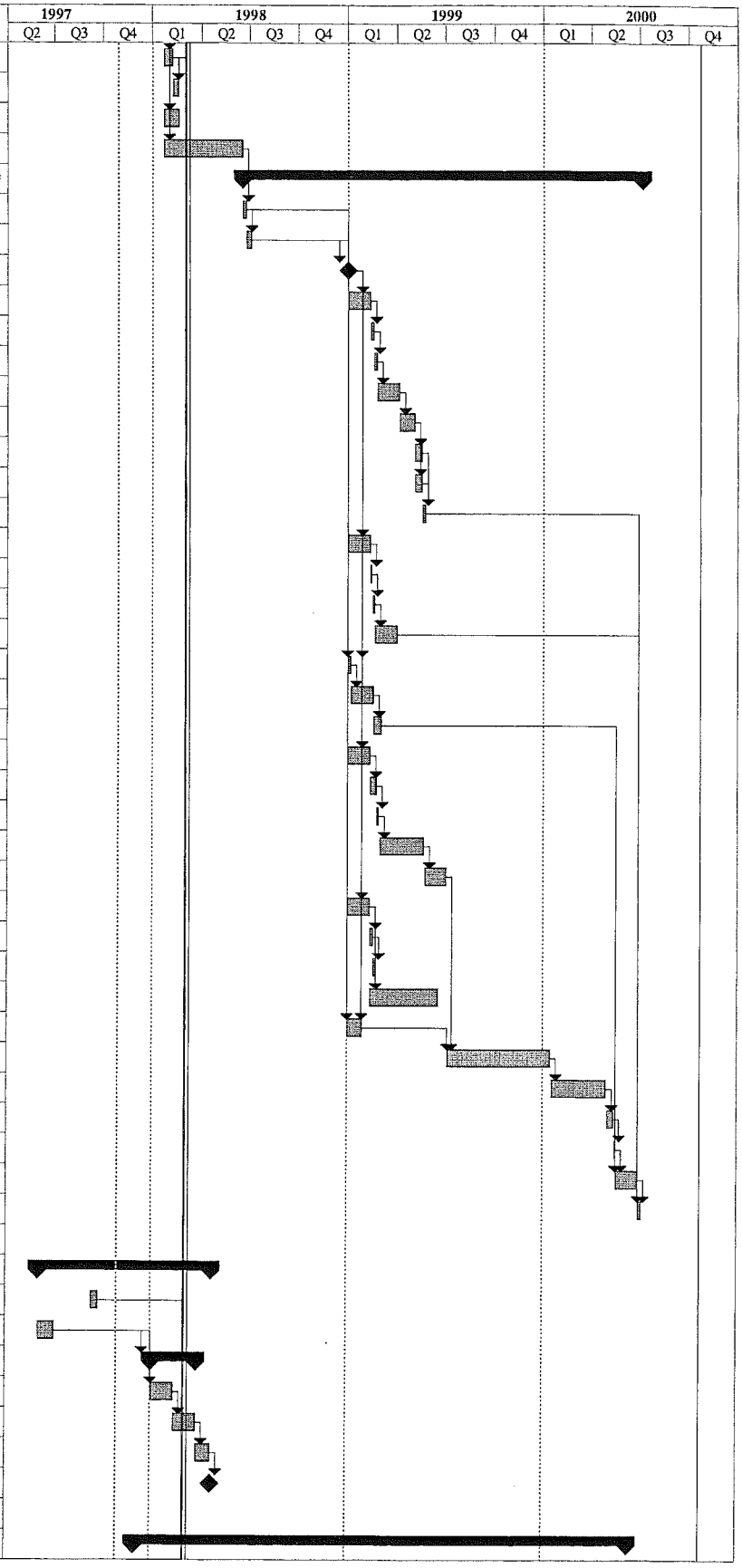

WBS	Name
4.1	**Prototype Phase**
4.1.1	Optics Studies
4.1.2	Cerenkov Specs
4.1.3	Design Cerenkov Modules
4.1.4	Design Gas System
4.1.5	Design Module Support
4.1.6	Design Electronics
4.1.7	PMT Spec
4.1.8	Build Prototype
4.1.9	Test Prototype PMT, Base
4.2	**Manufacture, Testing and Installation Phase**
4.2.1	Finalize Cerenkov Module Design
4.2.2	Finalize Module Support Design
4.2.3	Finalize Gas System Design
4.2.4	Obtain Misc. Material
4.2.5	RFP for Electronics
4.2.6	Electronics Delivery
4.2.7	Assemble and Test Electronics
4.2.8	Install Electronics
4.2.9	Install Wiring
4.2.10	RFP for Cerenkov Module
4.2.11	First Half Cerenkov Module Delivery
4.2.12	Ship Cerenkov Modules to ASU
4.2.13	Second Half Cerenkov Module Delivery
4.2.14	Ship Cerenkov Modules to ASU
4.2.15	Fabricate Cerenkov Support
4.2.16	Fabricate Cerenkov Gas System
4.2.17	Cerenkov tube, base shield delivery
4.2.18	Cerenkov tube, base shield delivery
4.2.19	Install Tubes and Test Modules
4.2.20	Install Tubes and Test Modules
4.2.21	Ship Cerenkov to Bates
4.2.22	Ship Cerenkov to Bates
4.2.23	Install Cerenkov
4.2.24	System Checkout
4.2.25	Cerenkov System Complete
5	**Recoil Detector Branch**
5.1	Develop Recoil Detector Phase 1
5.2	Develop Recoil Detector Phase 2
6	**Neutron Detector Branch**
6.1	**Prototype Phase**
6.1.1	Freeze Neutron Detector Design
6.1.2	Neutron Detector Specs
6.1.3	PMT Specs
6.1.4	Light Guide Specs
6.1.5	Neutron Detector Configuration
6.1.6	Design Neutron Detector and Support
6.1.7	RFQ for PMTs

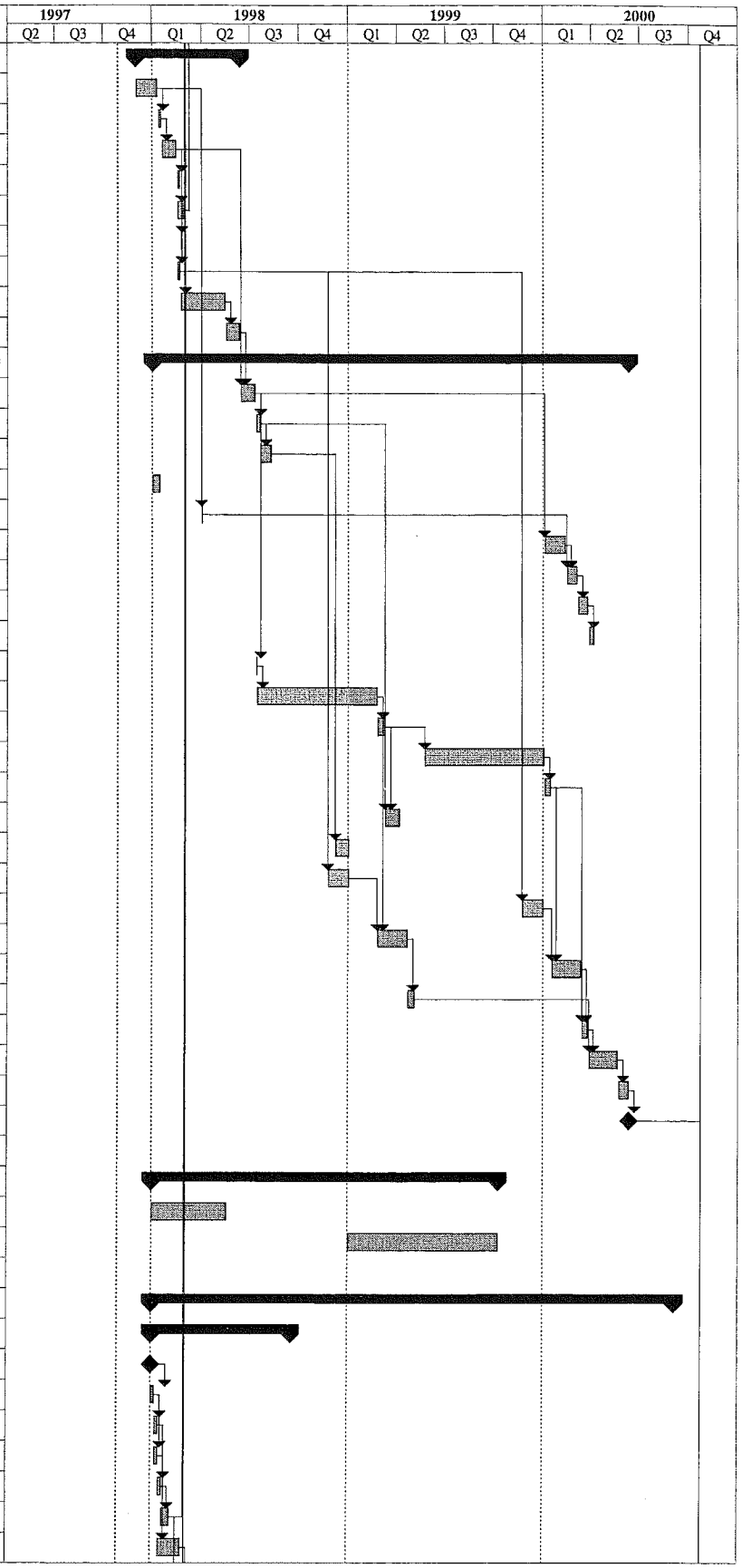

WBS	Name
6.1.8	RFP for PMTs
6.1.9	PMT Delivery
6.1.10	RFQ for Neutron Detector scintillator/guide
6.1.11	RFP for Neutron Detector Scintillator/Guide
6.1.12	Scintillator/Guide Delivery
6.1.13	Procure Misc. Material
6.1.14	Glue, Wrap and Assemble
6.1.15	Test Neutron Detector
6.2	**Manufacture, Testing and Installation Phase**
6.2.1	Finalize Design
6.2.2	Detail Neutron Detector Support
6.2.3	Green Light to Proceed
6.2.4	RFQ for Electronics
6.2.5	Review Electronics Bids
6.2.6	RFP for Electronics
6.2.7	Electronics Delivery
6.2.8	Assemble and Test Electronics
6.2.9	Install Electronics
6.2.10	Install Wiring
6.2.11	Test Electronics
6.2.12	RFP for Support Material
6.2.13	Support Material Delivery
6.2.14	Fabricate Supports
6.2.15	RFQ for PMTs
6.2.16	RFP for PMTs
6.2.17	PMT Delivery
6.2.18	Test PMTs
6.2.19	PMT Delivery
6.2.20	Test PMTs
6.2.21	Procure Misc. Material
6.2.22	RFQ for Neutron Detector
6.2.23	RFP for Neutron Detector
6.2.24	Scintillator/Guide Delivery
6.2.25	Glue, Wrap and Assemble
6.2.26	Test Neutron Detector
6.2.27	Scintillator/Guide Delivery
6.2.28	Glue, Wrap and Assemble
6.2.29	Test Neutron Detector
6.2.30	Crate Neutron Detectors for Shipping
6.2.31	Ship Neutron Detectors
6.2.32	Install Neutron Detectors
6.2.33	Neutron Detector System Checkout
6.2.34	Neutron Detectors Complete
7	**Drift Chamber Branch**
7.1	**Prototype Phase**
7.1.1	Freeze Chamber Concept
7.1.2	Chamber Specs
7.1.3	Electronics Specs

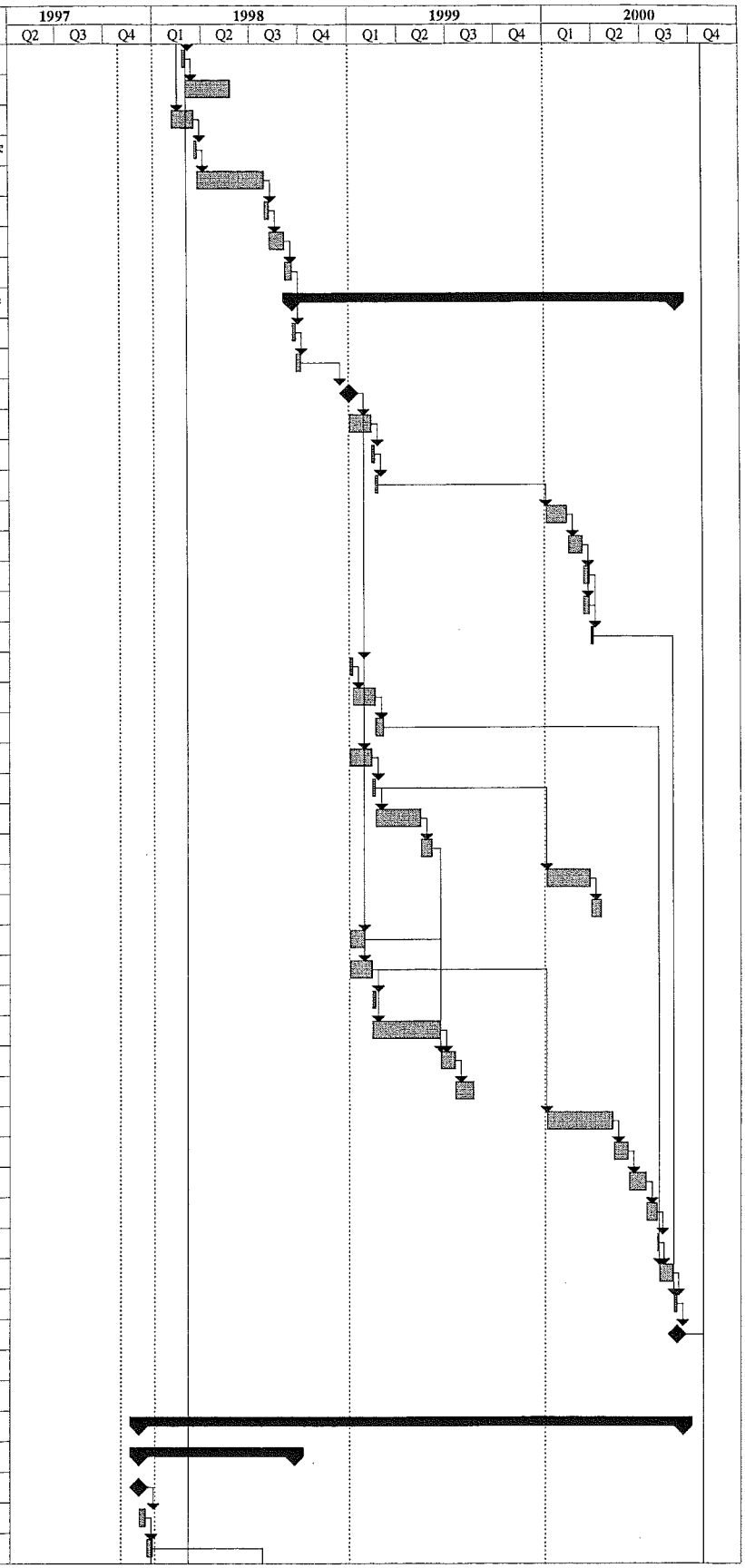

WBS	Name
7.1.4	Specify Survey Fiducials
7.1.5	Finalize Prototype Design
7.1.6	Green Light to proceed
7.1.7	RFP for Wall Material
7.1.8	Frame Material Delivery
7.1.9	RFP for Wire, Feedthroughs
7.1.10	Wire, Feedthrough Delivery
7.1.11	Machine Wall Material
7.1.12	Assemble Chamber Walls
7.1.13	Install Feedthroughs
7.1.14	String Wires
7.1.15	Procure Misc. Materials
7.1.16	Assemble Prototype Chamber
7.1.17	Acquire Test Electronics
7.1.18	Test Prototype Chamber
7.1.19	Prototype Phase Complete
7.2	**Manufacture, Testing and Installation Phase**
7.2.1	**Electronics Subphase**
7.2.1.1	Green Light to Proceed
7.2.1.2	RFQ for FASTBUS
7.2.1.3	RFQ for Amp/Disc
7.2.1.4	Review FASTBUS Bids
7.2.1.5	RFP for FASTBUS
7.2.1.6	FY 99 FASTBUS Delivery
7.2.1.7	Review Amp/Disc Bids
7.2.1.8	RFP for Amp/Disc
7.2.1.9	FY 2000 FASTBUS Delivery
7.2.1.10	FY 2001 FASTBUS Delivery
7.2.1.11	FY 99 Amp/Disc Delivery
7.2.1.12	FY 2000Amp/Disc Delivery
7.2.1.13	RFQ for HV
7.2.1.14	Review HV Bids
7.2.1.15	RFP for HV
7.2.1.16	HV System Delivery
7.2.1.17	Cable Runs from BLAST to Electronics
7.2.1.18	Cable Runs from BLAST to Amp/Disc
7.2.1.19	Assemble and Test FASTBUS
7.2.1.20	Assemble and Test Amp/Disc
7.2.1.21	Install Electronics
7.2.1.22	Install Additional Wiring
7.2.1.23	Chamber Electronics Complete
7.2.2	**Drift Chamber Fabrication Subphase**
7.2.2.1	Design Chambers
7.2.2.2	Design Support
7.2.2.3	Finalize Design
7.2.2.4	Green Light to proceed
7.2.2.5	RFP for Gas System Components
7.2.2.6	First Gas System Component Delivery
7.2.2.7	Second Gas System Delivery
7.2.2.8	Assemble and Test First Gas System

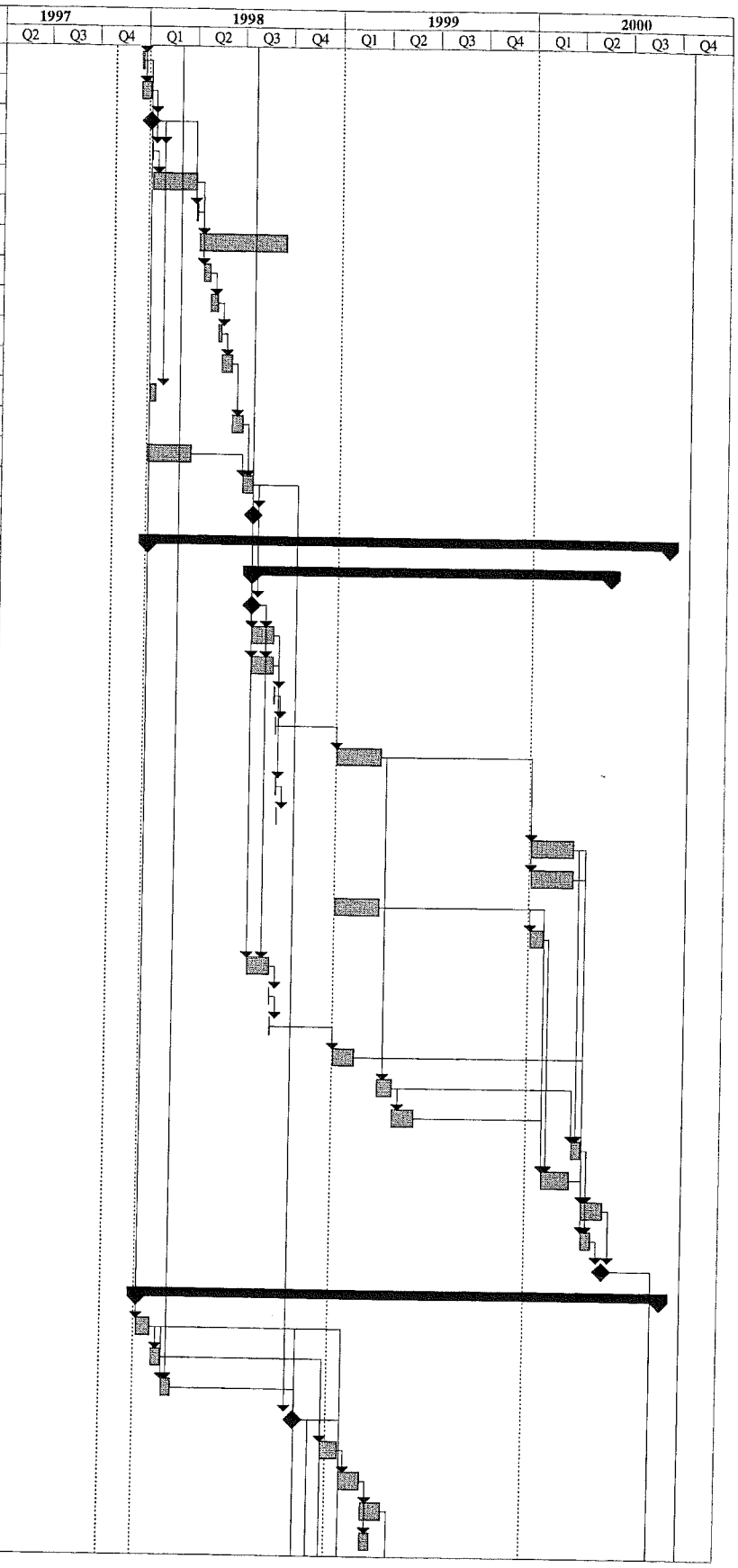

WBS	Name
7.2.2.9	Assemble and Test Second Gas System
7.2.2.10	RFP for Support Material
7.2.2.11	Support Material Delivery
7.2.2.12	Fabricate First Supports
7.2.2.13	Fabricate Second Supports
7.2.2.14	Assemble/Test Supports
7.2.2.15	Assemble/Test Supports
7.2.2.16	RFP for Frame Material
7.2.2.17	Frame Material Delivery
7.2.2.18	Frame Material Delivery
7.2.2.19	RFP for Wire, Feedthroughs
7.2.2.20	Wire, Feedthrough Delivery
7.2.2.21	Wire, Feedthrough Delivery
7.2.2.22	Machine Frame Material
7.2.2.23	Machine Frame Material
7.2.2.24	Assemble Chamber Frames
7.2.2.25	Assemble Chamber Frames
7.2.2.26	Install Feedthroughs
7.2.2.27	Install Feedthroughs
7.2.2.28	String Wires
7.2.2.29	String Wires
7.2.2.30	Procure Misc. Materials
7.2.2.31	Assemble and Test Unit
7.2.2.32	Assemble and Test Unit
7.2.2.33	Install Chambers
7.2.2.34	Install Chambers
7.2.2.35	System Checkout
7.2.2.36	System Checkout
7.2.2.37	Drift Chambrs Complete
8	**Data Acquisition Branch**
8.1	**Physics Software**
8.1.1	Specify Physics Software
8.1.2	GEANT Simulation
8.1.3	GEANE Tracking
8.1.4	Fast Tracking
8.1.5	Fast Particle Identification
8.1.6	Particle Correlation Software
8.1.7	Physics Simulation Complete
8.1.8	Convert Simulation to DAQ Format
8.1.9	Write Host Physics Code
8.2	**System Software and Hardware**
8.2.1	Specify DAQ Hardware and Software
8.2.2	Obtain CODA Software
8.2.3	Design DAQ Host System
8.2.4	RFP for Host System
8.2.5	DAQ System Bid Cycle
8.2.6	Review DAQ Host System Bids
8.2.7	RFP for DAQ Host System
8.2.8	Initial DAQ Host System Delivery

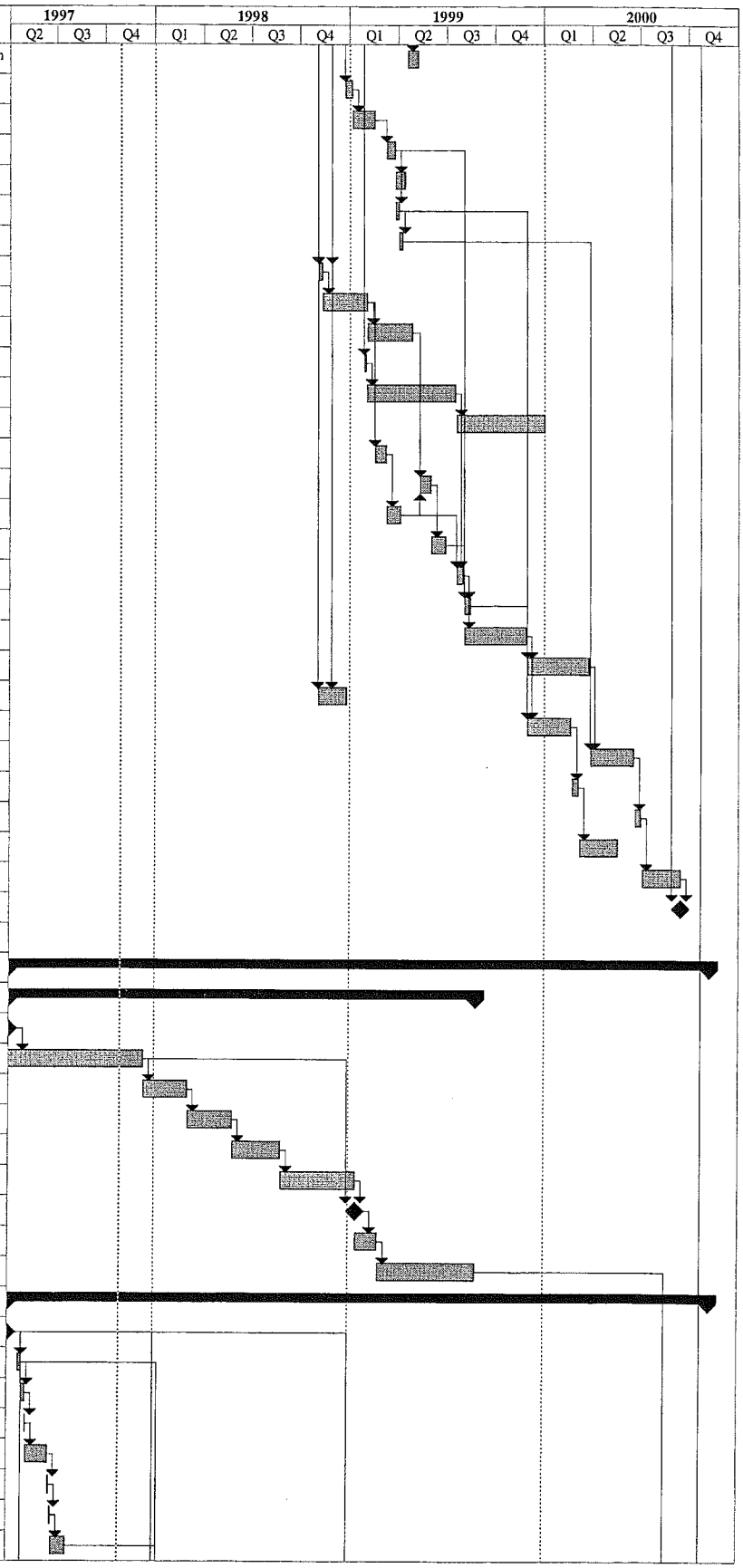

WBS	Name
8.2.9	Install CODA Host Software
8.2.10	Make BLAST Specific Changes
8.2.11	Test BLAST System Software
8.2.12	Specify RISC Workstations
8.2.13	RFQ for RISC Workstations
8.2.14	RISC Workstation Bid Cycle
8.2.15	Review RISC Workstation Bids
8.2.16	RFP for RISC Workstation
8.2.17	Install CODA Workstation Software
8.2.18	Delivery of CODA Workstations
8.2.19	Specify FASTBUS RoC, Mem Spy Crates
8.2.20	RFQ For FASTBUS
8.2.21	RFP for FASTBUS
8.2.22	Delivery of First System FASTBUS/VME
8.2.23	Delivery of FY 98 System FASTBUS
8.2.24	Delivery of FY 00 System FASTBUS
8.2.25	Delivery of Balance of System FASTBUS
8.2.26	Delivery of Racks
8.2.27	Procure Misc Material
8.2.28	Delivery of Balance of VME
8.2.29	Debug Installation
8.2.30	Install Dedicated LAN
8.2.31	Install DAQ Hardware in Counting House
8.2.32	Install BLAST DAQ Hardware in Electronic
8.2.33	Test Initial DAQ Hardware Configuration
8.2.34	Test Final DAQ Hardware Configuration
8.2.35	Write FASTBUS Calibration Software
8.2.36	Test FASTBUS Calibration SW
8.2.37	Write HV, Run control Software
8.2.38	Test Control Software
8.2.39	Write Trigger Control SW
8.2.40	Test Trigger Control SW
8.2.41	Write Diagnostic SW
8.2.42	Test Diagnostic SW
8.2.43	System Software complete
8.2.44	Install Host Physics Code
8.2.45	Test Installed Physics Code
8.2.46	DAQ Physics Code Complete
9	**Trigger Branch**
9.1	Specify Trigger Hardware
9.2	Purchase Trigger Hardware
9.3	Purchase Trigger Hardware
10	**Counting House Complete**
11	**BLAST and Detector Package Complete**

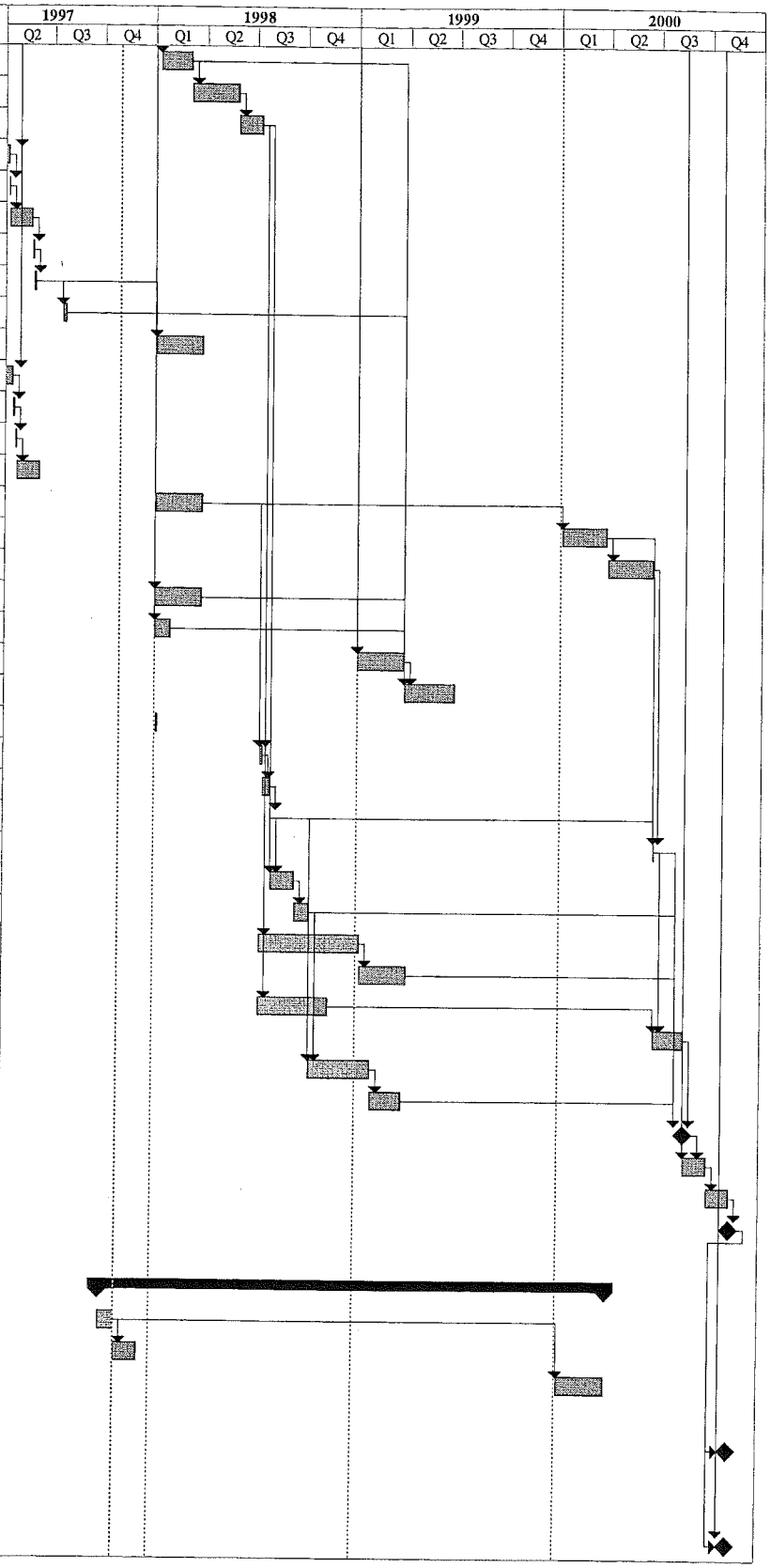

References

[1] S. Glashow, Physica **96A**, 27 (1979).

[2] G. B. V. Vento and A. Jackson, Phys. Lett. **102B**, 97 (1981).

[3] G. K. N. Isgur and R. Koniuk, Phys. Rev. **D25**, 2394 (1982).

[4] S. A. C. R. D. Viollier and A. K. Kerman, Nucl. Phys. **A407**, 269 (1983).

[5] M. V. N. Murphy and R. K. Bhaduri, Phys. Rev. Lett. **54**, 745 (1985).

[6] N. Isgur and G. Karl, Phys. Rev. **D18**, 4187 (1978).

[7] N. Isgur and G. Karl, Phys. Rev. **D19**, 2653 (1979).

[8] K. Baetzner *et al.*, Phys. Lett. **39B**, 575 (1972).

[9] R. Siddle *et al.*, Nucl. Phys. **B35**, 93 (1971).

[10] J. C. Alder *et al.*, Nucl. Phys. **B46**, 573 (1987).

[11] C. Mistretta *et al.*, Phys. Rev. **184**, 1487 (1969).

[12] K. Baetzner *et al.*, Nucl. Phys. **B76**, 1 (1974).

[13] S. Nozawa and T.-S. H. Lee, Nucl. Phys. **A513**, 511 (1990).

[14] S. Nozawa *et al.*, Nucl. Phys. **A513**, 459 (1990).

[15] S. Nozawa and T.-S. H. Lee, Nucl. Phys. **A513**, 543 (1990).

[16] J. M. Laget, Nucl. Phys. **A481**, 765 (1988).

[17] J. M. Laget, in *Workshop on Electronuclear Physics with Internal Targets and the BLAST Detector*, edited by R. Alarcon and M. Butler (World Scientific, Singapore, 1992), p. 71.

[18] R. K. Bhaduri, *Models of the Nucleon from Quarks to Soliton* (Addison-Wesley Publishing Co. Inc., Redwood City, California, 1988).

[19] H. Henning *et al.*, Phys. Rev. **C52**, R471 (1995).

[20] M. Ferro-Luzzi *et al.*, Phys. Rev. Lett. **77**, 2630 (1996).

[21] T. Eden *et al.*, Phys. Rev. **C50**, R1749 (1994).

[22] Bates proposal, 1991, MIT-BATES # 91–09.

[23] T. Donnelly and A. Raskin, Annals of Physics **169**, 247 (1986).

[24] R. Prepost, R. M. Simmonds, and B. H. Wiik, Phys. Rev. Lett. **21**, 1271 (1968).

[25] M. Garcon *et al.*, Phys. Rev. **C49**, 2516 (1994), and references therein.

[26] M. E. Schulze *et al.*, Phys. Rev. Lett. **52**, 597 (1984).

[27] V. F. Dimitrev *et al.*, Phys. Lett. **157B**, 143 (1985).

[28] S. Popov *et al.*, in *AIP Conf. Proc.* (AIP, New York, 1995), Vol. 339, p. 530.

[29] R. Gilman *et al.*, Phys. Rev. Lett. **65**, 1733 (1990).

[30] R. Schiavilla and D. O. Riska, Phys. Rev. **C43**, 437 (1990).

[31] E. Hummel and J. A. Tjon, Phys. Rev. **C42**, 423 (1990).

[32] P. L. Chung, F. Coester, B. D. Keister, and W. N. Polyzou, Phys. Rev. **C37**, 2000 (1988).

[33] P. G. Blunden, W. R. Greenberg, and E. L. Lomon, Phys. Rev. **C40**, 1541 (1989).

[34] C. E. Carlson, Nucl. Phys. **A508**, 481c (1990).

[35] W. Leidmann, E. L. Tomusiak, and H. Arenhövel, Phys. Rev. **C43**, 1022 (1991).

[36] W. Leidmann, E. L. Tomusiak, and H. Arenhövel, Phys. Rev. **C46**, 455 (1992).

[37] S. Galster *et al.*, Nucl. Phys. **B32**, 221 (1971).

[38] F. Klein, 1996, PANIC96 Conference, Williamsburg, Virginia.

[39] L. Frankfort and M. Strikman, Phys. Reports **160**, 235 (1988).

[40] E. Lomon, private communications.

[41] C. Woodward *et al.*, Phys. Rev. Lett. **65**, 698 (1990).

[42] A. Thompson *et al.*, Phys. Rev. Lett. **68**, 2901 (1992).

[43] J.-O. Hansen *et al.*, Phys. Rev. Lett. **74**, 654 (1995).

[44] E. Brash *et al.*, Phys. Rev. **C47**, 2064 (1993).

[45] M. Meyerhoff *et al.*, Phys. Lett. B. **327**, 201 (1994).

[46] K. Lee *et al.*, Phys. Rev. Lett. **70**, 738 (1993).

[47] M. Miller *et al.*, Phys. Rev. Lett. **74**, 502 (1995).

[48] P. Anthony *et al.*, Phys. Rev. Lett. **71**, 959 (1993).

[49] M. A. Espy *et al.*, Phys. Rev. Lett. **76**, 3667 (1996).

[50] HERMES proposal, 1990, DESY No. PRC–90–01.

[51] Measurement of Quasielastic Spin-Dependent Electron Scattering from a Polarized ^{3}He Internal Target, 1994, NIKHEF Experiment #94–05.

[52] CEBAF proposal, 1994, experiment #94–10.

[53] CEBAF proposal, 1995, experiment #95–01.

[54] R. Schulze and P. Sauer, Phys. Rev. **C48**, 38 (1993).

[55] R. Milner *et al.*, Phys. Lett. **B379**, 67 (1996).

[56] S. Frullani and J. Mougey, in *Single-particle properties of nuclei through* (e, e'p) *reactions*, Vol. 14 of *Advances in Nuclear Physics*, edited by J. W. Negele and E. Vogt (Plenum Press, New York, 1984).

[57] M. Epstein *et al.*, Phys. Rev. **C32**, 967 (1985).

[58] S. Ishikawa *et al.*, Phys. Lett. **B339**, 293 (1994).

[59] K. Dow *et al.*, Phys. Rev. Lett. **61**, 1706 (1988).

[60] J.-M. Laget, Phys. Lett. B **273**, 367 (1991).

[61] J.-M. Laget, Phys. Lett. B **276**, 398 (1992).

[62] H. Gao *et al.*, Phys. Rev. **C50**, R546 (1984).

[63] J.-O. Hansen, in *Proceedings of the VII Workshop on Perspectives in Nuclear Physics at Intermediate Energies, ICTP* (World Scientific, Singapore, 1996).

[64] S. Platchkov *et al.*, Nucl. Phys. **A510**, 740 (1990).

[65] H.J.Lipkin and T.-S.H.Lee, Phys. Lett. B **183**, 22 (1987).

[66] R. Milner and T. Donnelly, Phys. Rev. C **37**, 870 (1988).

[67] J.-M. Laget, J. Phys. **G 14**, 1445 (1988).

[68] Bates proposal, 1991, MIT-BATES # 91–10.

[69] M. Oka and K. Yazaki, in *Quarks and Nuclei*, edited by W. Weise (World Scientific Press, Singapore, 1984), p. 490.

[70] The BLAST Collaboration, A proposal for the Bates Large Acceptance Spectrometer Toroid, 1992, MIT-BATES.

[71] Bates proposal, 1991, MIT-BATES # 89–21.

[72] NIKHEF-K proposal, 1991, experiment #91–12.

[73] T. Zwart *et al.*, Nucl. Instr. Meth. **384A**, 299 (1997).

[74] R. Holt, in *AIP Conf. Proc.* (AIP, New York, 1987), Vol. 161, p. 138.

[75] R. Holt, in *AIP Conf. Proc.* (AIP, New York, 1984), Vol. 123, p. 499.

[76] in 9^{th} *Intl. Symposium on High Energy*, edited by K. Althoff and W. Meyer (Springer-Verlag, New York, 1993), p. 151.

[77] M. Barner *et al.*, in *AIP Conf. Proc.* (AIP, New York, 1994), Vol. 293, p. 14.

[78] K. Lee *et al.*, Nucl. Instrum. Meth. **A333**, 294 (1993).

[79] A. Kastler, J. Phys. Radium **11**, 225 (1950).

[80] W. Happer, Rev. Mod. Phys. **44**, 169 (1972).

[81] L. Kramer *et al.*, Nucl. Instr. and Meth. **A365**, 49 (1995).

[82] W. Korsch *et al.*, (to be published).

[83] Z.-L. Zhou *et al.*, Nucl. Instrum. Meth. **A378**, 40 (1996).

[84] K. Coulter *et al.*, Phys. Rev. Lett. **68**, 174 (1992).

[85] C. Tschalaer, Bates Technical Note, Bates (1997).

[86] P. B. Wilson, 1989, SLAC-PUB-4547, SLAC/AP-66.

[87] E. Chumbes, Injection Flash Studies of the Bates SHR Using GEANT, MIT/LNS (1992).

[88] N. P. Vodinas *et al.*, 1995, International Workshop on Polarized Beams and Polarized Gas Targets, Cologne, Germany, June 6-9.

[89] Bates proposal, 1991, MIT-BATES # 89–12.

[90] C. Bloch *et al.*, Nucl. Instrum. Meth. **A354**, 437 (1995).

[91] T. Chupp, R. Holt, and R. Milner, Ann. Rev. Nucl. and Part. Sci. **44**, 373 (1994).

[92] K. Ackerstaff *et al.*, to be published in Phys. Lett. B hepex/9703005.

[93] F. Colegrove, L. Schearer, and G. Walters, Phys. Rev. **132**, 2561 (1963).

[94] C. L. Bohler *et al.*, J. Appl. Phys. **63**, 2497 (1988).

[95] W. Lorenzon *et al.*, Phys. Rev. **A47**, 468 (1993).

[96] M. Ferro-Luzzi *et al.*, Nucl. Instrum. Meth. **A364**, 44 (1995).

[97] M. Ferro-Luzzi *et al.*, 1997, (to be published).

[98] H. Bulten *et al.*, 1997, (to be published).

[99] Z.-L. Zhou *et al.*, Nucl. Instrum. Meth. **A379**, 212 (1996).

[100] Z.-L. Zhou *et al.*, 1997, (submitted for publication).

[101] J. van den Brand *et al.*, Phys. Rev. Lett. **78**, 1235 (1997).

[102] IUCF proposal, 1996, experiment CE66.

[103] M. Poelker *et al.*, Phys. Rev. **A50**, 2450 (1994).

[104] H. Gao, 1995, Intl. Workshop on Polarized Beams and Targets, Cologne.

[105] J. Stenger *et al.*, Phys. Rev. Lett. **78**, 4177 (1997).

[106] J. Fedchak, 1995, Intl. Workshop on Polarized Beams and Targets, Cologne.

[107] J. Kelsey, BLAST Report 97–01, Bates (1997).

[108] T. Hasegawa *et al.*, Nucl. Instr. Meth. **342A**, 383 (1994).

[109] D. W. Higinbotham, 1997, (to be published in NIM).

[110] J. van den Brand, private communication, 1997.

[111] D. Doughty *et al.*, IEEE Trans. on Nucl. Sci. **NS 39**, 241 (1992).

[112] A. Young, M.S. Physics Thesis, MIT (1992).